

RE-245

PHOTOMETRIC MEASUREMENTS OF  
SIMULATED LUNAR SURFACES

April 1966

N66 27054

(ACCESSION NUMBER)

(THRU)

166  
(PAGES)

1  
(CODE)

OR-65365  
(NAAE CR OR TMX OR AD NUMBER)

30  
(CATEGORY)

FACILITY FORM 802

*Grumman*

RESEARCH DEPARTMENT

GPO PRICE \$

OFSTI PRICE(S) \$

Hard copy (HC)

Microfiche (MF)

4552 JUL 66

GRUMMAN AIRCRAFT ENGINEERING CORPORATION  
BETHPAGE NEW YORK

PHOTOMETRIC MEASUREMENTS OF  
SIMULATED LUNAR SURFACES

by

J. D. Halajian

and

F. A. Spagnolo

Geo-Astrophysics Section

April 1966

Final Report on NASA Contract No. NAS 9-3182

Approved by: *Charles E. Mack, Jr.*  
Charles E. Mack, Jr.  
Director of Research

## FOREWORD

This work represents the Final Report on "Photometric Measurements of Simulated Lunar Surfaces" for the National Aeronautics and Space Administration, Manned Spacecraft Center, Houston, Texas, under an extension of Contract NAS 9-3182 to the Grumman Aircraft Engineering Corporation, Bethpage, N. Y.

The follow-on contract authorized a seven-month study consisting of laboratory experiments and theoretical analyses aimed at correlating the physical and photometric properties of the lunar surface. The study was conducted under the cognizance of the Space Science Office with Mr. Robert L. Jones of the Lunar Surface Technology Branch, Geophysics Section, serving as Technical Representative.

### ACKNOWLEDGMENTS

The authors are indebted to H. B. Hallock of Grumman's Servo Engineering Department and to his assistants J. Grusauskas, D. R. Lamberty, and D. Schlaijker for improving, recalibrating and operating the photometric analyzer, building the "bead" models, and making the measurements. We are very grateful to K. Brand of Computing Sciences for his invaluable aid in programming the analyses of Phase II and Phase III. The helpful comments of Dr. G. McCoyd, J. Reichman, Dr. S. N. Milford, Dr. W. Egan, and L. L. Smith are also acknowledged.



## SUMMARY

The purpose of this study is to improve our knowledge of the engineering properties of the optical layer of the lunar surface by means of physical and theoretical models that obey the known photometric properties of that surface.

The Grumman Photometric Analyzer has been extensively overhauled and recalibrated. Assumed spectral responses of our photometric system and sun-sensor systems used in lunar observations are given. Major instrumental modifications include the addition of filters for spectrophotometric measurements and the enlargement of the beam splitter to record brightness changes near zero phase angles with higher fidelity.

In Phase I, measurements of albedo and brightness as a function of wavelength have been made on six natural specimens ranging from fine powders to massive slags. Most of the specimens exhibit the "opposition effect" recently observed on the moon. This phenomenon is tentatively attributed to color and roughness effects. Like the lunar surface, the albedo of the specimens is wavelength dependent. Their backscatter, however, is relatively insensitive to changes in wavelength within the investigated spectrum interval of about  $0.48\mu$  to  $1.0\mu$ . It is recommended that similar measurements on the moon and on terrestrial analogs be extended to larger wavelengths for possible additional clues to the microstructure of the lunar surface.

In Phase II, the photometry of "suspended particles" i.e., dust clouds, is studied by independent experimental and analytical means. Subject to the shortcomings of the laboratory models and the simplifying assumptions made in the analysis, both approaches appear to lead to similar negative results, and indicate that dust clouds fail to exhibit the general backscattering characteristics of the moon.

In Phase III, extensive computer analyses are performed to correlate the photometric and geometric properties of various idealized patterns consisting of horizontal and/or vertical elements. The effects of shadowing, albedo, and basic scattering laws on the photometric function are analyzed and evaluated. It is found that "vertical" elements, "horizontal" overhanging members, and numerous "secondary" pits are necessary building blocks for a model that backscatters light like the moon at all viewing and phase angles including those near opposition. The model may not be unique but its evolution toward a "cellular" rather than a "particulate" type of structure is interesting and its behavior under given inputs is instructive.

Current studies of lunar "models" based on crude data could culminate with studies of discrete areas of the moon if and when high resolution data on these areas become available. It is recommended that earth-based measurements of the reflection and emission properties of candidate lunar landing sites be made and analyzed as soon as possible.

## TABLE OF CONTENTS

<u>Item</u>	<u>Page</u>
Introduction .....	1
Method of Investigation .....	3
Modifications and Performance of the Grumman Photometric Analyzer .....	5
Filter Accommodations .....	5
Spectral Response Studies .....	5
Improvement of Beam Splitter .....	8
Performance of New Beam Splitter .....	8
Phase I - Spectral Photometry .....	10
Purpose .....	10
Test Specimens .....	10
Experiments .....	11
Discussion of Test Results .....	11
Spectral Albedo Measurements .....	13
Spectral Photometric Measurements .....	14
Phase II - Photometry of Suspended Particles .....	71
Purpose .....	71
Experimental Models .....	71
Discussion of Test Results .....	72
Analysis and Discussion of Results .....	73
Phase III - Geometry of Backscattering Surfaces .....	83
Purpose .....	83
Basic Analytical Models .....	83
Discussion of Analytical Results for Basic Models ...	85
Modifications of Basic T-Model .....	87
Discussion of Analytical Results for Modified T-Model .....	88

<u>Item</u>	<u>Page</u>
Conclusions .....	120
Recommendations .....	122
Lunar Observations .....	122
Terrestrial Observation .....	123
Laboratory Experiments .....	123
Theoretical Analyses .....	123
References .....	125
Appendix .....	127
List of Symbols.....	127
Discussion of Computer Program.....	128
Photogeometric Analysis of Contrived Models.....	131

## LIST OF ILLUSTRATIONS

<u>Figure</u>		<u>Page</u>
1.	The Grumman Photometric Analyzer .....	16
2.	Filter Slides Mounted at Light Source .....	17
3.	Spectral Responses at Integrated Visible (V) Light .....	18
4.	Spectral Responses with Blue (B) Filter .....	19
5.	Spectral Response Curves with Red (R) Filter .....	20
6.	Spectral Response Curves with Infrared (I) Filter .....	21
7.	New Improved Beam Splitter Mounted in Front of Light Source .....	22
8.	Hawaiian Volcanic Cinder Measured with New Beam Splitter .....	23
9.	Close-up View of Light Trap .....	26
10.	Wall Installation of Light Trap .....	27
11.	Photometric Function of Magnesium Carbonate (Standard Diffuser) and Light Trap .....	28
12.	Albedo vs. Wavelength of Moon and Test Specimens .....	29
13.	Photometry of Volcanic Cinder No. 4 .....	30
14.	Photometry of Furnace Slag No. 1 .....	36
15.	Photometry of Coral No. 2 .....	42
16.	Photometry of Scoria No. 2 .....	48

<u>Figure</u>		<u>Page</u>
17.	Photometry of Copper Oxide Powder on Flat Board .....	54
18.	Photometry of Copper Oxide Powder on Foam .....	60
19.	Volcanic Cinder No. 4 .....	66
20.	Furnace Slag No. 1 .....	67
21.	Coral No. 2 .....	68
22.	Scoria No. 2 .....	68
23.	Copper Oxide .....	69
24.	Copper Oxide on Foam .....	70
25.	Experimental Models of Suspended Particles .....	78
26.	Photometry of Suspended Particles Model .....	79
27.	Analytical Suspended Particle (Dust Cloud) Model .....	81
28.	Photometry of Suspended Particle (Dust Cloud) Model .....	82
29.	Geometry of Five Contrived Photometric Models .....	93
30a.	Extent of Moon-Model Photometric Deviations - Suspended Strip Model (Lambert Scattering) .....	94
30b.	Extent of Moon-Model Photometric Deviations - Vertical Strip Model (Lambert Scattering) .....	95
30c.	Extent of Moon-Model Photometric Deviations - Furrow Model (Lambert Scattering) .....	96

<u>Figure</u>		<u>Page</u>
30d.	Extent of Moon-Model Photometric Deviations - T-Model (Lambert Scattering) .....	97
31.	Photometry of Basic Vertical and Suspended Strip Models (Lambert Scattering) ( $b \leq a$ ) .....	98
32.	Photometry of T and Furrow Models (Lambert Scattering) ( $b \leq a$ ) .....	99
33.	Photometry of T and Furrow Models (Lambert Scattering) ( $b \leq a$ ) .....	100
34.	Photometry of Furrow Model for Different Scattering Law and Albedo Conditions .....	101
35.	Photometry of Basic T-Model for Different Scattering Law and Albedo Conditions .....	107
36.	Photometry of Modified T-Model for Different Scattering Law and Albedo Conditions .....	113
37.	Evolution of Building Block for a Lunar Photometric Model .....	114

## INTRODUCTION

This Final Report on the extension to the Contract on "Photometric Measurements of Simulated Lunar Surfaces" includes the material presented in two previous quarterly progress reports (Refs. 1 and 2) and the work performed in the period from December 31, 1965, to March 10, 1966.

Work accomplished under the original contract is reported in detail in Ref. 3. This work consisted essentially of photometric measurements and analyses of "natural" and "artificial and controlled" models in an attempt to reproduce the standard or average lunation curves of the moon (measured with integrated visible light) and infer certain "engineering" properties of the lunar surface. This report presents the follow-on work as defined in "Proposal B" of Ref. 4 and consists of three phases, namely: "spectral" brightness vs. phase angle measurements of some of the natural specimens that passed the photometric test under integral lighting, experimental and analytical assessment of "suspended particles" (or "dust clouds") as a lunar photometric model and, finally, investigations of "contrived" models in an attempt to synthesize a lunar photometric model which, unlike the complex natural specimens, would incorporate relevant properties only and lend themselves to physical manipulation or mathematical analysis. It is believed that such a model would not only clarify the results obtained with the natural specimens but permit one to estimate the range and contribution of the relevant properties to the lunar photometric function.

The three phases are essentially interrelated but are treated as complete entities so that each section may be read independently of the others. Each phase contains a statement of purpose, description of test specimens and discussion of experiments and their results. Each phase is preceded by a general discussion of method of analysis. They are followed by tentative conclusions regarding the nature of the lunar surface and a number of recommendations for additional lunar photometric observations and related earth-based experiments.

Photometric investigations are an important step toward the definition of an "engineering" lunar surface model that is consistent with all the known reflection and emission properties of the lunar surface measured at various wavelengths. Such a model



might be useful in identifying problem areas that may be encountered in engineering operations on the moon and in simulating lunar exercises related to these problems such as visibility (i.e., obstacle recognition, photography, etc.), landing, astronaut foot sorties, etc. An equally important objective of these earth-based investigations is to determine how they could verify, complement, or augment the findings of unmanned lunar probes in paving the way to manned lunar landing.

## METHOD OF INVESTIGATION

Interpretation of lunar photometric data (the major objective of this program) can be approached in various ways. One way is to search for natural specimens (i.e., fine dust, coarse cinders, massive slags, etc.) that reproduce the photometric properties of the moon and try to learn from these experimental comparisons which physical properties of the lunar surface may or may not be inferred. Another way is to focus attention on the phenomenon that characterizes the reflection laws of the moon, namely, backscattering, and to inquire as to which physical properties of reflecting surfaces in general determine their ability to backscatter light and what, in particular, these properties teach us about the nature of the lunar surface.

The first approach is expedient but limited in its usefulness. We used this technique with some success in Phase I of the previous contractual investigation (Ref. 3) in which we discovered several natural specimens other than fine dust that reproduce the average photometric curves of the moon at all viewing and phase angles. We found that changes in material composition, strength, consistency, depth, grain size, etc., do not affect uniquely the photometry of a surface but changes in albedo, porosity, relative micro- and macro-roughness, slope orientation, etc., do. It was then concluded that the direct model-matching approach could at best reveal gross properties that are photometrically relevant and that it should be complemented by "synthetic" studies in order to assess the relative contribution of the relevant variables. The usefulness of this approach was illustrated in Phases II and III of the preceding contractual investigation (Ref. 3) where an attempt was made to study the effects of slopes, "first and second order roughnesses," the relative size and distribution of the predominant first order roughness, albedo, grain size, porosity, etc. on the lunar photometric function.

This approach is further pursued in Phase III of the present study, as an outgrowth of preliminary, qualitative analyses presented in Ref. 3. Essentially, the purpose is to synthesize analytically a lunar photometric model. The method consists of describing mathematically the photogeometric relationship of various promising models and letting the computer search for the geometry that gives the closest photometric match with the lunar data. The models consist of idealized patterns of horizontal and/or vertical planes that essentially simulate on a macro-scale (i.e., visible

to the naked eye) the complex microstructure of "fairy castles" and illustrate graphically how changes of light and shadow on and within a porous "surface" affect the photometric signature of that surface.

In our over-all search for a lunar surface model, of which the present investigation is a part, we are shifting our emphasis from "model-matching" per se to model-behavior. It is becoming increasingly apparent that greater insight and potentially useful quantitative data can be gained into the engineering properties of lunar landing sites by studying the behavior of various candidate models under given inputs than in trying to develop "best fit" models which by themselves may not be very revealing at this time because of their nonuniqueness and the meagerness and poor quality of the lunar data to which they are compared. A more useful exercise at this time would be to identify and assess experimentally and/or analytically all the physical and geometrical properties of a surface that affect the "signature" of that surface at a given wavelength. When high resolution lunar data at various wavelengths is obtained for a distinct area on the moon, then model-matching may be attempted on the basis of knowledge acquired from our present investigations of model behavior as attempted in this report and in Ref. 3. We are currently developing a similar technique in studying the polarimetric and thermophysical properties of the lunar surface (Refs. 5 and 6) which in many ways complement photometric and other studies in defining engineering lunar surface models. In a subsequent study, an attempt will be made to show how these model-matching exercises could contribute to the selection of LEM landing sites when they are preceded or followed by high resolution earth-based lunar observations and on-site or orbital measurements by means of unmanned lunar probes.

## MODIFICATIONS AND PERFORMANCE OF THE GRUMMAN PHOTOMETRIC ANALYZER

After the completion of the experiments reported in Ref. 3, the Grumman Photometric Analyzer was extensively overhauled and recalibrated to make spectral photometric measurements and to improve photometer response to brightness changes transmitted through the beam splitter in the "opposition regions." A detailed description of these instrumental changes and refinements follows:

### Filter Accommodations

A general view of the Grumman Photometric Analyzer is shown in Fig. 1. To perform spectral photometric measurements, the rotating light source of the analyzer has been provided with 5 filters or 6 filters and a clear space, manually selectable from the floor level as shown in Fig. 2. The filters are inserted between the diffuser disks and the field stop. The source radiance has been improved by a large factor by use of a 1 KW tungsten-iodine lamp and two quartz diffuser disks in series whereas flashed opal diffusers of greater density had been used previously.

Although the filters are shielded by the diffuser disks and a certain amount of structural shielding, the thermal problem resulting from the use of a 1 KW lamp is severe. Trial of a dense red filter showed a temperature of about 200 °F at the surface of this filter. This particular filter cracked. Temperature fluctuations of such a degree can result in large color changes as well as mechanical failure. The design has been reviewed from a thermal standpoint and improved by providing high absorptivity radiation heat sink surfaces for the filter and improving the conduction transfer paths. A blower has been used throughout to circulate air through the source assembly. The filters have been placed adjacent to the source rather than the photometer phototube for reasons of convenience and timesaving in operation. The filter problem could also be alleviated by the use of filters which have low radiation absorption, or as in polarimetry (Ref. 5) by placing the filters outside the lamp housing.

### Spectral Response Studies

Throughout the photometric investigations conducted by Grumman to date, an assumption was made that the spectral response resulting from combining an artificial light source (tungsten-iodine lamp)

and the sensor (S-4 or S-11 phototube) did not differ from the spectral response of photography on the sunlit moon to such an extent as to invalidate our measurements. The sensitivity of photometric functions of models to these spectral parameters was investigated under this contract. Figure 3 shows the approximate comparison of the integrated spectral response of our photometric analyzer with that of direct lunar photography. Much of the photographic data is rather old. Therefore, under the assumption that emulsions of different optical red sensitization have been used to acquire these data, a probable range of response is shown in Fig. 3. Film Emulsion IV represents the extreme red sensitization that might be incorporated into the direct lunar data, whereas Film Emulsion II represents the other extreme of an older blue-sensitive emulsion. The various assumed spectral curves that have been multiplied together to achieve a response curve for the laboratory equipment include the following:

- 1) A 3200 °K black body curve representing the output of a 3400 °K tungsten-iodine lamp filtered through two diffuser disks. The exact amount of spectral reddening of the 3400 °K source by the diffusers is unknown. However, the transmission of directional light through the diffusers is influenced by preferential scattering from the beam of blue over red.
- 2) The spectral transmission of two objective lens assemblies, one representing the collimating lens for the source, and the other the photometer objective.
- 3) The spectral reflectance curves for two rhodium mirrors.
- 4) The spectral response curve of a typical S-11 photoemissive surface (e.g., for the 6199 multiplier phototube).

The comparison of integrated response predicted for the photometric analyzer with the two sunlight-emulsion curves indicates that the analyzer is far too responsive in the red to represent photography with blue-sensitive emulsion, but is at least a possible compromise for photography with high red sensitization. In all probability, it is too red-responsive to represent most lunar photography.

More recent photometric data, including that reported by Gehrels et al., (Ref. 7), have been acquired with the use of phototubes rather than more indirectly through photography. With these data, the comparison is between the product curves of the phototube spectral responses and the source curves, sunlight in one case and the tungsten-iodine lamp in the other. Of course, the optics used modify somewhat both product curves. However, the major difference lies between sunlight (5700 °K) and artificial light (3200 °K), with the peak of the former occurring near 5000Å and the latter near 9000Å. Once again, the photometric analyzer weighs the data too heavily in favor of the red if the same photodetector surface is used in both direct lunar data and laboratory data. One can attempt to balance the integrated response by the use of filters, or by using different photodetectors, or combination of both.

However, the emphasis in this report is not placed on making close comparison with any given set of direct lunar observations, but on discovering general trends in the effect of spectral band pass on the photometric function. The integrated visual response photometric data have been taken with the RCA 6199 multiplier phototube. For the blue (B), the filter combination is the Schott GG-13 combined with the Corning 5-57. The (B) photometric functions were taken with the RCA 6199 phototube also. The integrated visual response curve is shown in Fig. 1. The integrated spectral (B) curve of the photometric analyzer with these filters is shown in Fig. 4.

For the red (R), the filters are Schott BG-38 and the Corning 2-64. For the infrared (I), the filter is the Corning 7-56 with the upper wavelength cutoff being furnished by the photodetector. For these two band pass arrangements, the RCA 7102 multiplier phototube was used and the integrated response curves are derived and shown in Figs. 5 and 6.

It should be noted that the spectral curves submitted in this report are based upon typical S-11 and S-1 room temperature curves (for RCA 6199 and RCA 7102, respectively), and not upon calibration data for specific phototubes. For very narrow spectral band pass, the spectral curves of all other components become insignificant compared to that of the filter since all photometric curves are normalized "relative value" curves. As the band pass increases, additional significance may be attached to the other component spectral curves. However, an examination of the data on all models tested under this contract shows a lack of pronounced spectral effect, and, therefore, small significance to exact spectral data.

## Improvement of Beam Splitter

The beam splitter used in previous experiments has been widened in order to enable a more meaningful simulation and study of the "opposition effect" recently reported in the literature (Ref. 7). As has been explained in a previous report (Ref. 3), the Grumman Photometric Analyzer makes use of a beam splitter to generate photometric functions which pass through zero phase angle. Furthermore, this beam splitter is mounted in such a way that it can be replaced readily with a complete first-surface mirror of the same size for use at phase angles greater than about  $6^\circ$ . A second first-surface mirror inclined  $45^\circ$  about an axis normal to the source axis and also normal to the axis of the first mirror is provided to de-polarize the source for other than zero phase region.

Astrophysical data reported by Gehrels et al. (Ref. 7) have shown a very pronounced "opposition" effect, much sharper near zero phase angle than earlier data. These new data are based on measurements of the lunation photometric function much closer to zero degrees phase angle than had been reported previously. By comparison with the Grumman Photometric Analyzer data taken on many models, it can be seen that this trend toward a sharp peak exists in the laboratory data also, but because the valid data taken through the beam splitter are effectively confined to about  $1\frac{1}{2}$  degree phase angle, the exact shape of the curve over a range of  $\pm 6^\circ$  phase angle cannot be verified. Furthermore, the interval of time the old beam splitter takes to travel this narrow angular distance is not sufficient to allow the recorder to respond in time to the actual brightness sensed by the photometer. To increase the Grumman capability of reading out the slope and peak of this significant part of the photometric signature of a model, a large beam splitter has been built especially for this range. The large beam splitter is used solely for readings near zero phase angle and is removed and replaced with a mirror for readings at larger phase angles. The approximate range which this beam splitter will cover is  $-7^\circ$  to  $+13^\circ$  as can be seen from sample recordings, Fig. 8c. A photograph of the unit attached to the rotating collimated source arm is shown as Fig. 7.

## Performance of New Beam Splitter

A test run was made on the Hawaiian volcanic cinder No. 1 at  $0^\circ$ ,  $30^\circ$  and  $60^\circ$  viewing angles as shown in Fig. 8a to c, in order to evaluate the performance of the modified beam splitter.

A comparison with similar curves on the same specimen obtained by the old, narrower beam splitter as presented in Fig. 17 of Ref. 3, indicates a significant improvement in the quality of the data obtained. The brightness peak, at zero degree phase, measured by the old beam splitter was only about 10 percent greater than the 1.0 normalization point on the ordinate of the curve whereas the corresponding value measured by the new beam splitter is in excess of 30 percent, not counting the fact that at the normal viewing position the brightness surge at zero degree phase was so intense that the recording pen went off the paper, as may be seen in Fig. 8a.

In addition to measuring the brightness peak more accurately, the new beam splitter reveals the change in the slope of the photometric curve in the region where the opposition effect takes place and thus permits direct comparison with the measured lunar data in this region. The similarity of Gehrels' data (Ref. 7) with our new measurements is more striking than with the previous measurements obtained through the old beam splitter.

The discovery that many models possess a seeming strong "opposition effect" at zero phase (as illustrated by Phase I experiments) led to a closer analysis of the equipment to determine whether any part of the "opposition" signature was spurious, or equipment-generated. This matter was investigated with the use of a special light trap, one of which is pictured in Fig. 9. The trap consists of a 45° "shiny black" reflector at 45° to the line of sight reflecting a specular component into a black flock cloth absorber at 90° to the line of sight. The reflection from this light trap is extremely low. Three of these traps are installed on the wall of the laboratory opposite the "zero phase" position of the rotating source to minimize false intensification of the zero phase brightness. The wall installation is shown in Fig. 10.

One of these light traps was used as a sample and an attempt was made to derive a "photometric function" of this sample. The data is submitted as Fig. 11. Obviously, the equipment did not generate a significant "opposition effect" of its own. The conclusion is drawn that the strong opposition effect shown in this report for many models is valid. There is an evident spectral band pass influence on the strength of this effect on several models. It has been discovered also that nominally "good" cosine-law diffusers like magnesium-carbonate, exhibit slight specularly or opposition effect, as shown in Fig. 11. However, the effect is very small. The demonstration of the new beam splitter illustrates again the importance of adequate or refined instruments in lunar model-matching experiments. Judging from these results, the time and effort spent in improving this particular aspect of our photometric analyzer appear to have been justified.



## PHASE I — SPECTRAL PHOTOMETRY

### Purpose

The purpose of this phase is to study, by means of laboratory measurements, the wavelength dependence (in the  $0.48\mu$  to  $1.0\mu$  range) of the albedo and backscatter of natural specimens that are photometrically analogous to the moon under integrated visible light. An equally important objective of these experiments is to simulate and study the "opposition effect" recently observed on the moon.

### Test Specimens

Six natural specimens were selected for spectrophotometric measurements on the basis of their photometric similarity to the moon under integrated visible light as reported in Ref. 3. These specimens, listed below, represent a wide range of grain size, material composition and surface texture.

	<u>Figure No.</u>
1. Volcanic cinder No. 4	13 and 19
2. Furnace slag No. 1 (original NASA sample)	14 and 20
3. Coral No. 2	15 and 21
4. Scoria No. 2	16 and 22
5. Copper oxide powder	17 and 23
6. Copper oxide powder on rough foam	18 and 24

A detailed description of these specimens may be found in Ref. 3. In connection with specimens No. 5 and 6, where silver chloride rather than copper oxide was originally specified, it was discovered that results with silver chloride are extremely dependent upon the accidental physical microstructure of the chemical as purchased. It was found that the microstructure changed in the sealed containers. Consequently, the material would no longer yield a good lunation signature. The "fairy castle" microstructure therefore could not be readily duplicated. The effect may be due to water of crystallization, however, other physical or chemical changes may have occurred.

As a result of the difficulties experienced in maintaining the albedo and microstructure of silver chloride powder constant it was decided that copper oxide be used instead in the preparation of the last two specimens. Copper oxide powder (an equally good backscatter) is more dependable in yielding repeatable experimental results. Unlike silver chloride, it is not susceptible to darkening under exposure to sunlight.

## Experiments

Albedo and brightness vs. phase angle measurement of all the six specimens listed above were made at  $0^\circ$ ,  $30^\circ$ , and  $60^\circ$  viewing angles under integrated visible lighting and spectral lighting including the blue, red and near infrared regions.

Albedo values at various viewing angles and wavelengths are listed in Table 1 and plotted in Fig. 12. A total of 72 photometric curves (12 for each specimen) at specified viewing angles and wavelengths are shown in Figs. 13 through 18. Photographs of the specimens are shown in Figs. 19 through 24. Measurement procedures are described in Ref. 3. This reference also includes a discussion of the lunar photometric standards to which the test results are compared. These standards appear as shaded "bands" in the figures where the test results are shown.

## Discussion of Test Results

The investigation of the six natural specimens presented in this report differs from the investigation of the same specimens in Ref. 3 in the following respects:

- 1) Albedo and photometric measurements were made at separate wavebands including the blue, red, and infrared regions, in addition to those measured through the visible spectrum.
- 2) More reliable measurements of the change in brightness near  $0^\circ$  phase angle (the "opposition" region) were made at all the specified wavelengths by means of the improved beam splitter.

### ALBEDO - COLOR CHART

\*Angles refer to viewing angles  
\*\*Ref. 5.

## Spectral Albedo Measurements

Albedo values at all of the measured viewing angles and colors are listed in Table 1. Most of the albedos are within lunar ranges and like the lunar surface are nearly independent of viewing angle and dependent upon wavelength. Volcanic Cinder No. 4 exhibits an unusually higher albedo in the red and infrared regions than in the blue and visible.

Plots of albedo vs. wavelength for the test specimens and the moon are shown in Fig. 12. Scoria No. 2 shows the least color dependence whereas CuO powder shows the most. In the region of the spectrum shown in Fig. 12, Scoria No. 2 and Furnace Slag No. 1 show a better fit with the albedo-color curves of the moon than the other specimens we examined.

It is reasonable to attribute the viewing angle independence of albedo exhibited by the moon and our specimens to geometry effects or roughness of the surface, but it is not clear whether roughness also plays a role in the color dependence of albedo or whether this dependence is entirely a compositional effect. The moon appears to show considerable enhancement in brightness at longer wavelength. Recently reported lunar measurements at  $3.6\mu$  (not shown in Fig. 12) reveal albedo peaks of 0.25 for the maria and 0.55 for the highlands (Ref. 8). Similarly, brightness measurements of Mare Tranquilitatis from a balloon altitude of 83,500 feet reveal a uniform rise in albedo with wavelength to an apparent peak of 0.20 at about  $2.5\mu$  (Ref. 11). These values are considerably higher than those in the optical region of the spectrum and could possibly account for the increased contrast between illuminated and shadowed areas of the lunar surface revealed by recently published near infrared ( $1\mu$  to  $2\mu$ ) photographs of the moon (Ref. 12).

Further discussion of this subject is not very meaningful at this time in view of the limited extent of albedo-color data on the moon and terrestrial specimens. One may note, however, that if the brightness of the moon is much greater in the near infrared than it is in the optical region, as it appears to be according to data in Refs. 8 and 11, then additional albedo-color data on the moon and laboratory specimens would be very useful in compositional mapping of the moon and in interpreting photographs or data obtained at these relatively unexplored near infrared wavelengths. Within the range of lunar surface temperatures, it is safe to assume that at these wavelengths thermal emission is negligible and that the observed phenomena are predominantly due to scattering.

## Spectral Photometric Measurements

Figures 13 through 18 show the visual and spectral photometric curves of six natural specimens. The photographs of these specimens are shown in Figs. 19 through 24. Twelve measurements were made on each specimen at B, R, I, and V wavebands for each of the  $0^\circ$ ,  $30^\circ$ , and  $60^\circ$  viewing angles. As previously noted, lunar photometric standards to which the test results are compared are taken from Ref. 3.

With the exception of the copper oxide powder and to a lesser extent sea coral, all the specimens show a more pronounced surge of brightness at zero phase angle than they did during the previous measurements reported in Ref. 3. Volcanic Cinder No. 4 is the most notable in this respect. The difference between the old and new results in the "opposition" region is due to the already reported modification of the beam splitter used during near zero phase angle measurement. The new results at these difficult-to-measure phase angles are, we believe, superior in quality to the old ones and are in better agreement with corresponding lunar data recently published by Gehrels et al. (Ref. 7).

It is of interest to compare the spectral-photometric behavior of the test specimens at very small and very large phase angles. The four photometric curves at B, R, I, and V of each specimen at any one of the three viewing angles are shown on opposite pages so that this comparison can be readily made.

The wavelength dependence of brightness at zero phase angle (in the "opposition" region) is clearly noticeable in Volcanic Cinder (Fig. 13), Furnace Slag (Fig. 14), and Scoria (Fig. 16). This dependence is in the direction of increased brightness with wavelength and is consistent with the albedo vs. wavelength data discussed above, except for the coral specimen where we notice an opposite trend although at a much attenuated scale. Recalling the fact that the test curves are normalized at  $4^\circ$  phase angle, we notice that (with the exception of the coral) the opposition effect is the least pronounced in the blue and the most pronounced in the red or infrared depending upon the specimen. In most cases,  $0^\circ$  phase brightness at V is comparable to the brightness at R or I. It is also of interest to note that the opposition effect on the CuO powder sprinkled on a flat surface is barely noticeable (Fig. 17) but it is clearly visible when the same powder is sprinkled on the rough "picked out" foam (Fig. 18). This experiment indicates that the opposition effect is roughness dependent and suggests that the scale of roughness of the lunar surface is larger than the micron size CuO powder.

The large phase angle regions of the test curves are also of interest in view of Gehrels' recent observation of "reddening" of the moon at these angles.\* The test data, as presented herein, enable one to look for such an effect by comparing visually the brightness of a specimen at various colors at a given large phase angle. We notice that the coral is the only specimen that exhibits this effect. In this case, we may attribute the "bulge" in the lower part of the brightness-phase curve to actual "reddening" rather than to other causes that may produce the same result such as geometry effects (discussed in Phase III) or specularly of the surface. The latter effect may be ruled out on the basis of the fact that the "bulge" appears only under spectral light and is more pronounced in the red and infrared than in the blue. Moreover, the reddening exhibited by the coral at large phase angles is consistent with its anomalous spectral behavior in the opposition region as noted above.

As far as the six natural specimens indicate, their over-all photometric behavior under integrated light does not seem noticeably different under "spectral" conditions. This observation is particularly true for fine copper oxide powder on a flat surface which shows the least color dependence and opposition effect. The differences in the very small and very large phase angle regions exhibited by the other specimens, as discussed above, appear to be due primarily to color and albedo effects since the geometry of the specimens remains the same. It is not clear at this point whether the very fine powdery makeup of copper oxide is responsible for its anomalous behavior. It is reasonable to conjecture that the spectrophotometric properties of the moon in the optical region, like those of our test specimens, are not significantly different from the photometric properties at integrated visible light. New lunar photometric measurements should preferably be made at wavelengths beyond the optical region. Additional back-scattering data at longer wavelengths could be useful in inferring a more meaningful lower limit for the microroughness of the lunar surface. The study of the phase variation of the moon and laboratory models in the near infrared (up to  $3\mu$ ) would be of great value in this respect. Earth-based measurements of the photometric properties of the moon at these wavelengths are possible and would be very useful at this time in furthering our knowledge of the microstructure and other properties of the lunar surface.

---

\* Gehrels gives the following relationship to describe this effect:  
 $B - V = +0.84 + 0.0017 |\alpha|$  for  $-50 < \alpha < +60^\circ$ , where  $B - V$  is the color index and  $\alpha$  is the phase angle.



Fig. 1 The Grumman Photometric Analyzer

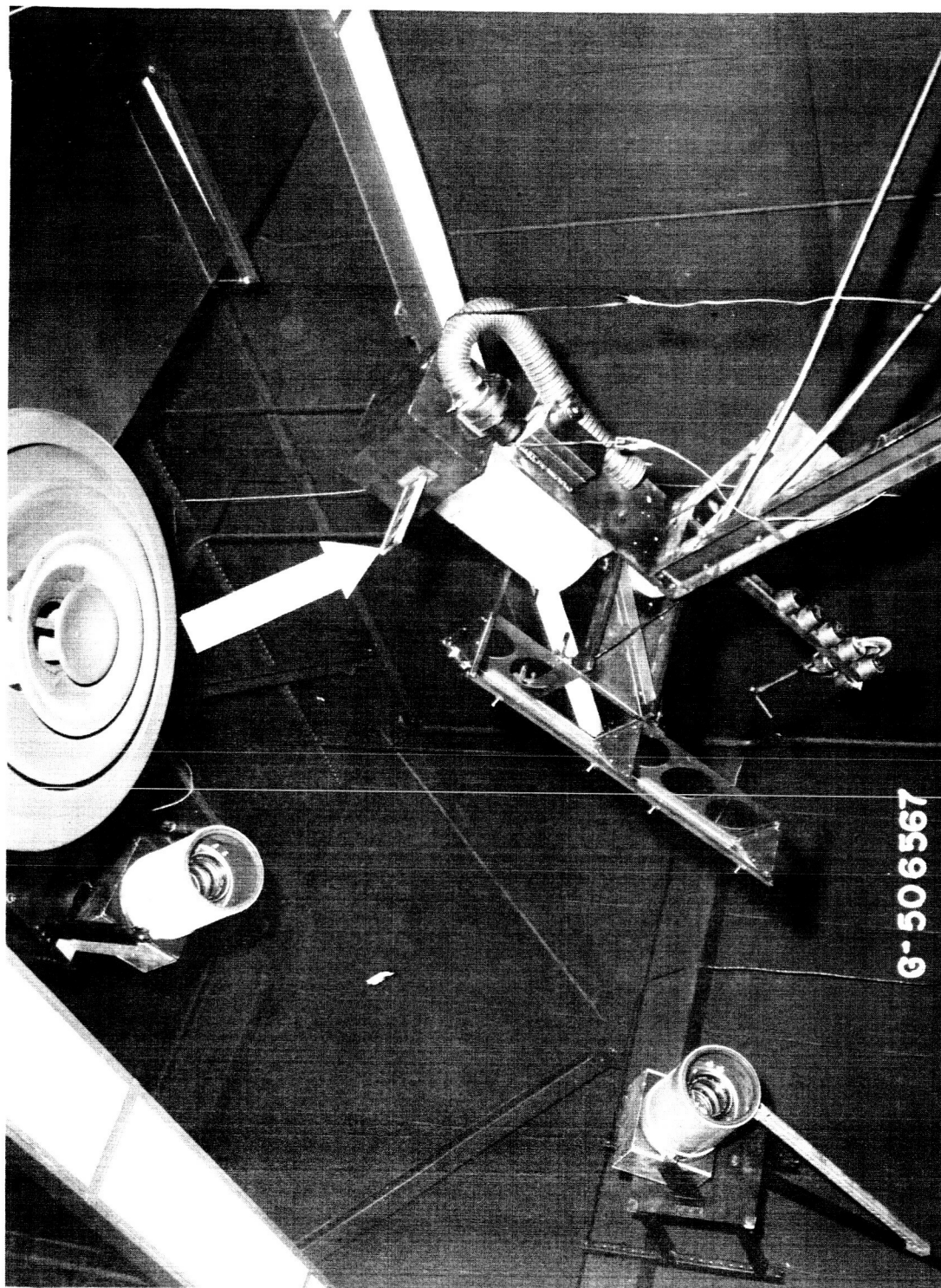


Fig. 2 Filter Sliders (Arrow) Mounted at Light Source



S-11, 3200° K Blackbody, 2 Rhodium Mirrors  
and 2 Lenses Product Curve

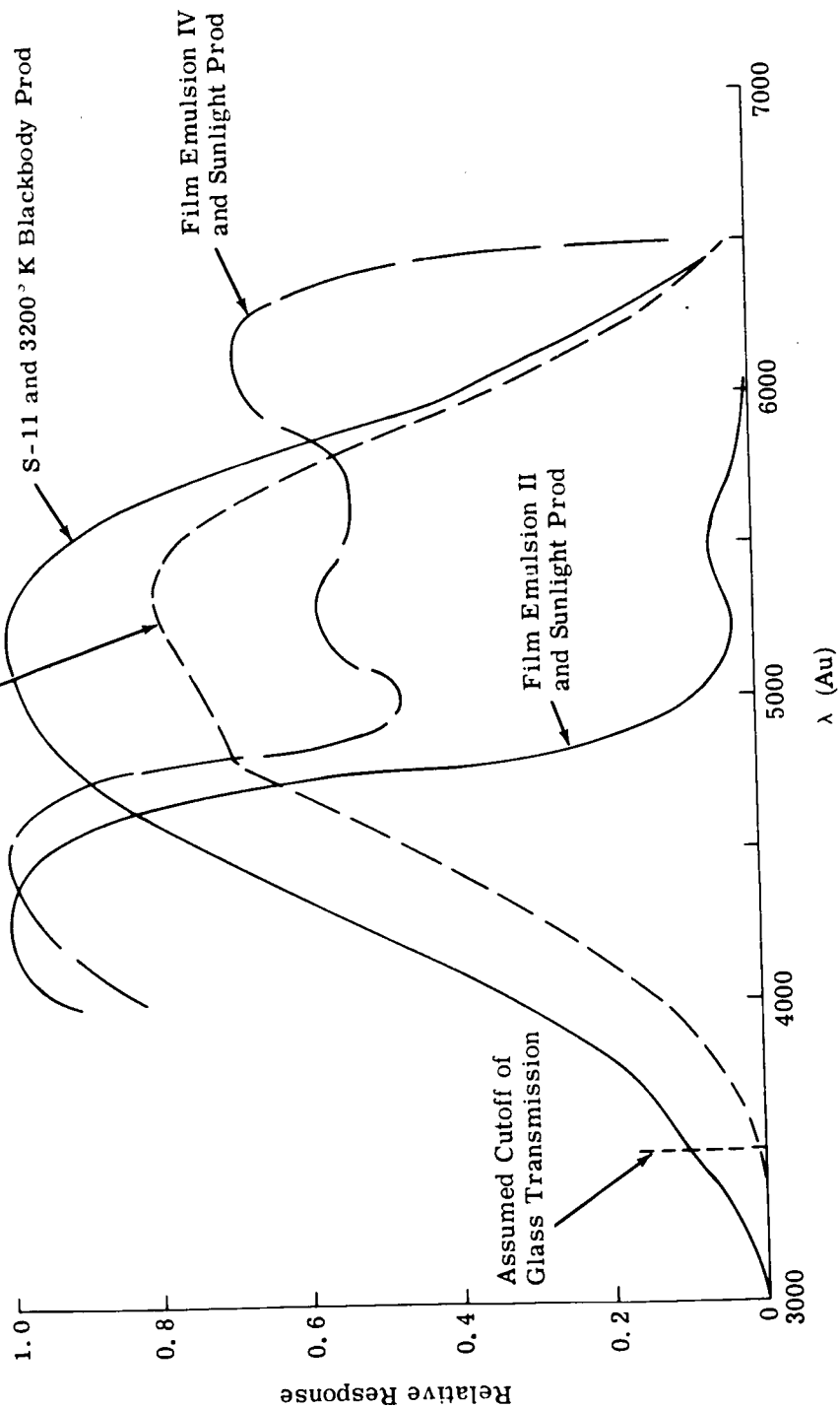


Fig. 3 Spectral Responses at Integrated Visible (V) Light

Code:

- ① ——— Tungsten - Iodine Lamp Thru Two Diffusers (3200° K Blackbody)
- ② ——— RCA #6199 Photomultiplier Tube Detector
- ③ ——— Filter (GG13 and 5-57 Product) Blue
- ④ ——— Lamp, Detector and Filter Product
- ⑤ ——— Lamp, Detector, Filter and System Lenses Product

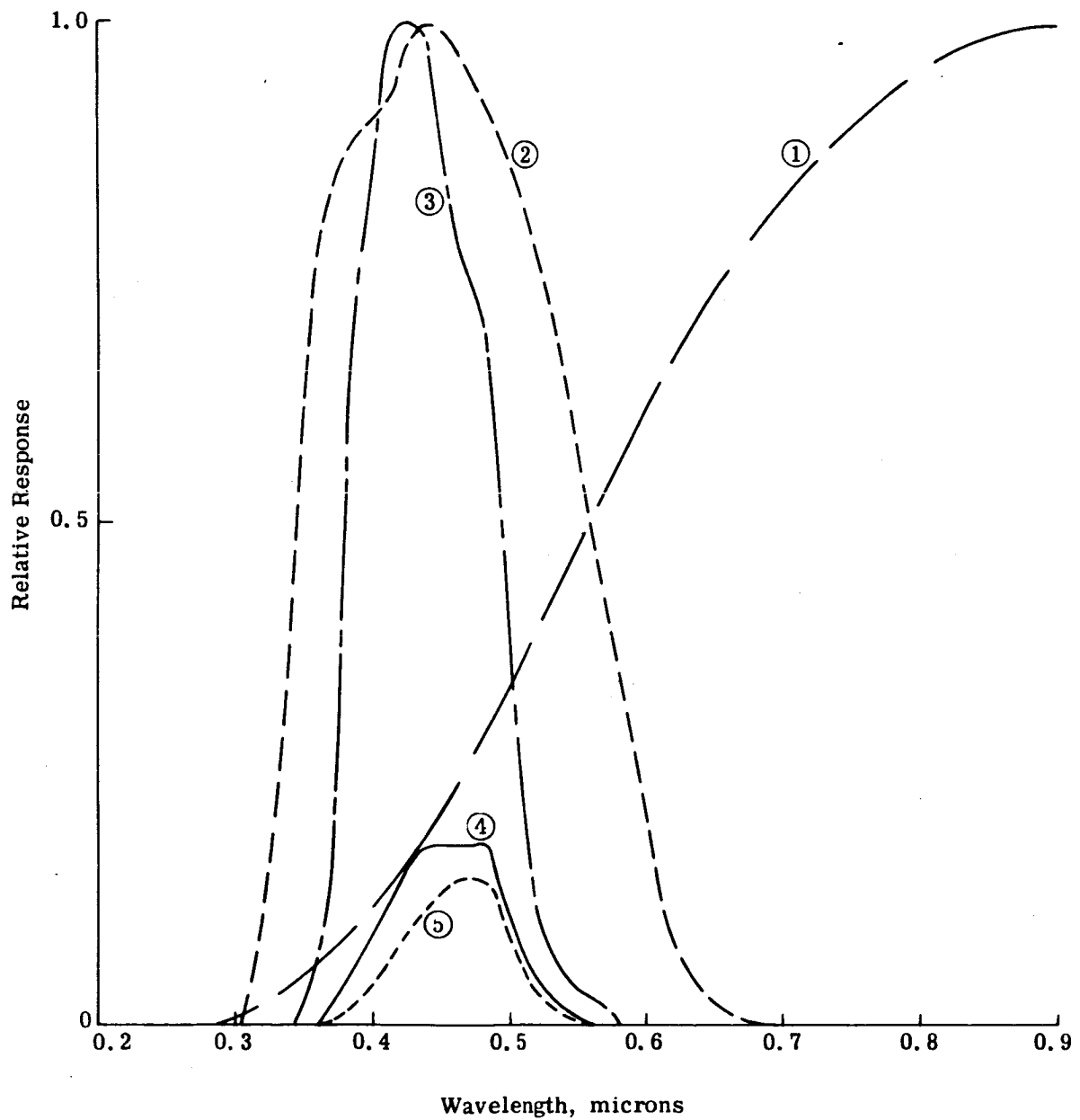


Fig. 4 Spectral Responses with Blue (B) Filter

Code:

- ① ——— Tungsten - Iodine Lamp Thru Two Diffusers (3200° K Blackbody)
- ② ——— RCA #7102 Photomultiplier Tube Detector
- ③ ——— Filter (BC 38 and 2-64 Product) Red
- ④ ——— Lamp, Detector and Filter Product
- ⑤ ——— Lamp, Detector, Filter and Two Rhodium Surface Mirror Product

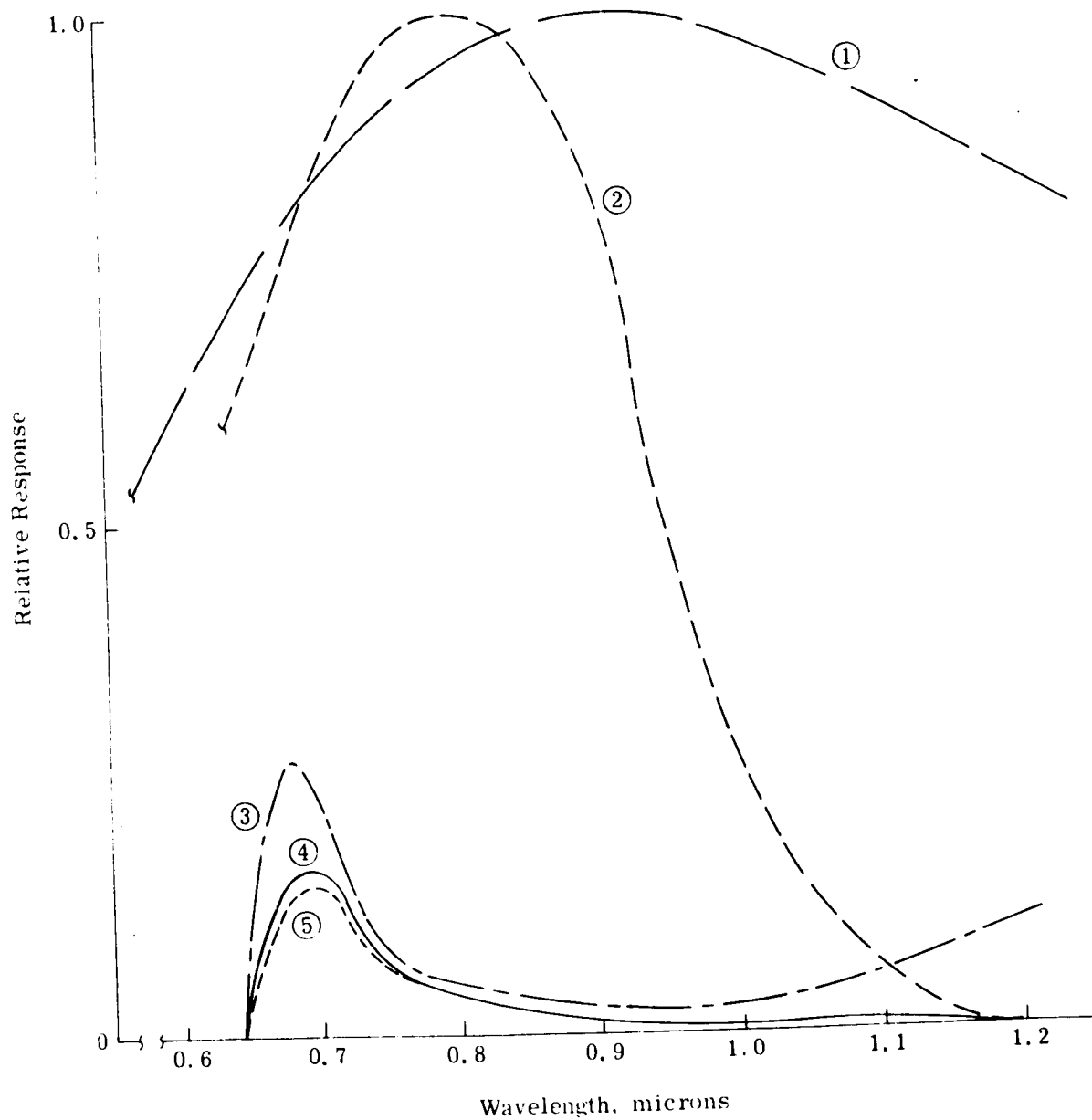


Fig. 5 Spectral Response Curves with Red (R) Filter

Code:

- ① ——— Tungsten - Iodine Lamp Thru Two Diffusers (3200° K Blackbody)
- ② ——— RCA #7102 Photomultiplier Tube Detector
- ③ ——— Filter (IR 7-56)
- ④ ——— Lamp, Detector and Filter Product
- ⑤ ——— Lamp, Detector, Filter and Two Rhodium Surface Mirror Product

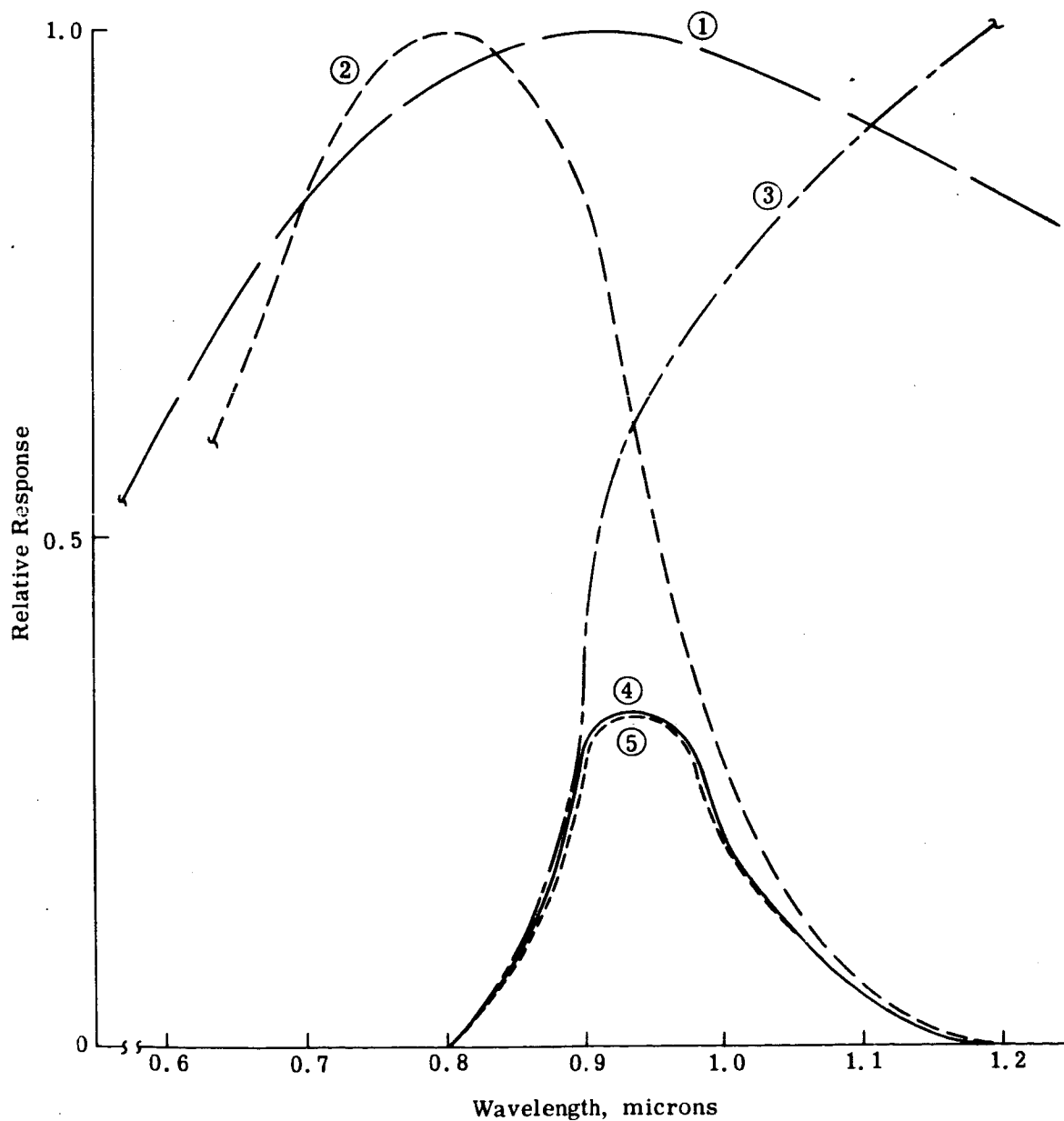


Fig. 6 Spectral Response Curves with Infrared (I) Filter

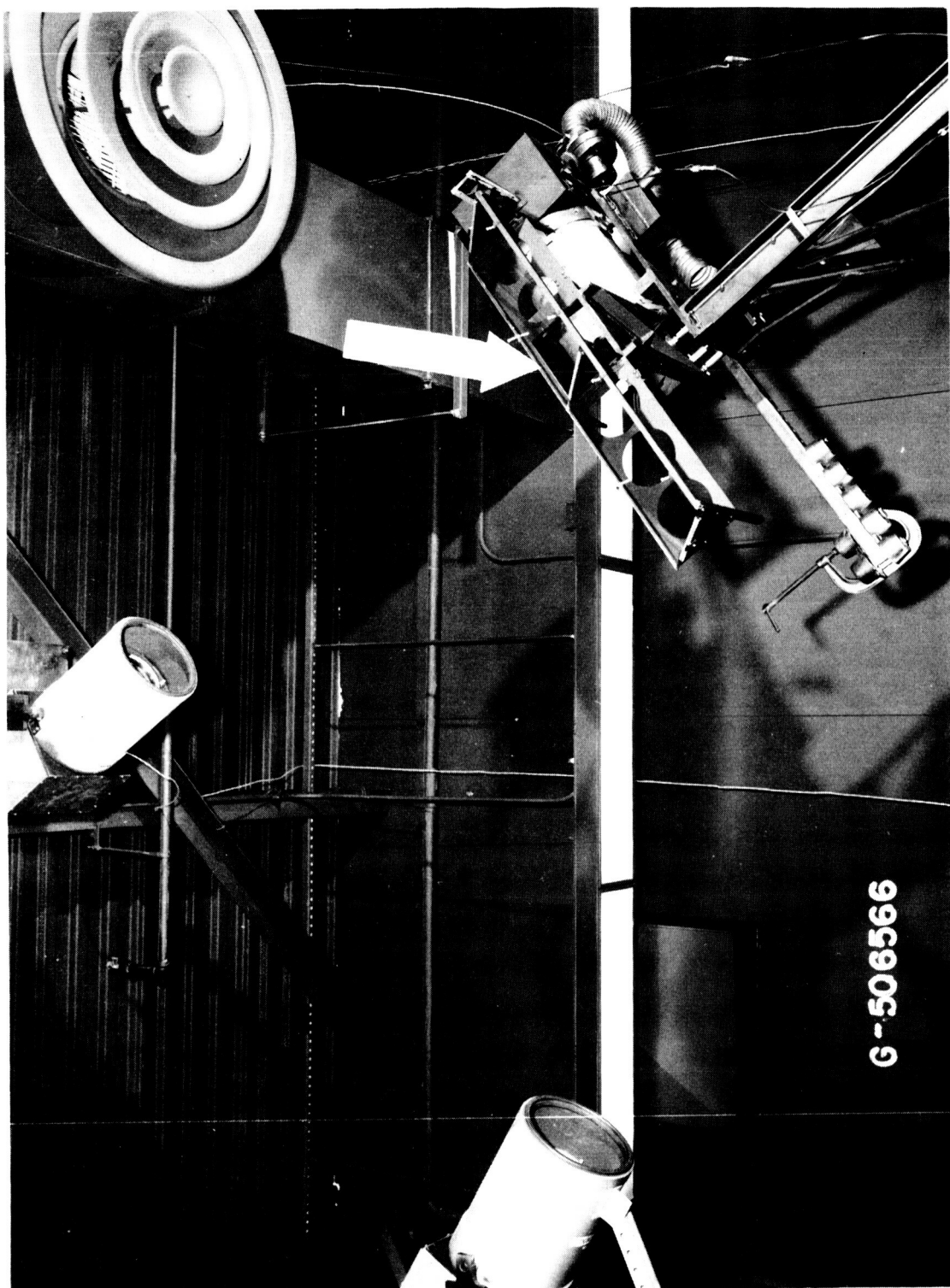


Fig. 7 New Improved Beam Splitter Mounted in Front of Light Source

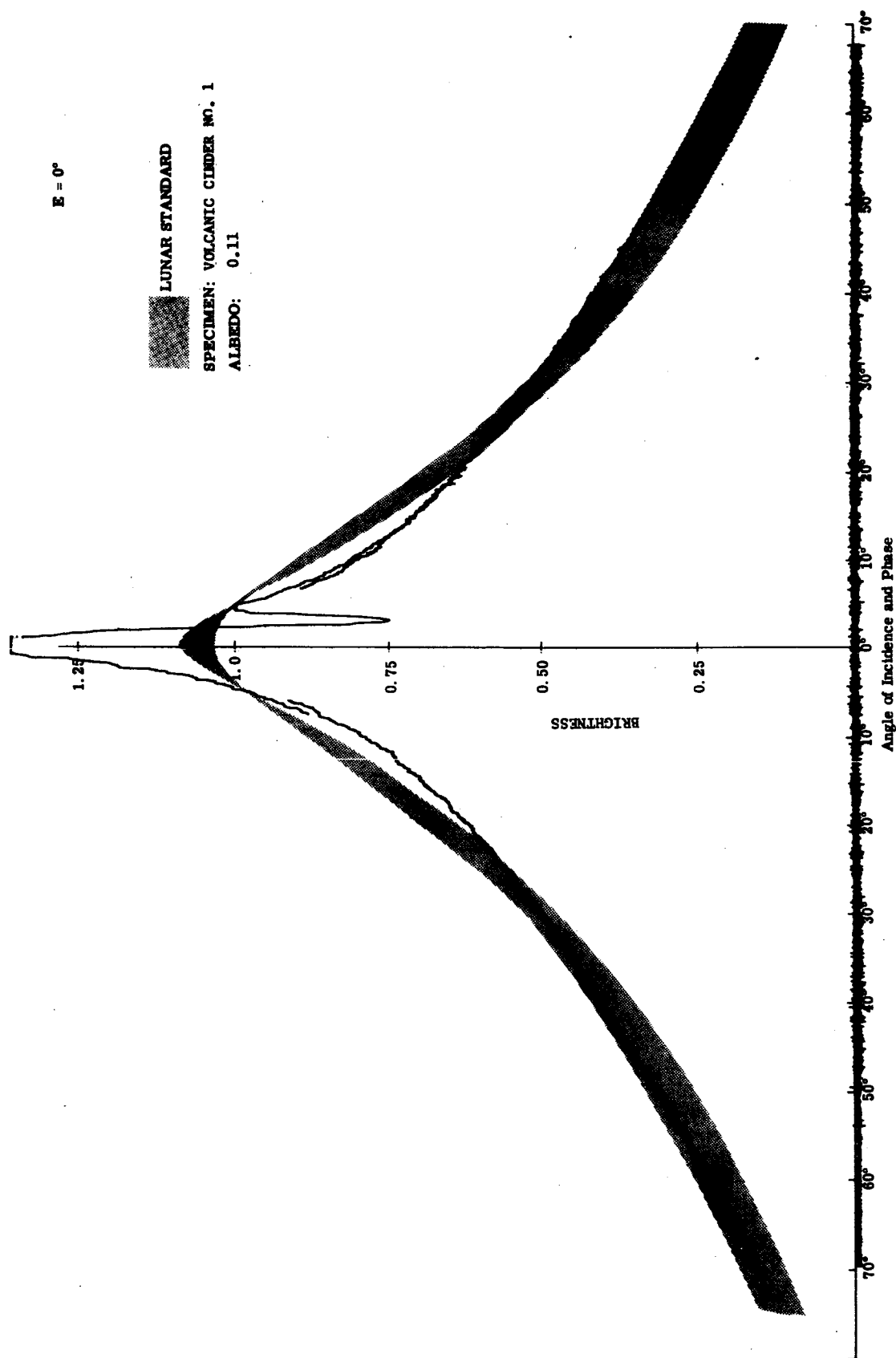


Fig. 8a Hawaiian Volcanic Cinder Measured with New Beam Splitter

$E = 30^\circ$

LUNAR STANDARD  
SPECIMEN: VOLCANIC CINDER NO. 1  
ALBEDO: 0.11

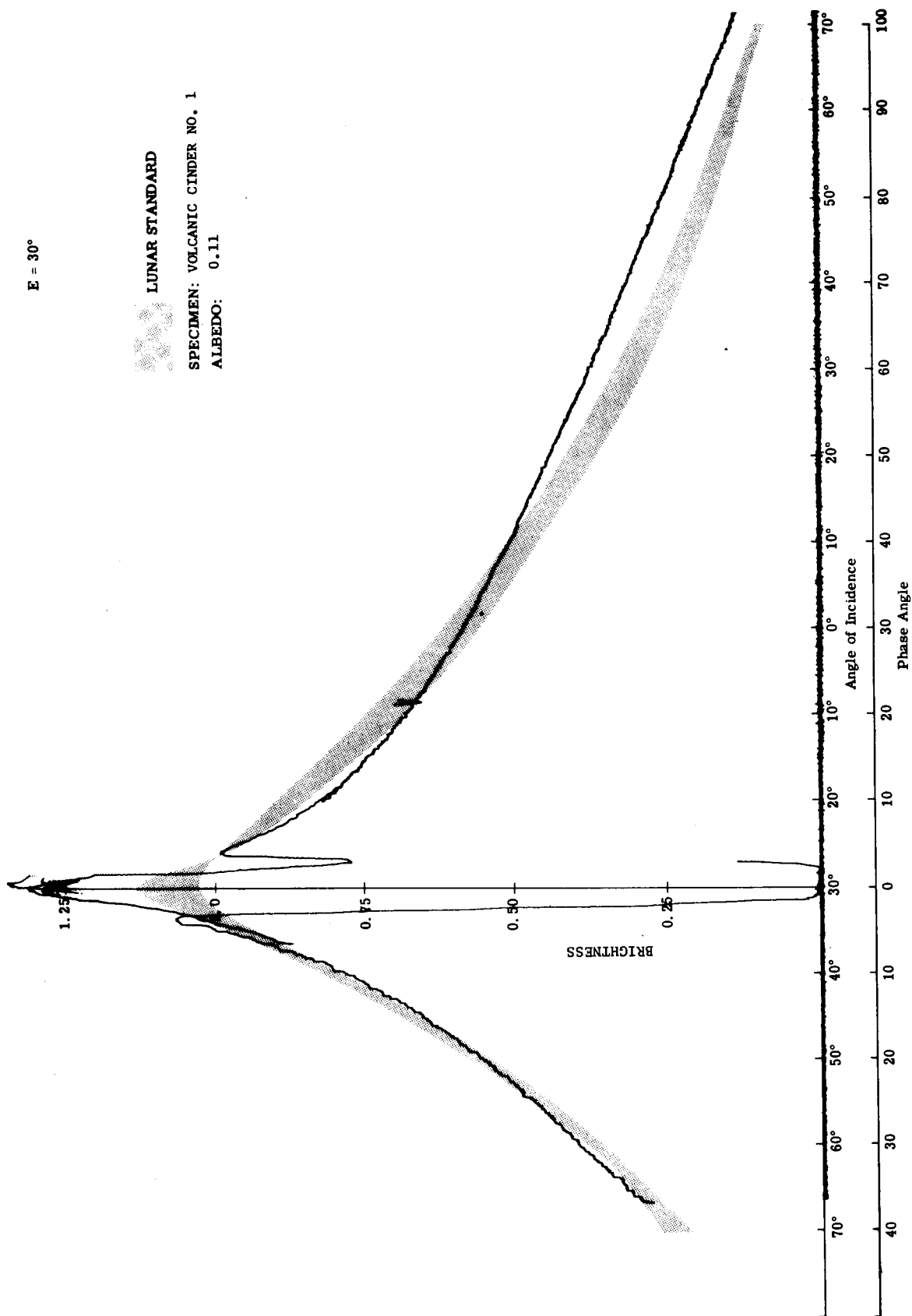


Fig. 8b Hawaiian Volcanic Cinder Measured with New Beam Splitter

E = 60°

LUNAR STANDARD

SPECIMEN: VOLCANIC CINDER NO. 1

ALBEDO: 0.11

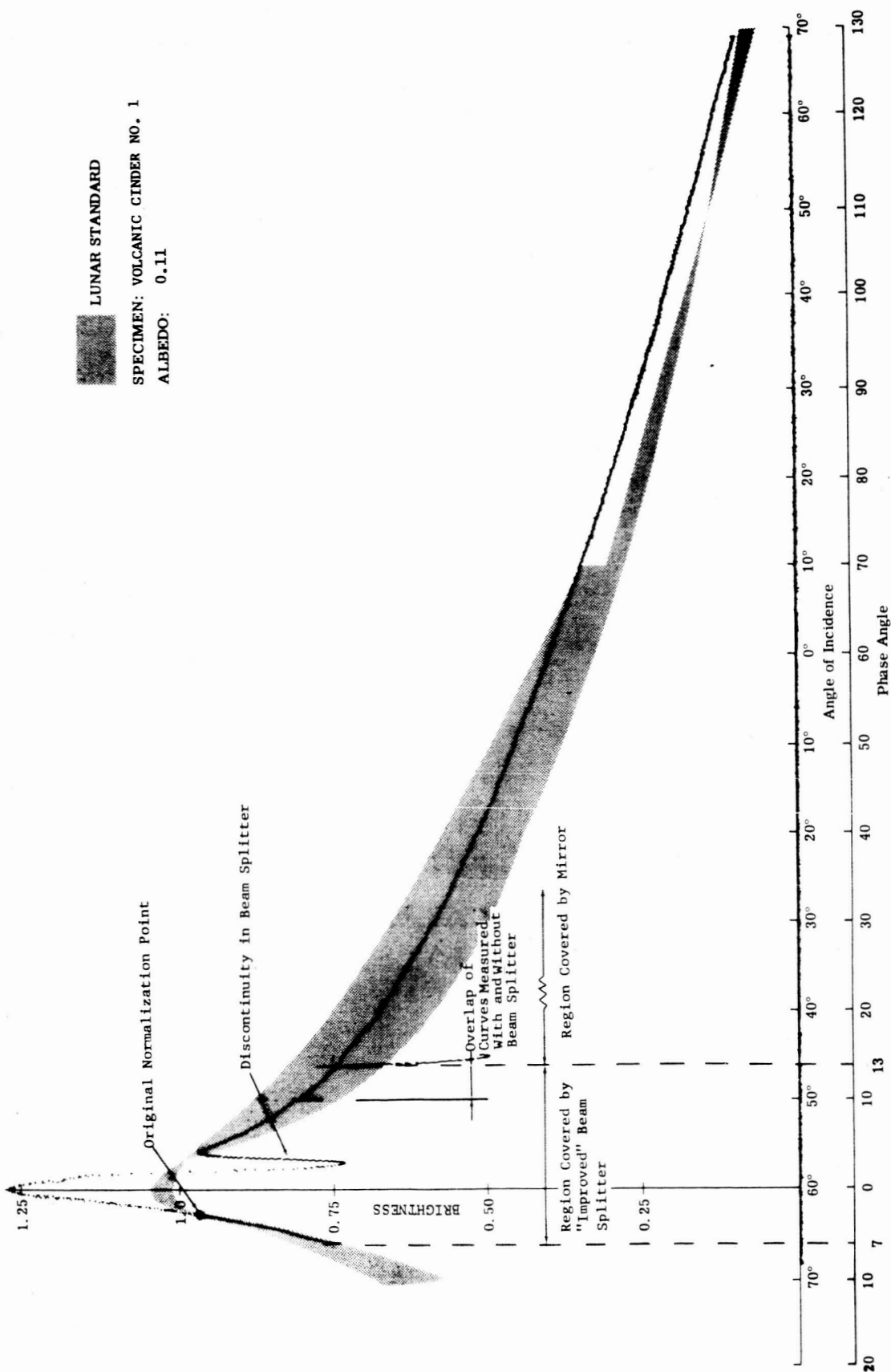


Fig. 8c Hawaiian Volcanic Cinder Measured with New Beam Splitter



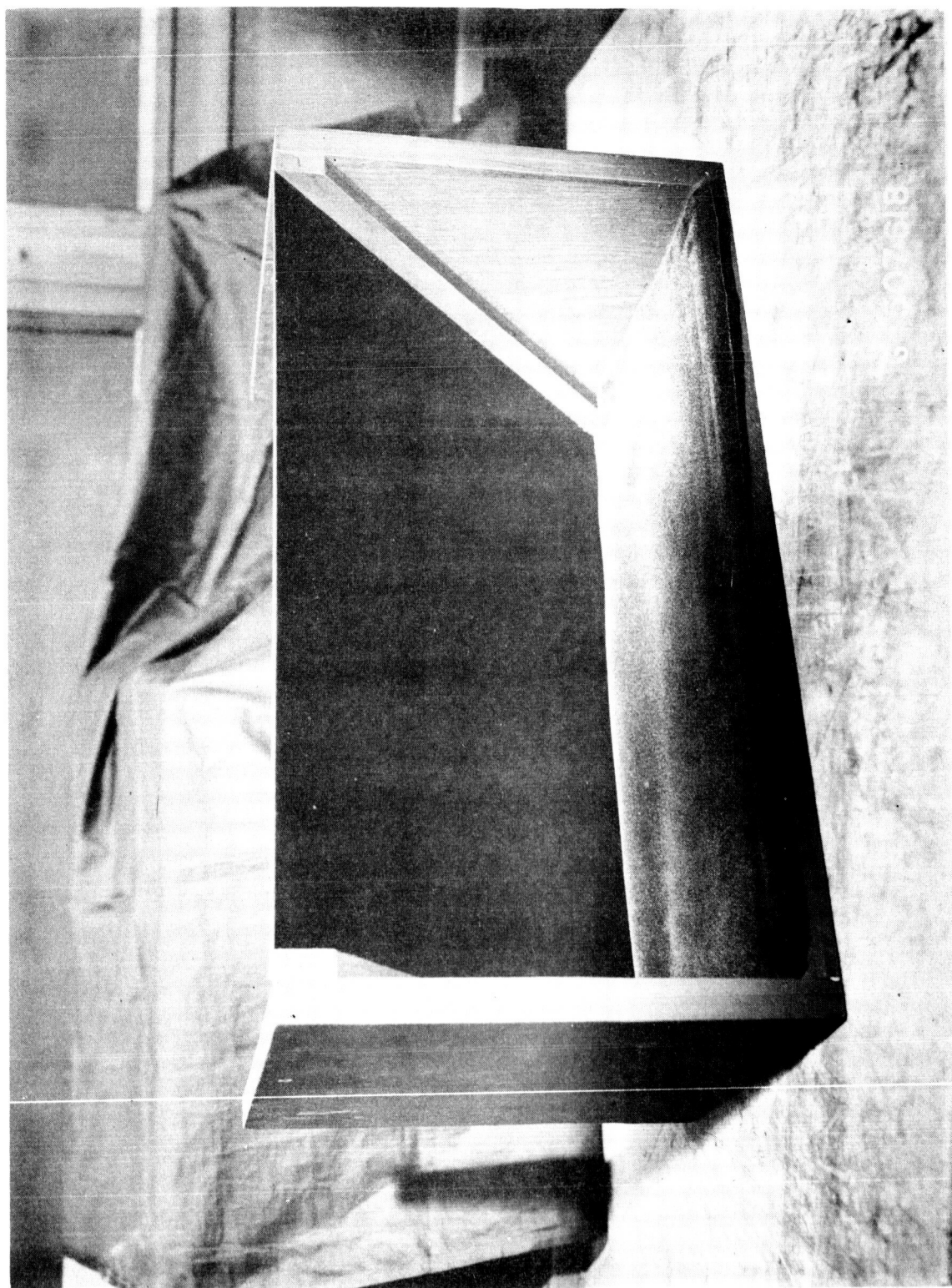


Fig. 9 Close-up View of Light Trap

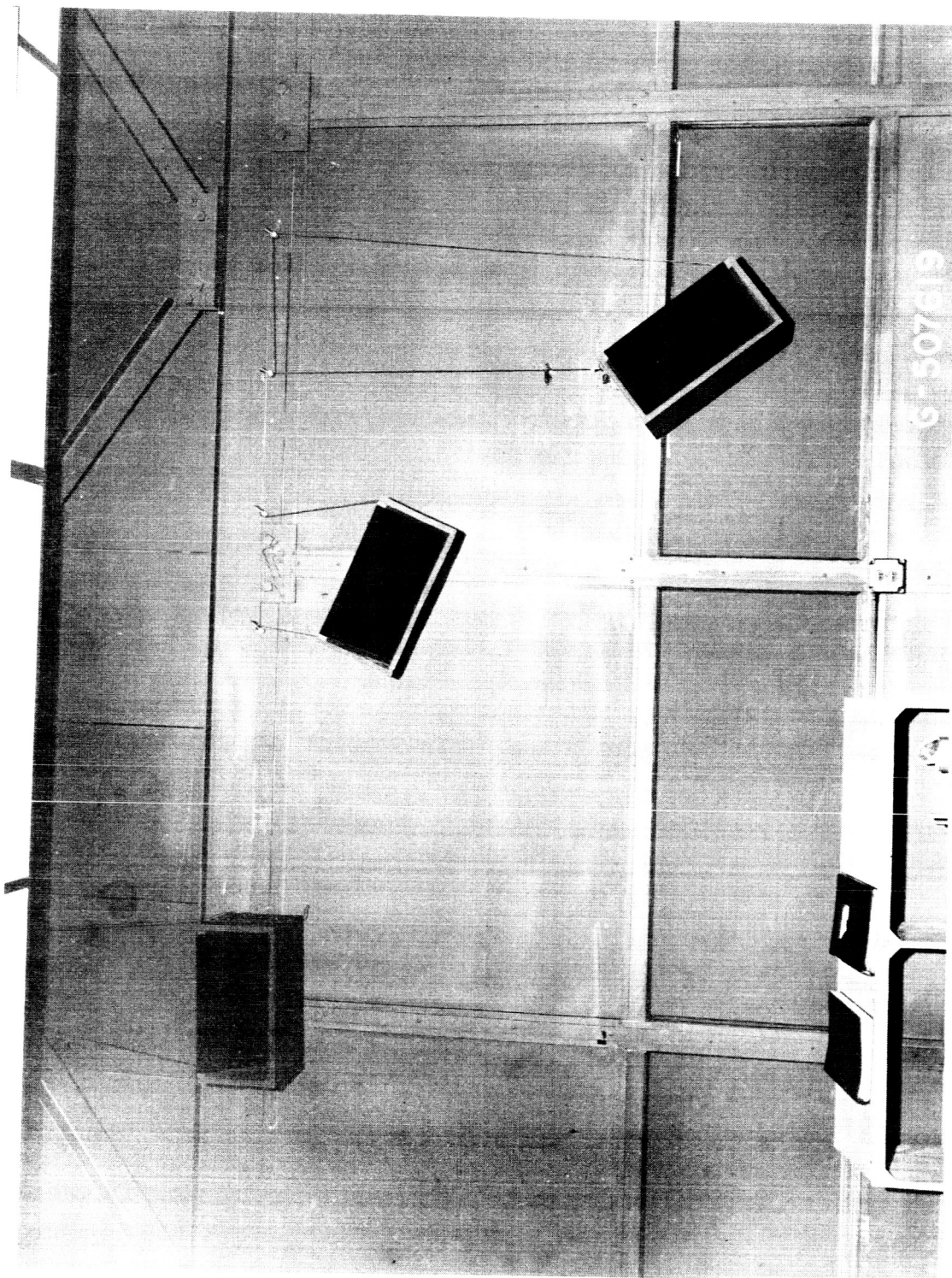


Fig. 10 Wall Installation of Light Trap

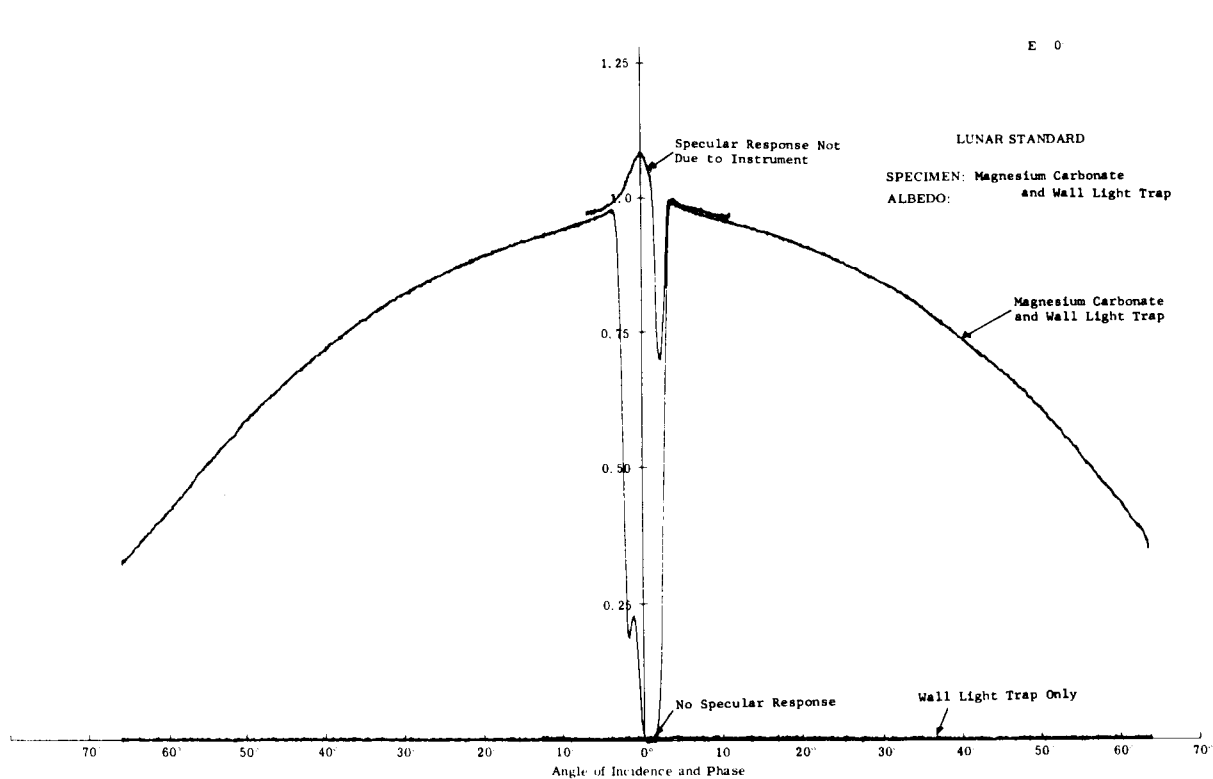


Fig. 11 Photometric Function of Magnesium Carbonate (Standard Diffuser) and Light Trap

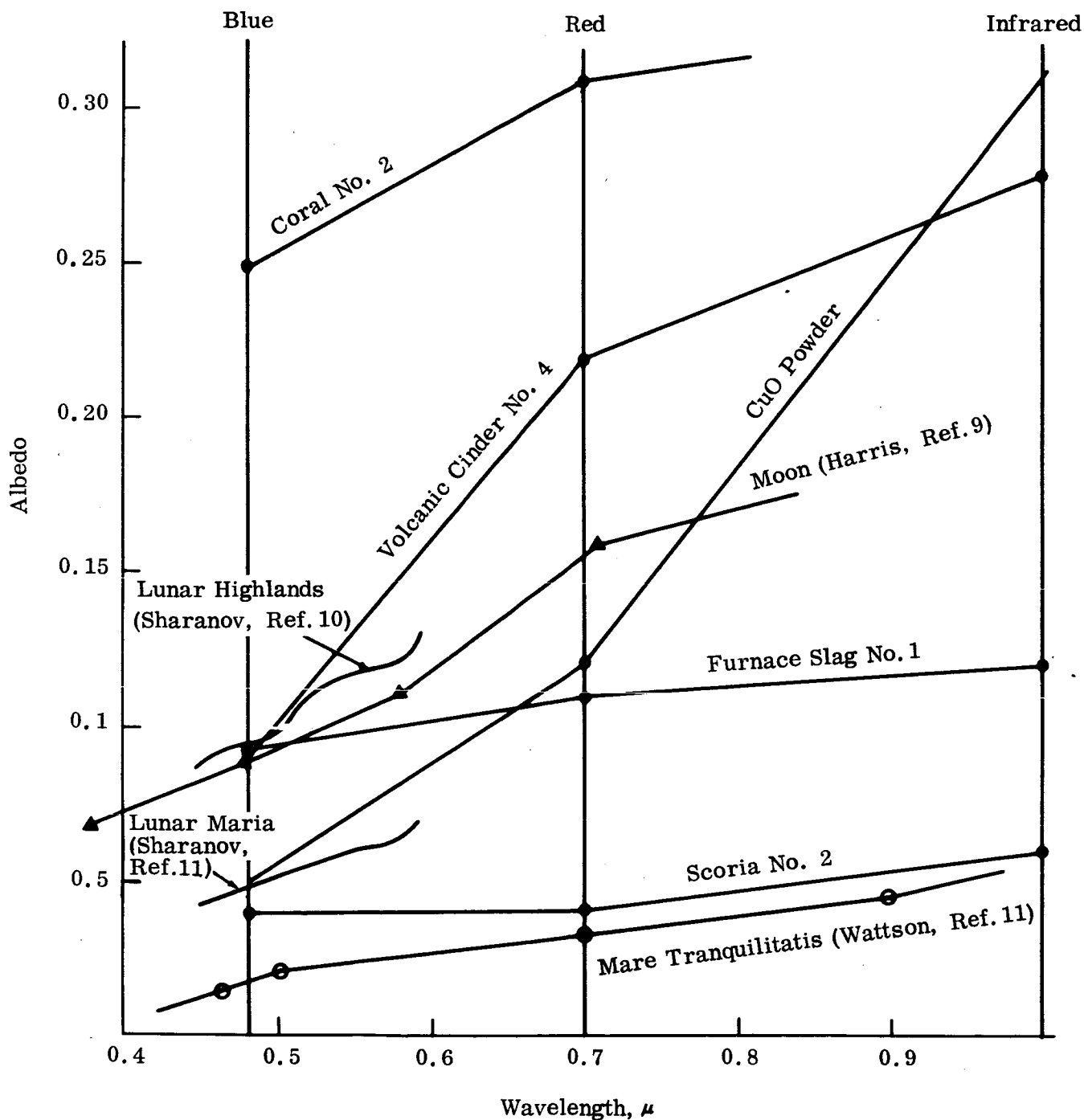
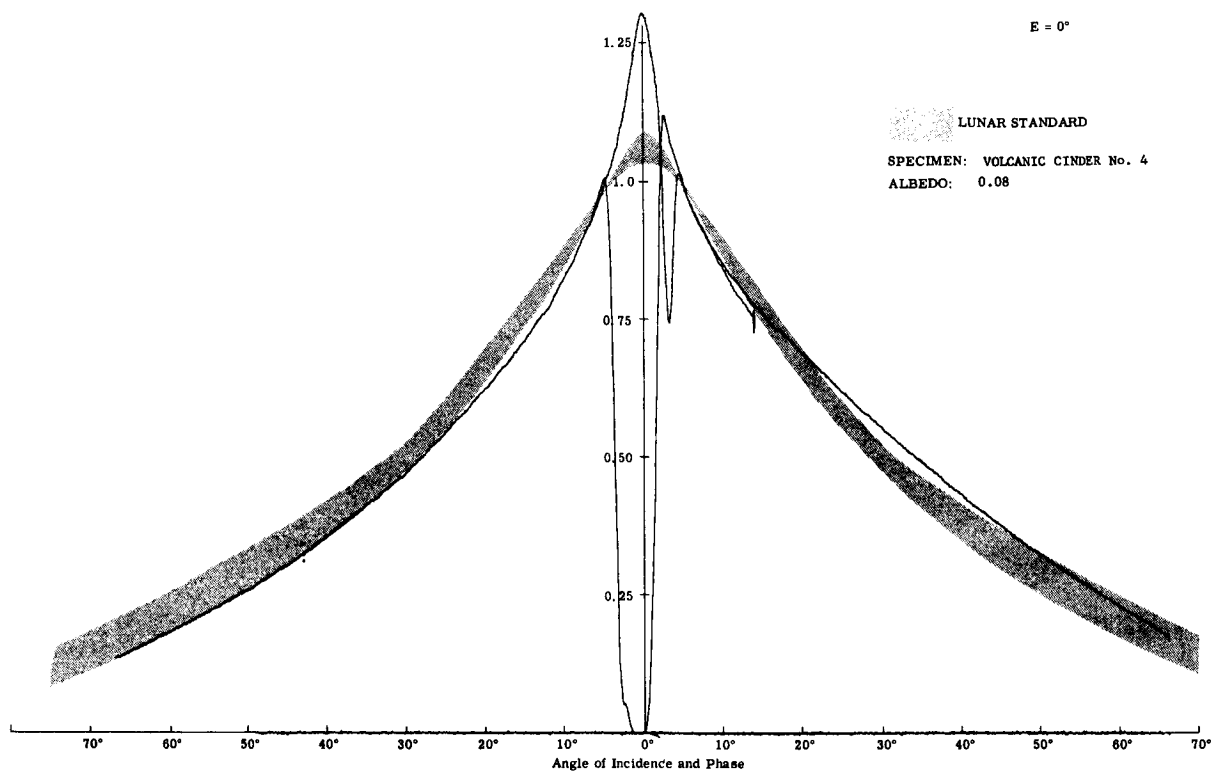
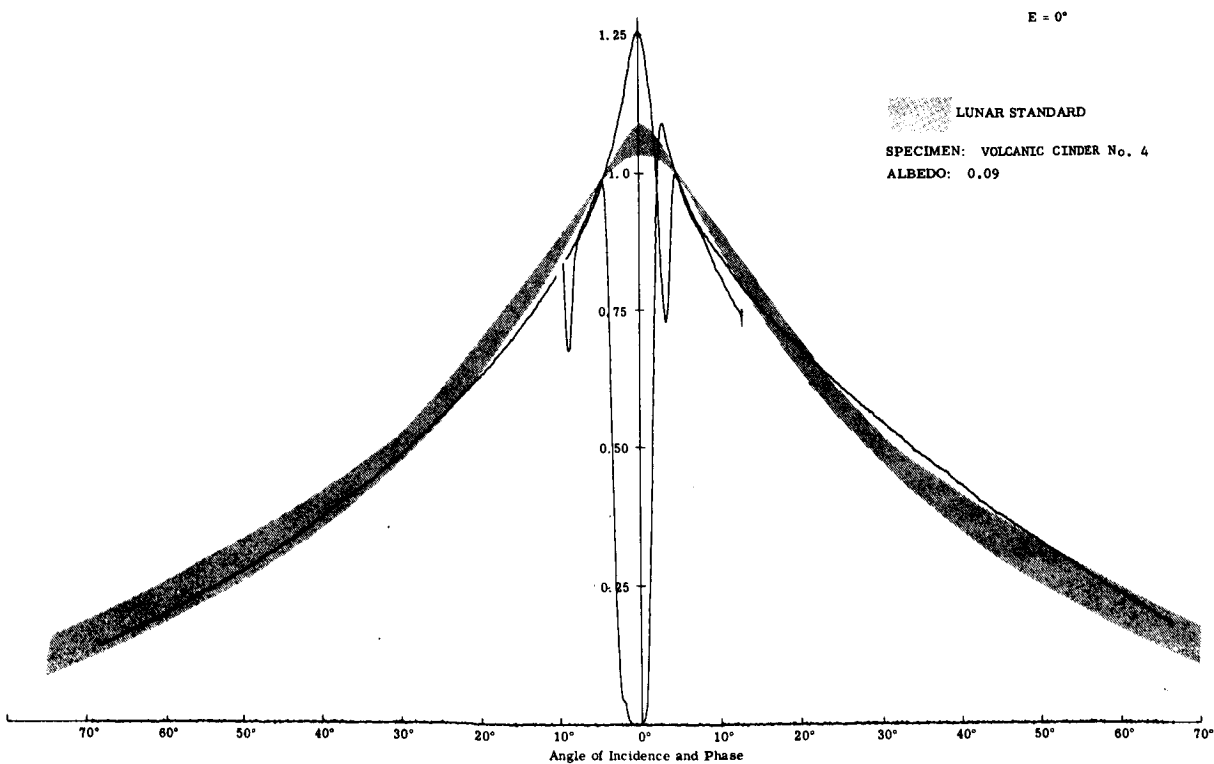


Fig. 12 Albedo vs Wavelength of Moon and Test Specimens

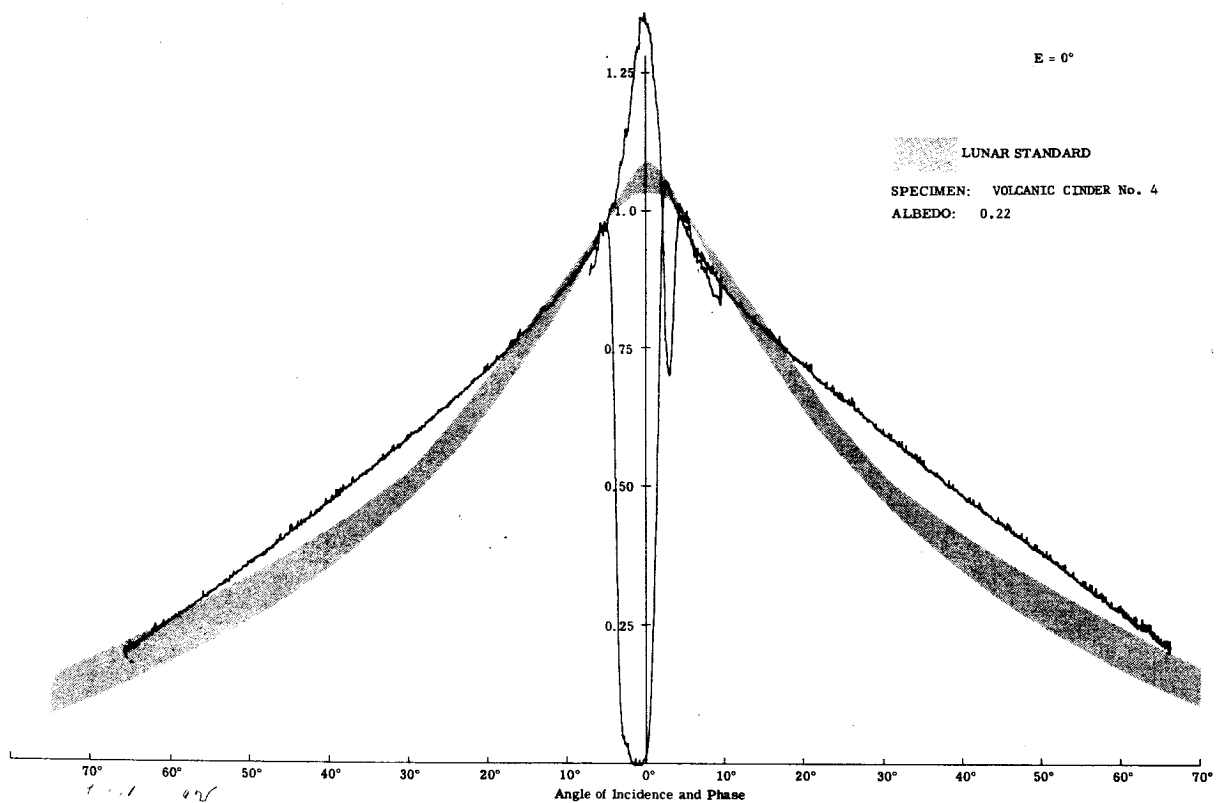


Visible

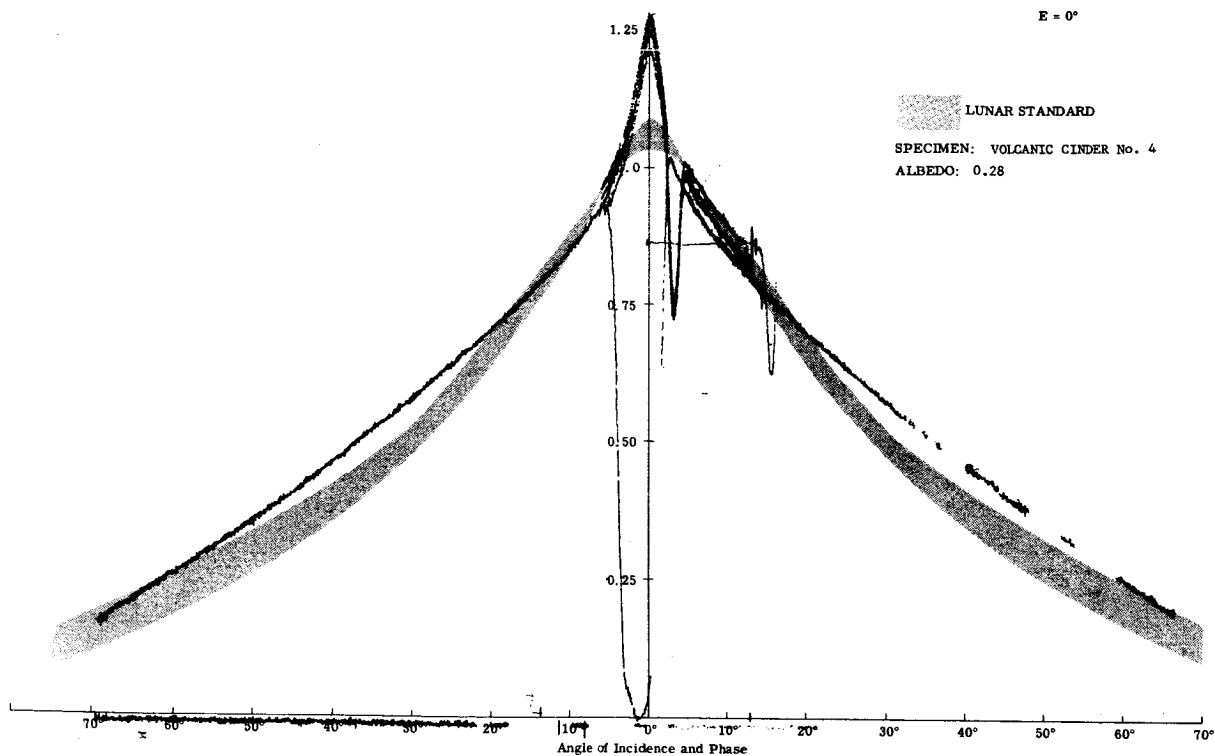


Blue

Fig. 13a Photometry of Volcanic Cinder No. 4 ( $E = 0^\circ$ )

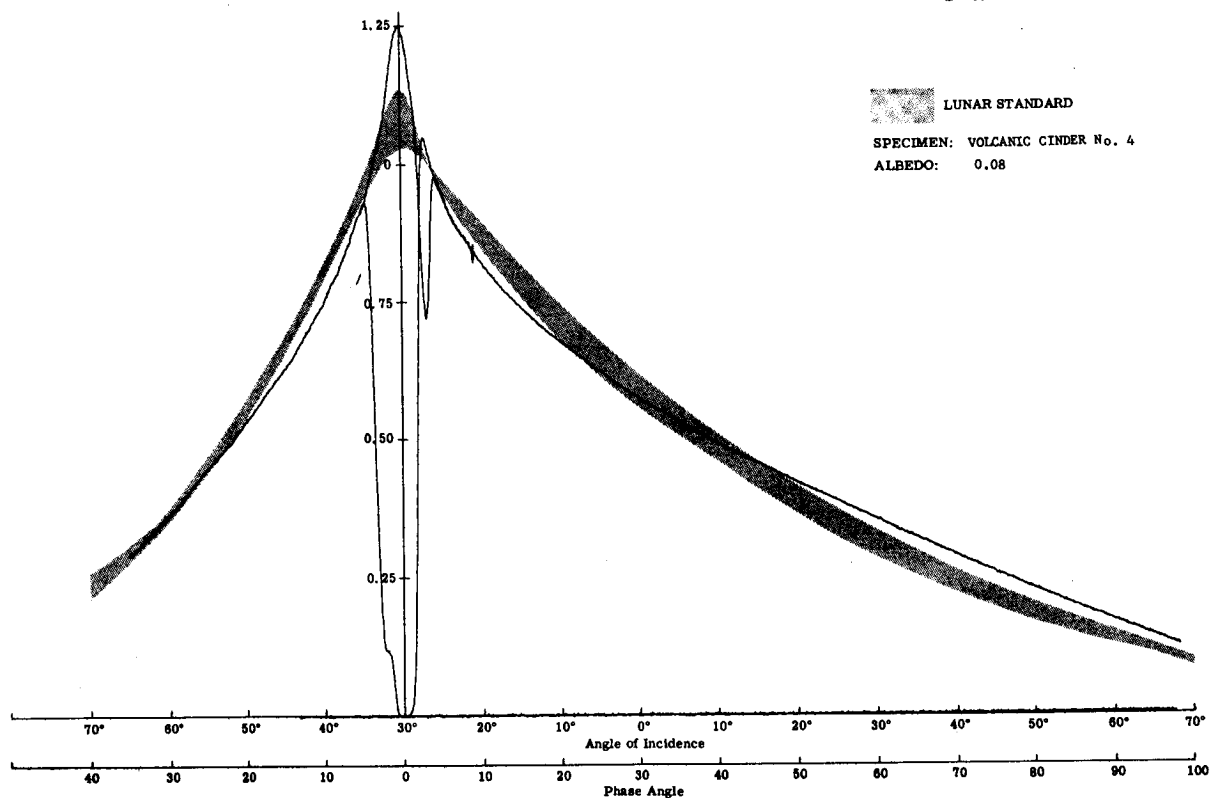


Red

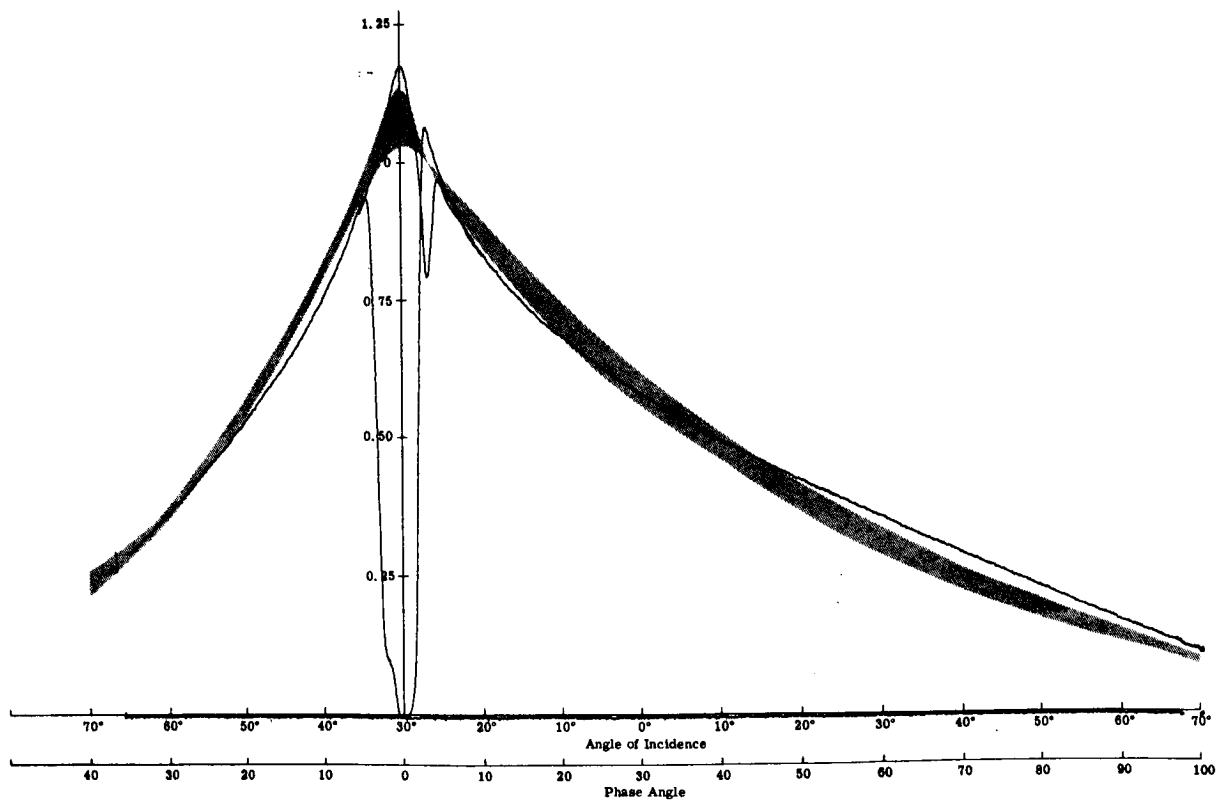


Infrared

Fig. 13a (cont) Photometry of Volcanic Cinder No. 4 (E = 0°)



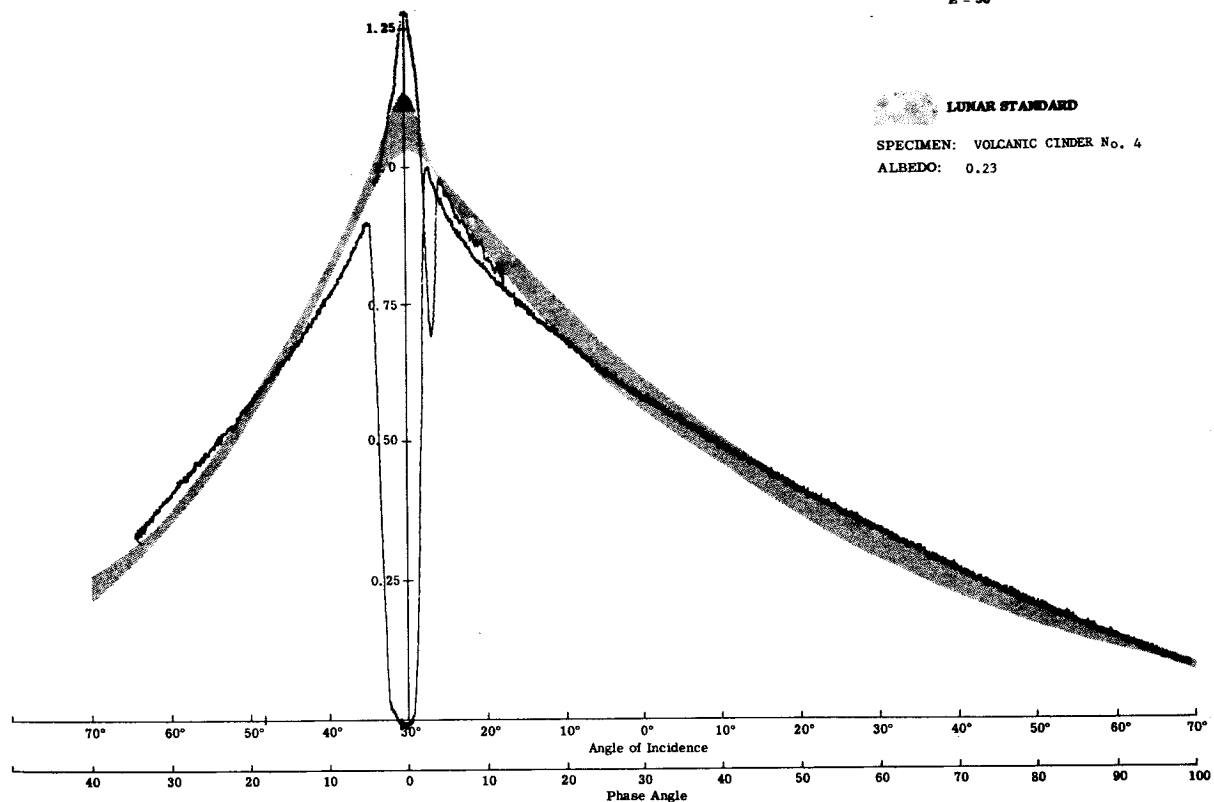
Visible



Blue

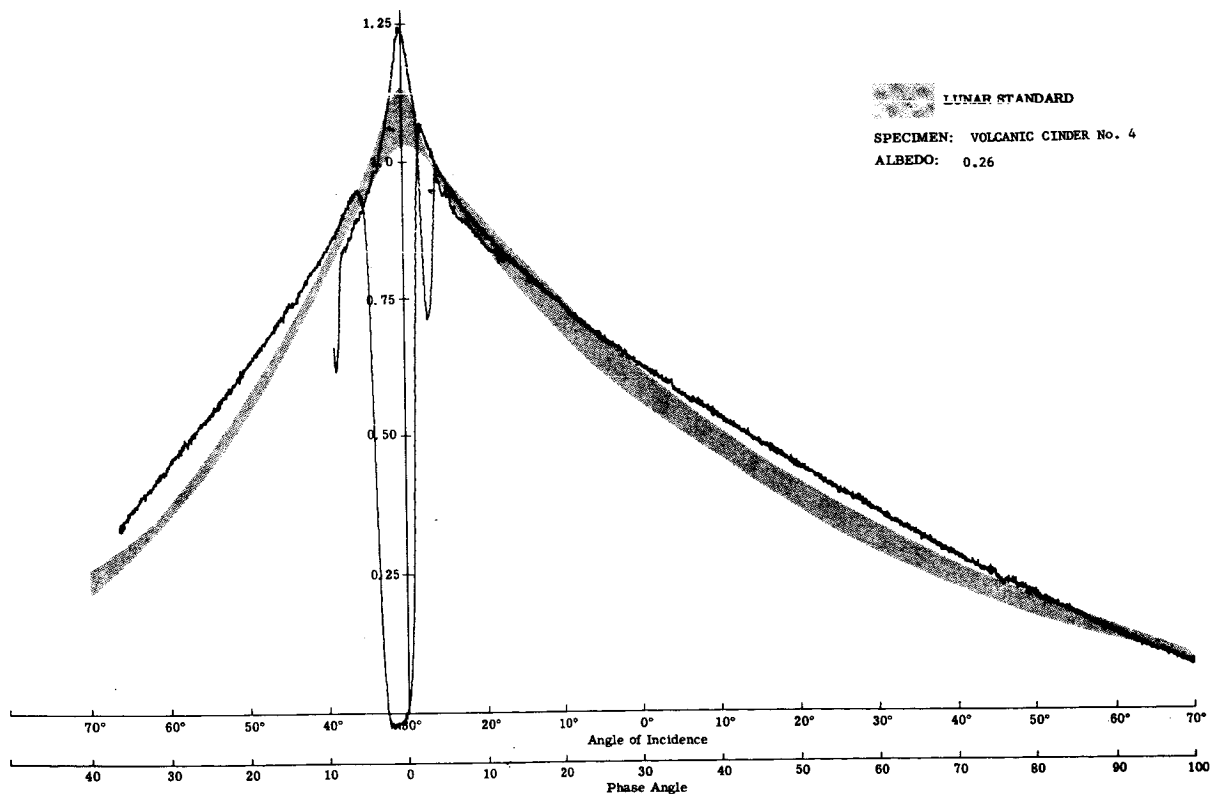
Fig. 13b Photometry of Volcanic Cinder No. 4 (E = 30°)

E = 30°



Red

E = 30°



Infrared

Fig. 13b (cont) Photometry of Volcanic Cinder No. 4 (E = 30°)



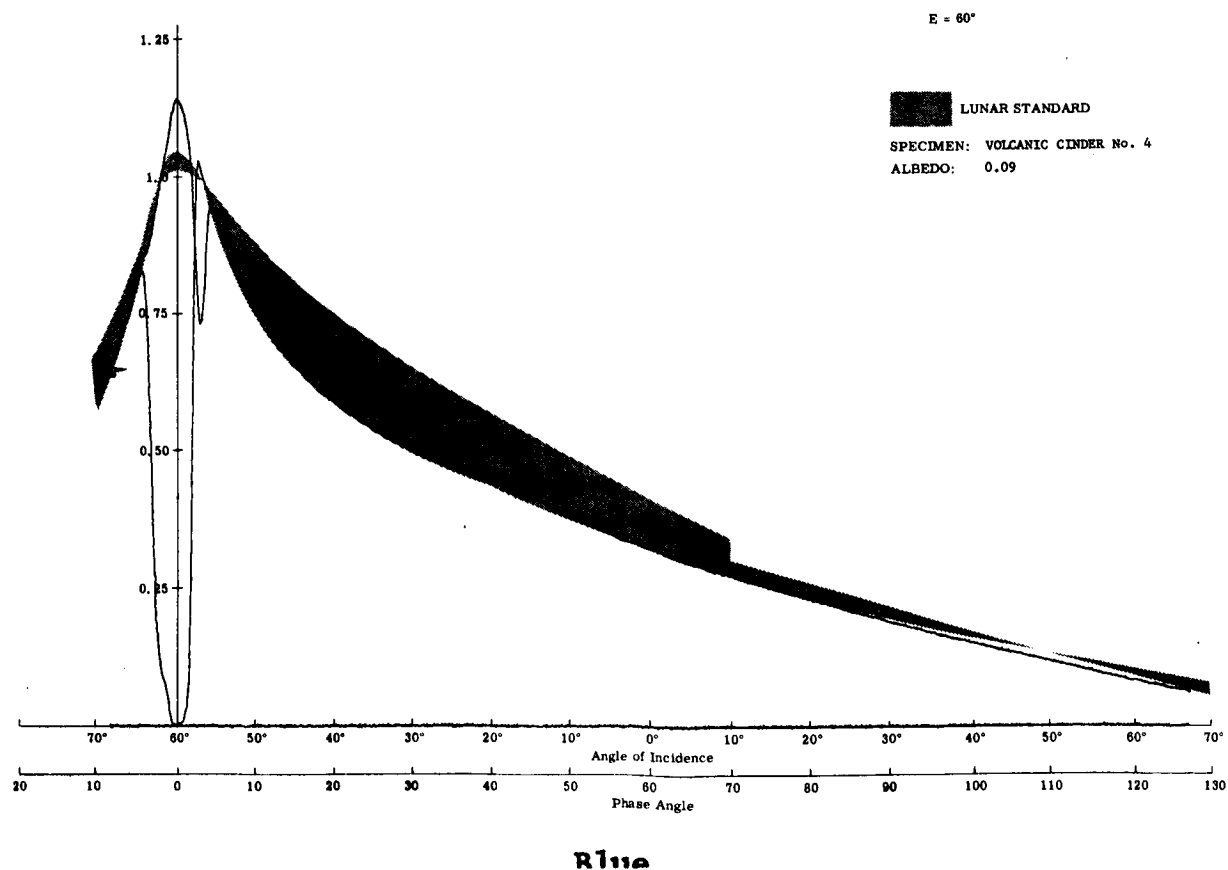
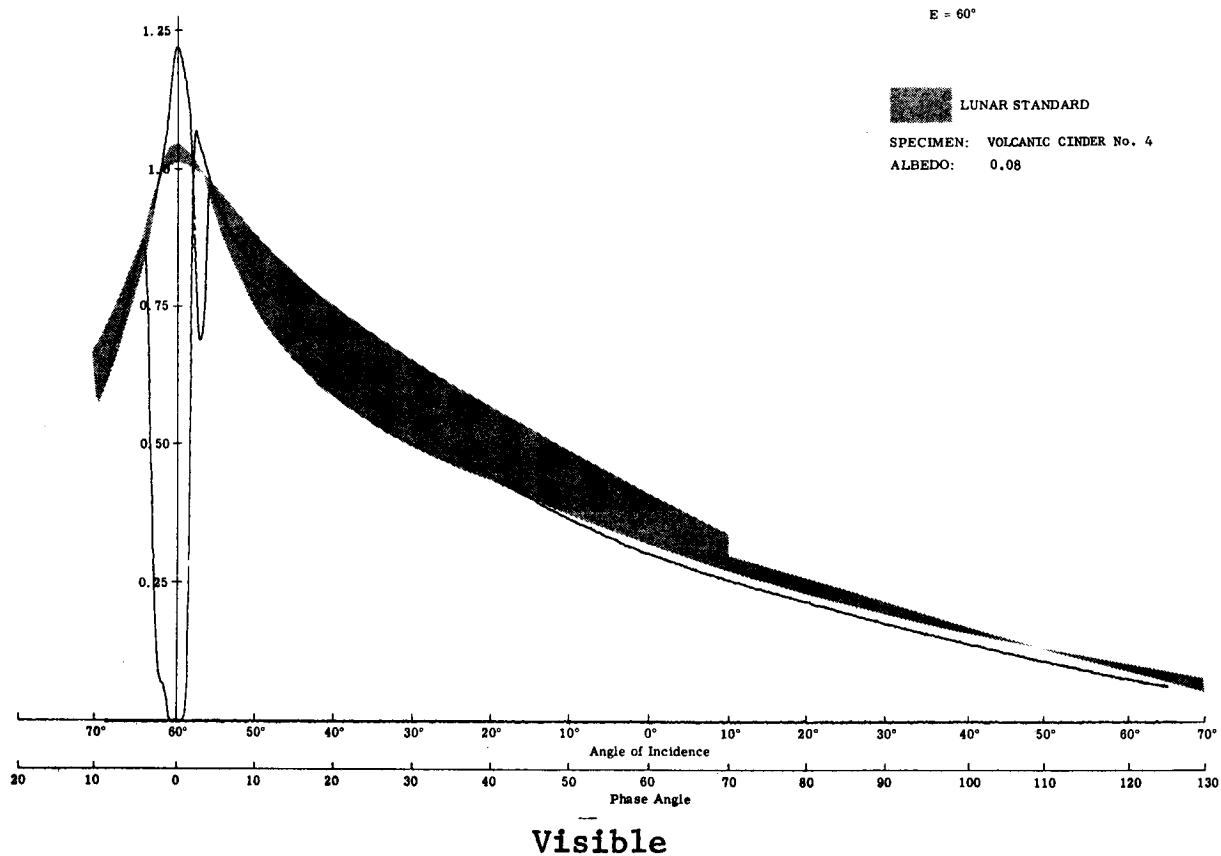


Fig. 13c Photometry of Volcanic Cinder No. 4 ( $E = 60^\circ$ )

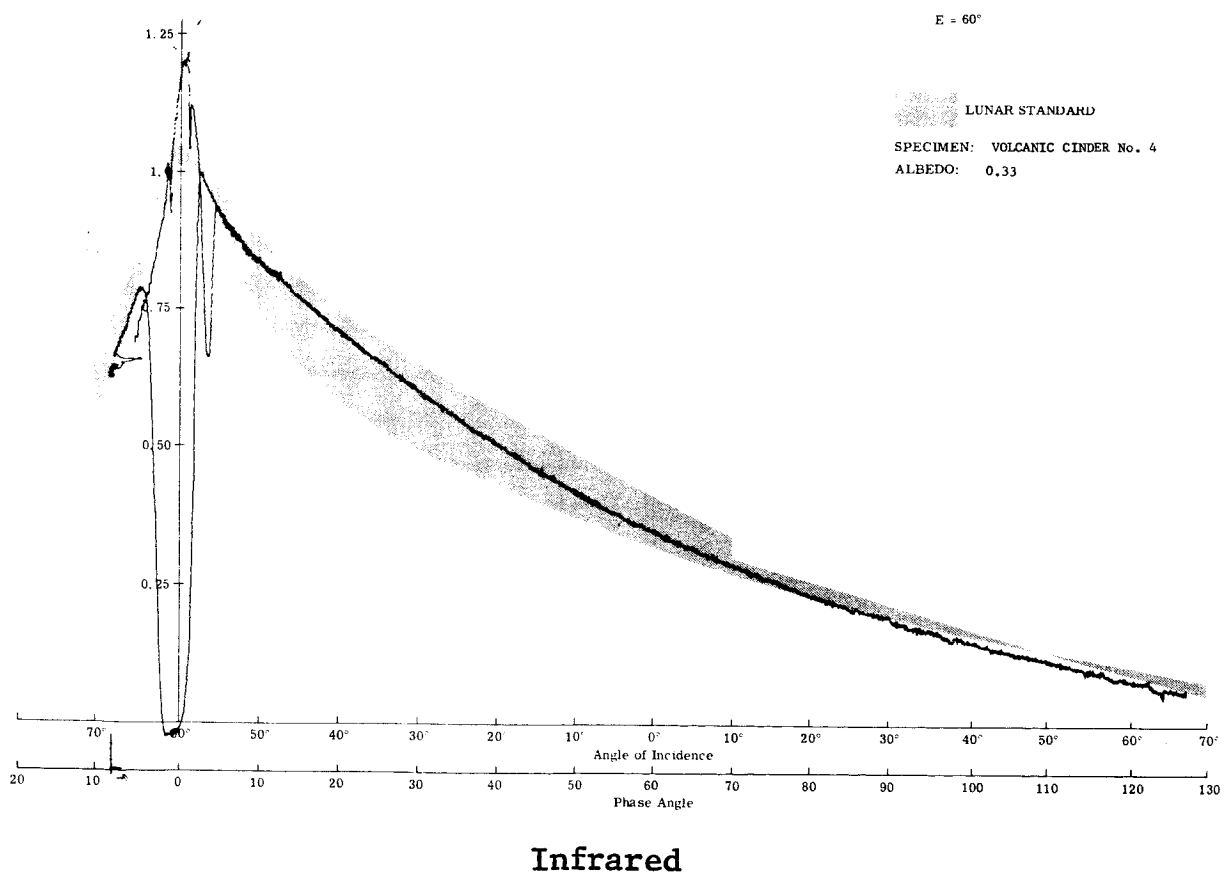
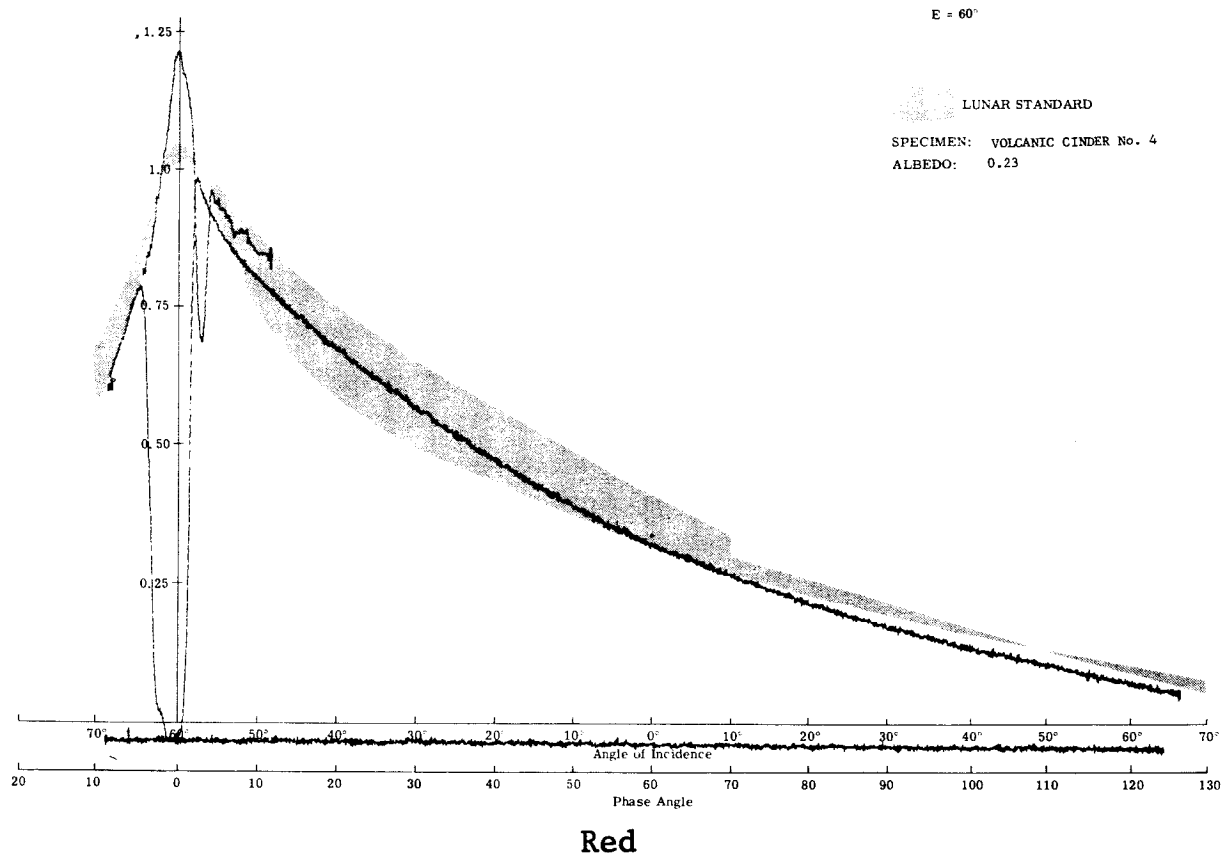
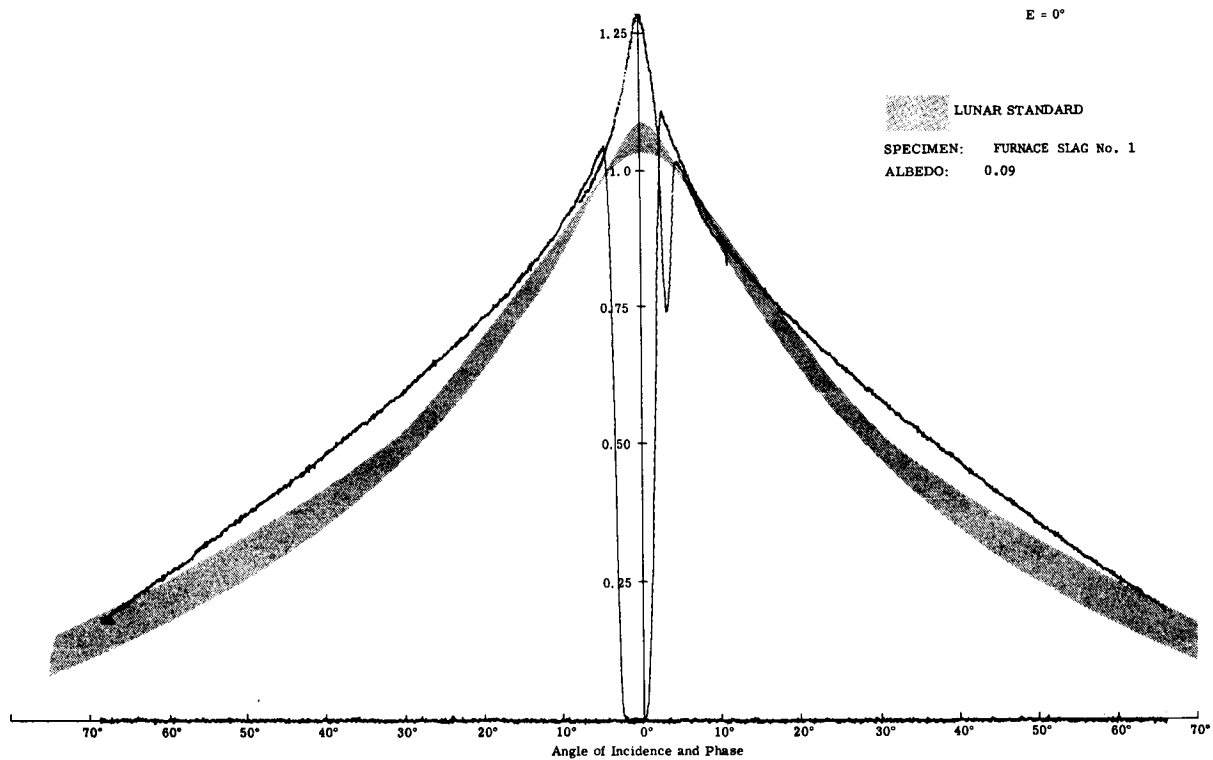
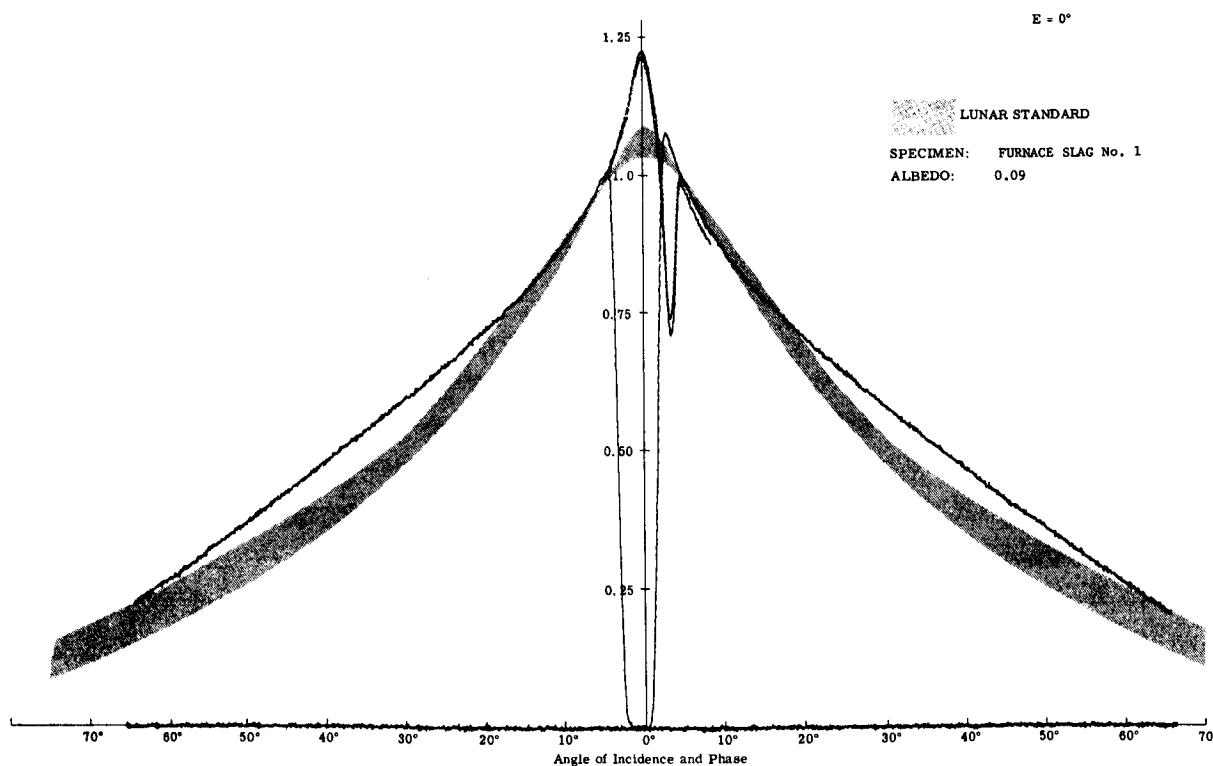


Fig. 13c (cont) Photometry of Volcanic Cinder No. 4 ( $E = 60^\circ$ )

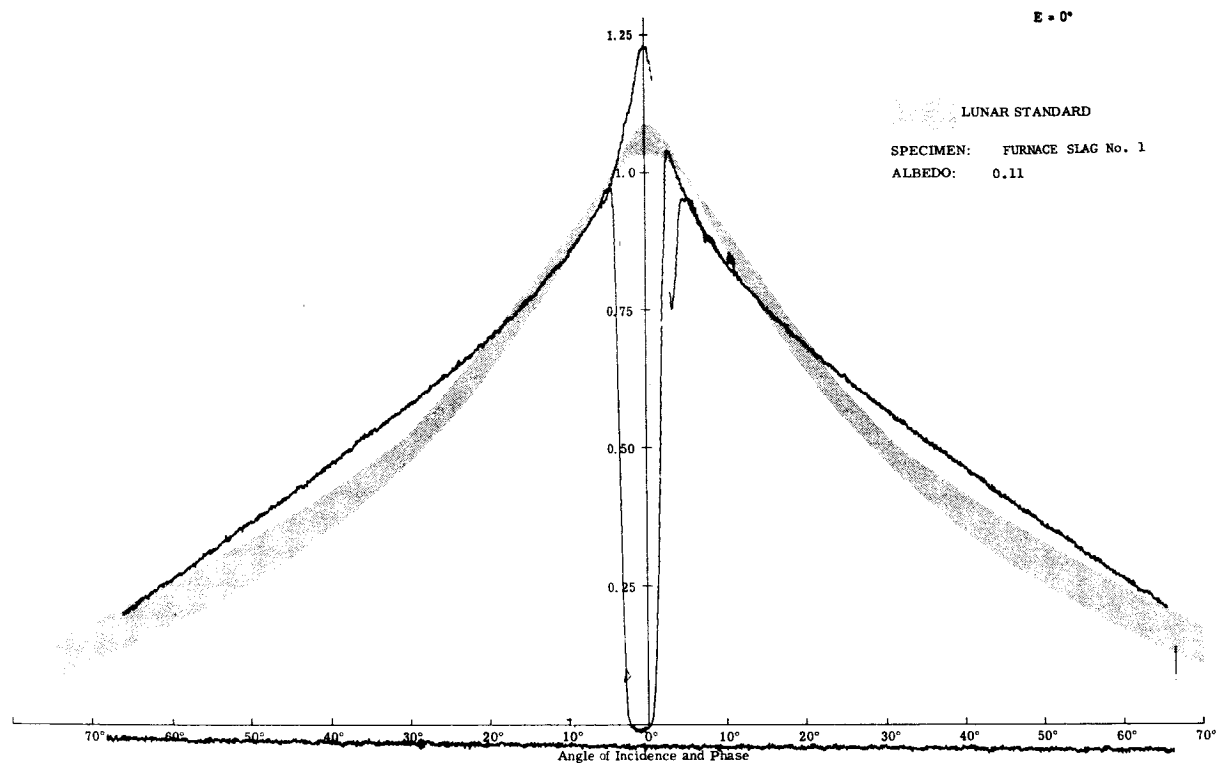


Visible

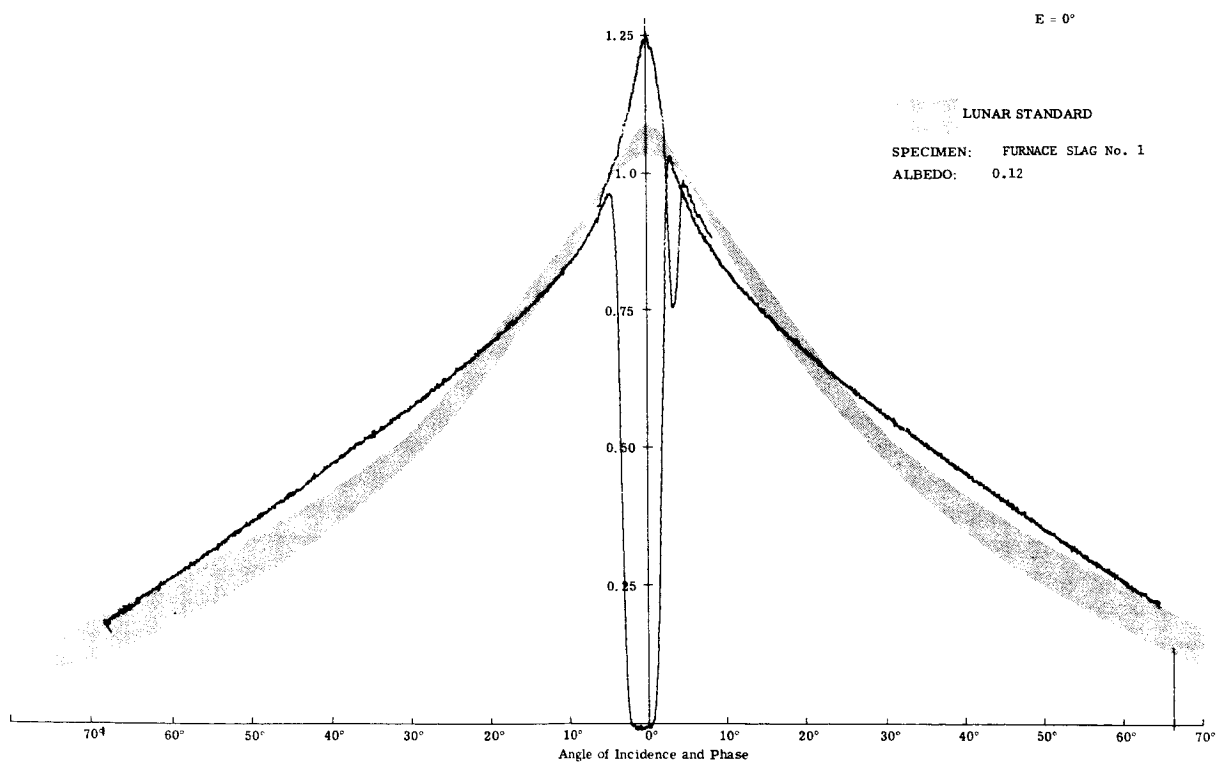


Blue

Fig. 14a Photometry of Furnace Slag No. 1 ( $E = 0^\circ$ )



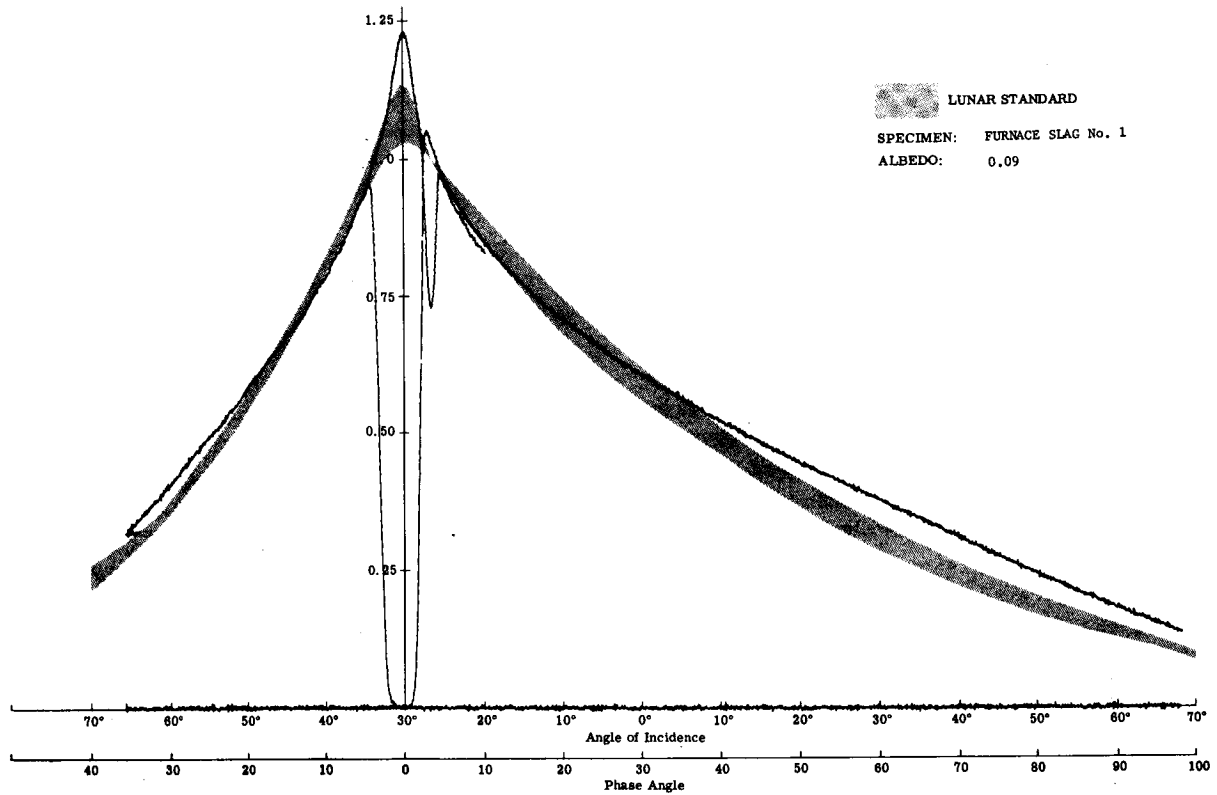
Red



Infrared

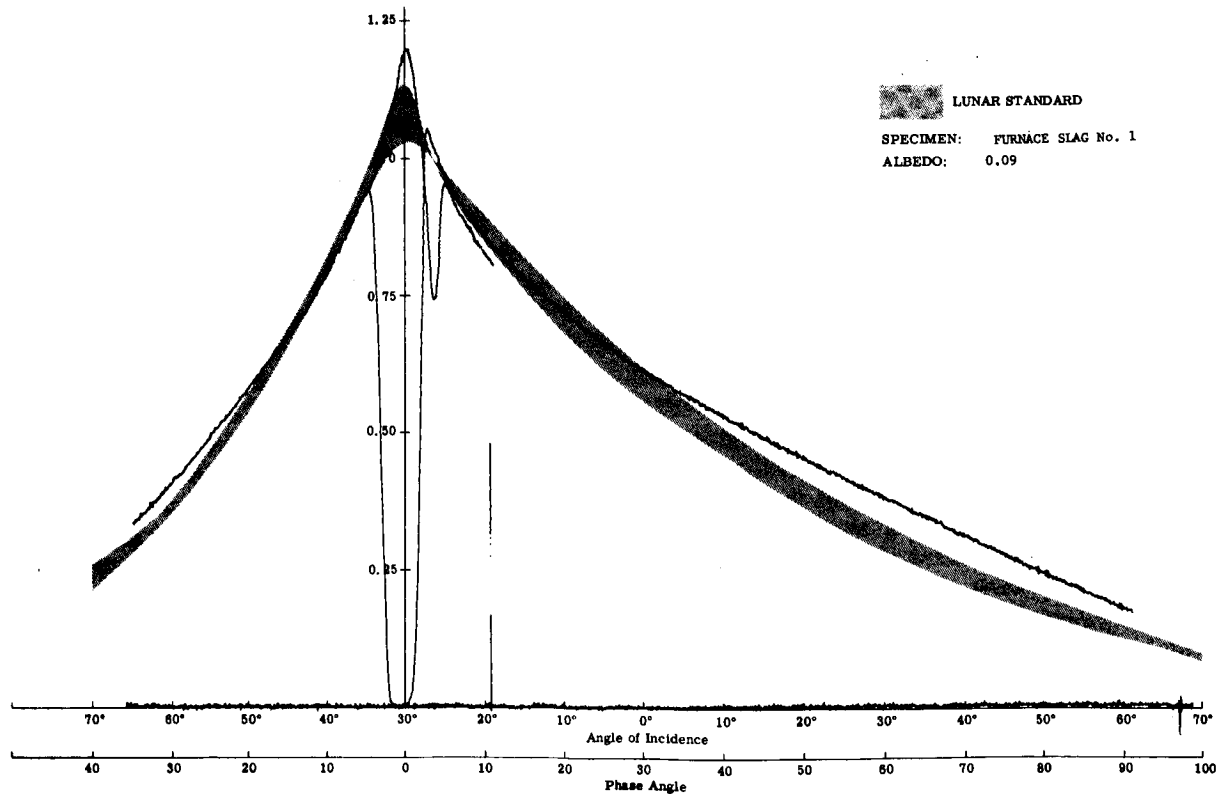
Fig. 14a (cont) Photometry of Furnace Slag No. 1 ( $E = 0$ )

E = 30°



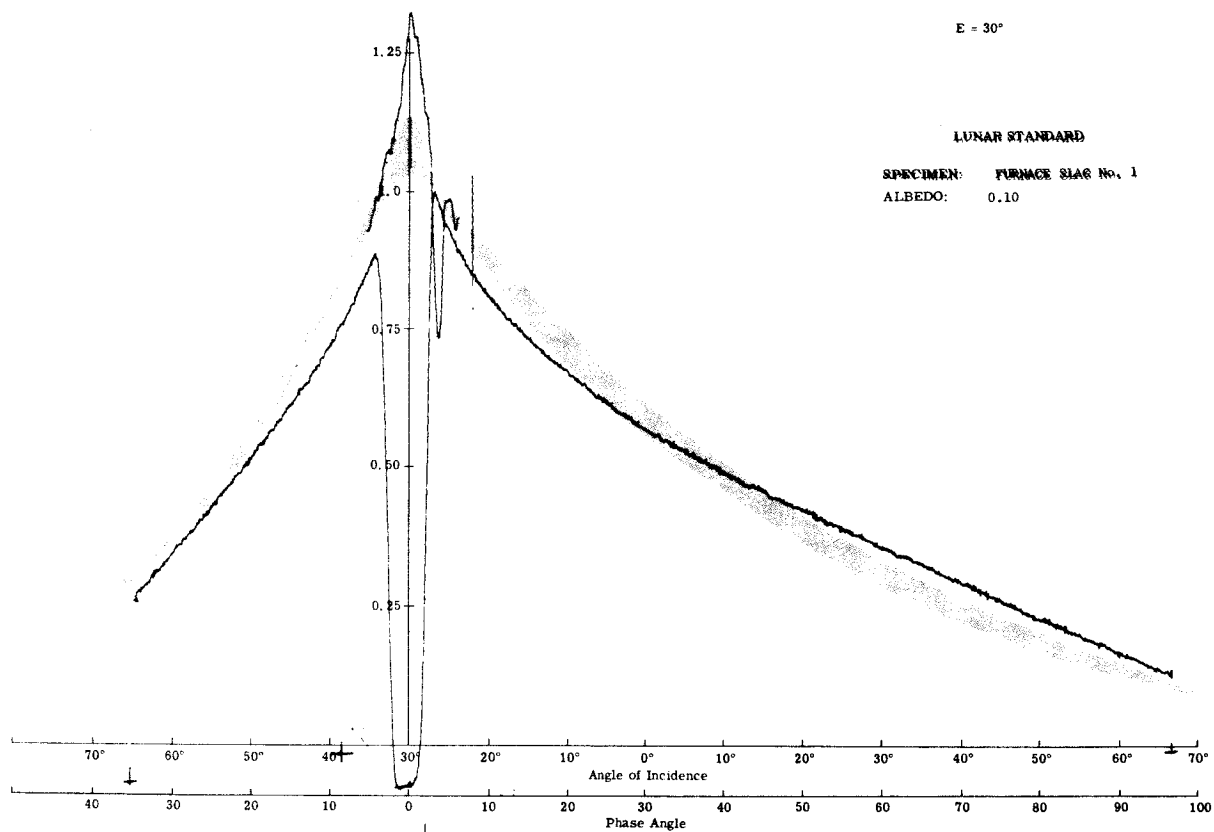
Visible

E = 30°

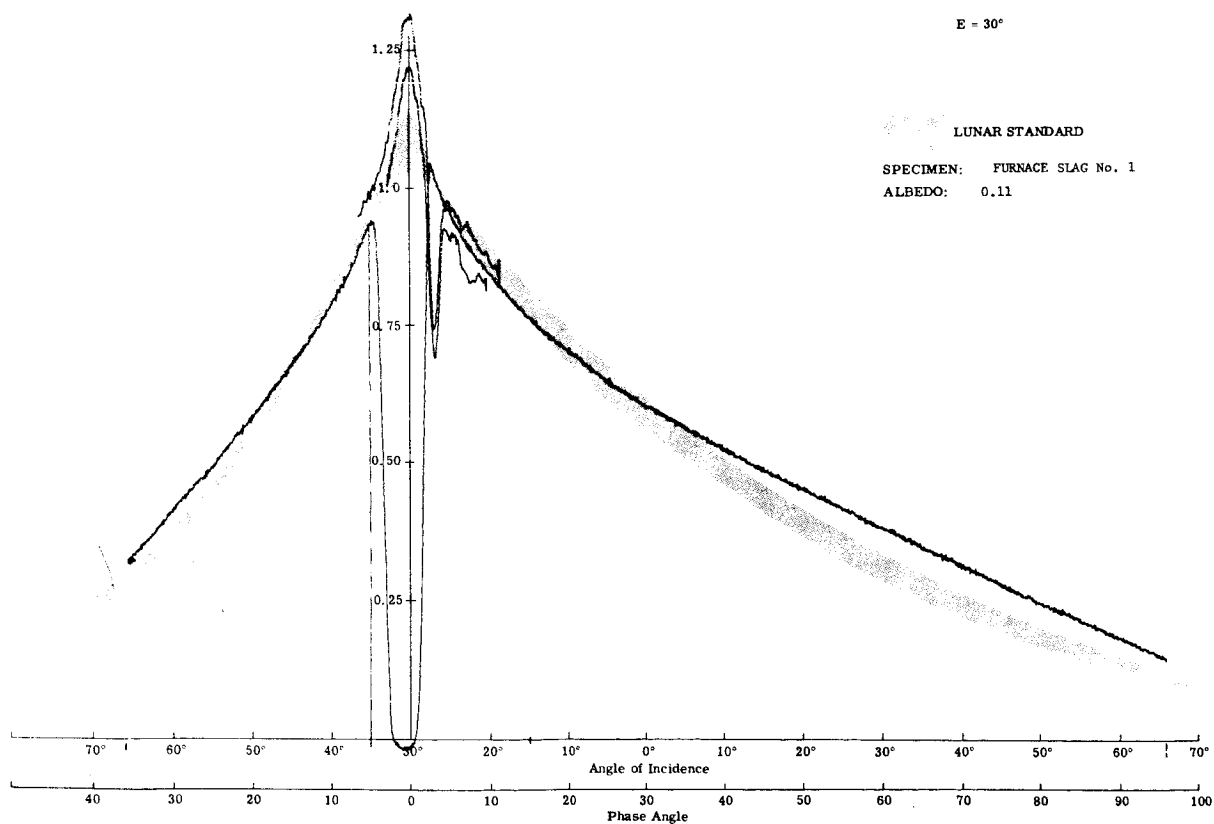


R1110

Fig. 14b Photometry of Furnace Slag No. 1 (E = 30°)

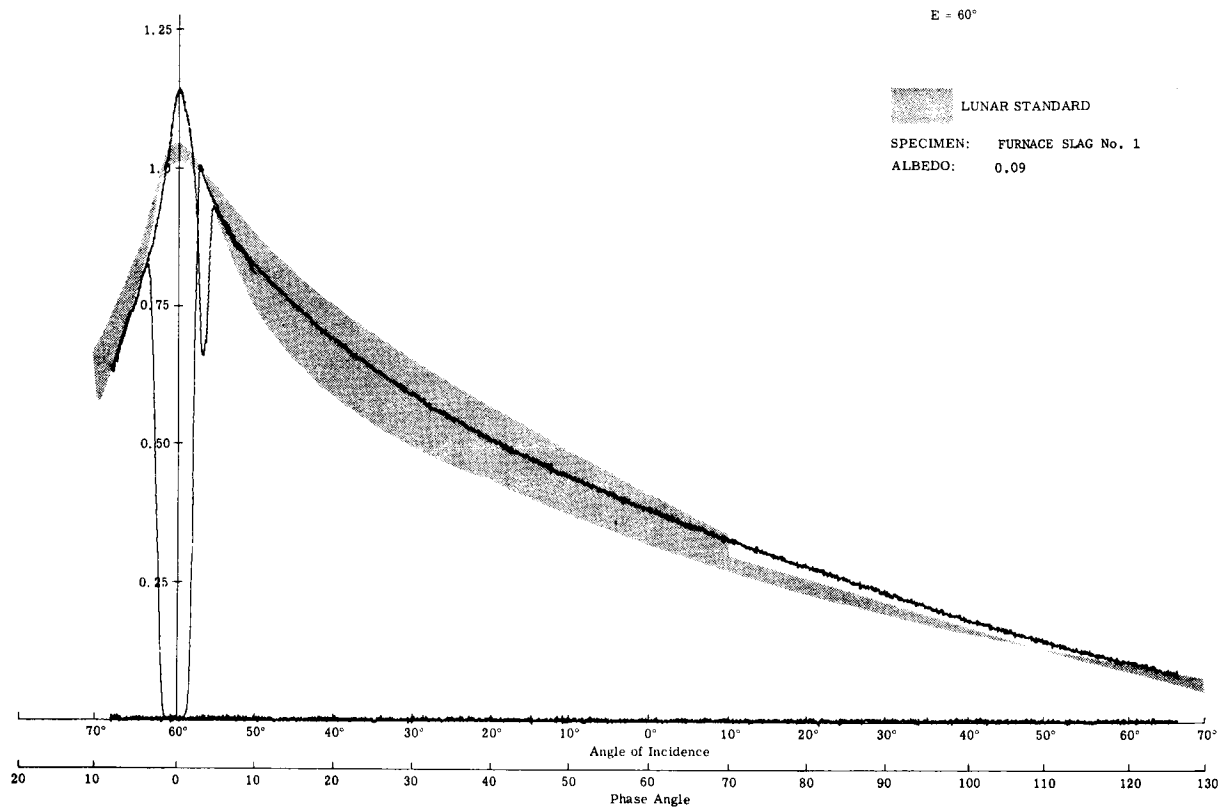


Red

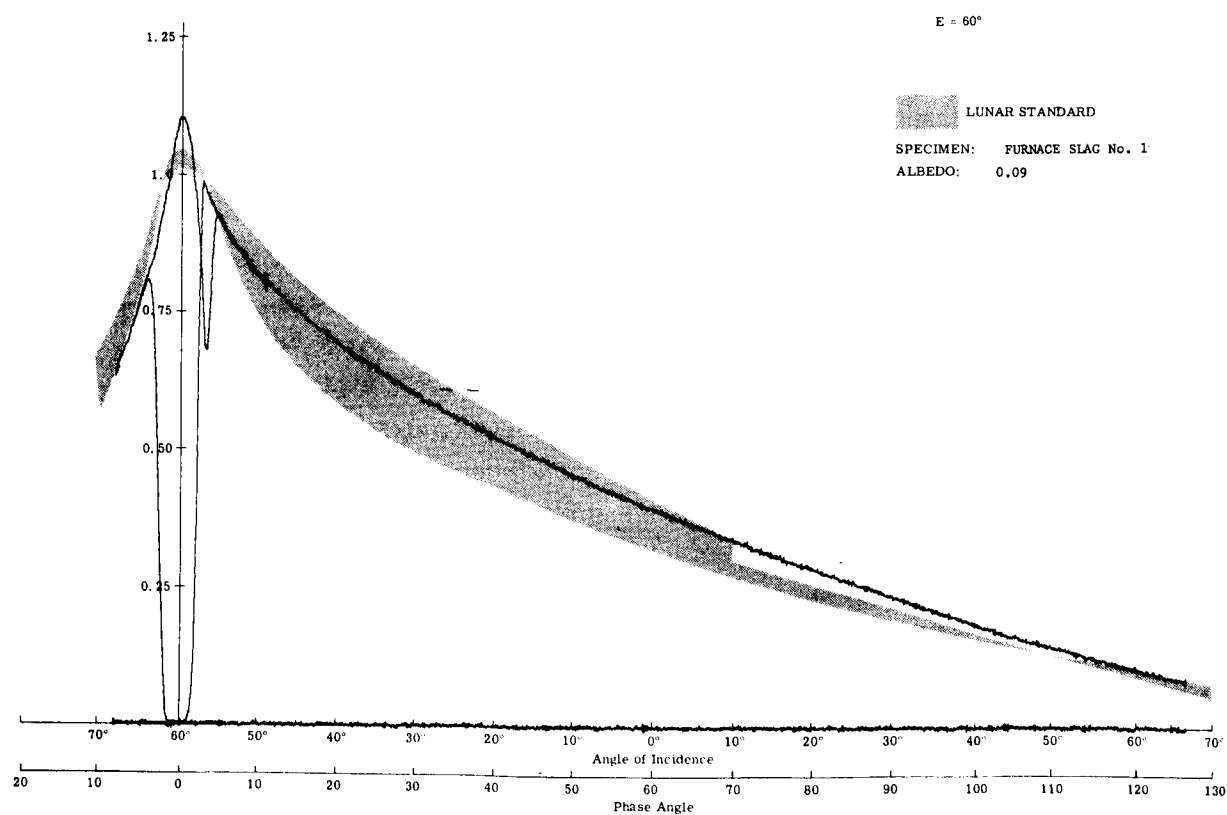


Infrared

Fig. 14b (cont) Photometry of Furnace Slag No. 1 (E = 30°)

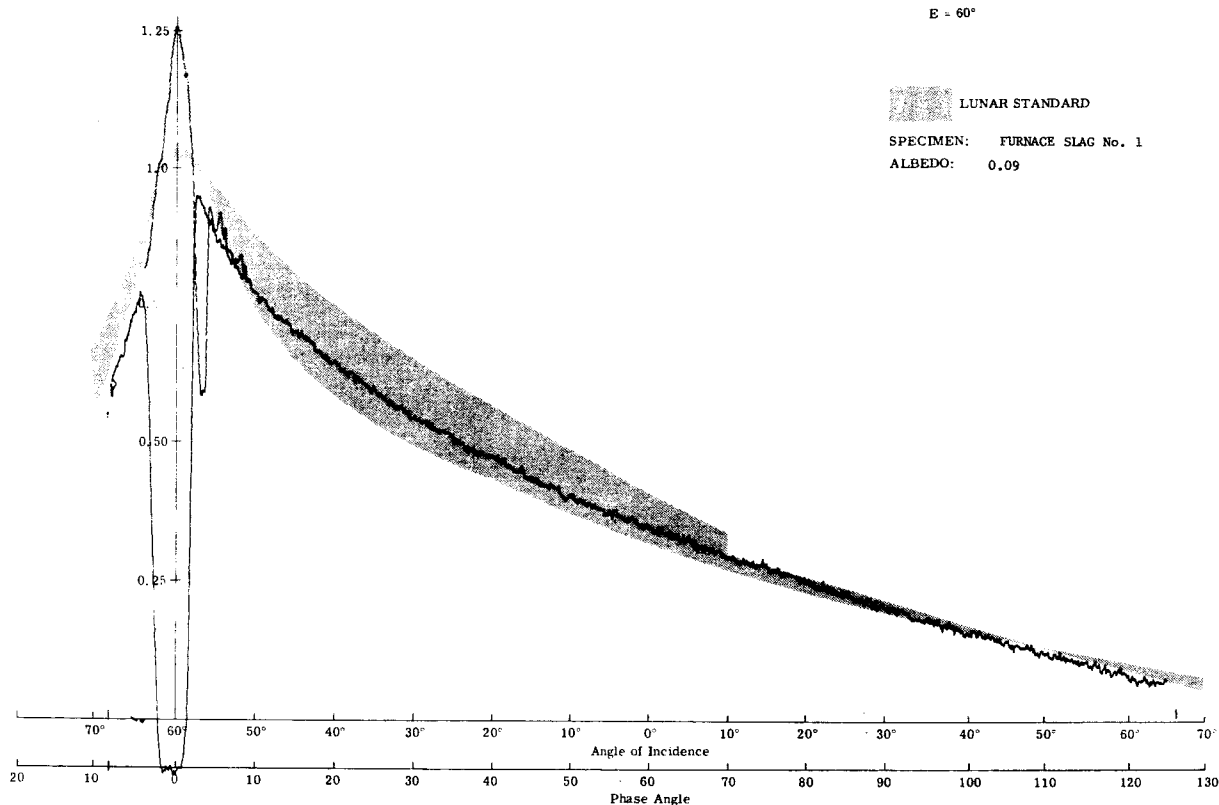


Visible

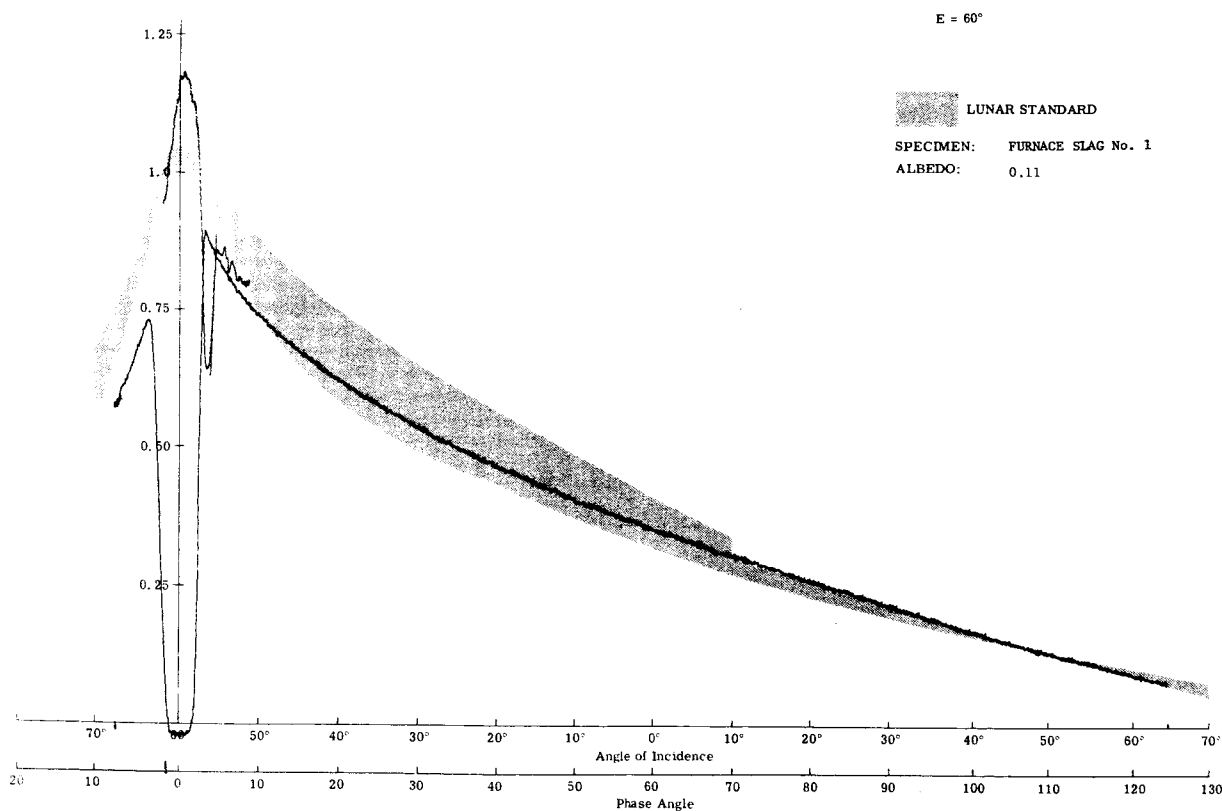


Blue

Fig. 14c Photometry of Furnace Slag No. 1 ( $E = 60^\circ$ )



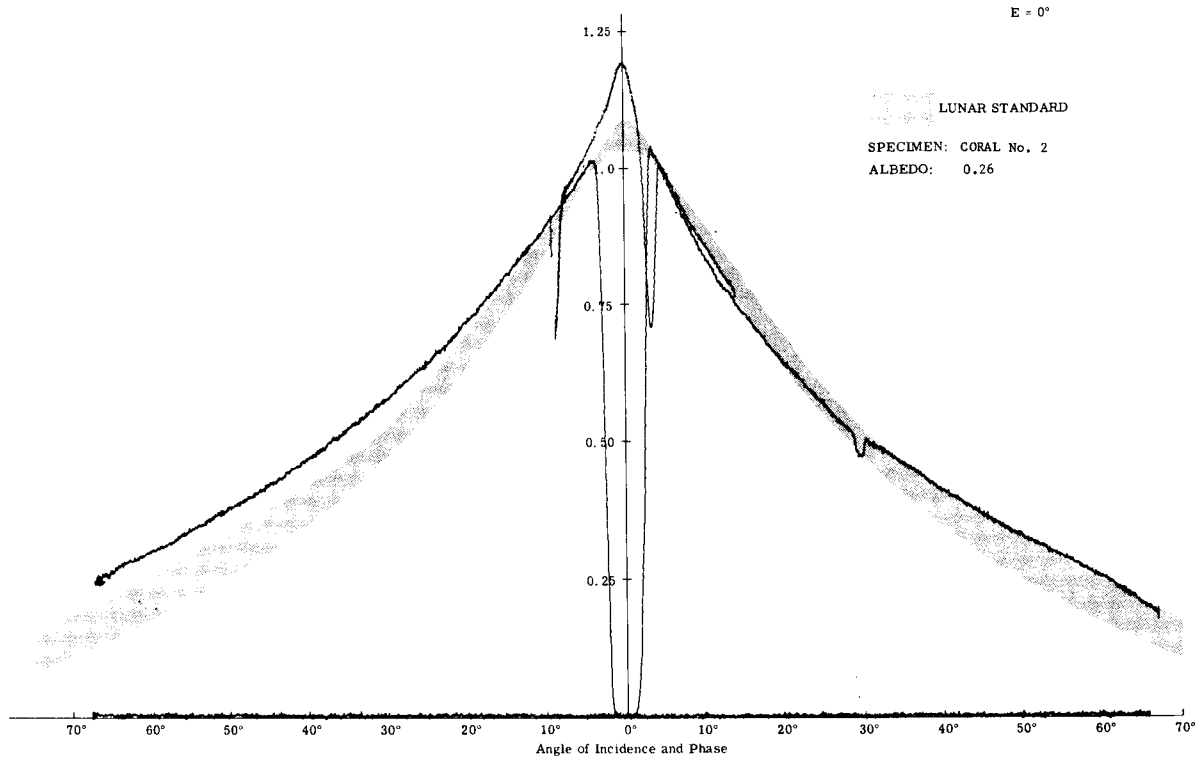
Red



Infrared

Fig. 14: (cont) Photometry of Furnace Slag No. 1 (E = 60°)





Visible

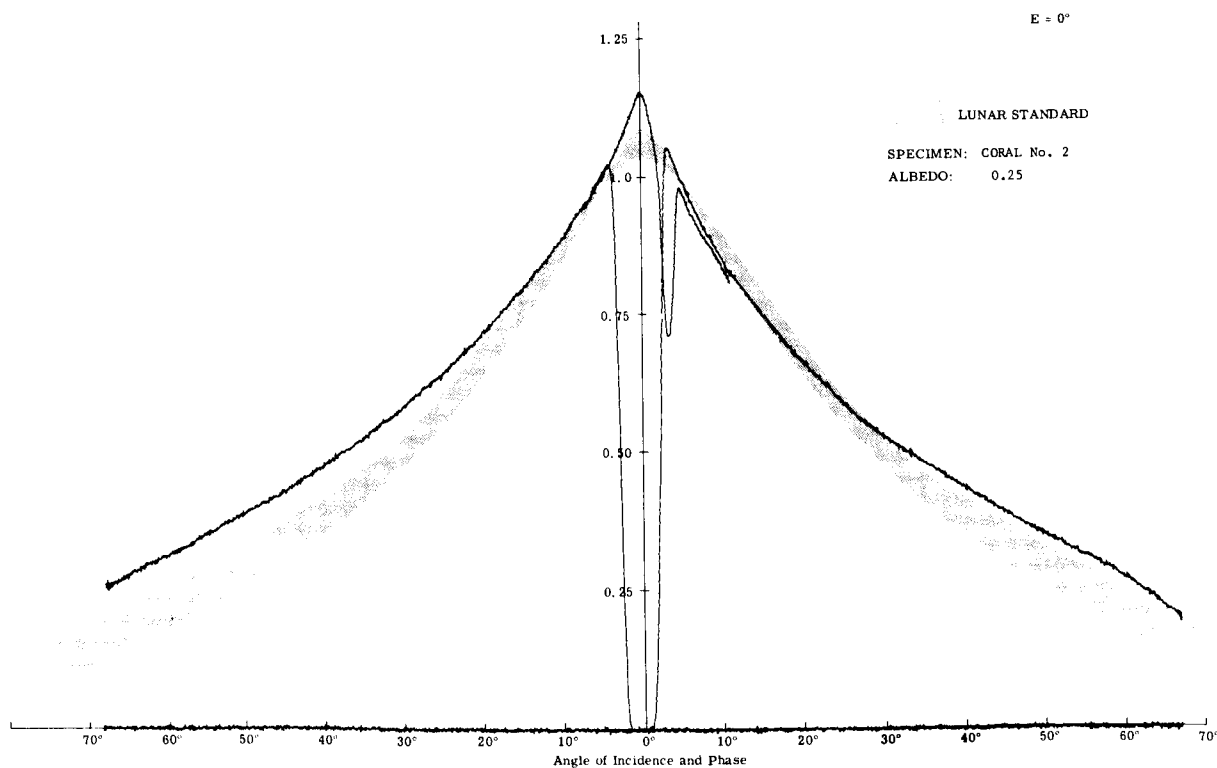
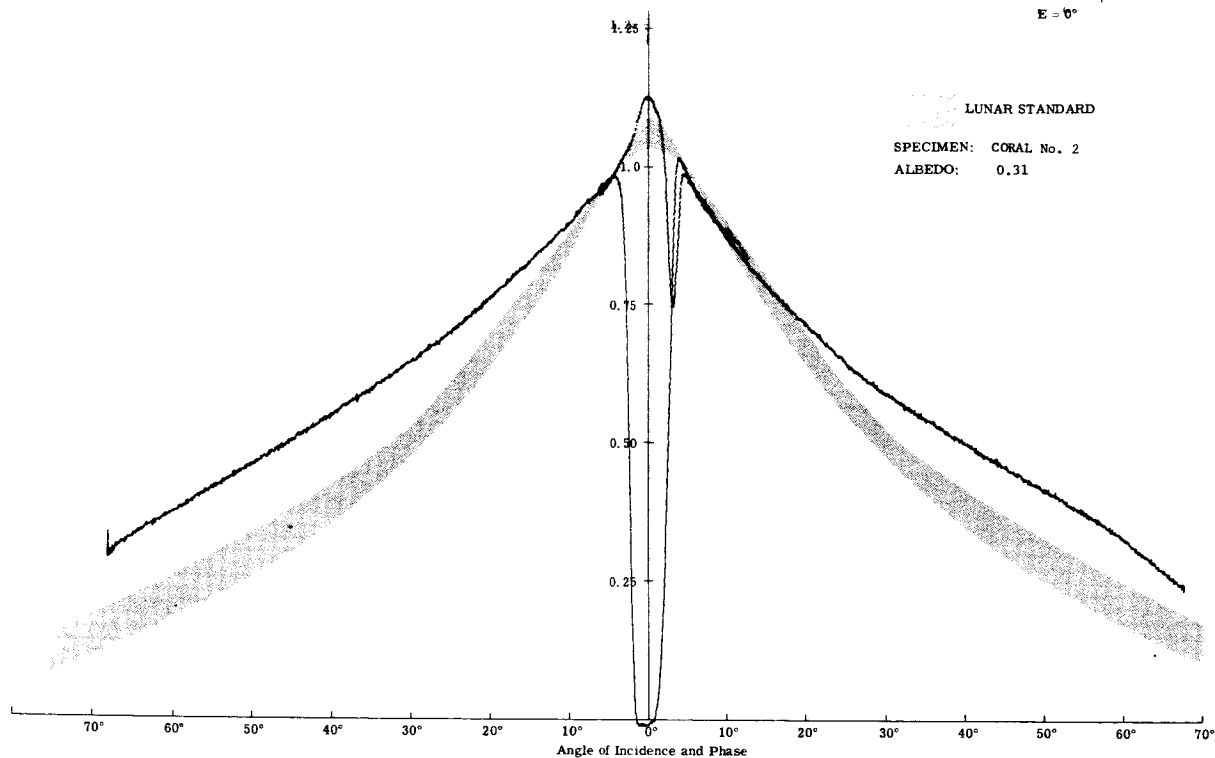
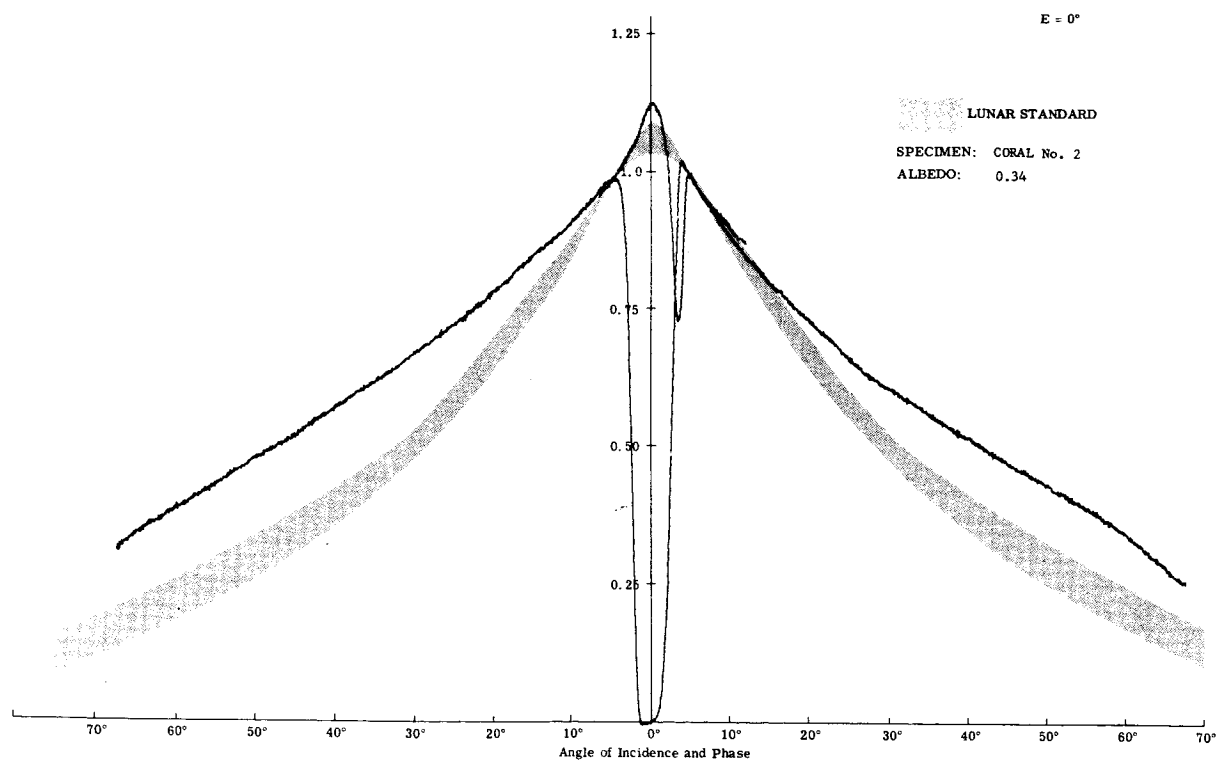


Fig. 15a Photometry of Coral No. 2 ( $E = 0^\circ$ )



Red



Infrared

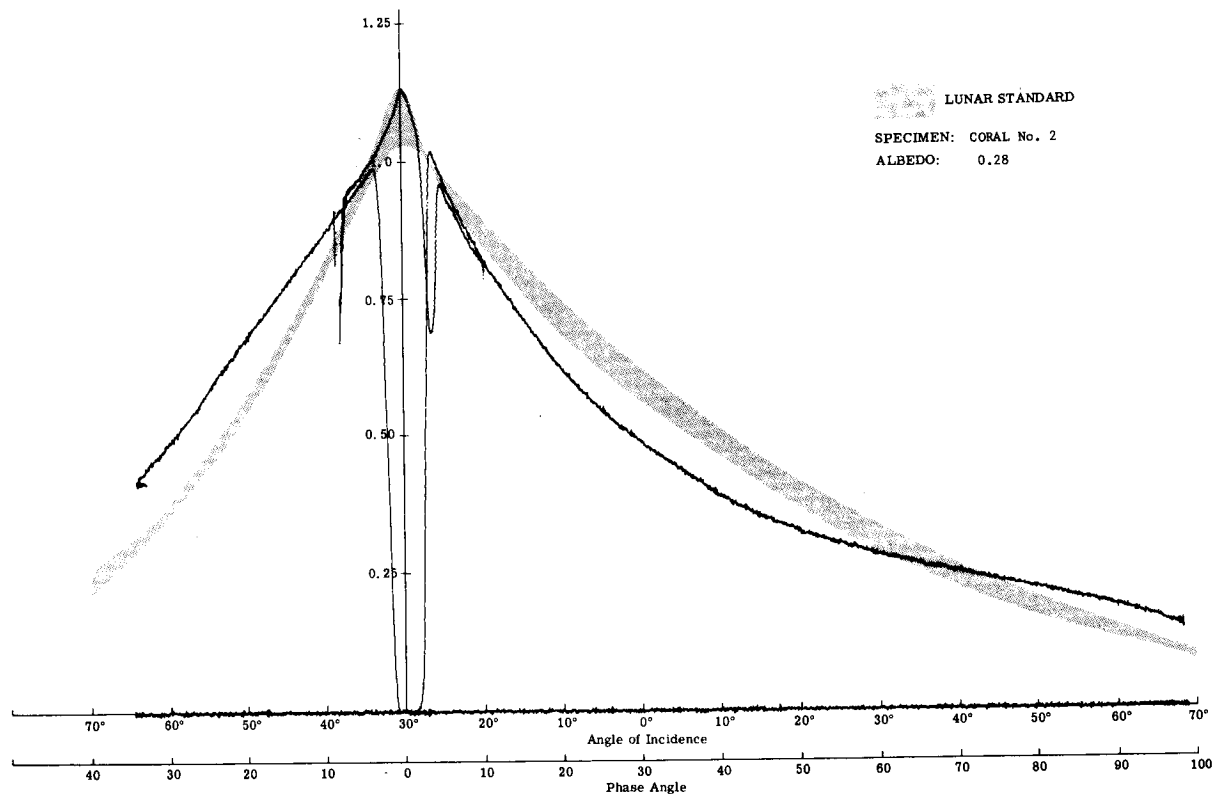
Fig. 15a (cont) Photometry of Coral No. 2 ( $E = 0^\circ$ )

Research Department

RE-245

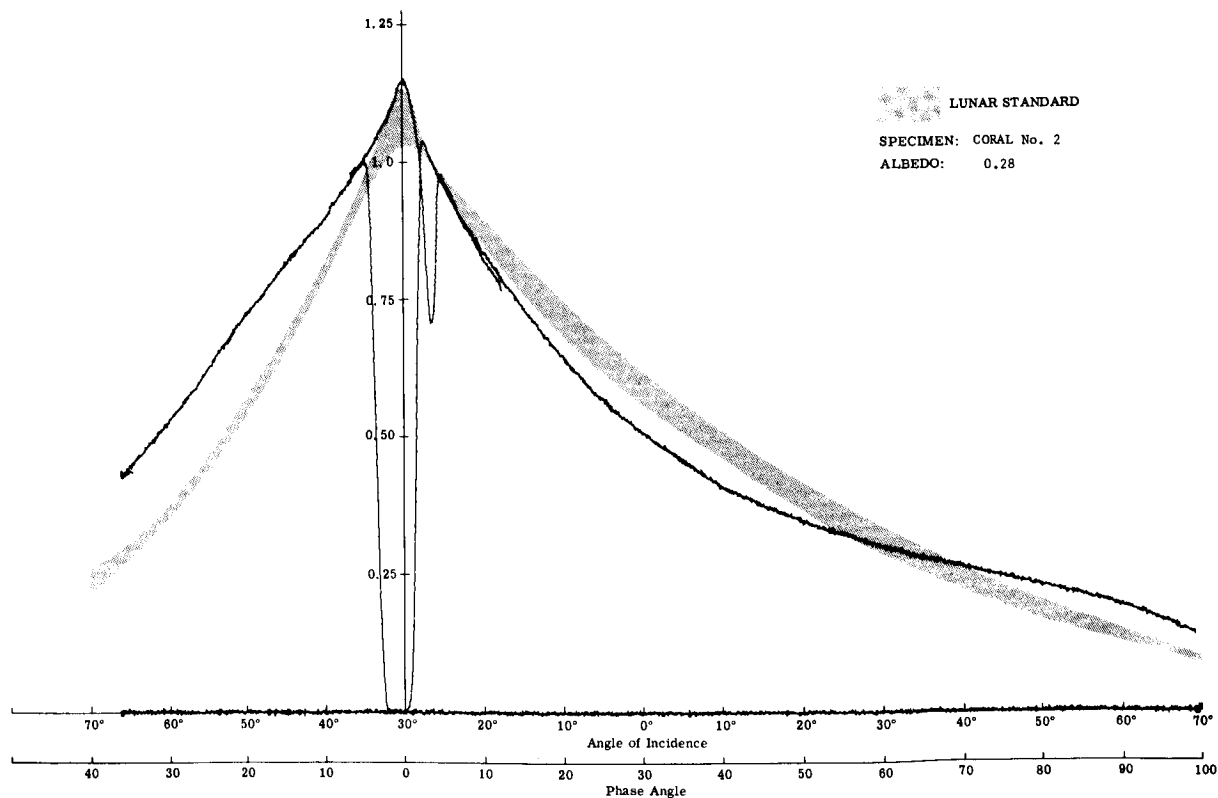
April 1966

E = 30°



Visible

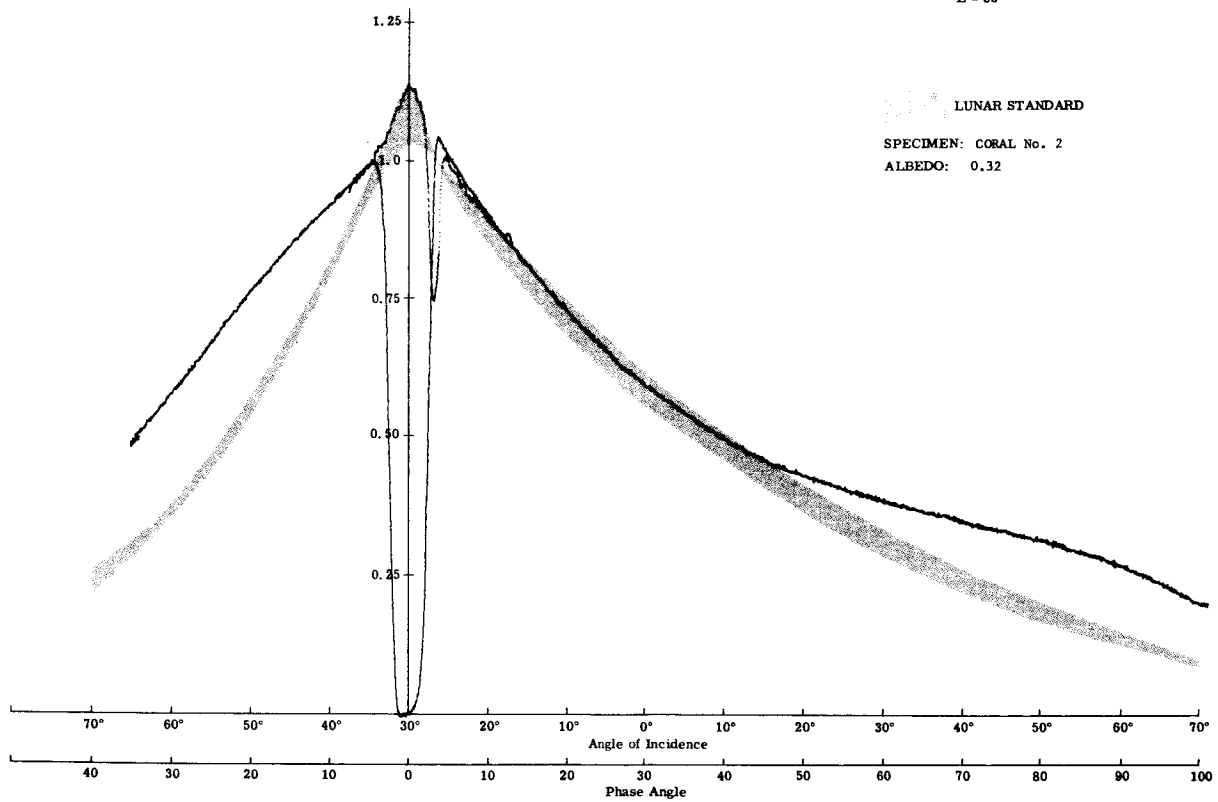
E = 30°



Blue

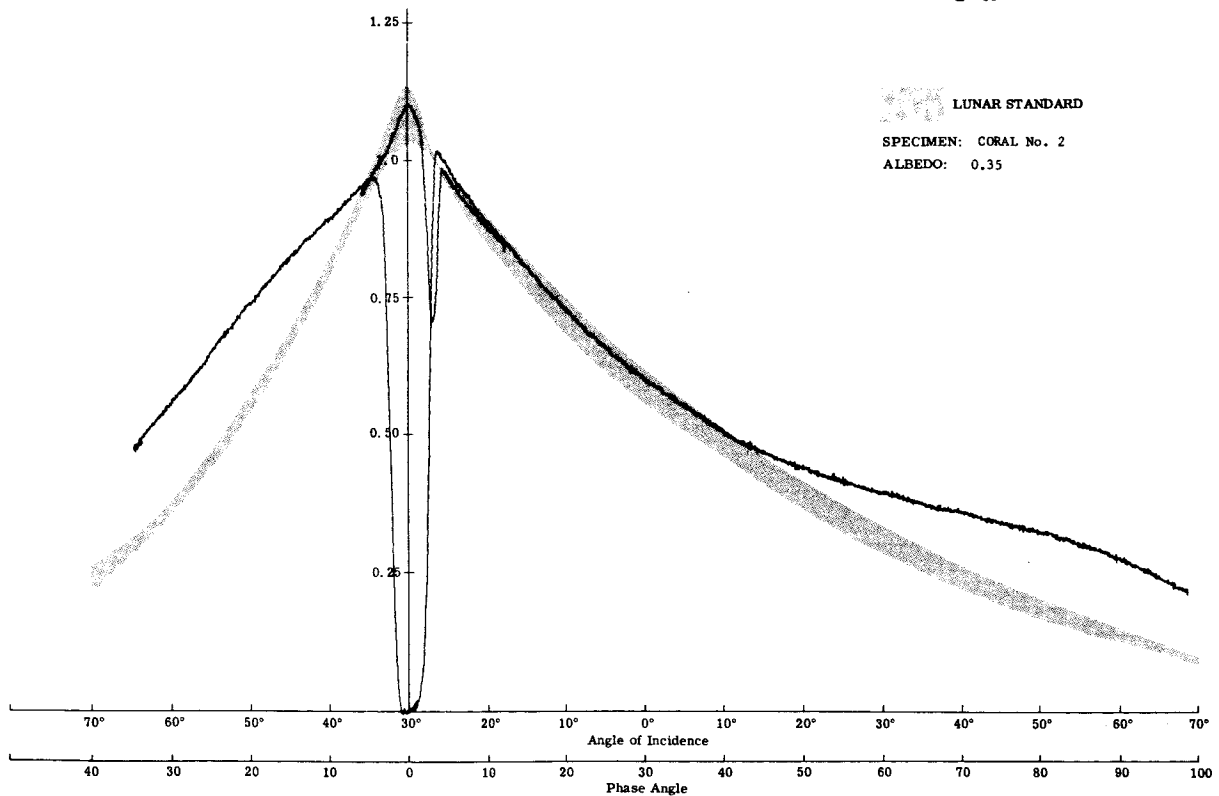
Fig. 15b Photometry of Coral No. 2 (E = 30°)

E = 30°



Red

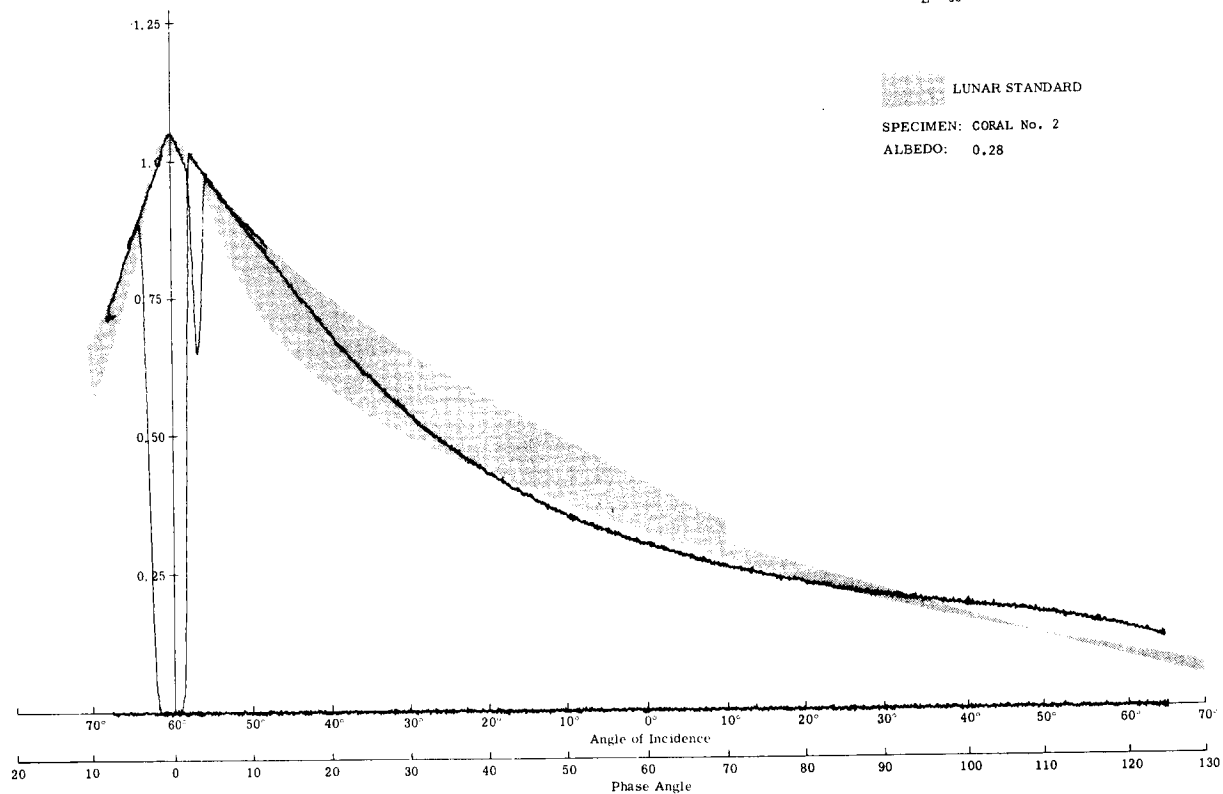
E = 30°



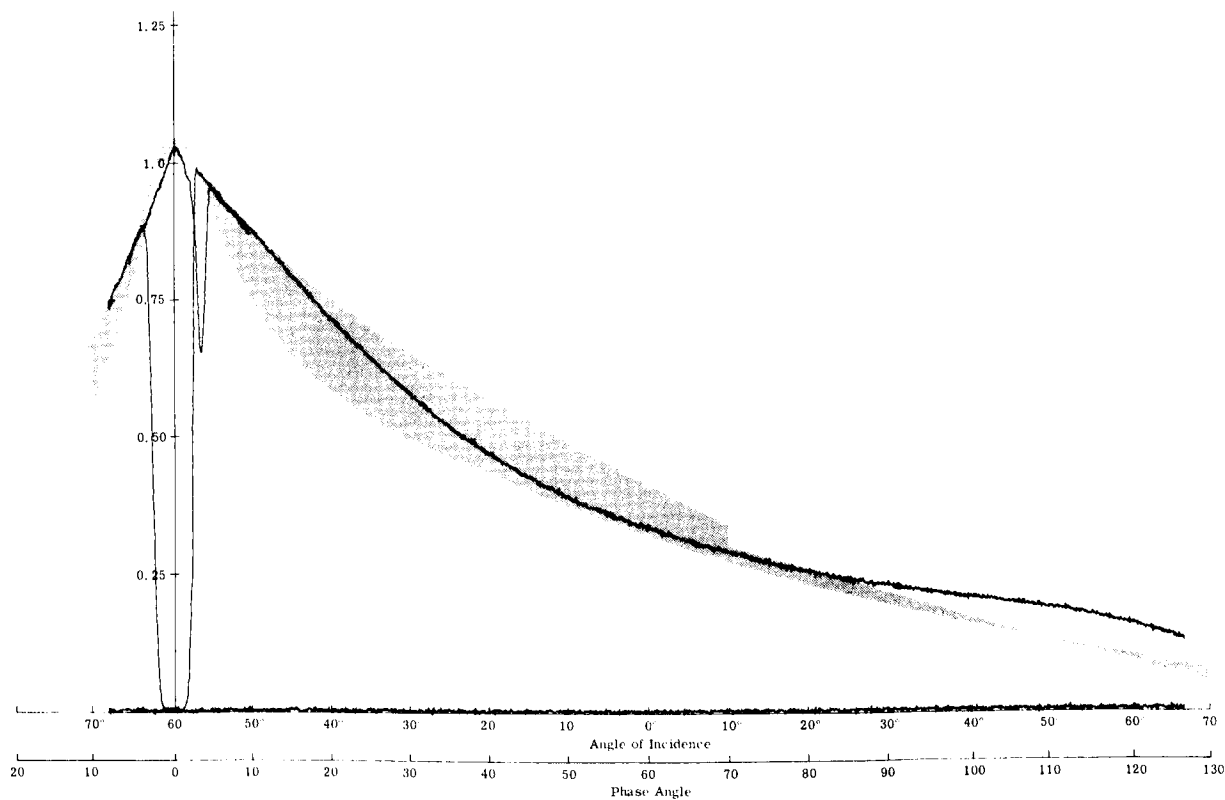
Infrared

Fig. 15b (cont) Photometry of Coral No. 2 (E = 30°)

E = 60°

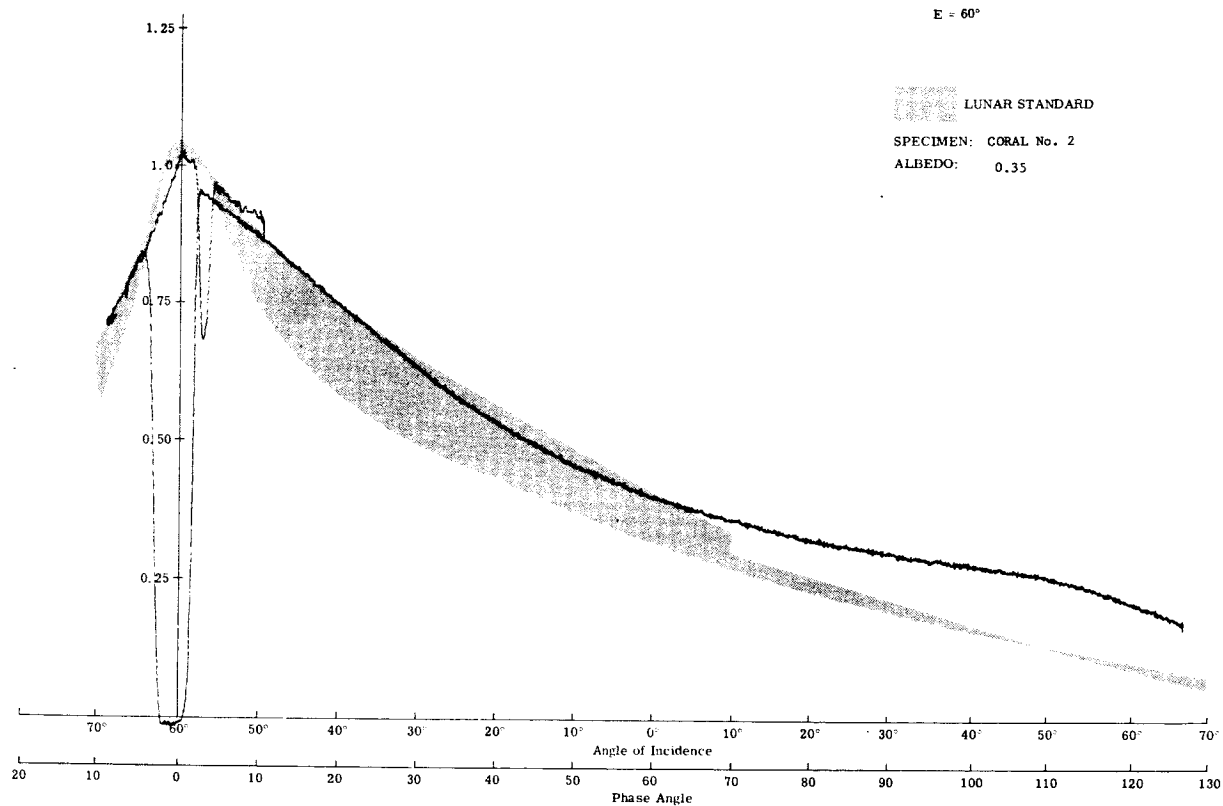


Visible

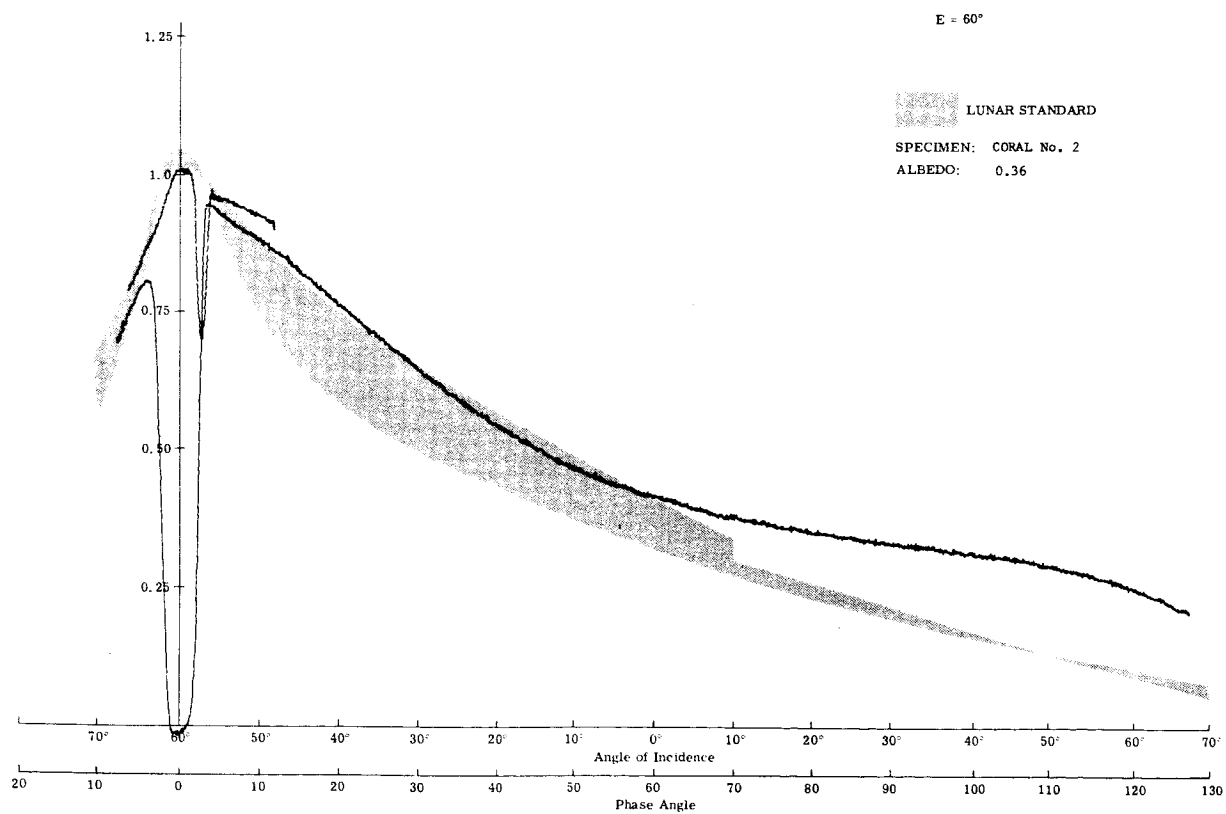


Blue

Fig. 15c Photometry of Coral No. 2 (E = 60°)

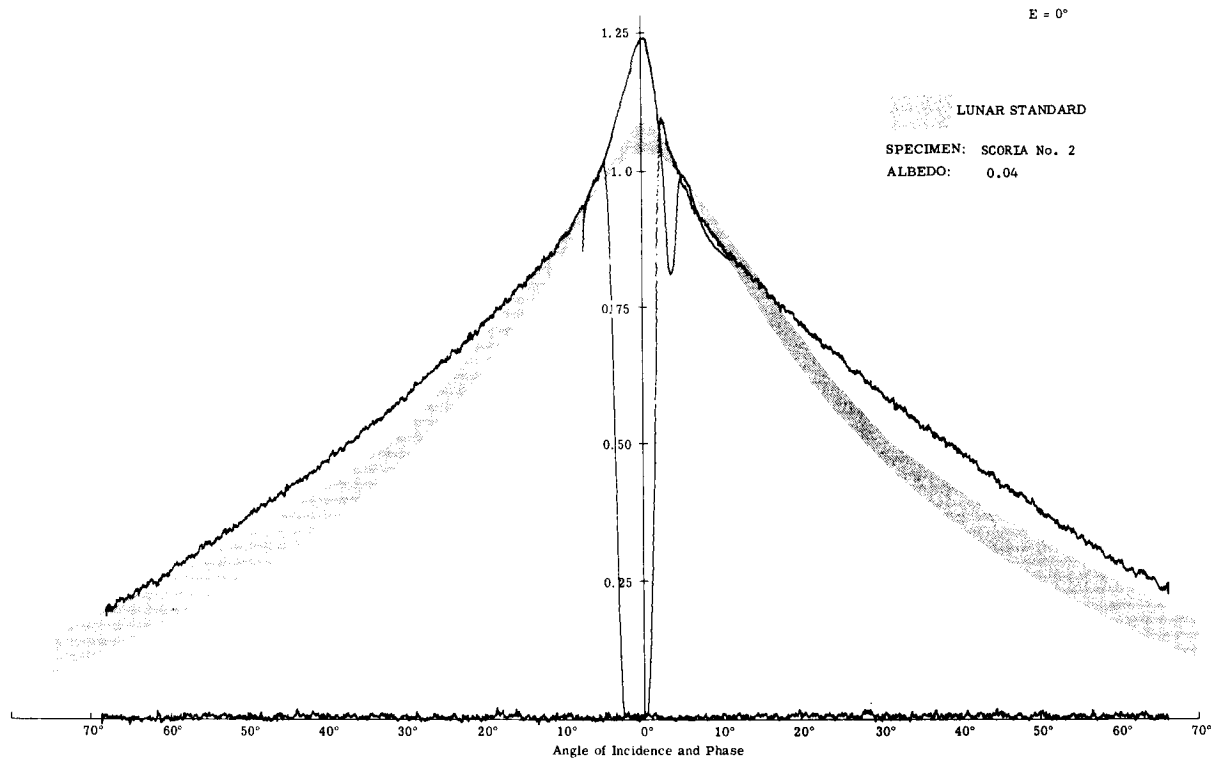


Red

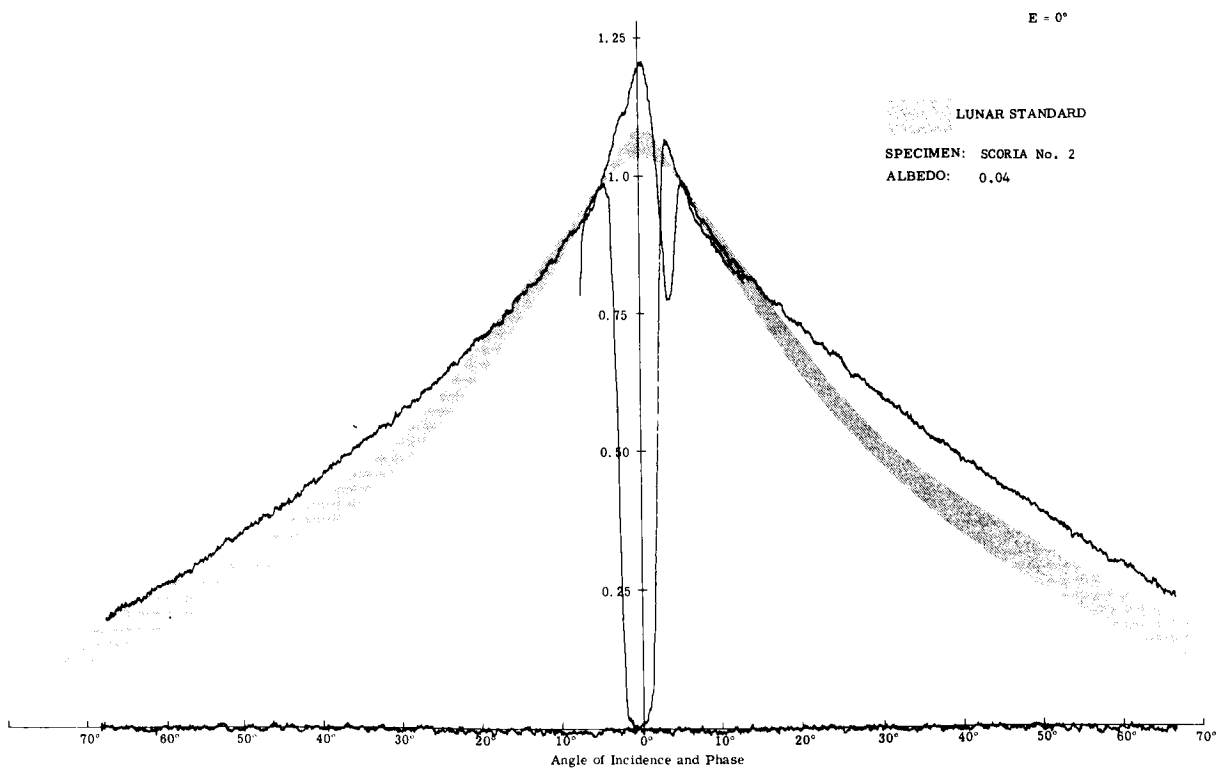


Infrared

Fig. 15c (cont) Photometry of Coral No. 2 ( $E = 60^\circ$ )

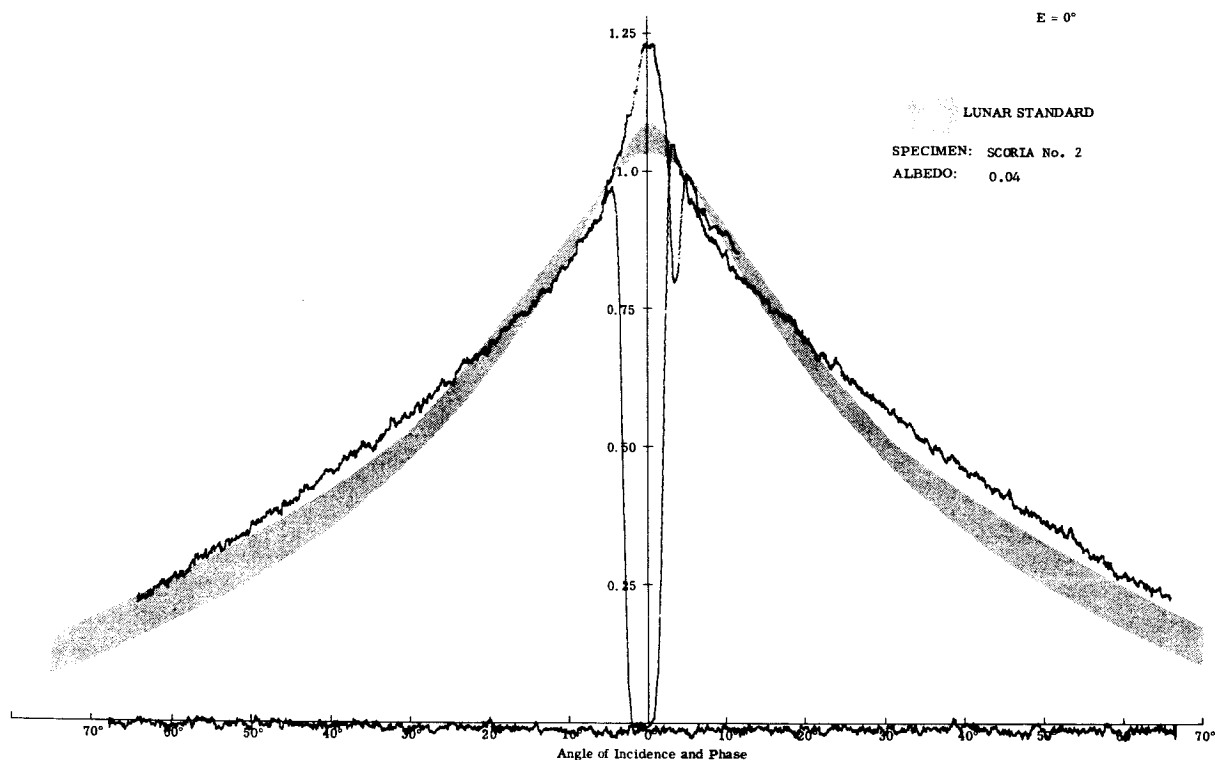


Visible

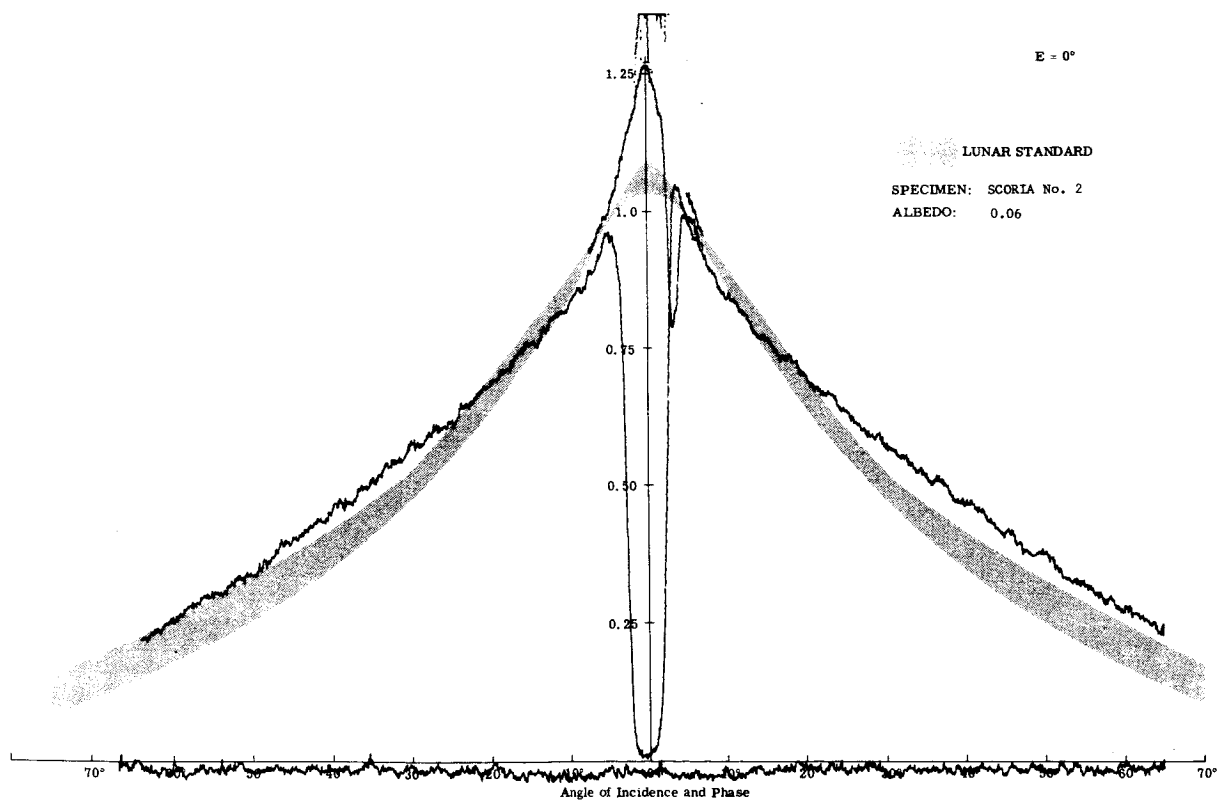


Blue

Fig. 16a Photometry of Scoria No. 2 ( $E = 0^\circ$ )



Red



Infrared

Fig. 16a (cont) Photometry of Scoria No. 2 ( $E = 0^\circ$ )

Research Department  
RE-245  
April 1966



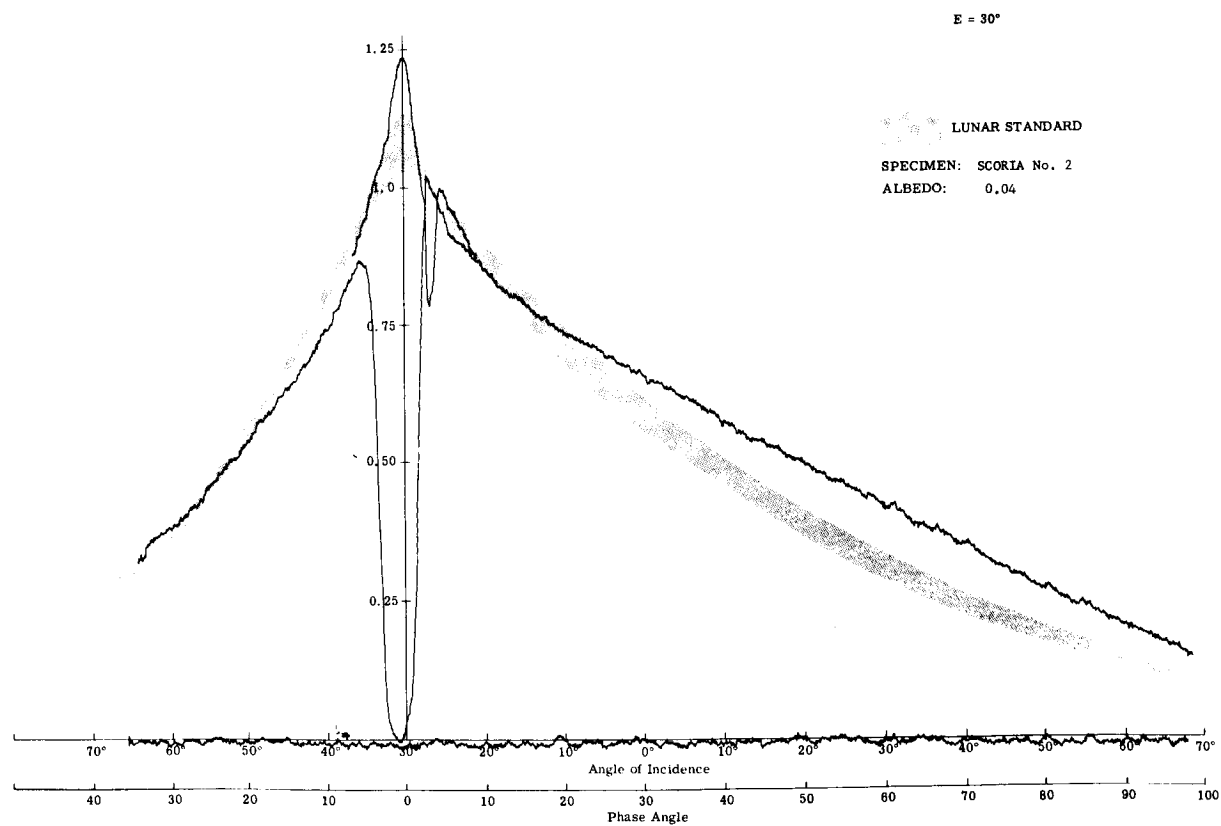
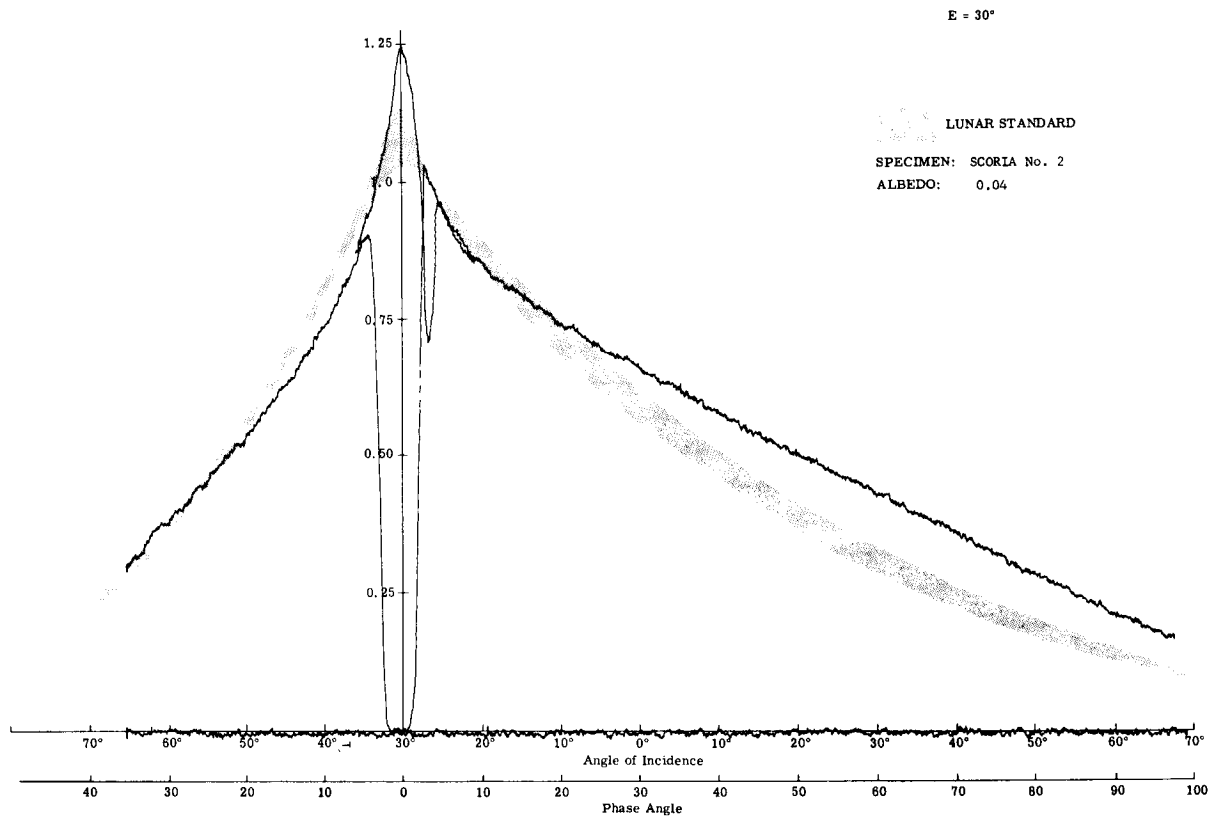
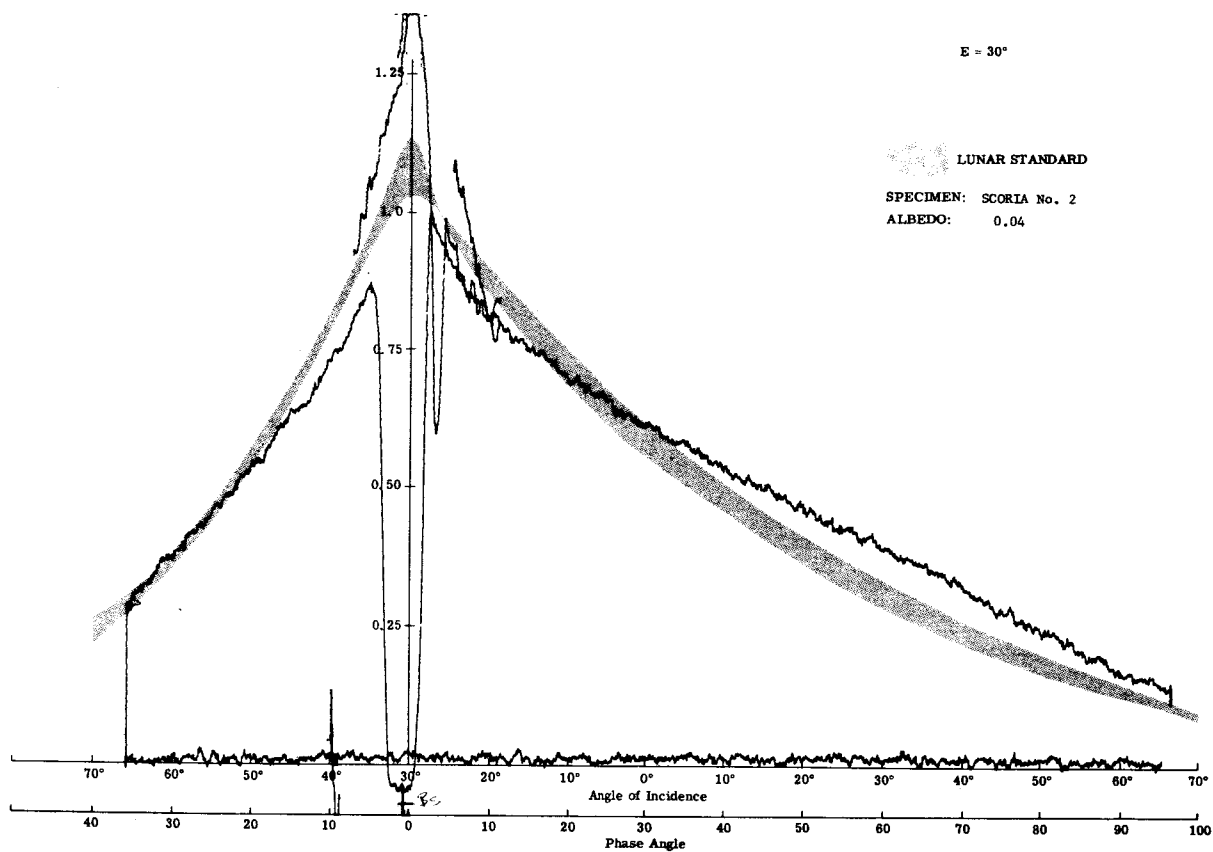
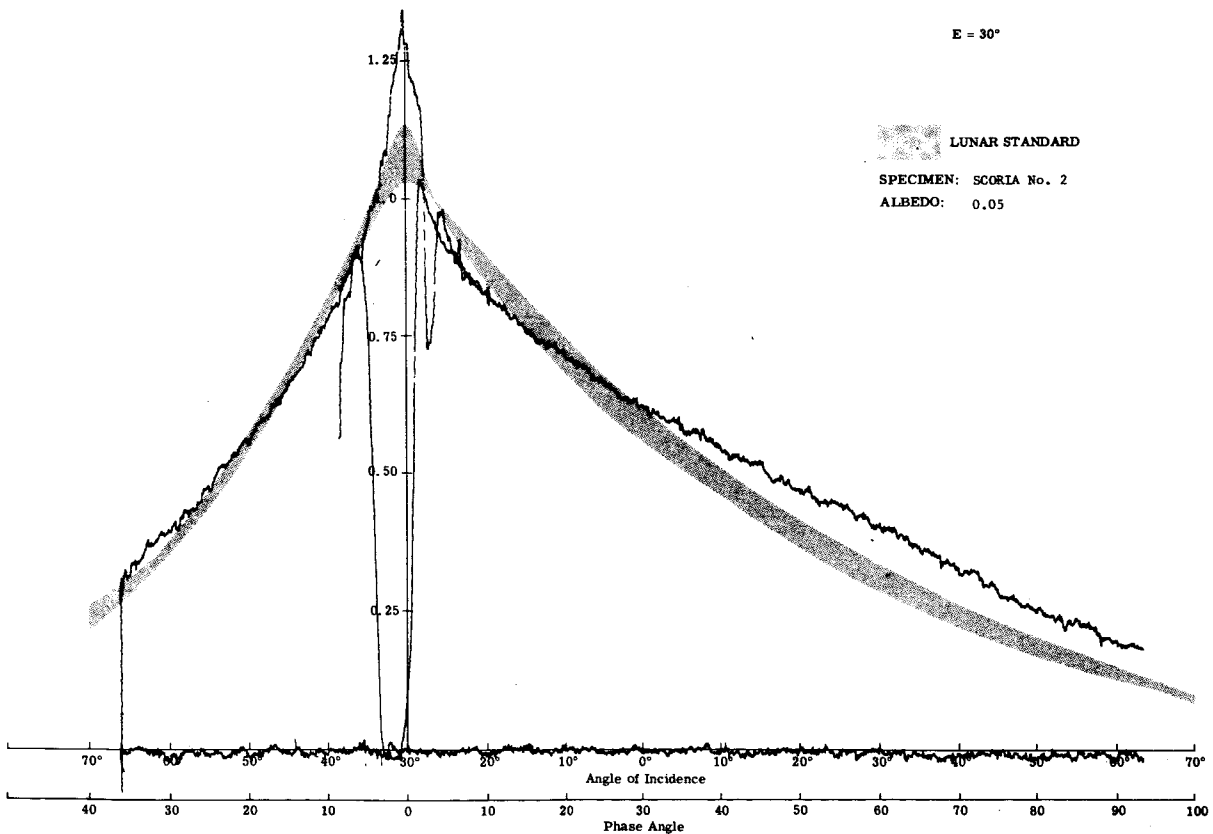


Fig. 16b Photometry of Scoria No. 2 (E = 30°)



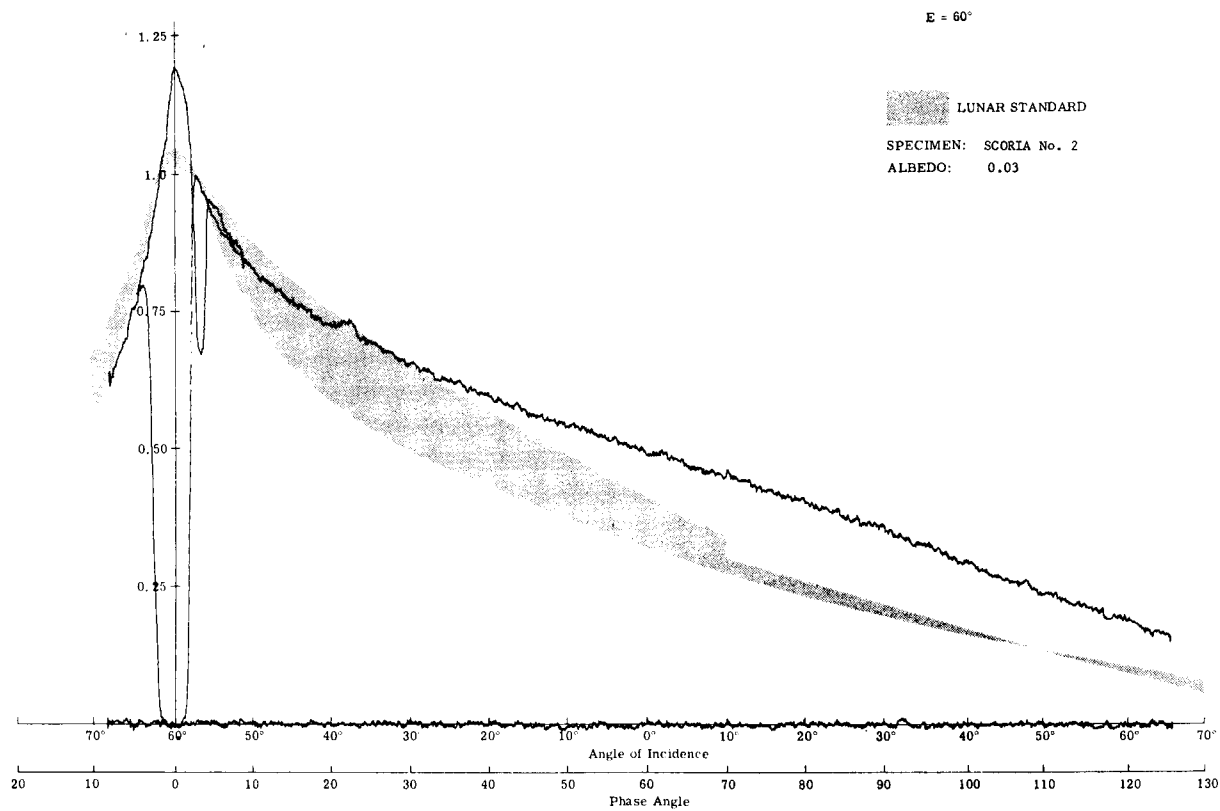
Red



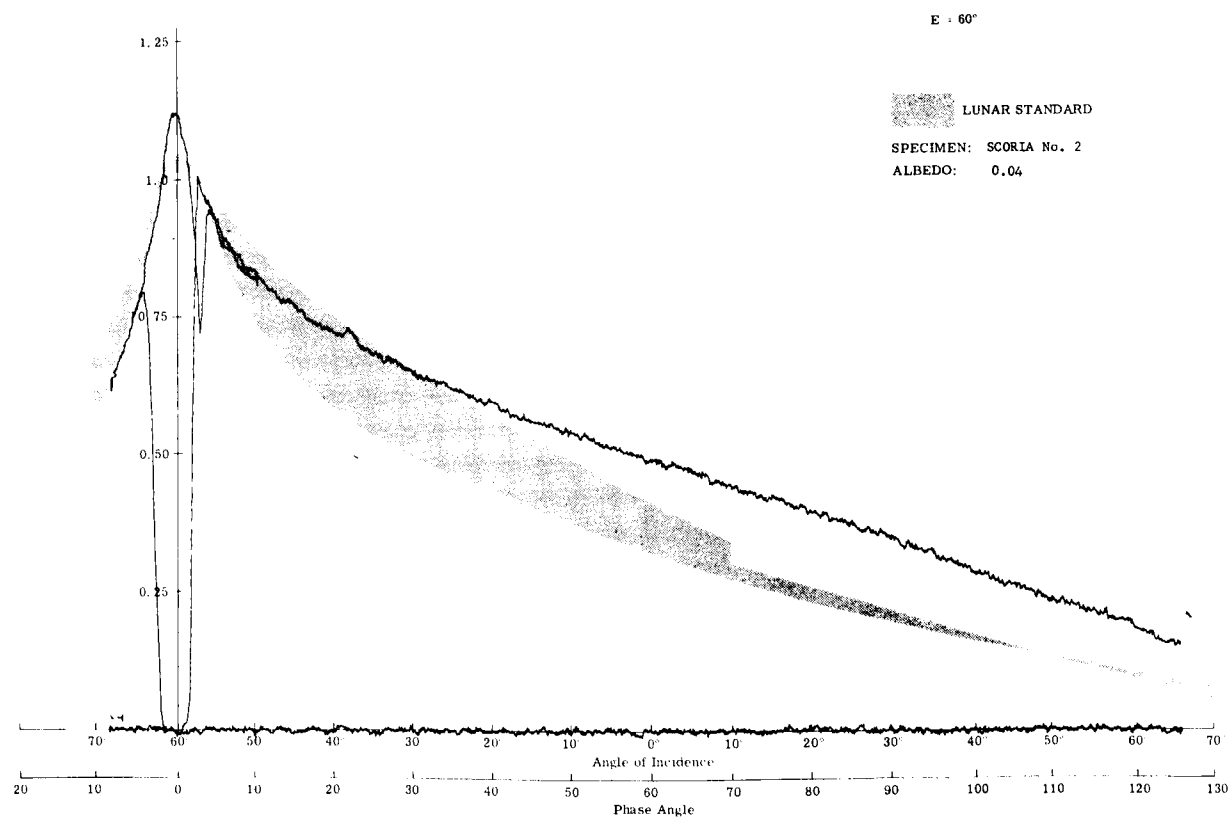
Infrared

Fig. 16b (cont) Photometry of Scoria No. 2 ( $E = 30^\circ$ )

Research Department  
RE-245  
April 1966

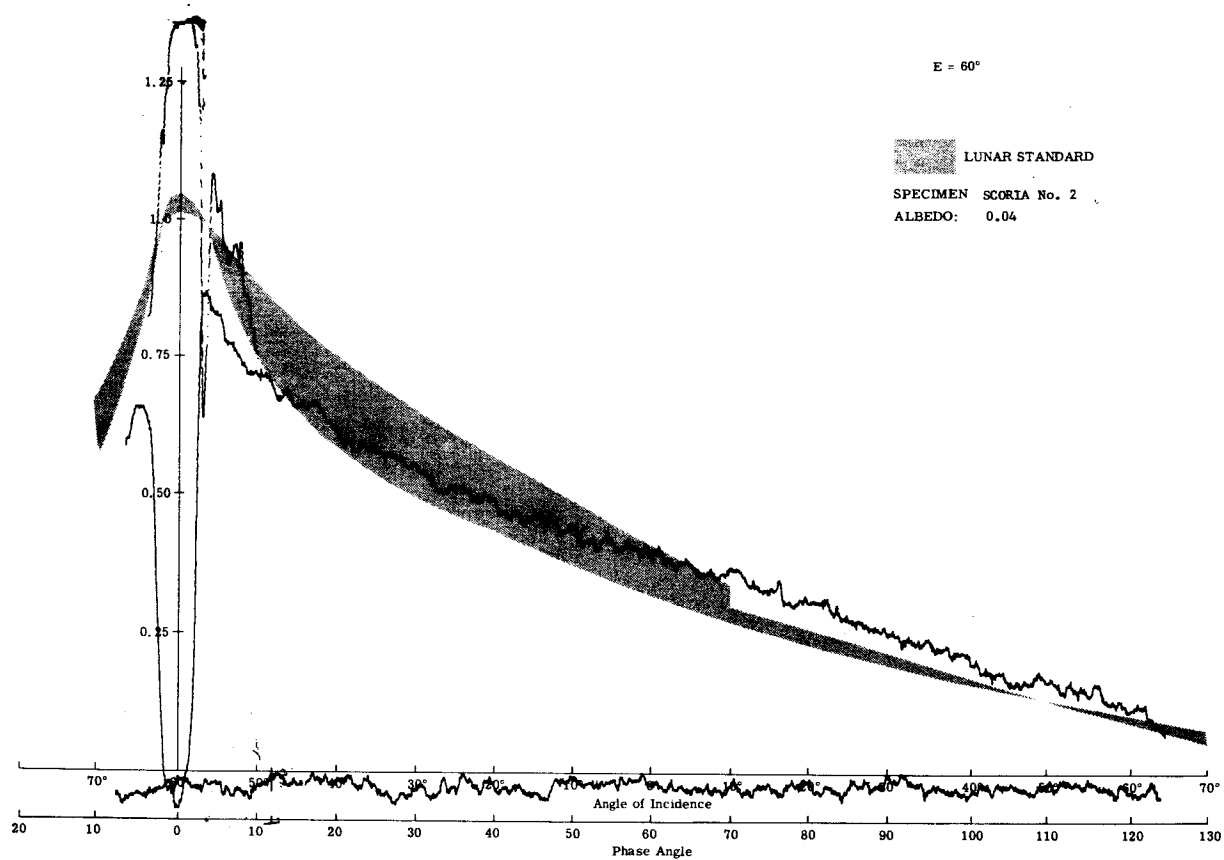


Visible

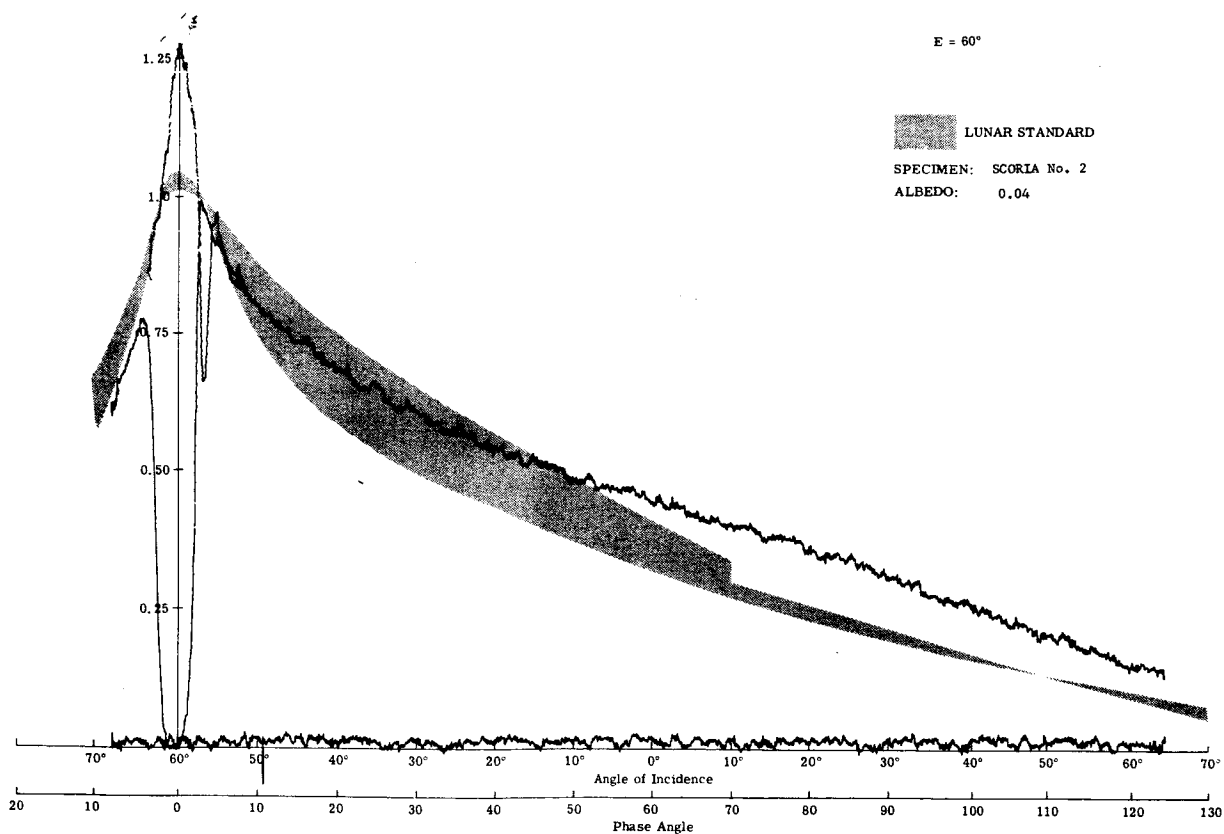


Blue

Fig. 16c Photometry of Scoria No. 2 ( $E = 60^\circ$ )



Red



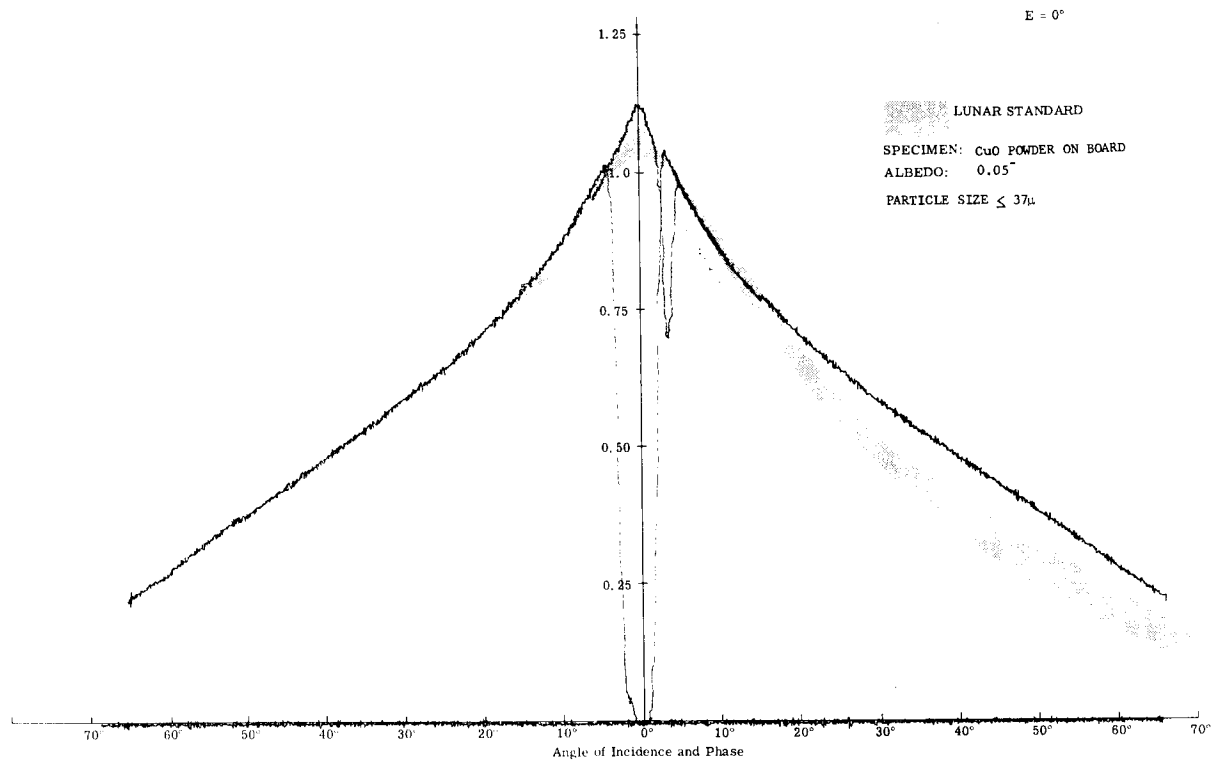
Infrared

Fig. 16c (cont) Photometry of Scoria No. 2 ( $E = 60^\circ$ )

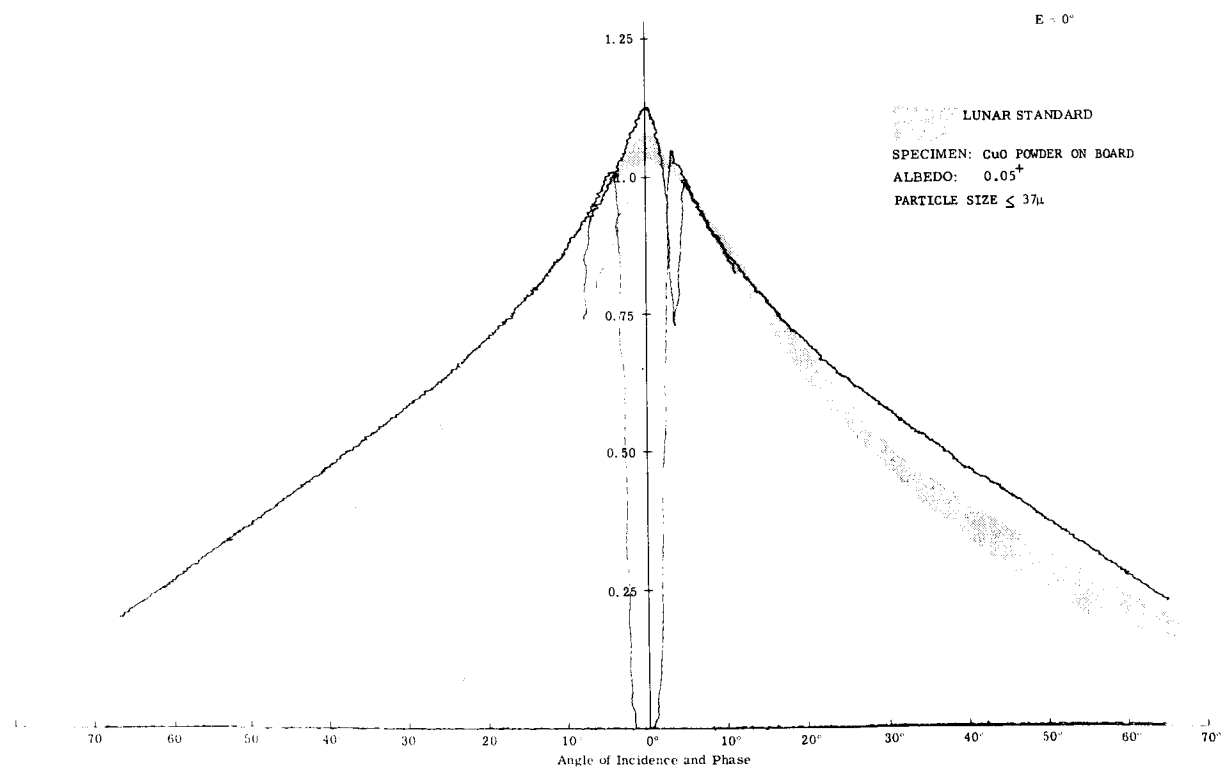
Research Department

RE-245

April 1966

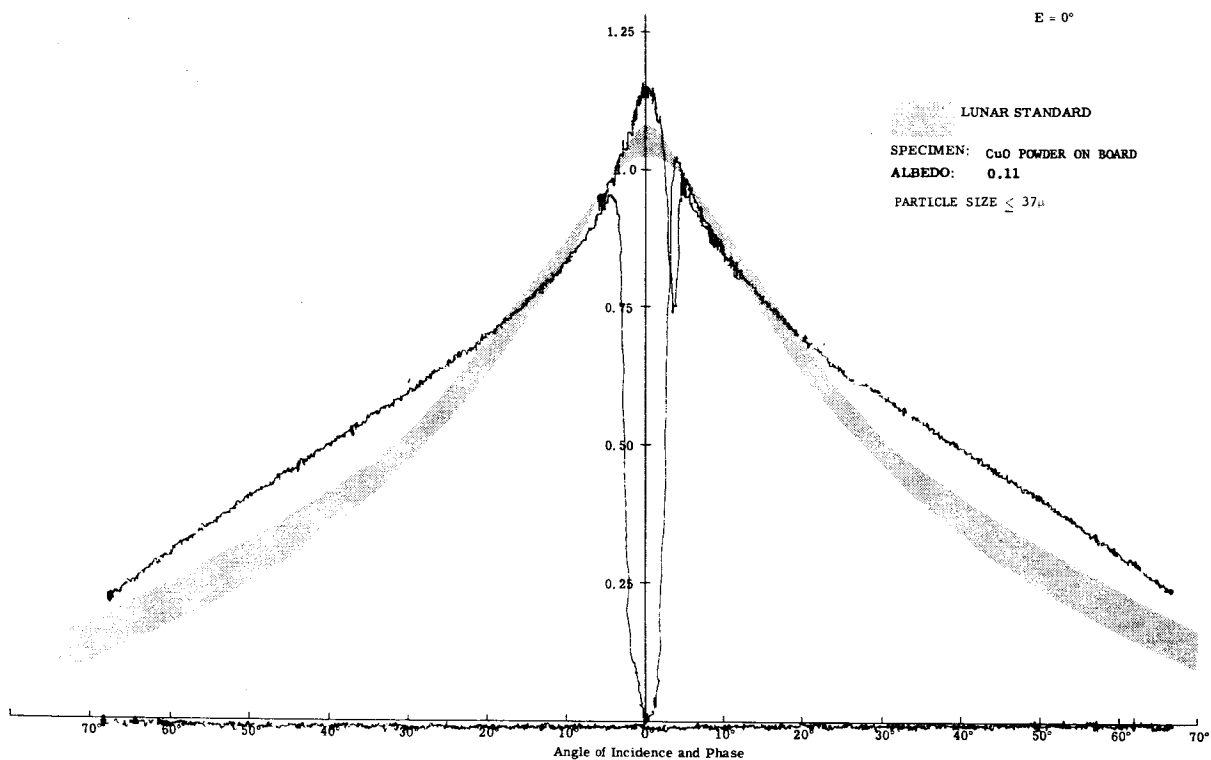


Visible

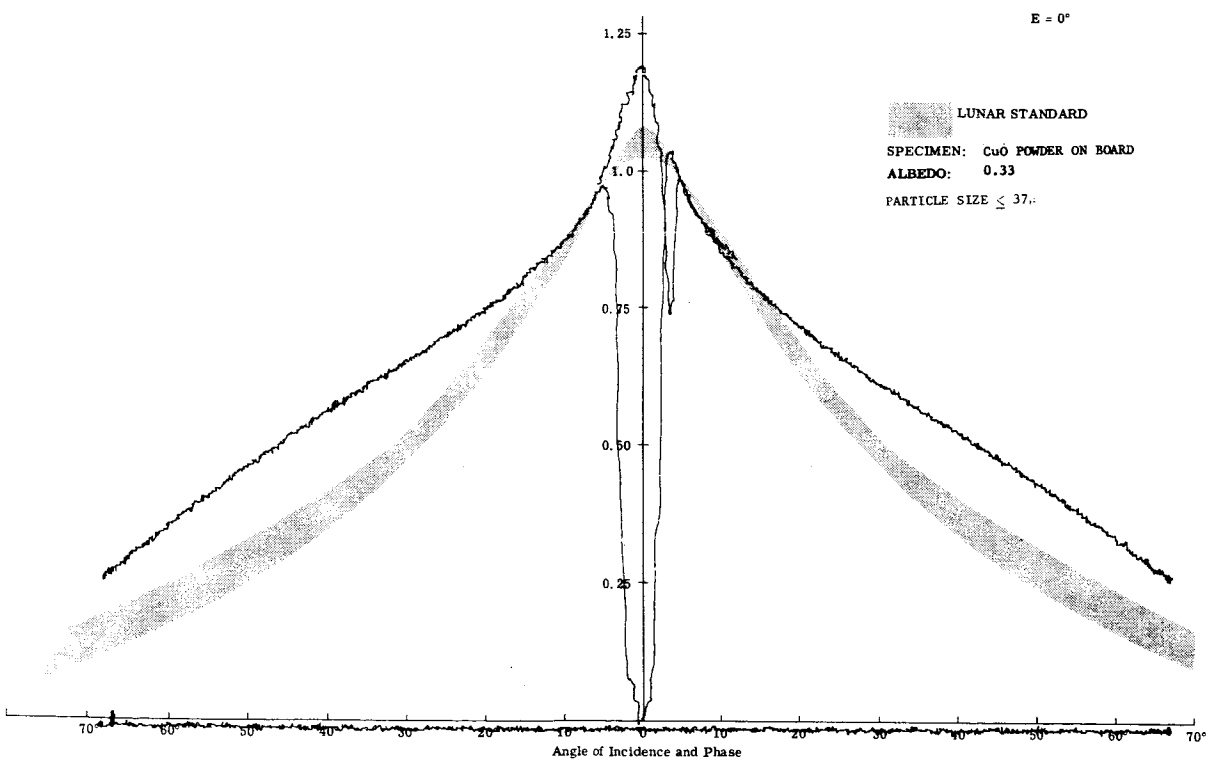


Blue

Fig. 17a Photometry of Copper Oxide Powder  
on Flat Board ( $E = 0^\circ$ )

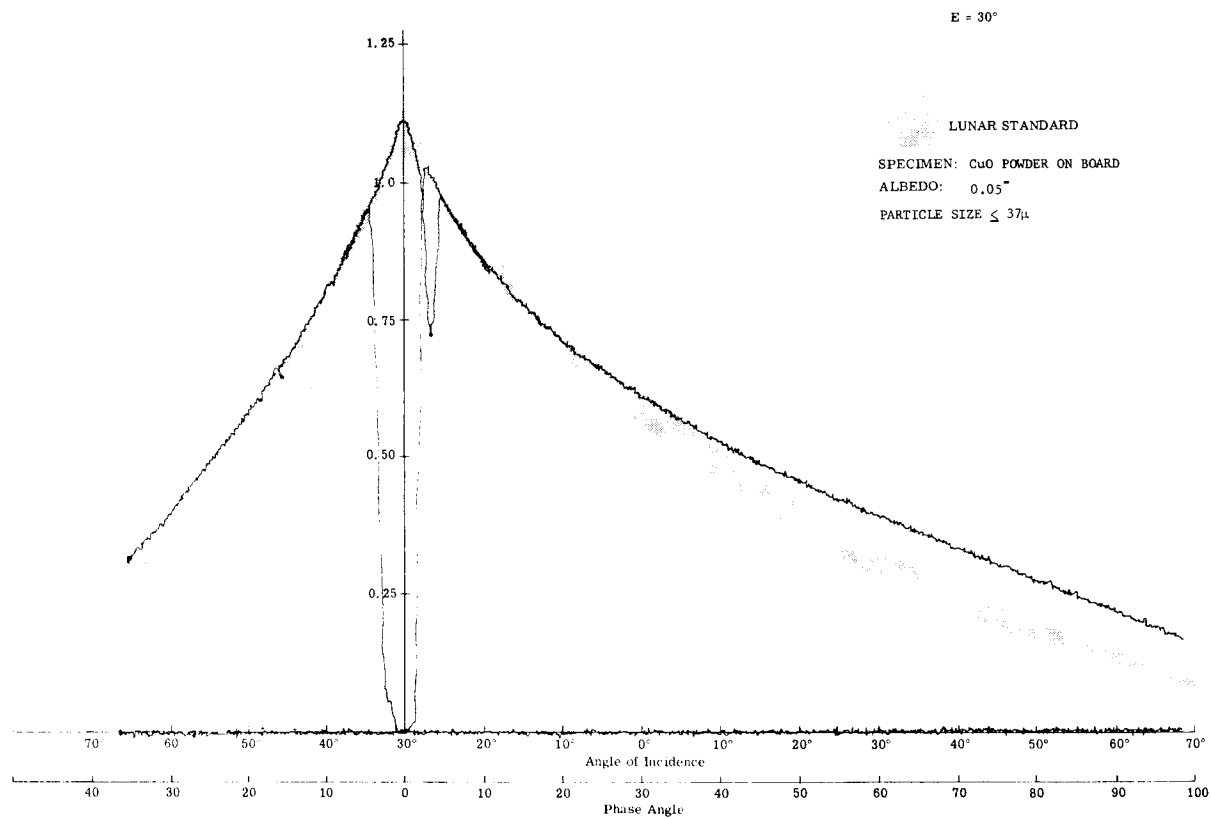


Red

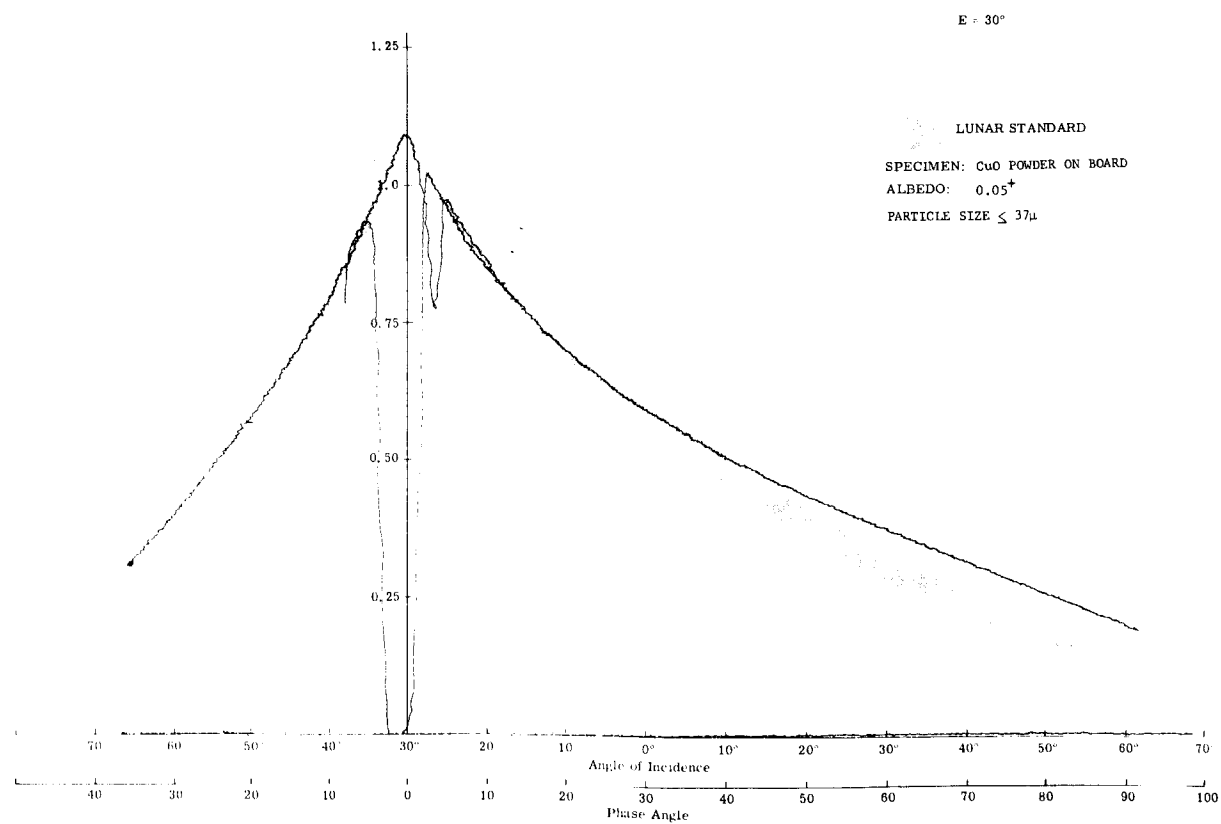


Infrared

Fig. 17a (cont) Photometry of Copper Oxide Powder  
on Flat Board ( $E = 0^\circ$ )

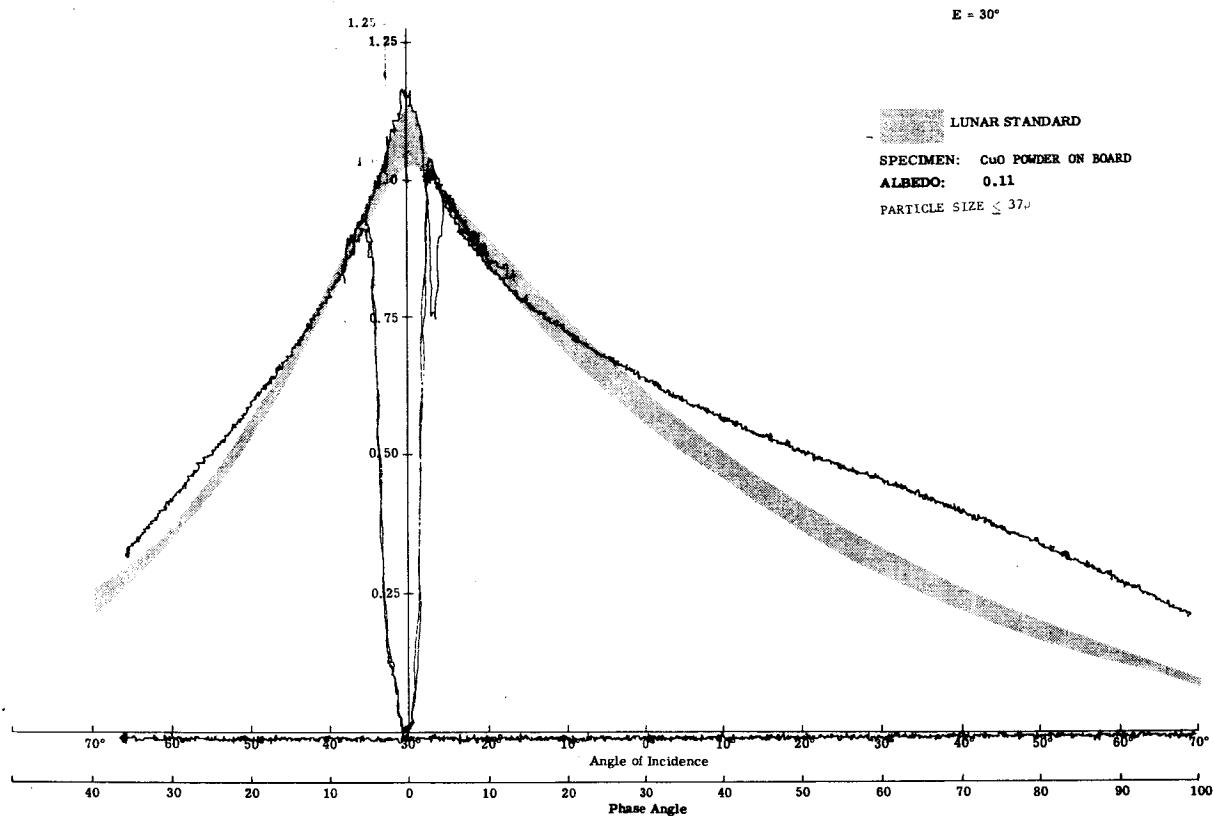


Visible

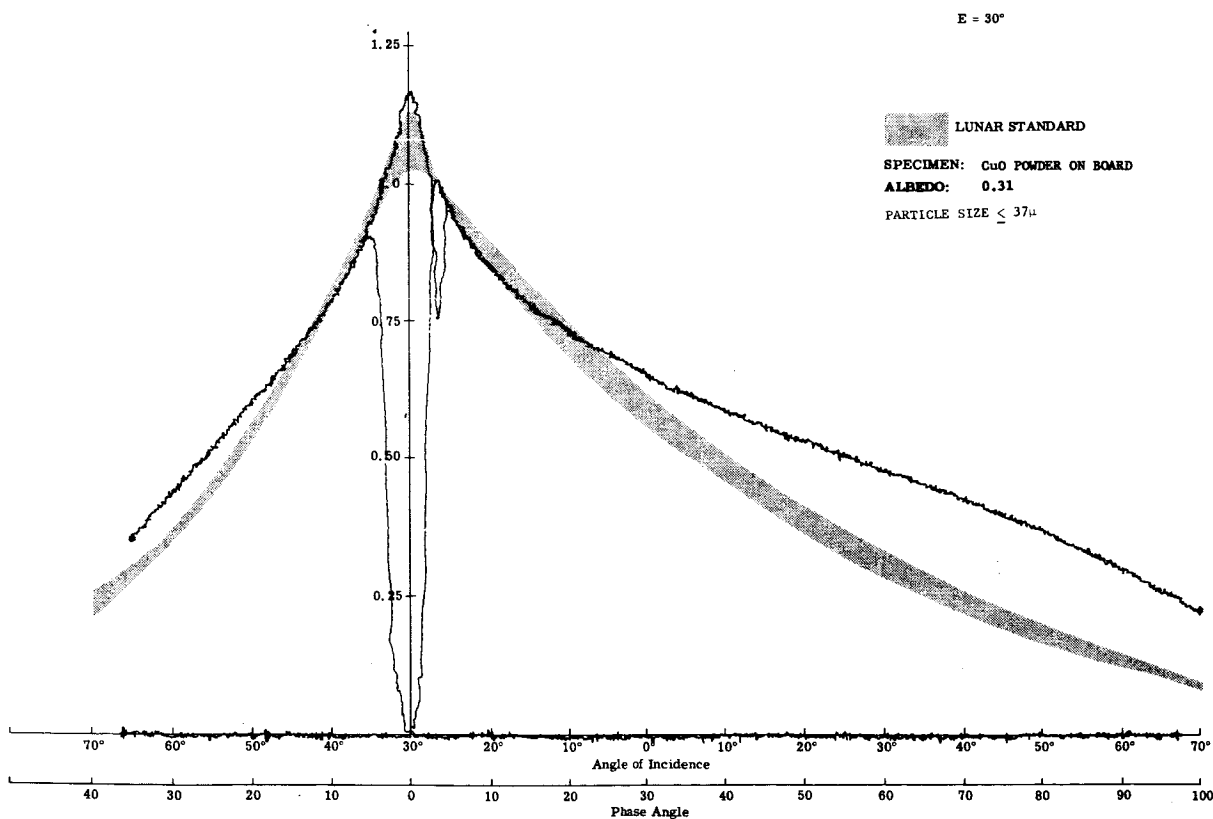


Blue

Fig. 17b Photometry of Copper Oxide Powder  
on Flat Board ( $E = 30^\circ$ )



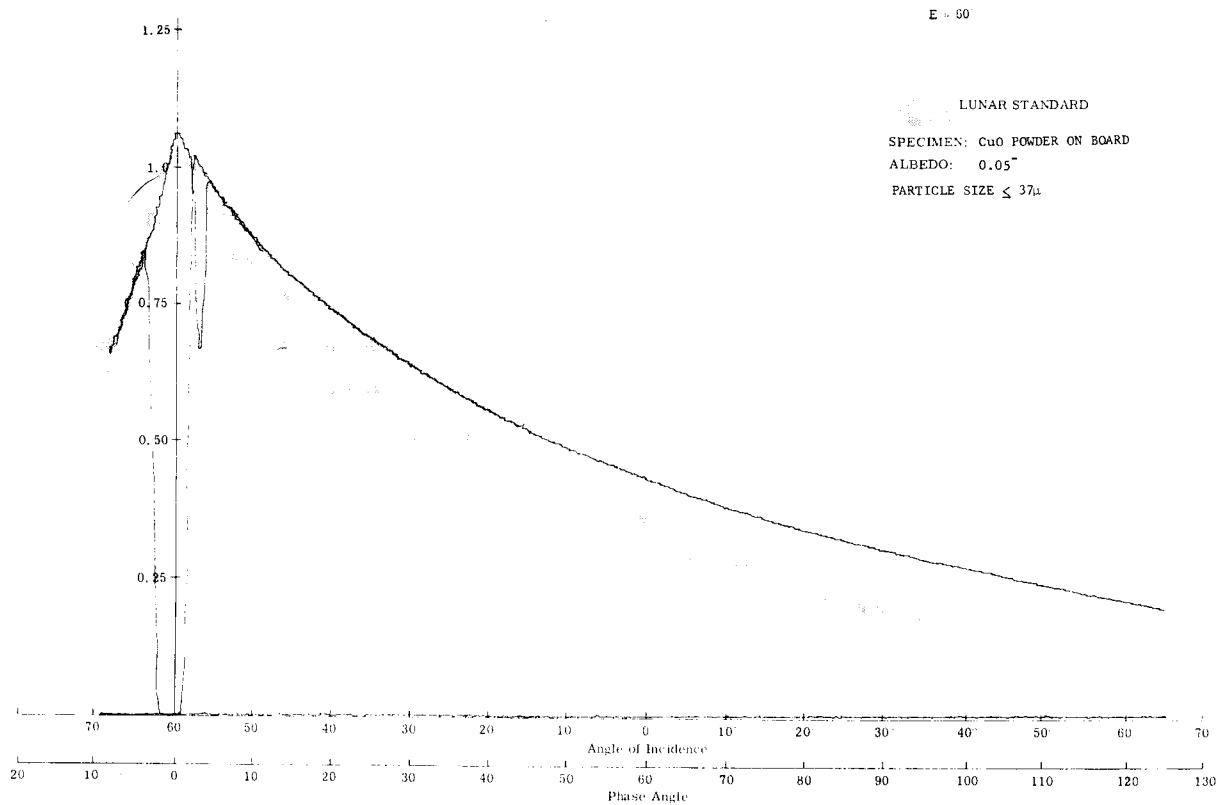
Red



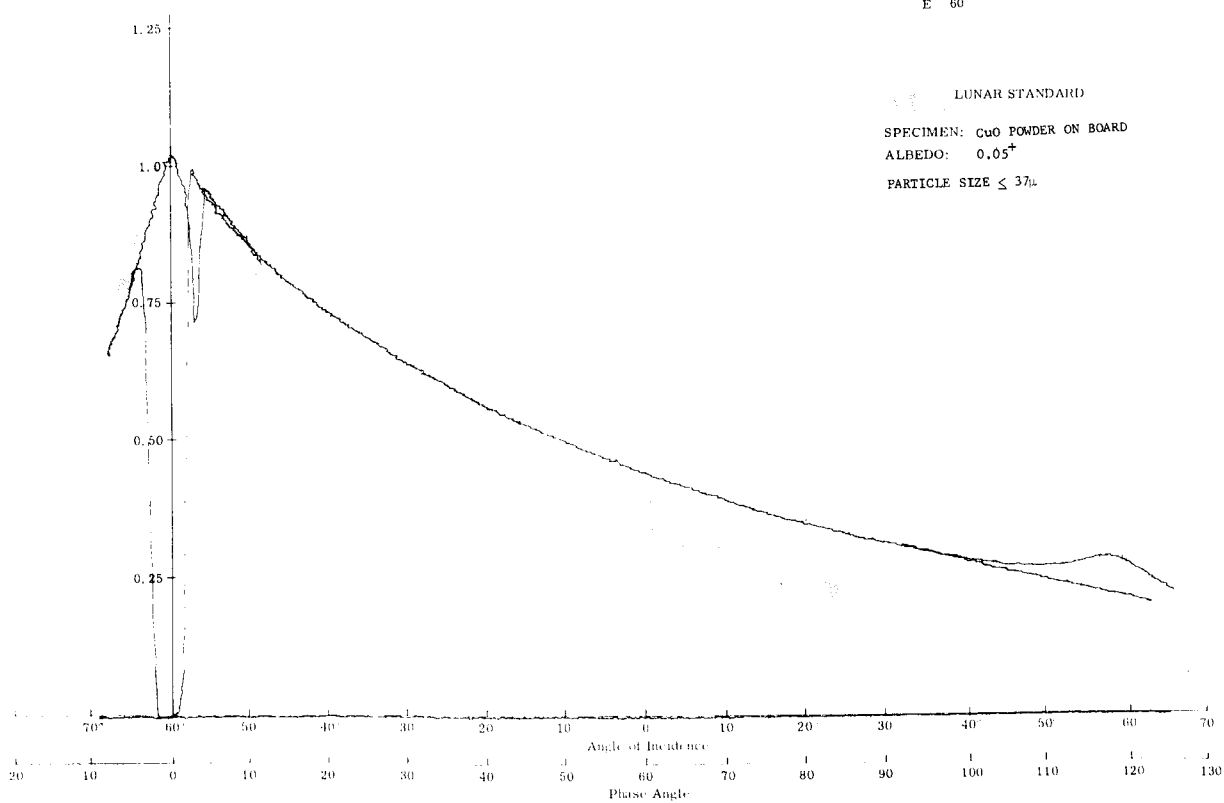
Infrared

Fig. 17b (cont) Photometry of Copper Oxide Powder  
on Flat Board ( E = 30° )



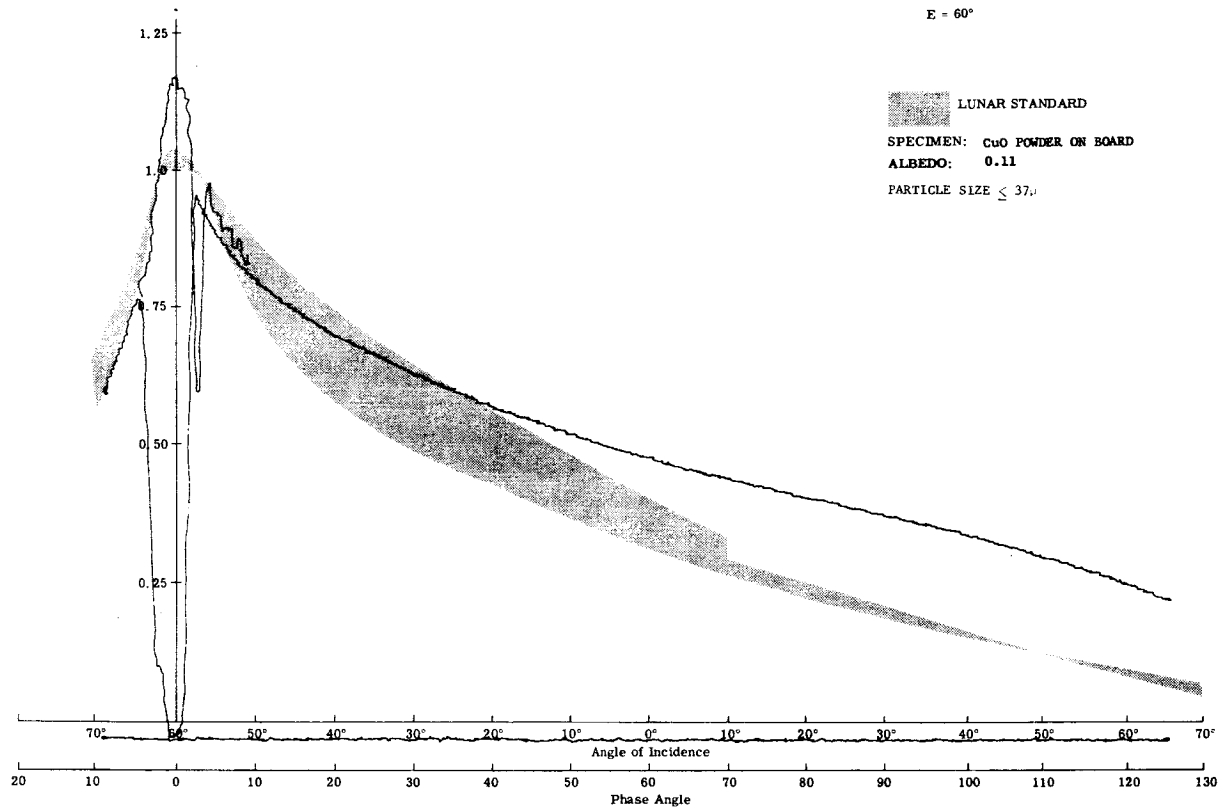


Visible

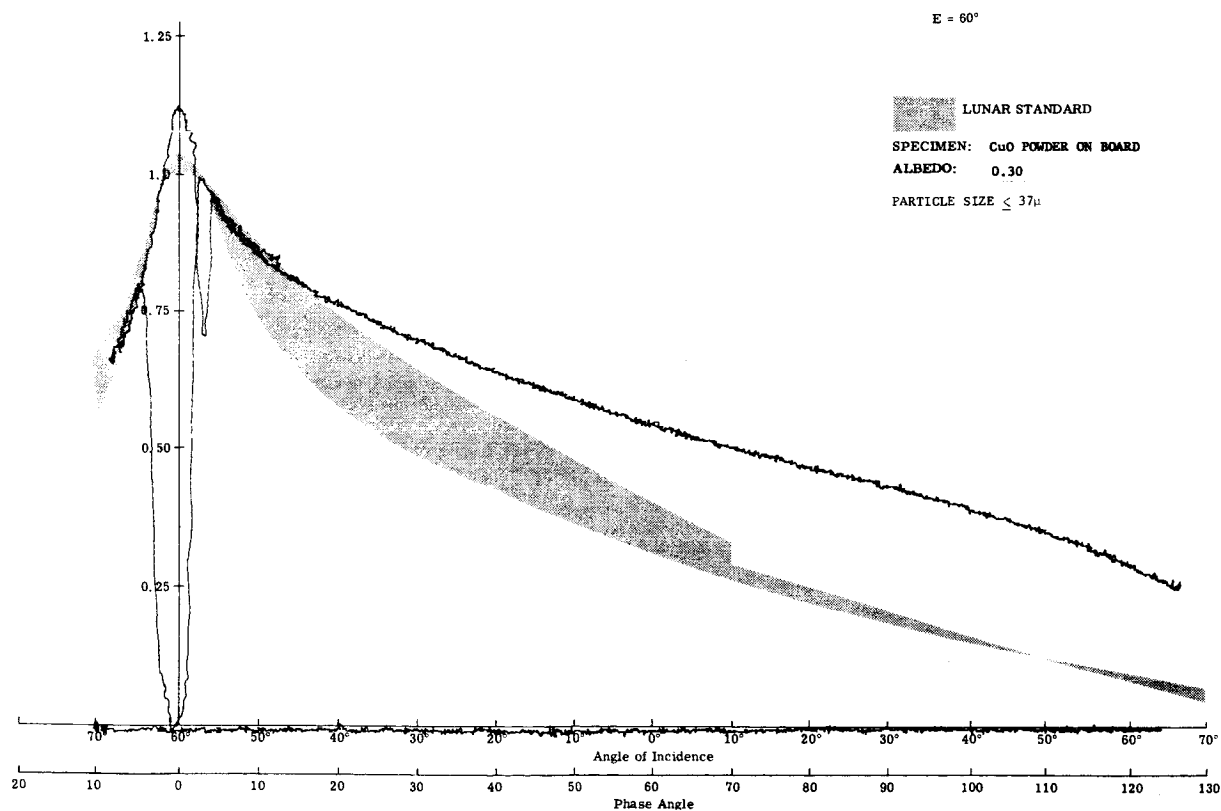


Blue

Fig. 17c Photometry of Copper Oxide Powder  
on Flat Board ( $E = 60^\circ$ )

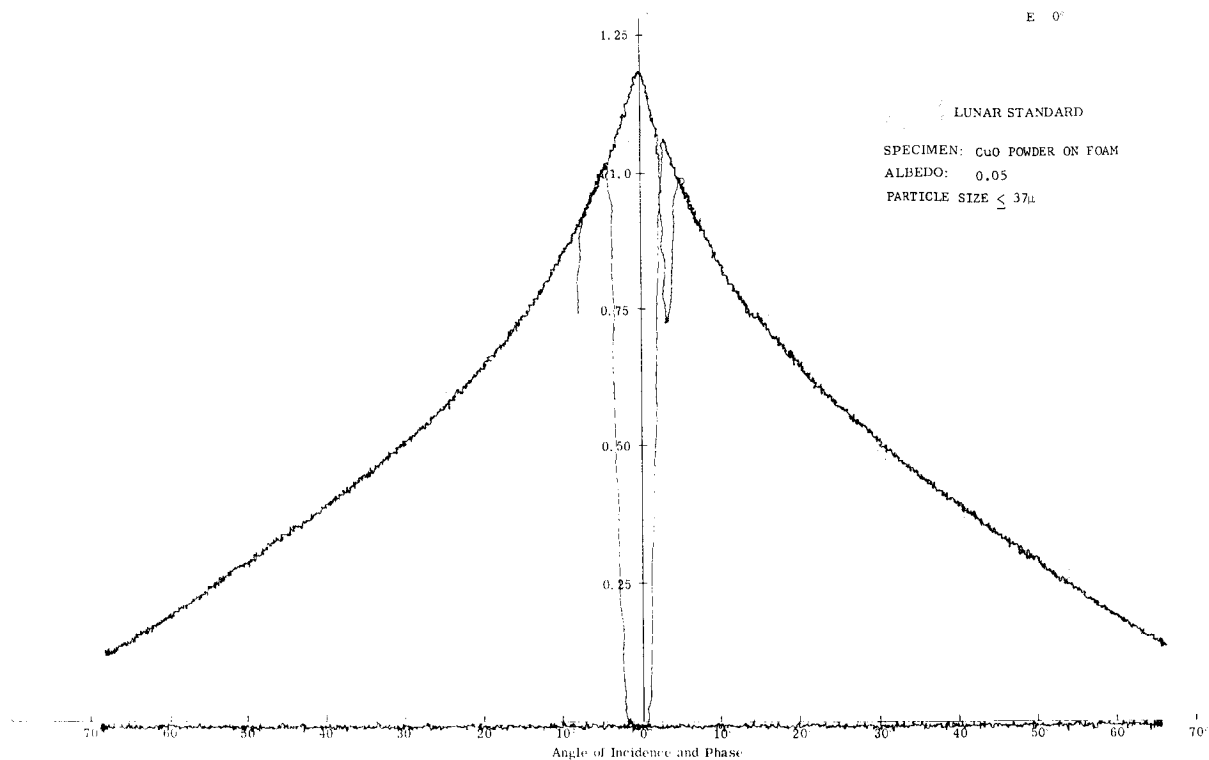


Red

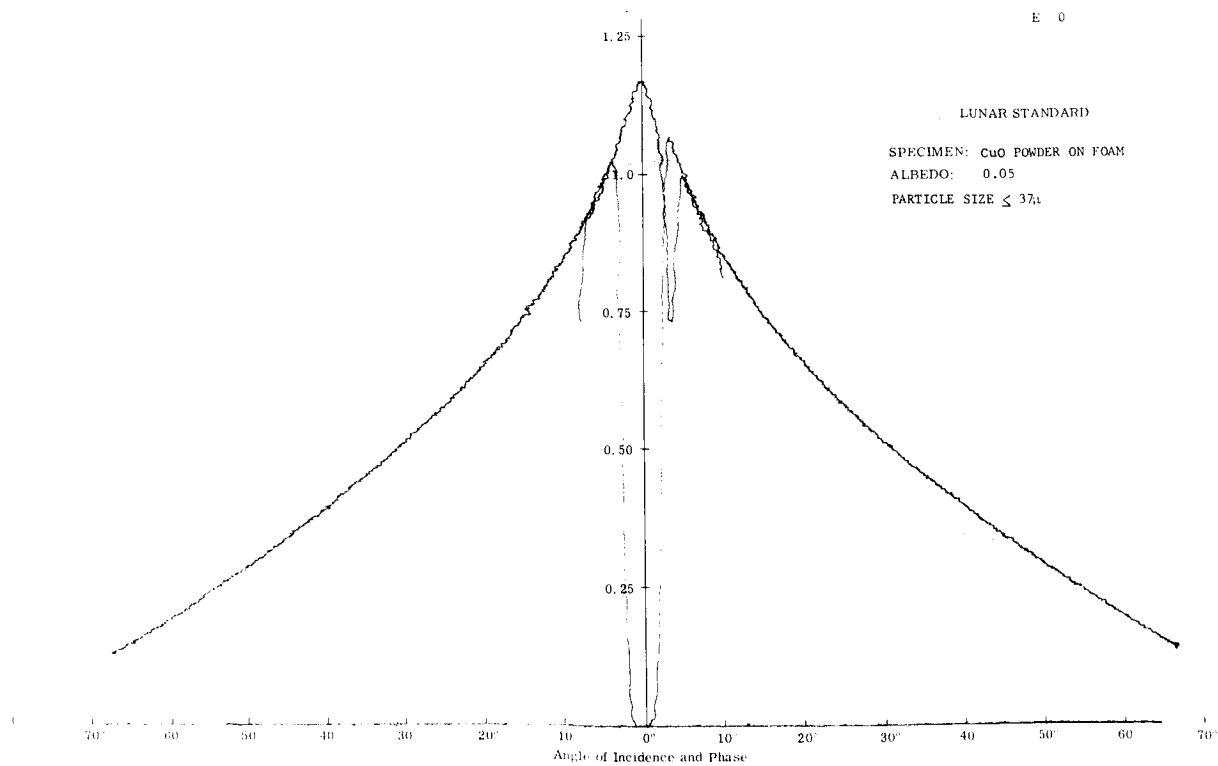


Infrared

Fig. 17c (cont) Photometry of Copper Oxide Powder  
on Flat Board ( $E = 60^\circ$ )

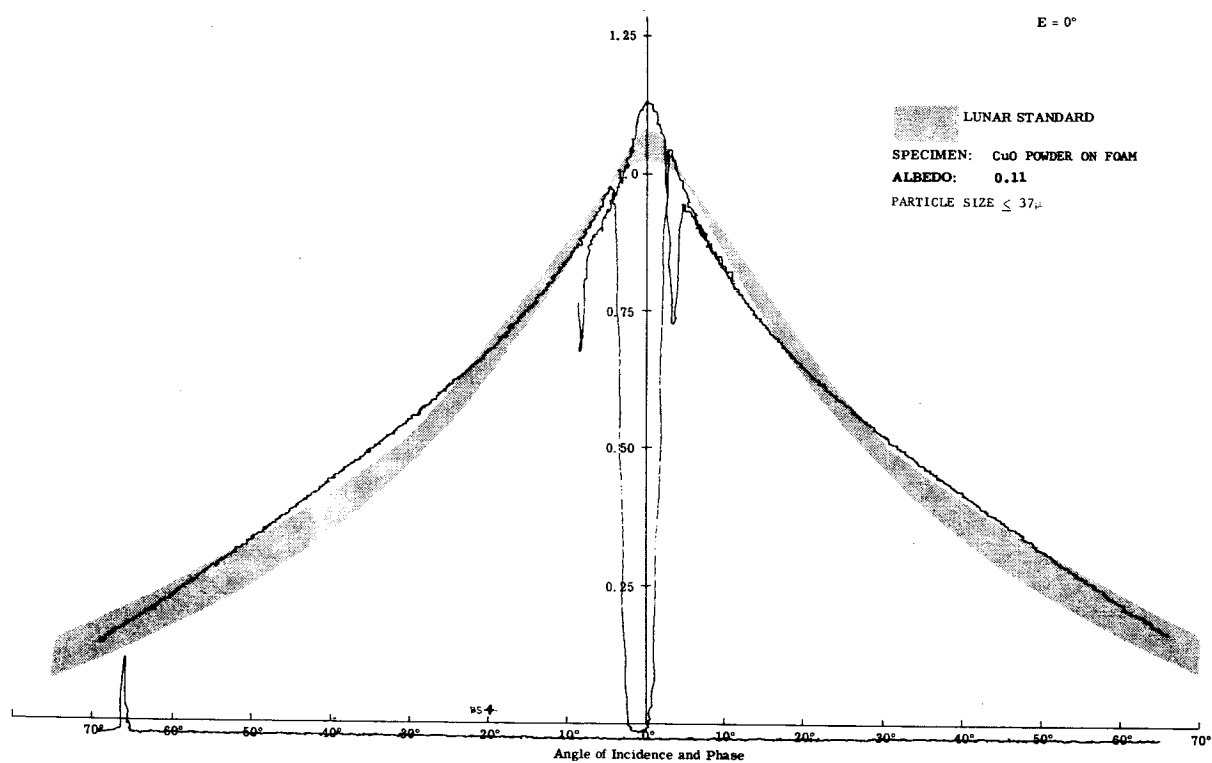


Visible

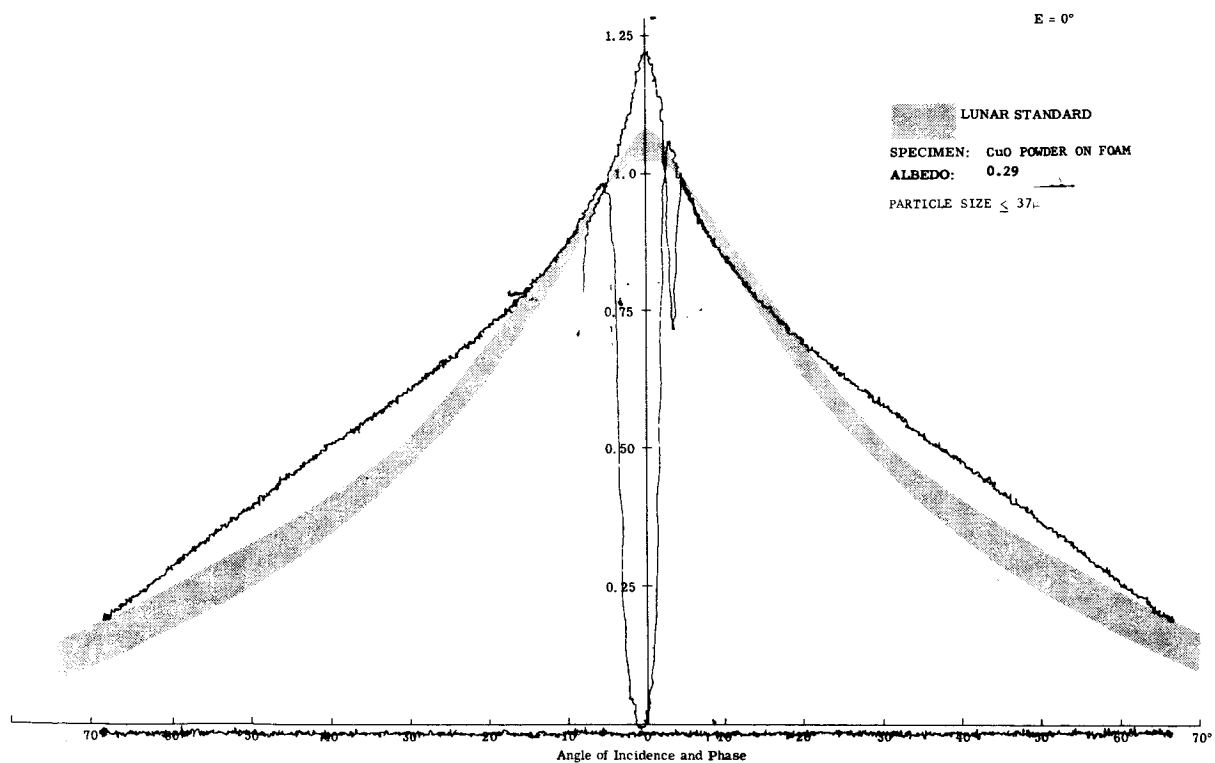


Blue

Fig. 18a Photometry of Copper Oxide Powder  
on Foam ( $E = 0^\circ$ )

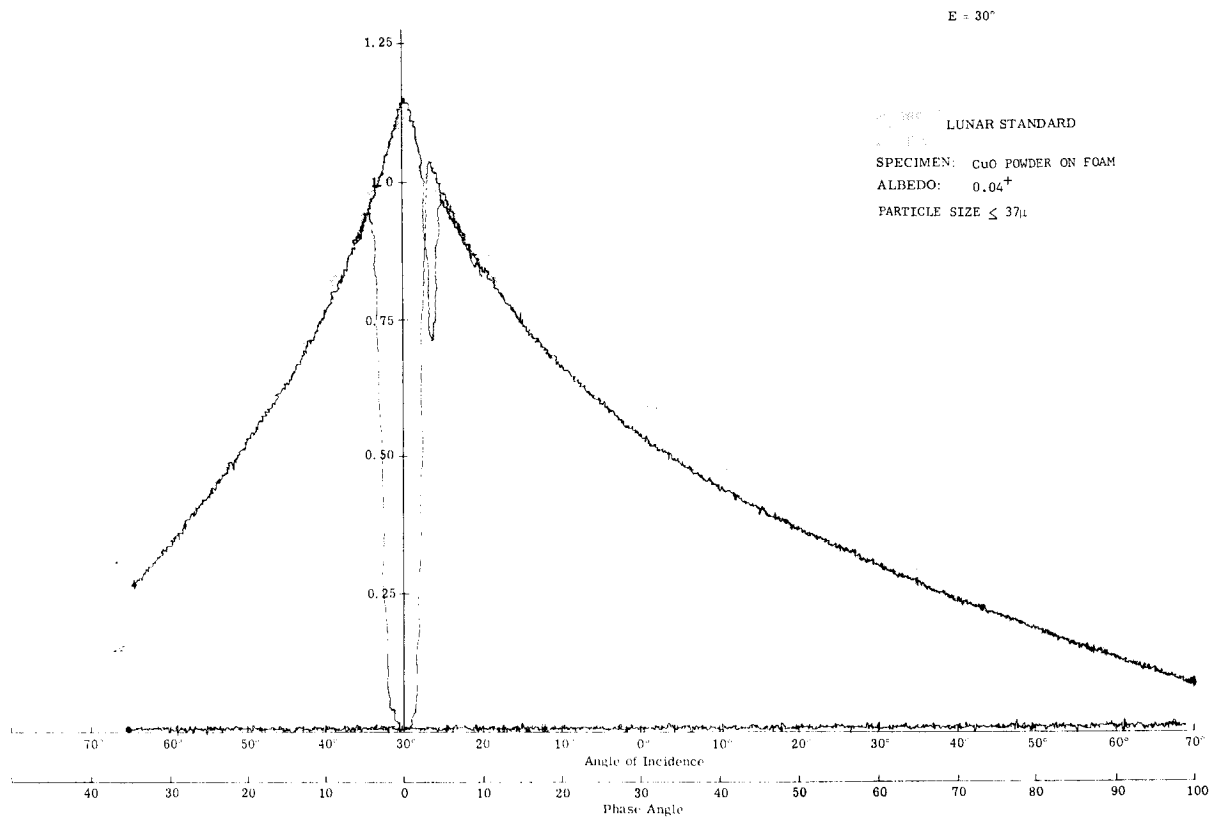


Red

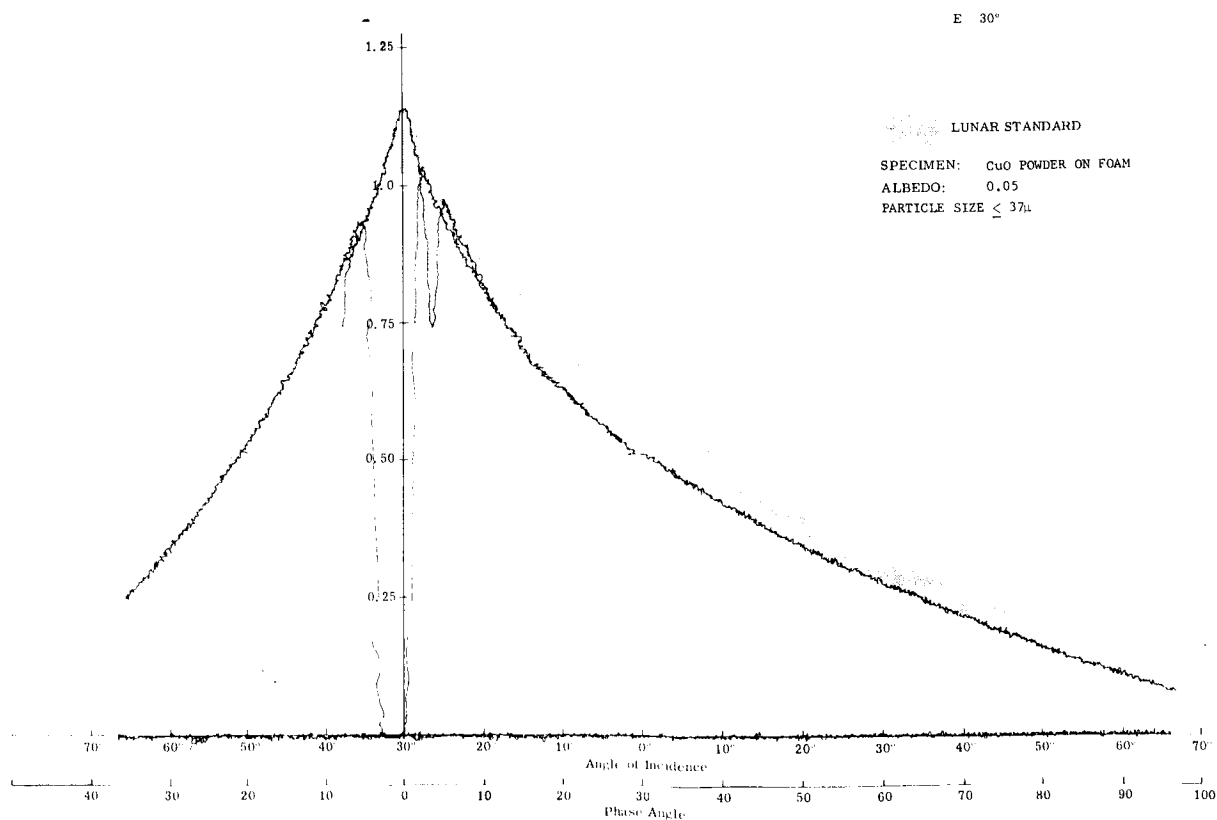


Infrared

Fig. 18a (cont) Photometry of Copper Oxide Powder  
on Foam ( $E = 0^\circ$ )

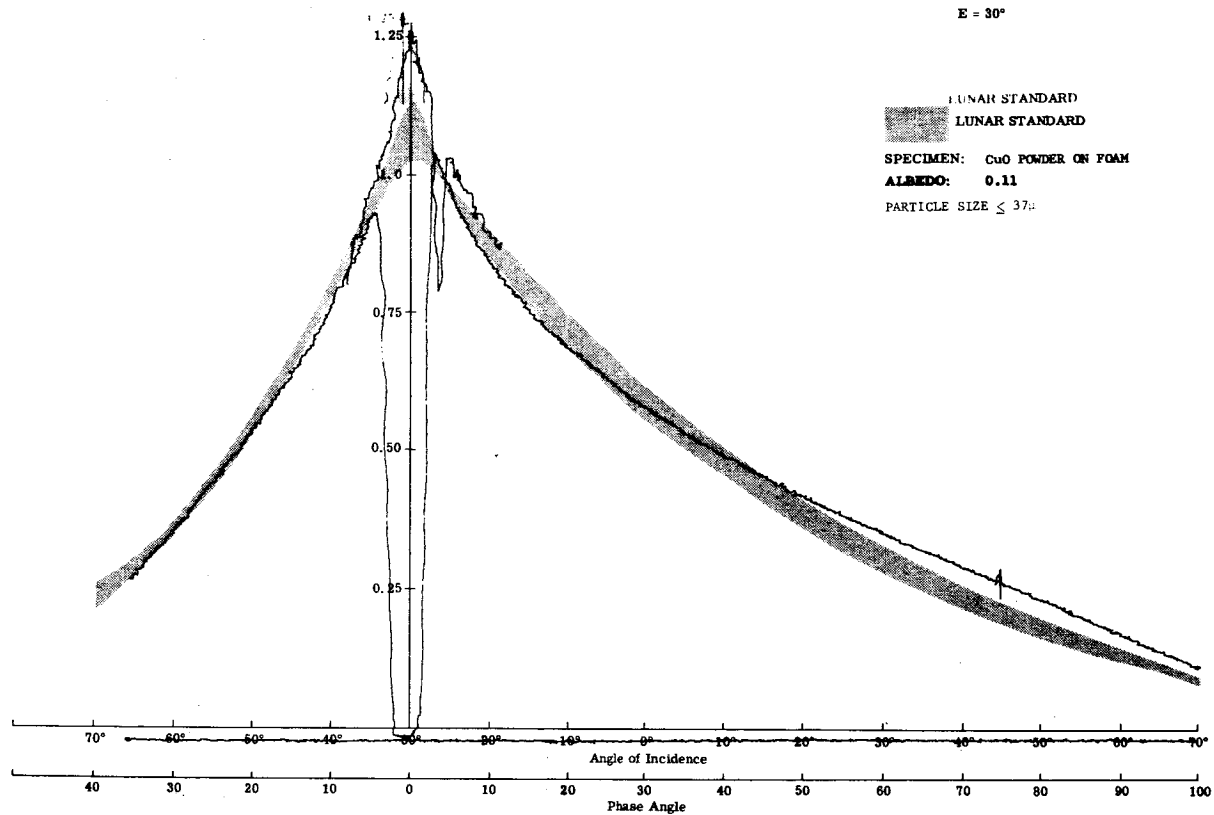


Visible

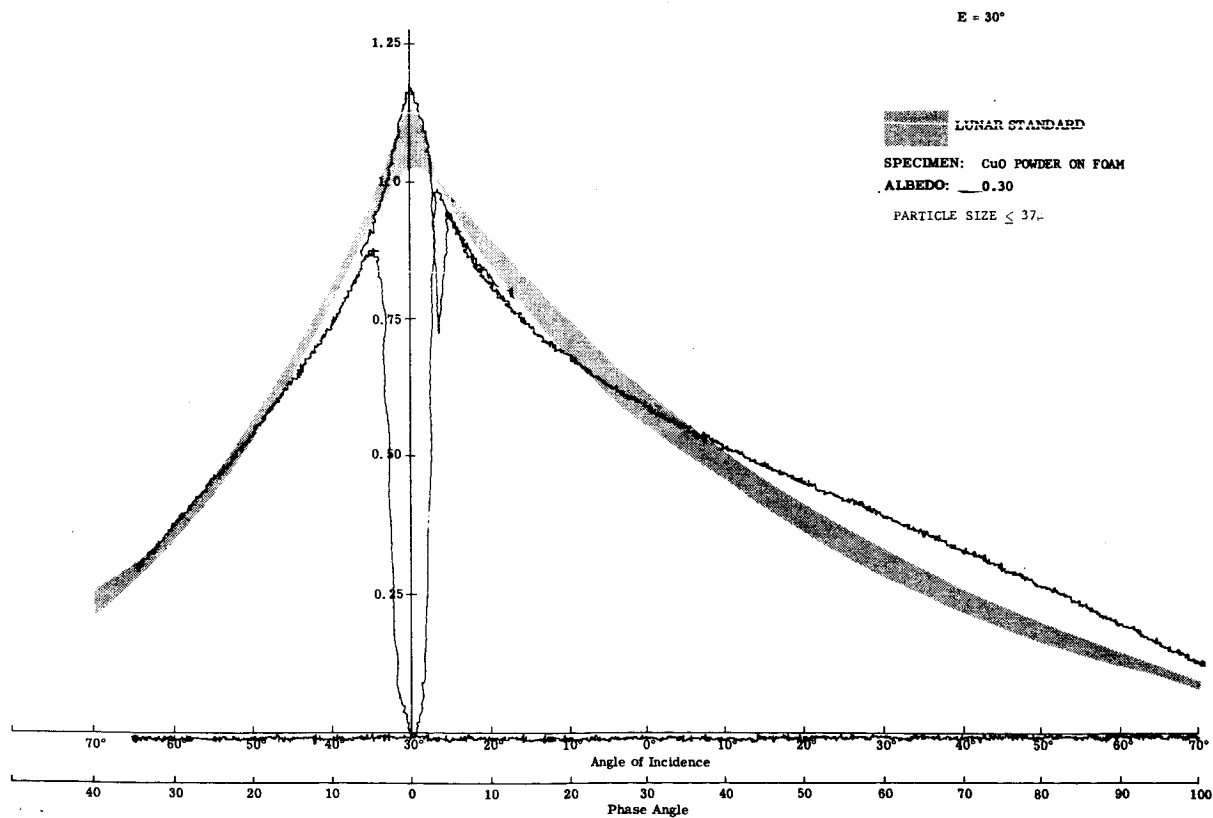


Blue

Fig. 18b Photometry of Copper Oxide Powder  
on Foam (E = 30°)



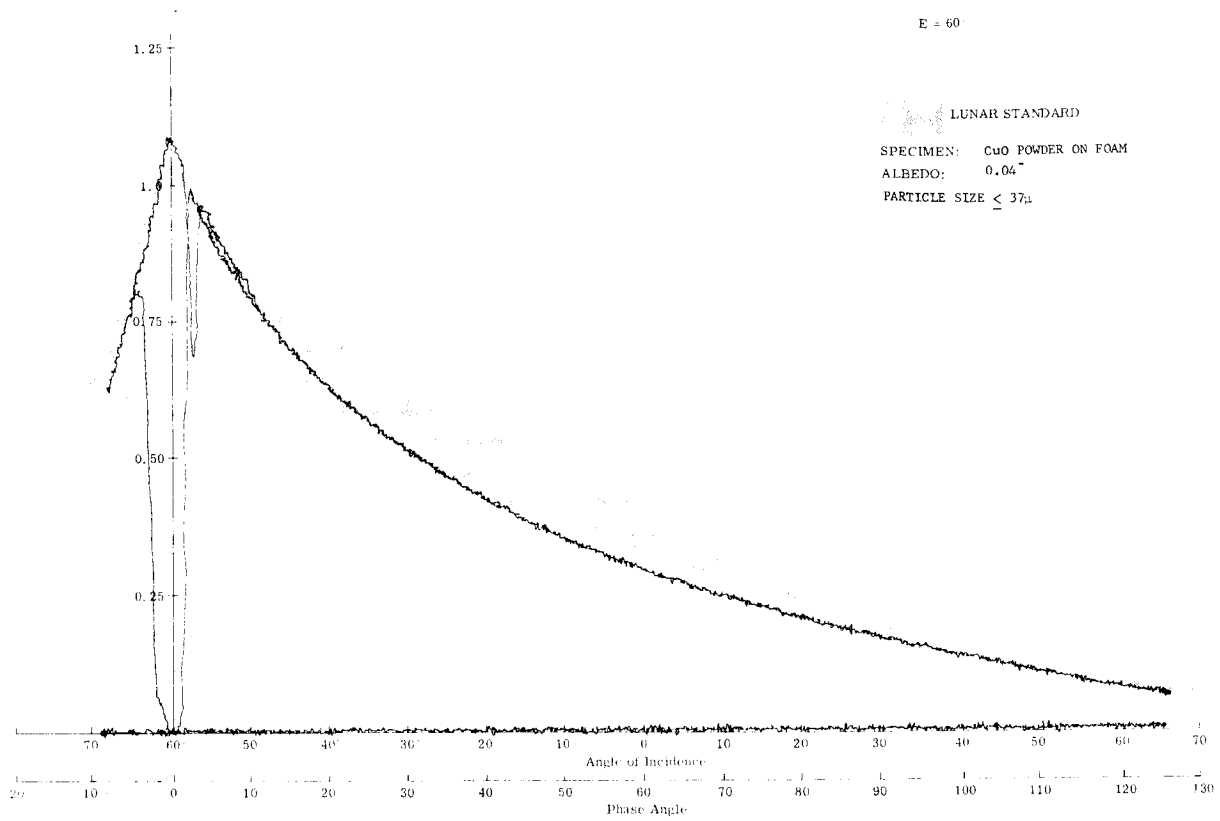
Red



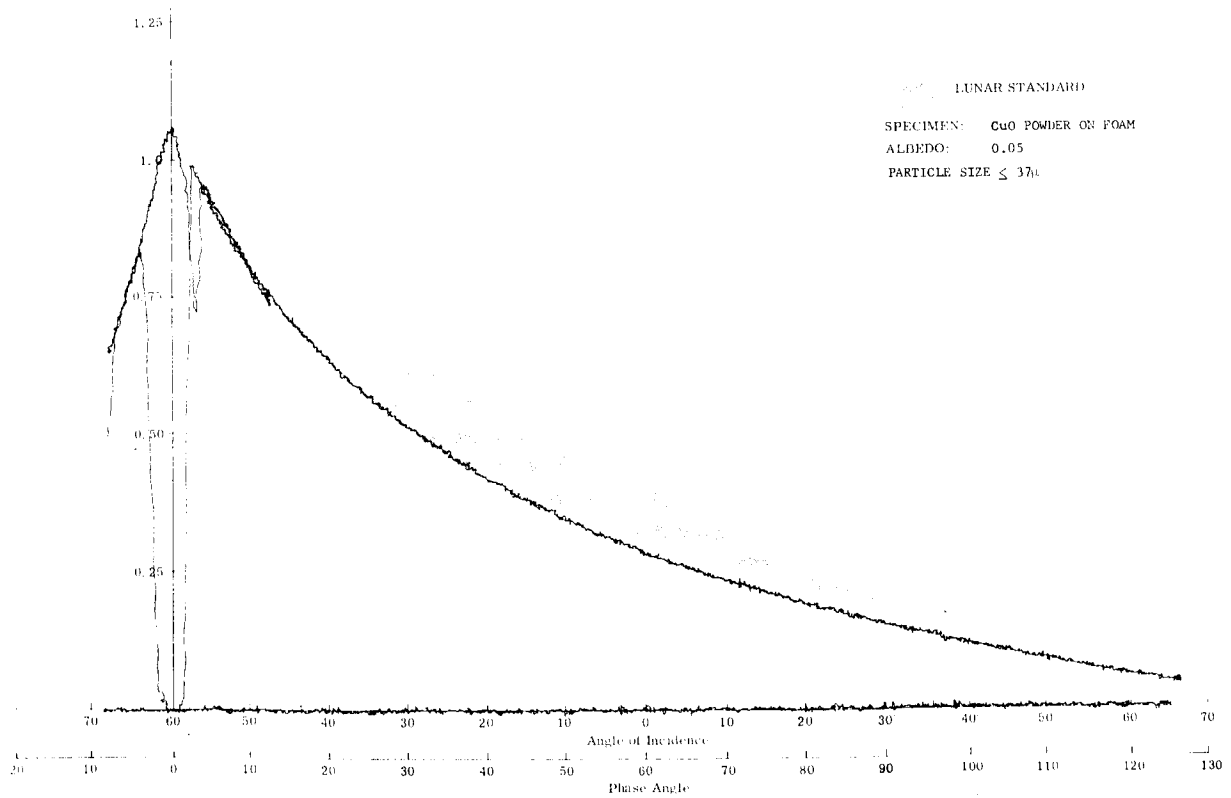
Infrared

Fig. 18b (cont) Photometry of Copper Oxide Powder  
on Foam (E = 30°)

E = 60

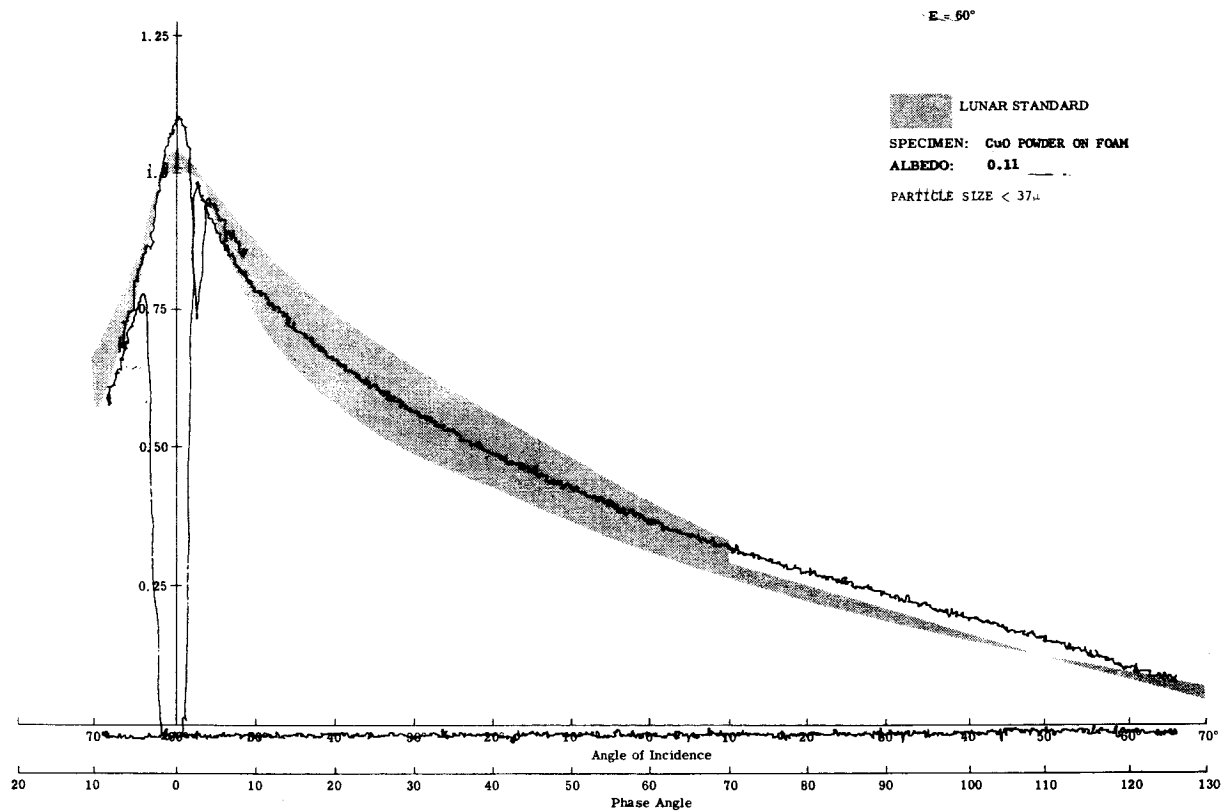


Visible

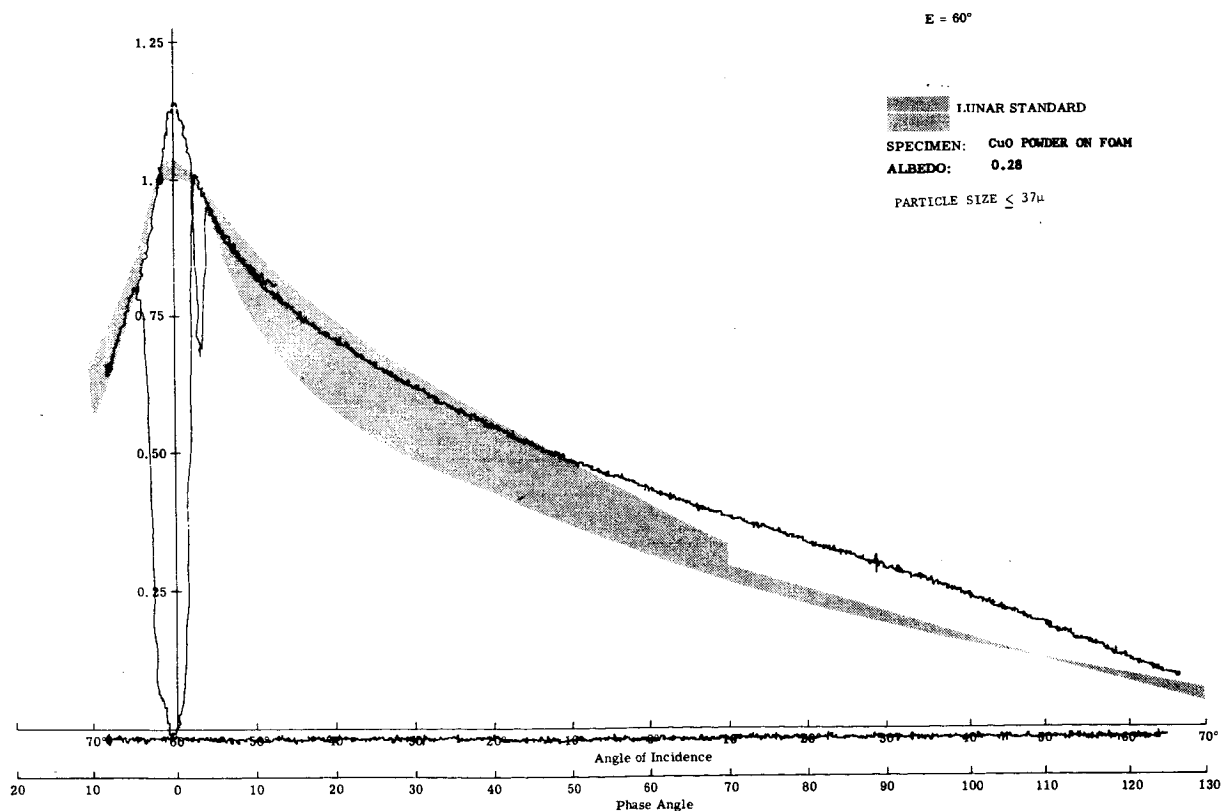


Blue

Fig. 18c Photometry of Copper Oxide Powder  
on Foam (E = 60°)



Red



Infrared

Fig. 18c (cont) Photometry of Copper Oxide Powder  
on Foam ( $E = 60^\circ$ )





Fig. 19 Volcanic Cinder No. 4



Fig. 20 Furnace Slag No. 1

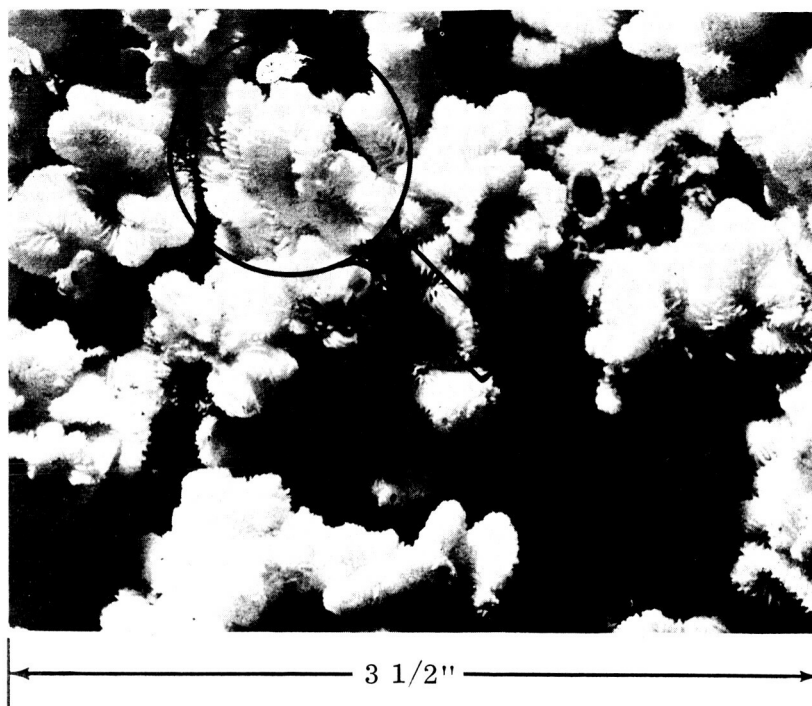


Fig. 21 Coral No. 2



Fig. 22 Scoria No. 2

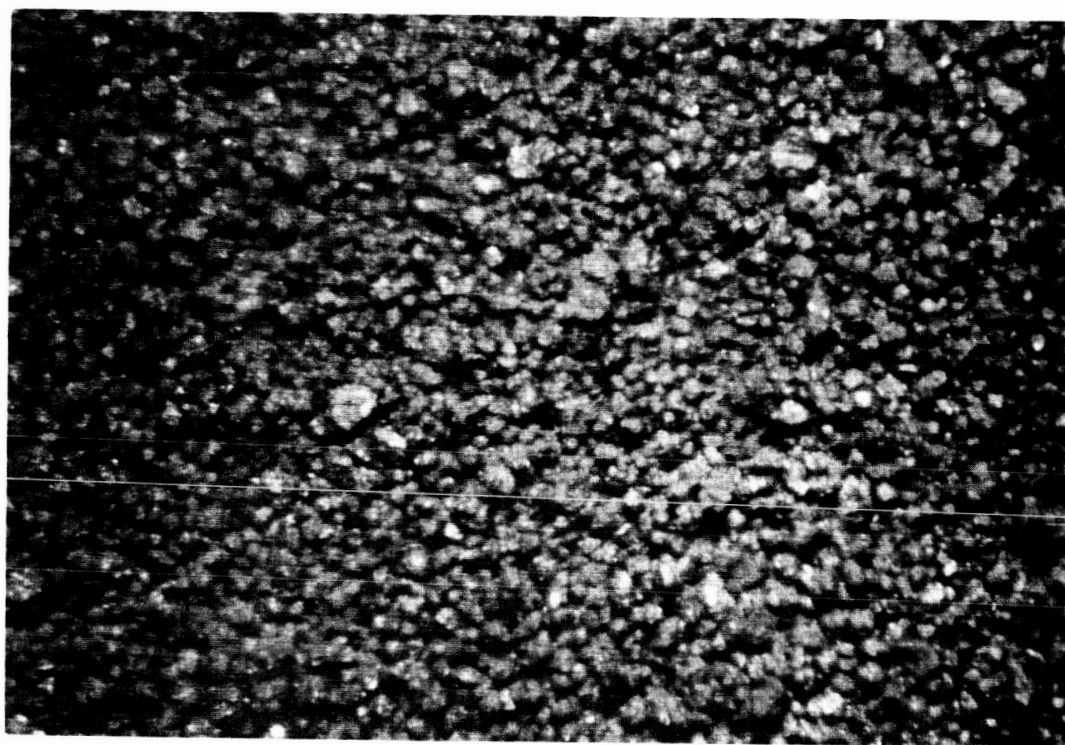


Fig. 23 Copper Oxide (Magnified 25X)

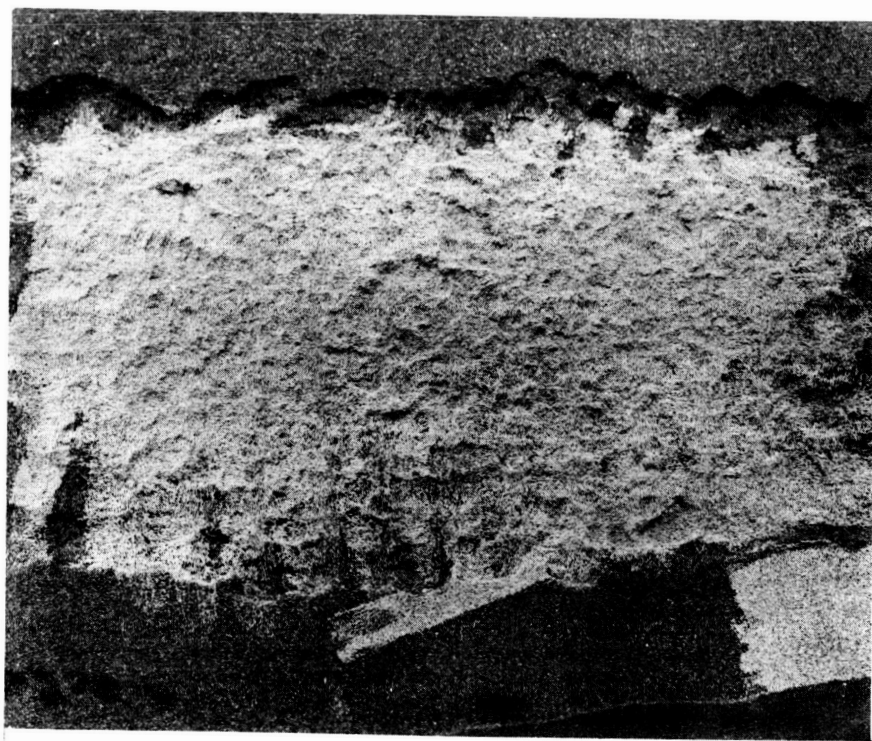


Fig. 24    Copper Oxide on Foam

## PHASE II — PHOTOMETRY OF SUSPENDED PARTICLES

### Purpose

This phase is used to study, by means of analysis and experiment, the reflection properties of "suspended particles" (dust clouds) recently proposed in the literature as a lunar photometric model. It is not our purpose in this study to propose any such model of the lunar surface but rather, to investigate the photometric properties of such a hypothetical model under the most idealized conditions.

### Experimental Models

In addition to analytical studies discussed below, we have constructed models simulating suspended particles to measure the brightness-phase angle dependence. The experimental models consist of opaque "macroscopic" spheres or beads of uniform albedo and diameter suspended on thin strings of negligible shadow-casting-capability. The beads are 3 mm diameter plastic spheres with a hole through the center. Four frames of plywood were made with an open "working" area of 5 x 12 inches and an adjoining open "storage" area of 2 x 12 inches as shown in Fig. 26a.

The beads are strung on fine nylon string, 22 beads per strand. Each frame has 10 equally spaced (30 mm apart) strands of beads. The beads were sprayed with Krylon Flat Black Paint as a prime or base coat. The prime coat is necessary because the brown water paint desired for proper "Lambertian" reflection would not adhere to the smooth surface of the plastic beads.

The brown paint used was Series 600 Gothic nontoxic Tempera, made by Sargent Manufacturing Corporation of Hazelton, Pennsylvania. A similar surface treatment was given to a masonite flat board used as a backdrop to the beads during photometric measurement.

Five models have been investigated. These models, numbered from 1 to 5, are illustrated in Fig. 25 and are described as to the spacing-to-diameter ratios of the particles in the three orthogonal directions, the number of layers, and the number of particles per unit, 30 x 30 mm viewed area. The maximum particle spacing used is 30 mm, giving a particle spacing-to-diameter ratio of 10 to 1. A particle spacing to diameter ratio of 5 to 1 as used by Gehrels (Ref. 7) in his proposed lunar photometric model, was also studied.

## Discussion of Test Results

The following comments may be made at this time based on the preliminary test results shown in Figs. 26b through d:

- All of the investigated "suspended particle" models show a very poor fit with the lunar curves, as we generally expected, particularly at large phase and viewing angles.
- The photometric behavior of Model No. 2, having a 10 to 1 particle spacing-to-diameter ratio, is barely distinguishable from that of a similarly treated flat surface having no particles (Model No. 1).
- The models having a denser population of particles show a noticeable increase of backscatter with increasing particle density.
- The general trend of the five investigated models, all having porosities higher than 99 percent, indicates that very high porosities of this order are not compatible with the lunar photometric data.

The most dense model, No. 5, exhibits local, secondary brightness peaks that are probably due to the presence of a sufficient number of particles whose shadows come into view at certain phase angles (low spots on the curve) but disappear at larger phase angles (high spots) when light reaches these areas through the interstices of the particles. This phenomenon, which is not observed on the moon, is also exhibited by the "suspended strip" models discussed in Phase III.

The bead models are, at best, a crude simulation of a cloud of suspended particles. It would be premature at this time to look for further meaning in the test results and to speculate about their lunar implications without further experimental refinements. The models we used have at least two major shortcomings imposed mainly by experimental difficulties: 1) they are not sufficiently deep to approximate the condition of a relatively thick cloud, and 2) their surface treatment leaves much to be desired. Although the paint we used has the proper albedo, it has sufficient gloss to obscure the test results at large phase and viewing angles. The

deviation of the test curves from the lunar curve at  $30^\circ$  and  $60^\circ$  viewing angles in Figs. 26c and 26d are due to specularity in the paint. The results would be more meaningful if this effect is eliminated. We are currently looking for a paint that reflects light according to Lambert's Law.

In view of the difficulties associated with the construction and measurements of laboratory models, an attempt has been made to study, briefly, the photometry of dust clouds analytically. The assumptions and numerical results obtained are discussed in the section which follows.

### Analysis and Discussion of Results

Close-up photographs of the lunar surface made possible by the recent Soviet soft landing on the moon have raised some doubts as to the possible existence of a heretofore assumed layer of fine dust. However, if we wish to defer final judgment on this question until more conclusive evidence presents itself and assume for the moment that such a dust layer might exist, the most probable mechanism for its formation is micrometeoritic bombardment. This constant pulverization process is believed to have created over a period of many years a reasonably uniform surface layer comprised of suspended particles held apart by mutual electrostatic forces of repulsion. Estimates of the average size of the individual dust grains as well as the thickness of the dust layer differ by as much as several orders of magnitude. Based on a variety of sources, dust accumulations ranging from millimeters to kilometers in local areas have been proposed.

In his attempt to account for some photometric and polarimetric observations, Gehrels (Ref. 7) estimates that over a period of approximately  $10^7$  years a layer  $6 \times 10^{-2}$  mm thick, comprised of particles of average diameter  $1.6 \times 10^{-3}$  mm, has been deposited on the lunar surface by the accretion of interplanetary dust. Other investigators, i.e., Singer and Walker (Ref. 13), studying the transport of electrostatic dust on the lunar surface formed by meteoritic bombardment, estimate a thickness of approximately 50 cm with an average range of 20 cm to 100 cm in local shadow areas. These authors claim that particle diameters ranging approximately from  $3 \times 10^{-2}$  mm to  $1 \times 10^{-6}$  mm are possible.

In our study of the photometry of suspended particle models, we will assume the relatively simple model shown in Fig. 27 which consists essentially of a compact base material above which is an



electrostatically suspended, random distribution of spherically shaped dust grains. Without making reference to the complicated screening effects present near the surface, we simply assume that the dust grains, charged electrically by the action of UV radiation from the sun, remain suspended by the forces arising from the normal component of the electric field at the surface. The rather sharp distinction between regions as we have shown them in Fig. 27 is in reality a very poor approximation to what might actually be the situation. In fact it is most probable that a continuous distribution of particles exists in the uppermost layer with the individual grains being preferentially sifted by electrostatic means according to size.

The reflection of light from a medium consisting of discrete scatterers of varying size and interparticle distance is a complex problem in multiple scattering, necessitating an analysis far beyond the scope intended for the present investigation. Since we are predominantly concerned with the shadow casting property of suspended particles and the role it plays in determining the phase variation of the brightness of a model, several simplifying assumptions are made. To begin with, we will assume that the particles in suspension are opaque, diffuse scatterers, of uniformly low albedo. Their average diameter  $d$ , is such that:  $\lambda/d \leq 1/20$ , where  $\lambda$  is the wavelength of the incident radiation, and their interparticle distance to diameter ratio is of the order of 1.5 or greater. These assumptions when considered collectively enable us to regard the scattering processes for such a model as being independent, and further, to neglect multiple reflection and diffraction effects (Ref. 14). Since we are considering the limiting case in which the incident wavelength is small compared to the average size of the individual scattering obstacles we can avoid the use of Mie scattering theory and apply the laws of geometrical optics.

A useful analysis which satisfies the above conditions was developed by Walker (Ref. 15) who was interested in the formation of dust clouds produced by the impact of space vehicles and meteors on the lunar surface. Of primary concern was the question of whether or not a dust cloud thus formed could produce sufficient darkening or brightening of the surface so as to render telescopic observation of such events possible.

Walker considered the creation of a dust cloud arising from the impact of material originally ejected from the vehicle's primary impact crater. To form such a cloud, he assumes the lunar surface to be covered by a layer of fine, loosely bonded dust. We shall not elaborate further on the details of Ref. 15 but will

utilize some of the more pertinent results insofar as they have bearing on the present problem. Assuming a model similar to ours, Walker obtains an expression equivalent to the following for the apparent brightness of a surface covered by a dust cloud:

$$B(\alpha, E) = \frac{1}{1 + \sec(\alpha - |E|)} \left\{ I(\alpha) + \left[ (1 + \sec(\alpha - |E|)) B_0(\alpha) - I(\alpha) \right] \right. \\ \left. \times e^{-pn \left( \frac{1 + \sec(\alpha - |E|)}{\cos E} \right)} \right\} \quad (1)$$

In the above expression,  $E$  is the viewing angle,  $\alpha$  the phase angle,  $p$  the particle cross section,  $n$  the particle density per unit area,  $I(\alpha)$  the individual particle scattering function, and  $B_0$ , the brightness of the surface when there are no particles suspended above it. The above expression was derived by taking into account the fact that the suspended particles will not only cast their shadows on the surface but on other dust grains as well. Because we are considering diffuse reflection from a random distribution of macroscopic convex particles, we can replace the distribution with a very large sphere of the same material and surface condition (Ref. 14). Hence,

$$I(\alpha) = \frac{(\pi - \alpha) \cos \alpha + \sin \alpha}{\pi}, \quad (2)$$

which is the well-known backscattering function derived by Shoenberg for a sphere whose surface elements scatter in accordance with Lambert's law. The quantity  $pn$ , which is essentially the cloud coverage, can now be replaced by quantities related to the particle diameter  $d$ , average interparticle spacing,  $t$ , and  $h$ , the height of the dust layer, i.e.,

$$pn = \frac{\pi}{4} \left( \frac{d}{t} \right)^2 \frac{h}{t}. \quad (3)$$

A range on the upper limit of the size of particles which can be "floated" by the forces of electrostatic repulsion was obtained by Singer and Walker (Ref. 13) who equated the gravitational and electrical forces acting on the particle:

$$d_{\max} = 2 \left[ \frac{(3\epsilon_0 \phi E)}{(\rho g)} \right]^{\frac{1}{2}} . \quad (4)$$

In Eq. (4),  $\epsilon_0$  is the permittivity of space,  $\phi$  the electrostatic potential of the particle,  $E$  the electric field intensity at the lunar surface,  $\rho$  the particle material density, and  $g$ , the lunar gravitational constant. For values of  $\phi = 20$  volts,  $E = 67$  volts/meter, and  $\rho = 0.1$  gm/cm<sup>3</sup>, Singer and Walker obtain,  $d_{\max} \approx 3 \times 10^{-3}$  cm. For  $\rho = 1$  gm/cm<sup>3</sup>,  $d_{\max} \approx 1 \times 10^{-3}$  cm.

Numerical studies of Eq. (1) were carried out over a range of particle sizes, interparticle spacing to-diameter ratios, and dust layer thickness, with the assumption that the underlying base material scatters light according to Lamberts' law of diffuse reflection. For our computations, we have taken three values of particle diameter, namely:  $1 \times 10^{-3}$  cm,  $2 \times 10^{-3}$  cm, and  $3 \times 10^{-3}$  cm. For each such particle size, a dust layer thickness was selected and for each such combination of  $d$  and  $h$ , the ratio of  $(d/t)$  was varied from  $1/3$  to  $1/10$ . The depth of the dust layer,  $h$ , ranged from values of  $0.1$  cm to  $10$  cm.

The results of the calculations are shown in Fig. 28 where we have superimposed on the lunar standards several of the calculated brightness versus phase curves for different viewing angles and typical values of  $d$ ,  $t$ , and  $h$ . In addition to these curves, we have also shown the results for the two limiting cases of an infinitely thick, and a zero thickness layer (plane "Lambertian surface" with no particles suspended above it).

The general nature of the curves for all viewing angles is such that they do not display the characteristic steep rise in the "opposition" or small phase angle region. At large phase angles, or in the backscattering region, the results also leave something to be desired. As can be seen, the peak in the brightness curves shifts away from the brightness peak for the "Lambertian surface," the shift becoming increasingly greater at larger viewing angles but not sufficient to approach the lunar curves. The lack of conformity to the lunation curves in both the "opposition" and backscattering regions can be attributed to the fact that we have assumed surfaces that scatter light according to Lambert's law. Characteristically, this reflection law produces results which exhibit a broad peak at zero angle of incidence with rapidly decreasing brightness at incidence angles of  $\pi/2^\circ$  ("limb darkening").

There is no question that our substitution of a "Lambertian surface" for the case when no suspended particles are present above the base material plays a large role in the general shape of the curves obtained. The shift in the brightness peaks toward smaller phase angles is due essentially to the fact that the effective particle depth,  $n_E = n/\cos E$ , increases with increasing viewing angle. Since the individual particle scattering function  $I(\alpha)$  peaks for small phase angles, this results in a greater contribution to the brightness by the particles in the cloud than the underlying surface layer itself.

We have observed that dust clouds exhibit a shift of brightness peak from the Lambertian reflection which characterizes most terrestrial surfaces, to a lunar type reflection; however, the shift is hardly sufficient to qualify particulate media having porosities approaching 100 percent as lunar photometric models. Subject to the simplifying assumptions that made this analysis possible, we may conclude that suspended particle models such as we have assumed are not capable of backscattering light like the moon.


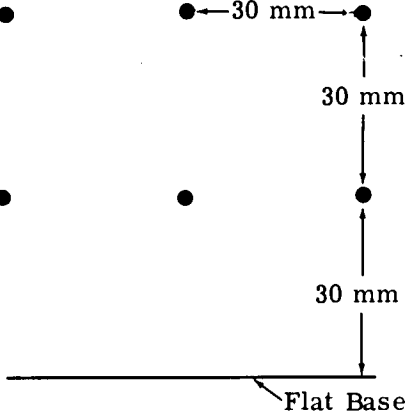
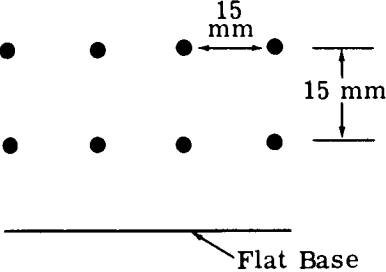
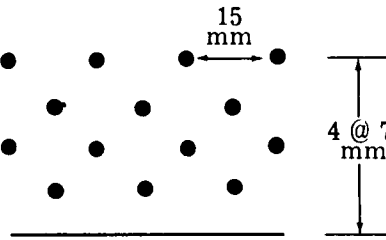
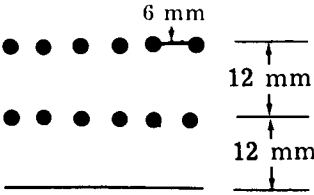
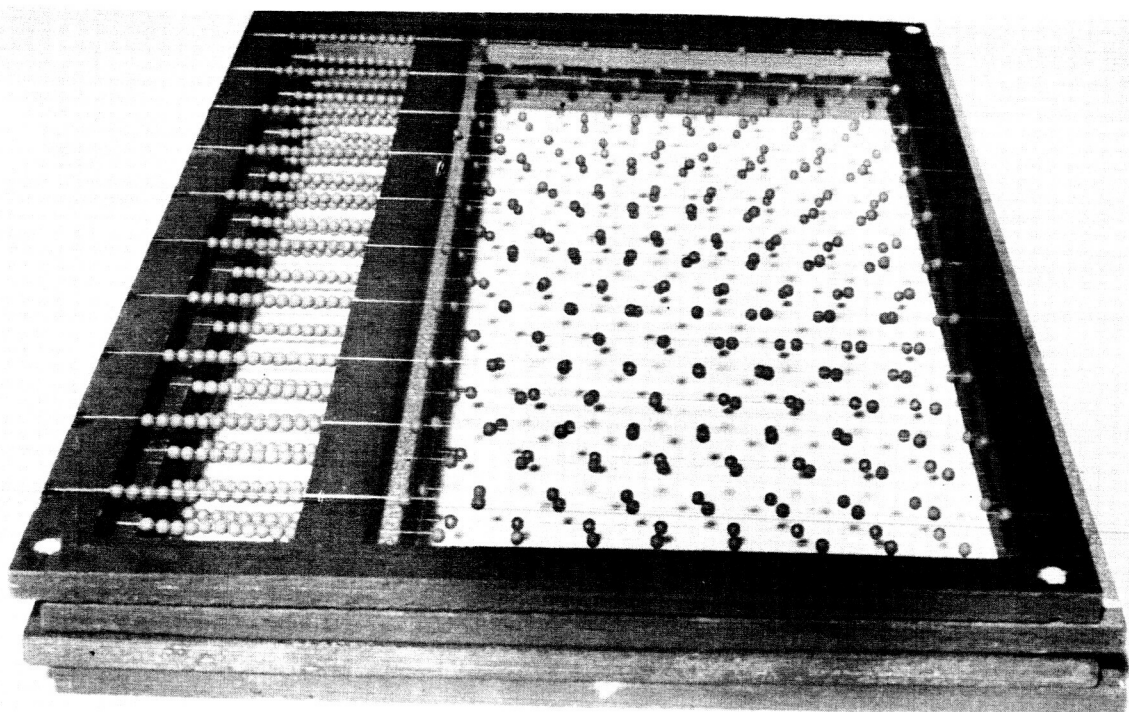
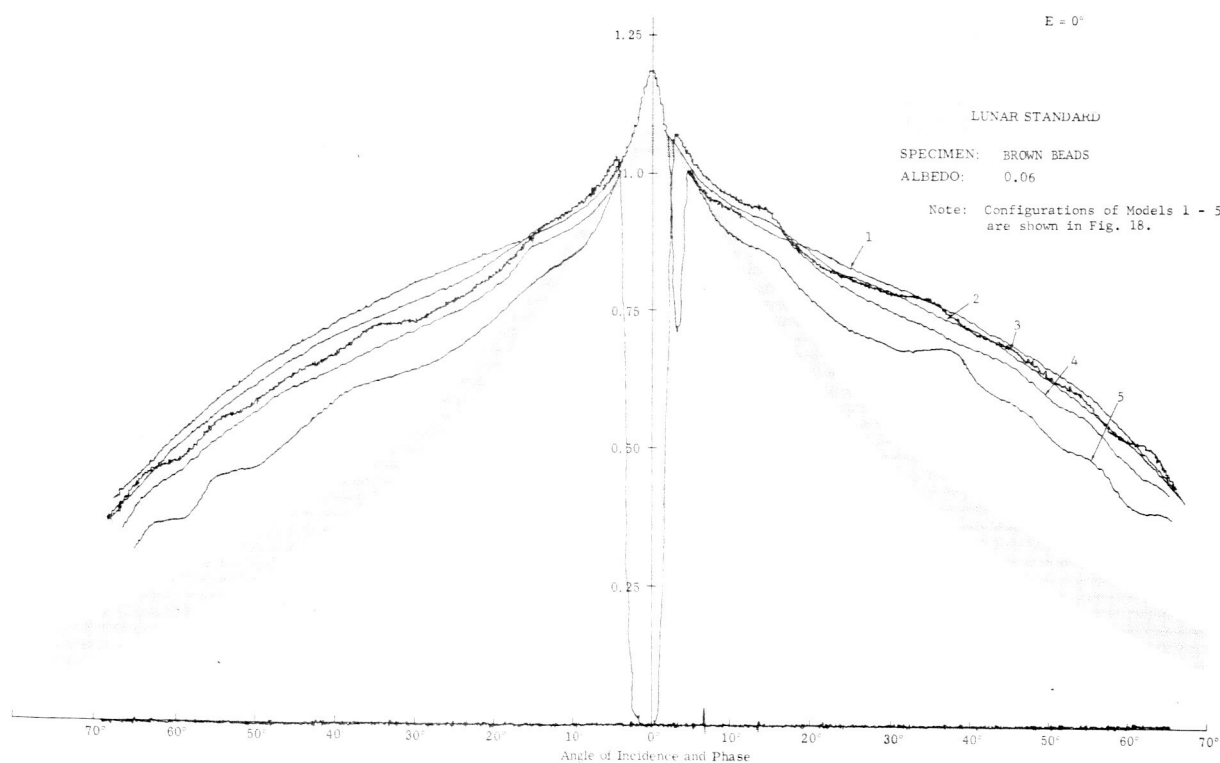
Model No.	Geometry	Particle Spacing to Diameter Ratio	Number of Particles per 30 x 30 mm viewed area
1	 Flat Base	(no particles)	0
2		10 : 1 in x, y and z directions	2
3		5 : 1 in x, y and z directions	8
4		x = 5:1 y = 5:1 z = 2:1	16
5		x = 2:1 y = 5:1 z = 4:1	20

Fig. 25 Experimental Models of Suspended Particles

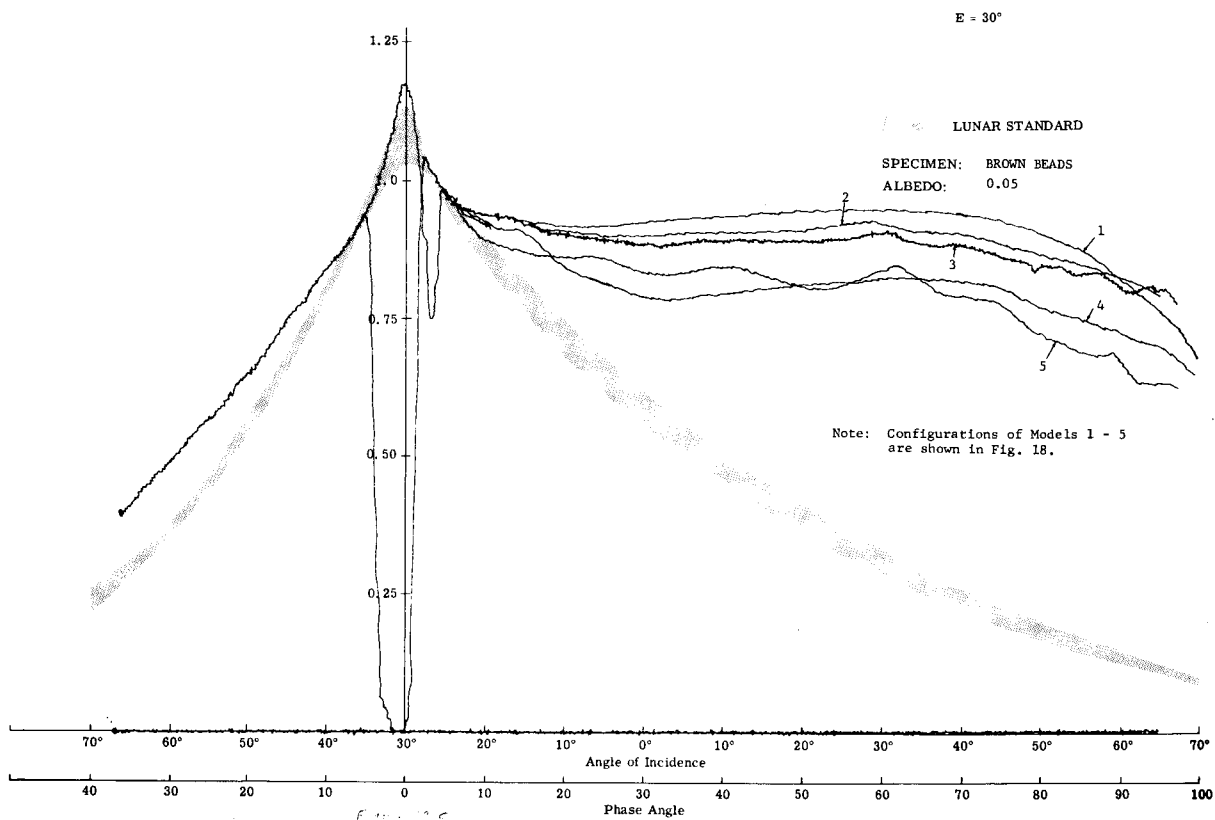


a) Photograph of Brown Beads Model

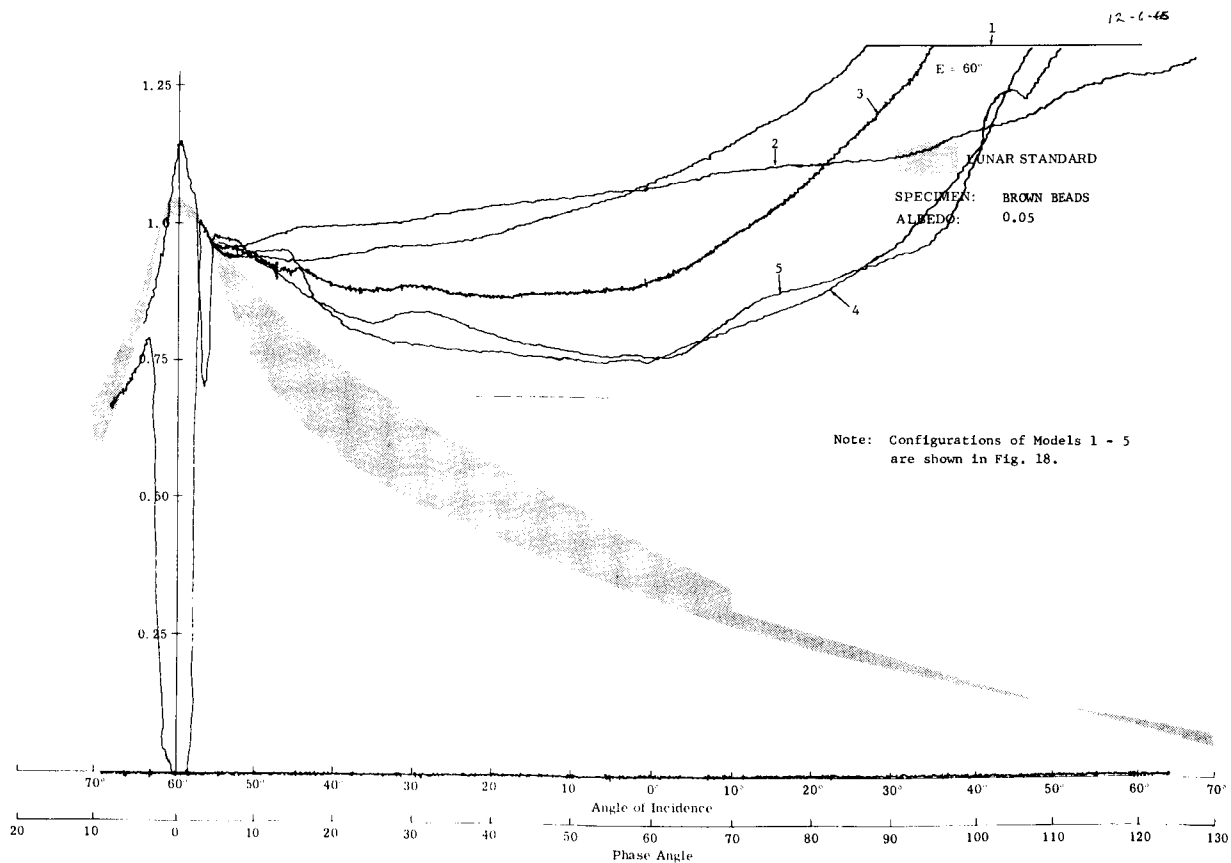


b) E = 0°

Fig. 26 Photometry of Suspended Particles Model



c)  $E = 30^\circ$



d)  $E = 60^\circ$

Fig. 26 (cont) Photometry of Suspended Particles Model

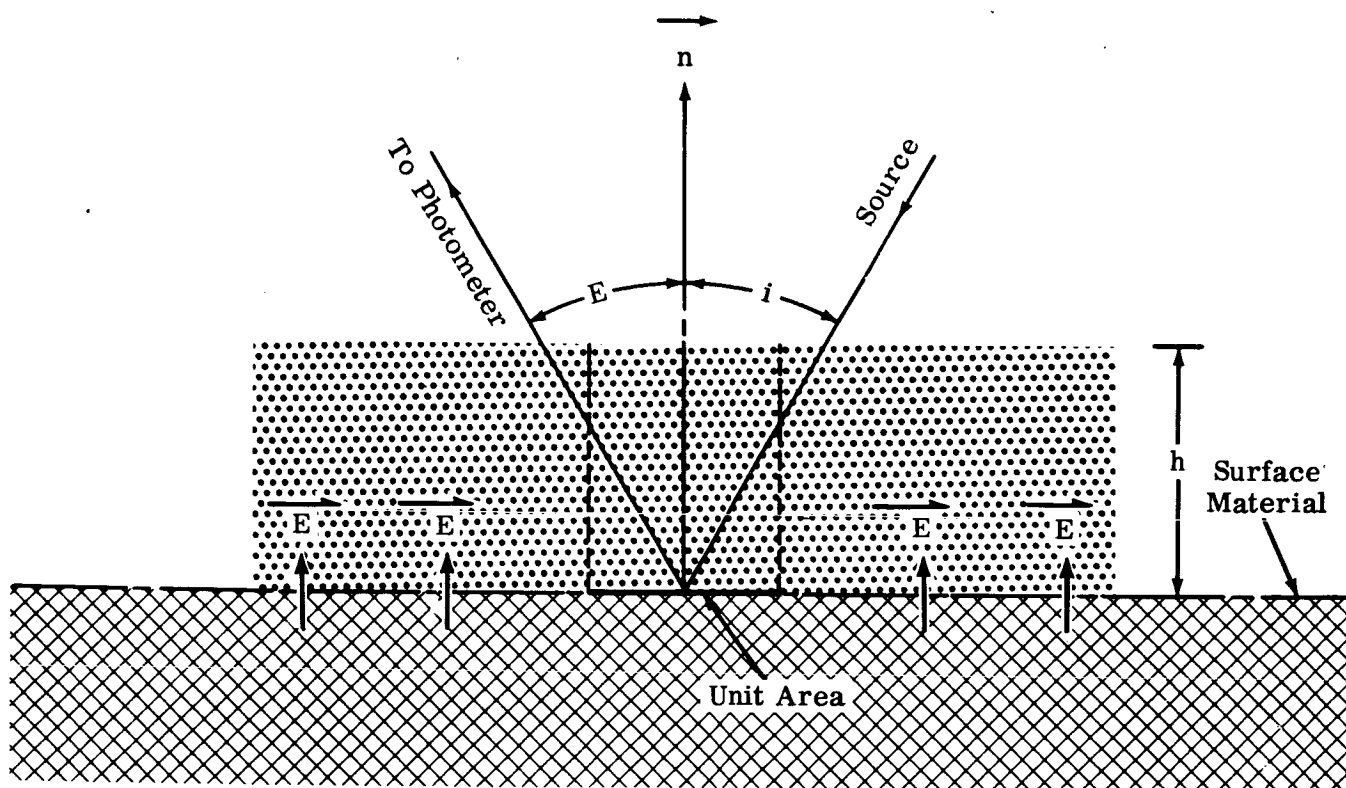


Fig. 27 Analytical Suspended Particle (Dust Cloud) Model



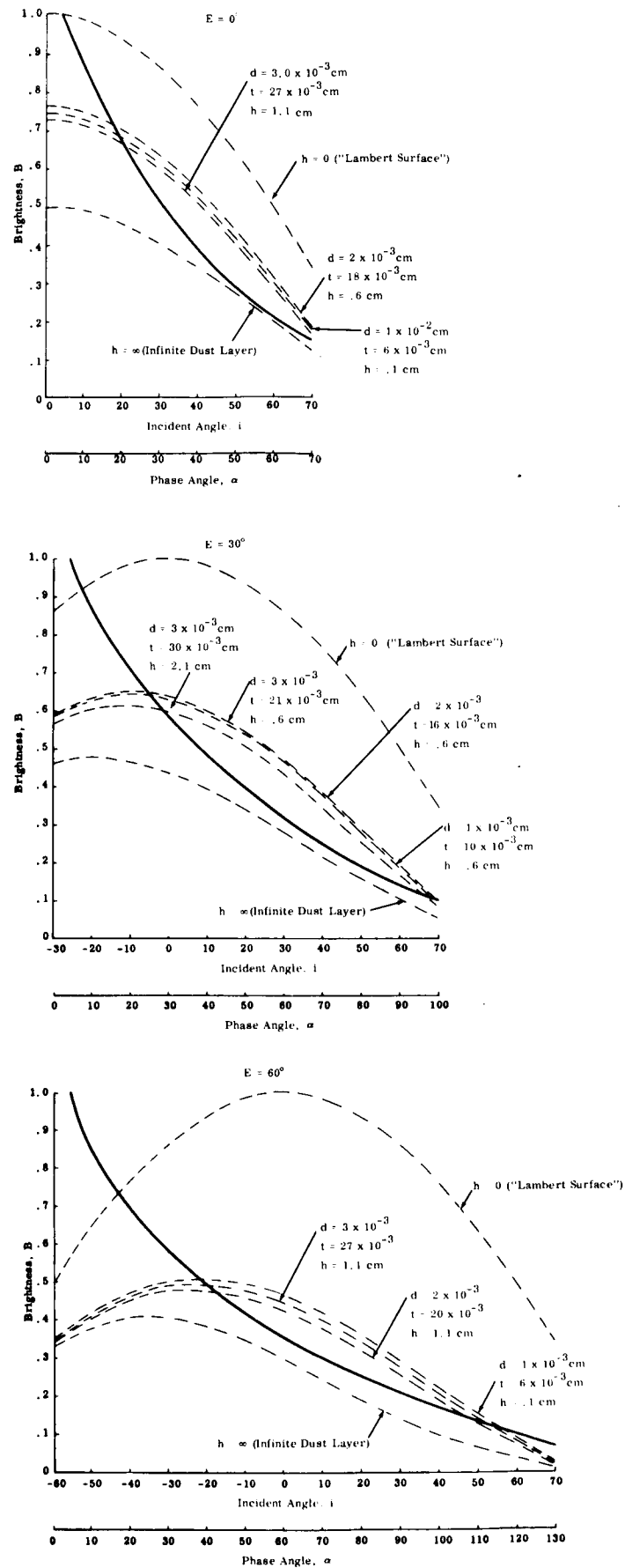


Fig. 28 Photometry of Suspended Particle (Dust Cloud) Model

## PHASE III — GEOMETRY OF BACKSCATTERING SURFACES

### Purpose

This phase was planned to investigate and develop empirical relationships, in terms of physical and optical properties of surfaces, that obey the reflection laws of the moon for both uniform and "composite" albedo conditions, in an attempt to determine a range of porosities consistent with existing lunar photometric observations.

The general purpose of this analytic exercise is not necessarily to proliferate the number of lunar photometric models for their own sake or to replace the natural specimens investigated herein or elsewhere, but to explain why surfaces in general reproduce or fail to reproduce the lunation curves of the moon, and to enable one to identify and estimate those useful "engineering" properties of the lunar surface that are photometrically relevant.

### Basic Analytical Models

In their quests to reproduce the lunation curves of the moon, several investigators in the past have constructed hypothetical surfaces comprised of elements of known geometry and albedo, arranged in a variety of patterns thought to be analogous to either natural specimens or to the moon itself. Examples of such controlled theoretical models are those of Barabashev (grooves and clefts), Shoenberg (spherical domes), and Bennet and Van Diggelen (hemiellipsoidal cups). In conjunction with the above variety of geometrical shapes, these investigators made use of different forms of the optical scattering law including those proposed by Lambert, Lommel-Seeliger, and Fessenkov. Though a moderate degree of success was achieved, the results in most cases were decisively negative with respect to lunar observations at large phase angles. Despite the limited success achieved thus far with these controlled models, the search still continues for a simplified lunar photometric model composed of elements that lend themselves to easy manipulation and analysis.

Based on the results of recent experiments (Ref. 3), there is strong likelihood that backscattering surfaces possess a tri-dimensional structure comprised of shadowcasting opaque elements larger in size than wavelengths in the optical region. With reference to the lunar surface, it appears quite possible that

the irregularities on the uppermost layer, whatever their particular form may be, may cast shadows that grow larger as the angle of incidence of the radiation from the sun increases. Because the shadow casting elements may not in fact be within the telescopic resolution of present day instruments, the peculiar photometric signature of the moon may be due in large part to the combined effects of a great number of superimposed shadows that behave additively and eventually become dominant.

Several of the "natural" and "artificial" specimens investigated experimentally at Grumman and elsewhere are known to possess a tridimensional structure, but any rigorous analysis based on the actual geometry of their surface is prohibitively difficult. To circumvent these theoretical difficulties, but at the same time accomplish something in the way of useful analysis in terms of relative geometry, and ratio of solid elements to voids, we have in this phase continued the work with tridimensional contrived models that was initiated and reported in Ref. 3. The five "simple" models selected for detailed quantitative analysis are those shown in Fig. 29 and are comprised essentially of an orderly array of horizontally suspended and/or vertical elements of low albedo. The elements themselves are oriented in such a way relative to the plane of vision that they cast shadows as the light source moves from left to right along the intensity equator.

The choice of a proper scattering law for the reflecting elements could be of some importance. It is probable that apart from geometrical and albedo effects an important analytical obstacle yet to be overcome in explaining the peculiar reflecting properties of the uppermost layer of the lunar surface is the discovery of a more accurate form of the scattering function. In remaining consistent with the over-all accuracy of the analytical approach taken at this time, we feel that despite their shortcomings, primitive forms such as those of Lambert and Lommel-Seeliger, are sufficient for our computations insofar as we are assuming the role of shadowing to be dominant. The assumption of low albedo allows us to neglect multiple reflections that would, if anything, tend to wash out those dark areas in shadow. As in Phase II, diffraction effects are neglected. This assumption greatly facilitates the analysis and follows from the fact that the relative sizes of the reflecting elements are chosen to be analogous to the lunar features only on a macrorough scale. Edge effects are also neglected.

Because of the periodic nature of each of the geometries selected and their assumed distance from the light source, the analyses (see Appendix) were performed in terms of the smallest possible unit structure of each of the configurations, utilizing parallel ray optics. These "unit structures" consist essentially of a horizontal or overhanging member and a portion of the underlying base material that is both illuminated and observed by the photometer. There is no question that the size of the "unit structure" and hence their number per unit area included in the field of view of the photometer, will affect the general character of the photometric signatures for all models considered under experimental conditions. Some preliminary experimental results (Ref. 3 ) using triangular prisms indicate that there is a general increased smoothing effect on the photometric curves as the size of the prisms is reduced and more are added to the field of view. At this point, it is believed that the smoothing effect is due to the decrease in the size of the shadows cast relative to those surfaces that are illuminated and viewed.

#### Discussion of Analytical Results for Basic Models

The results of the computer analysis described in the Appendix were abstracted and are presented graphically in Figs. 30 through 33. Figures 30a through 30d represent plots of the sum of the squares of the deviations ( $\Sigma \Delta^2$ ) as a function of  $b$ , at constant values of  $h$ , for some basic models. As can be observed, the general character of the curves is oscillatory with the deviations tending to reach minima with increasing values of  $b$ . In some cases the results for particular values of  $h$  were omitted, the reason being that these solutions were highly irregular. These omissions did not, however, lead to any loss in our ability to confirm some already existing notions as to what general set of configuration parameters and viewing angles would result in the minimum deviation from the known lunar observations. In all instances, it appears as though the best results are achieved for a viewing angle of  $0^\circ$ . This result is to be expected, since most of the difficulties, both theoretically and experimentally, seem to occur at the larger phase angles. In both the basic "T" and Furrow model cases, where the analyses were carried out for values of  $b$  greater than  $a$ , one can observe the "bottoming out" of the curves for the  $0^\circ$  viewing case. As this does not occur for the other viewing angles, we can only conclude that for these cases, sufficiently high values of  $b$  had not been achieved.

In Figs. 31 through 33 we have superimposed on the standard lunation curves those photometric signatures for the first four contrived models that represented the closest match, in the sense that the sum of the squares of the deviations from the lunar data were minima. Only the Lambert scattering law was used in the numerical calculations. In the interest of brevity, the results for the Suspended Strip and the Vertical Strip models, and the basic "T" and Furrow models, were grouped together so that for each graph three curves, including the lunar standard, are presented for comparison.

The results for the Suspended Strip, Vertical Strip, and basic "T" models tend to corroborate generally most of the features previously predicted for these models in Ref. 3. The "cosine type" curve obtained at large phase angles is due to the cessation of shadow lengthening in the areas viewed by the photometer and to the diffuse reflection of light from the other areas. In the case of the suspended strip model, the characteristic second brightness peak predicted by Hapke and us occurs for all viewing angles and is due to the illumination of those portions of the base material between adjacent "unit structures." Since there are no vertical strips present on this model to block either the photometer's field of view or the direction of the incident light, extra portions of the base material have to be accounted for in the calculation of the brightness. We can in summary make the following observations concerning the basic "T" and Furrow Models:

- 1) The generally closer matches for these models for values of  $b > a$  as opposed to those for  $b < a$ , suggest a higher estimate on the lunar surface porosity than had been suspected previously.
- 2) The  $E = 60^\circ$  viewing case is the most critical in the sense that the greatest deviations from the lunar standard occur here and decrease generally toward more favorable matches as we approach  $E = 0^\circ$ .
- 3) There is nothing unique about the  $E = 0^\circ$  viewing case since the results for both models in this instance are identical.

- 4) For the T-Model ( $b > a$ ), the optimum spacing is revealed at  $E = 60^\circ$ , whereas the optimum height is revealed at  $E = 30^\circ$ . At  $E = 60^\circ$ , all the  $(\Sigma\Delta^2)$ 's are alike for  $b = 2$  and  $h = 2$ , whereas for  $E = 30^\circ$  there is a unique  $h$  dimension. Hence, the  $30^\circ$  and  $60^\circ$  viewing angle data complement one another in suggesting a model that is unique insofar as horizontal spacing and vertical dimensions are concerned.
- 5) A comparison of the T-model, Fig. 33, with the suspended strip model, Fig. 31, clearly shows why vertical elements are necessary in a lunar photometric model. Such elements make the model less tenuous in terms of strength and give less validity to dust clouds as a lunar photometric model. This analysis merely confirms what we already observed experimentally with the "Thumb Tacks" models, as reported in Ref. 3, and the "suspended particle" model reported in Phase II of this work.
- 6) A comparison of the T and Furrow models, Fig. 33, shows the considerable improvement in the photometric match at small phase angles, derived from the presence of horizontal, overhanging members. We also notice that these members do not contribute much at larger phase angles. The next section describes various attempts that were made to improve the photometric match at the large phase angles.

#### Modifications of Basic T-Model

We notice in Fig. 33 that the match of the basic T-model with the lunar curves, although quite good at normal viewing, deteriorates at large viewing angles. To improve this match, the following modifications have been introduced:

- Short vertical elements called "lips" have been appended to the top of the T's with the anticipation that at large phase angles these elements would cast shadows on top of the T's which otherwise would have been exposed during the full lunation. It is reasoned that the additional shadowing will reduce the over-all brightness of the model particularly at large phase angles and, hence, narrow the gap between the lunar and model curves.

- Various elements of the model have been assigned different albedos. The top exposed surfaces are made darker than the interior, less-exposed surfaces. Albedos of 0.05, 0.10 and 0.15 are assigned to the top, bottom and vertical surfaces respectively (see Appendix). This modification is based on the possibility that age-darkening on the moon due to solar wind could be more extensive on the outermost surfaces than in the interior of the cavities shielded by these surfaces. As far as the photometric behavior of the model is concerned, it is reasoned that the assumed distribution of albedos will enhance the rate of brightness change since the brighter cavities are occulted sooner than the darker exterior surfaces.
- Basic scattering laws on which the photometric analysis is based have been modified. The Lambert and Lommel-Seeliger laws are considered and compared.

Four separate computer analyses have been performed to study the photometric behavior of the basic T-model under the following inputs:

- Geometry changes only (addition of lips)
- Albedo changes only
- Geometry and albedo changes
- Basic scattering law changes only

#### Discussion of Analytical Results for Modified T-Model

The computer programs on which the results are based are discussed in the Appendix. The results are shown in Figs. 33, 35, and 36. For convenience in comparing the various solutions, the curves resulting from the 4 inputs noted above, are presented for each viewing angle on opposite pages. It should be recalled that the results are best fit curves selected by the computer. Briefly, the major findings and their lunar implications are as follows:

- 1) As we anticipated, the addition of lips has considerably improved the backscattering of the basic T-model. This finding suggests the

presence on the moon of secondary shadow-casting roughnesses (simulated by the lips) whose contribution is most needed at large phase angles since the "primary" roughnesses (simulated by the basic T's) do not cast additional shadows. This analysis reveals graphically why the rapid change in brightness of the lunar surface is due to a continuous shortening or elongation of shadows, during a lunation, rather than to a mere change of light incidence. We may conclude that a surface that exhibits this peculiar reflection is necessarily complex and covered with innumerable roughnesses having a wide spectrum of size distribution. The opposition effect gives additional support to this view. This point is further discussed below.

- 2) The effect of composite albedo on the basic T-model, Fig. 35c, is similar to that produced by the lips, Fig. 36c. It is instructive to note that next to shadowing or geometry effects, the photometry of a porous surface appears to be quite sensitive to albedo differences within the model. Such differences in albedo have not been considered before. Photometric functions that have been proposed to date are based on uniform albedo. We may conclude from this analysis that if the lunar surface contains albedo differences similar to the ones we have assumed, then its porosity as inferred from its photometric function is not as high as it would otherwise be if its albedo were uniform. Therefore, porosity estimates based on uniform albedo are conservative in terms of bearing strength. Our current estimate of the porosity of the lunar "photometric layer," based on experiments reported in Ref. 3, is of the order of 70 to 80 percent. Further analysis and evolution of the contrived photometric model (see Fig. 37), could lead to an independent confirmation or additional refinement of this important engineering property of the lunar surface.
- 3) Since geometry and albedo effects, when properly manipulated, affect the photometric function in a similar manner, we notice in Figs. 35c and 36c how their cumulative effects increase the backscatter



of the model beyond that of the lunar standards. This fact could complicate but not necessarily obscure the interpretation of an unusually high lunar backscatter if and when such anomalous areas are found on the moon. Additional color vs. phase angle measurements may be necessary in order to sort out the relative contribution of roughness and composite albedo effects.

- 4) The effect on the model of different scattering laws, may be observed in Figs. 35c and 36. By comparing these results, we observe no substantial improvement in the over-all backscatter or match with the lunar curve produced by changing the Lambert law to the Lommel-Seeliger law. We may conclude that complexity in structure and nonuniformity in albedo have greater influence on the photometric function than nongeometrical considerations such as the choice of a law of reflection. Our original assumption of Lambertian scattering as well as the relative importance we attached to geometry and albedo effects appear to have been justified, at least for the contrived models we investigated.
- 5) The local inflections observed in the analytical curves can be attributed to the fact that only one "unit structure" was considered in the analysis. Smoothing of the curves would occur if the number of these structures within the viewed area is increased. A study of the "roughness to viewed area" ratios is of more than just academic interest. Knowledge of the effect on the photometric curve of roughness ratios could be useful in interpreting the detailed photometry of distinct areas of the lunar surface (if and when such data becomes available), in terms of topographical irregularities that are not visible through a telescope.
- 6) The addition of lips to the basic T-model makes this model less contrived than it might appear to be at first sight. It can easily be seen from Figs. 37a through d how we can progressively approach a vesicular structure which is quite realistic in terms of genetic process operating in the lunar environment, and the condition of the lunar surface conveyed by Luna 9 close-up photographs. The configuration of Fig. 37c lends itself to an

estimate of porosity once the outlines of the primary pores surrounding the basic lipped-T are determined on the basis of additional analysis or actual experiments. Analytical methods would probably be less laborious, but first, it will be necessary to derive a basic scattering law for spherical cavities. Such laws have been derived for spherical, convex surfaces but we do not know of similar work done on the concave surfaces which appear to predominate in a lunar model. If we consider the possibility that cellular cavities might be the most realistic building blocks of a lunar surface model, then a rigorous study of their reflection and emission properties may well be justified.

- 7) Contrary to our expectation, none of the modifications that we have introduced into the basic T-model had a noticeable effect in improving the backscatter in the opposition region. This is probably due to shortcomings that are inherent in contrived models. Additional modifications of the type shown in Fig. 37d may be necessary to improve the backscatter at small phase angles. Based on the experiments reported in Phase I of this work, we suspect that the opposition effect is due not only to innumerable cavities but also to a wide distribution in the size of these cavities. We will recall that fine copper oxide powder when sprinkled on a flat board did not register as sharp an opposition effect as when it was sprinkled on rough foam. The distribution of cavity sizes probably peaks in the millimeter to centimeter range of the spectrum. Current thinking favors a predominance of micron size particles to account for the lunar polarimetric data. This point of view is based on theoretically valid optical considerations which may not be necessarily unique or bear great influence on polarization phenomena. Be that as it may, the unusual surge of the brightness at full moon and more particularly before an eclipse suggests that smaller cavities which occur frequently have a much higher

depth to diameter ratio than the larger cavities which are less abundant (see Fig. 37). This effect is quite difficult to investigate but it does deserve some attention. As an important peculiarity of the photometry of the lunar surface, it could provide an additional clue to the microstructure, porosity and relative roughness of candidate lunar landing sites.

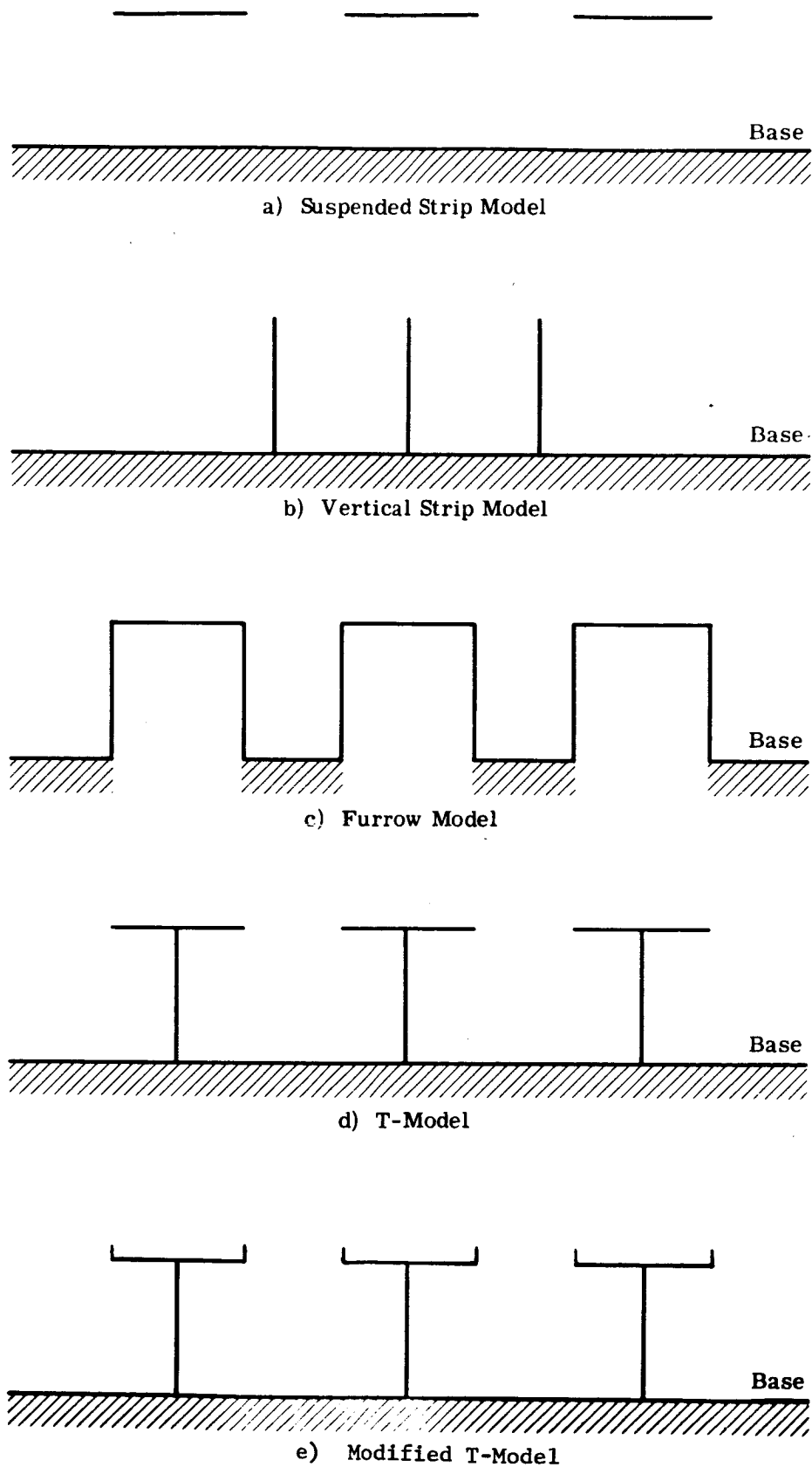


Fig. 29 Geometry of Five Contrived Photometric Models

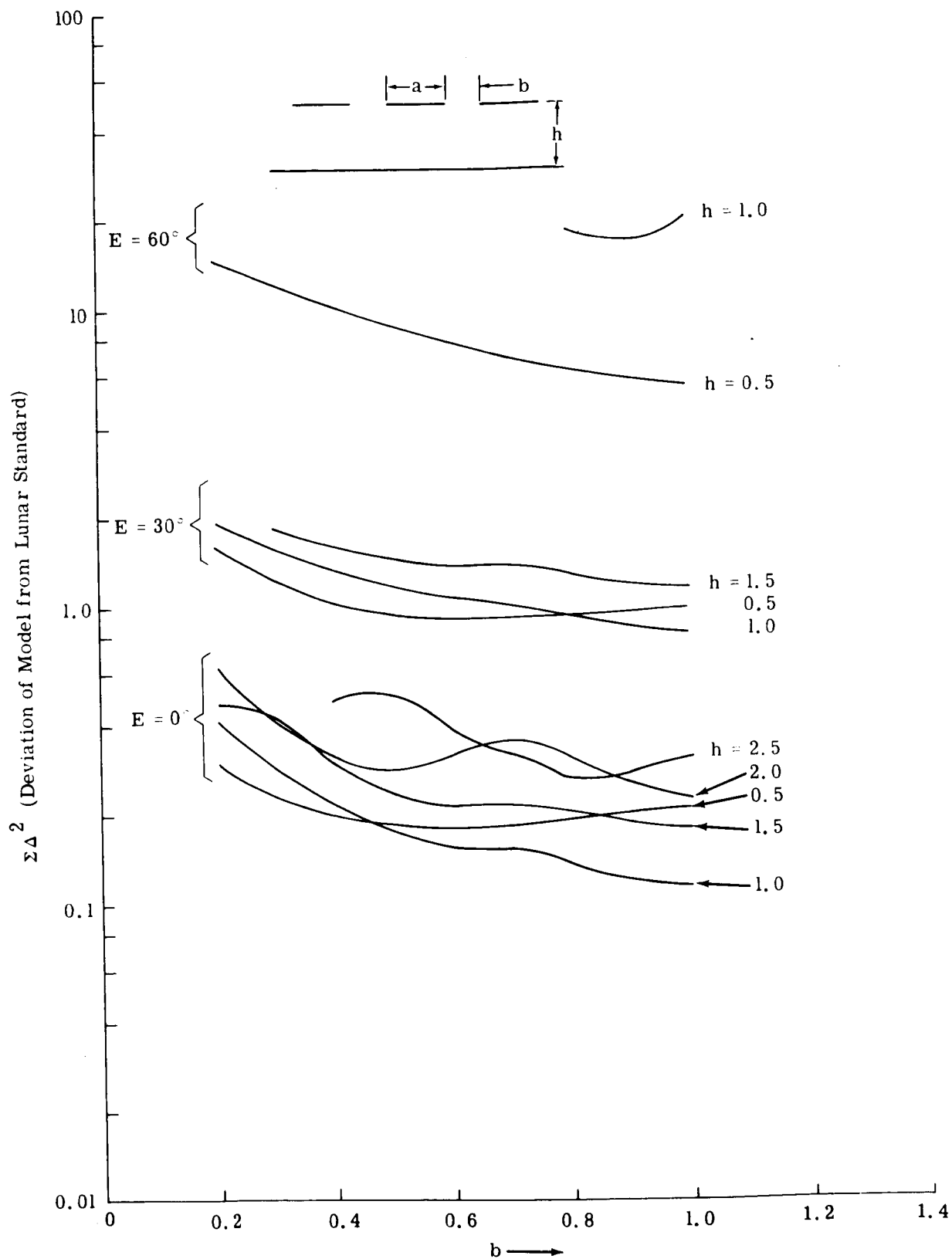


Fig. 30a Extent of Moon - Model Photometric Deviations - Suspended Strip Model (Lambert Scattering)

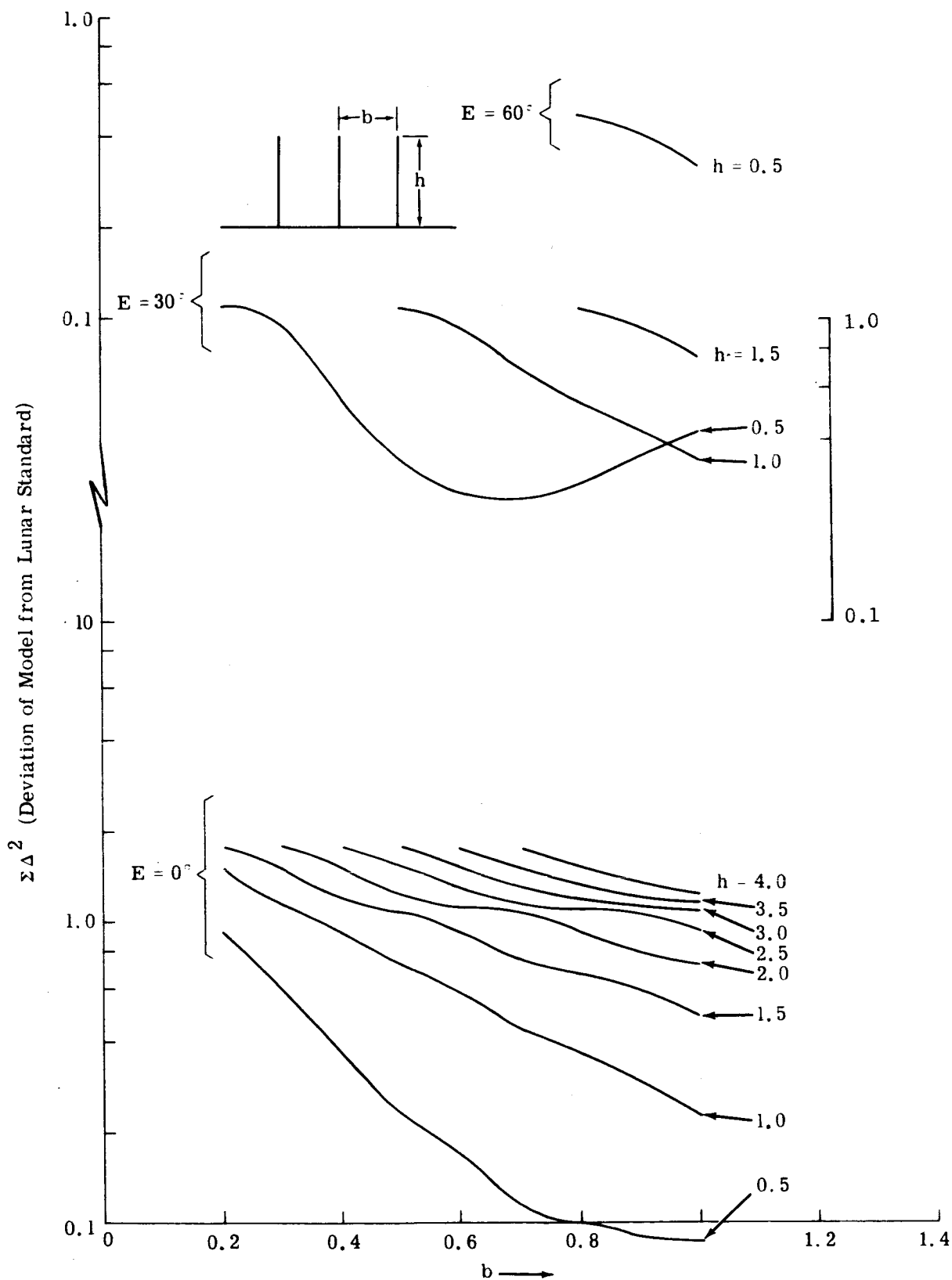


Fig. 30b Extent of Moon - Model Photometric Deviations - Vertical Strip Model (Lambert Scattering)

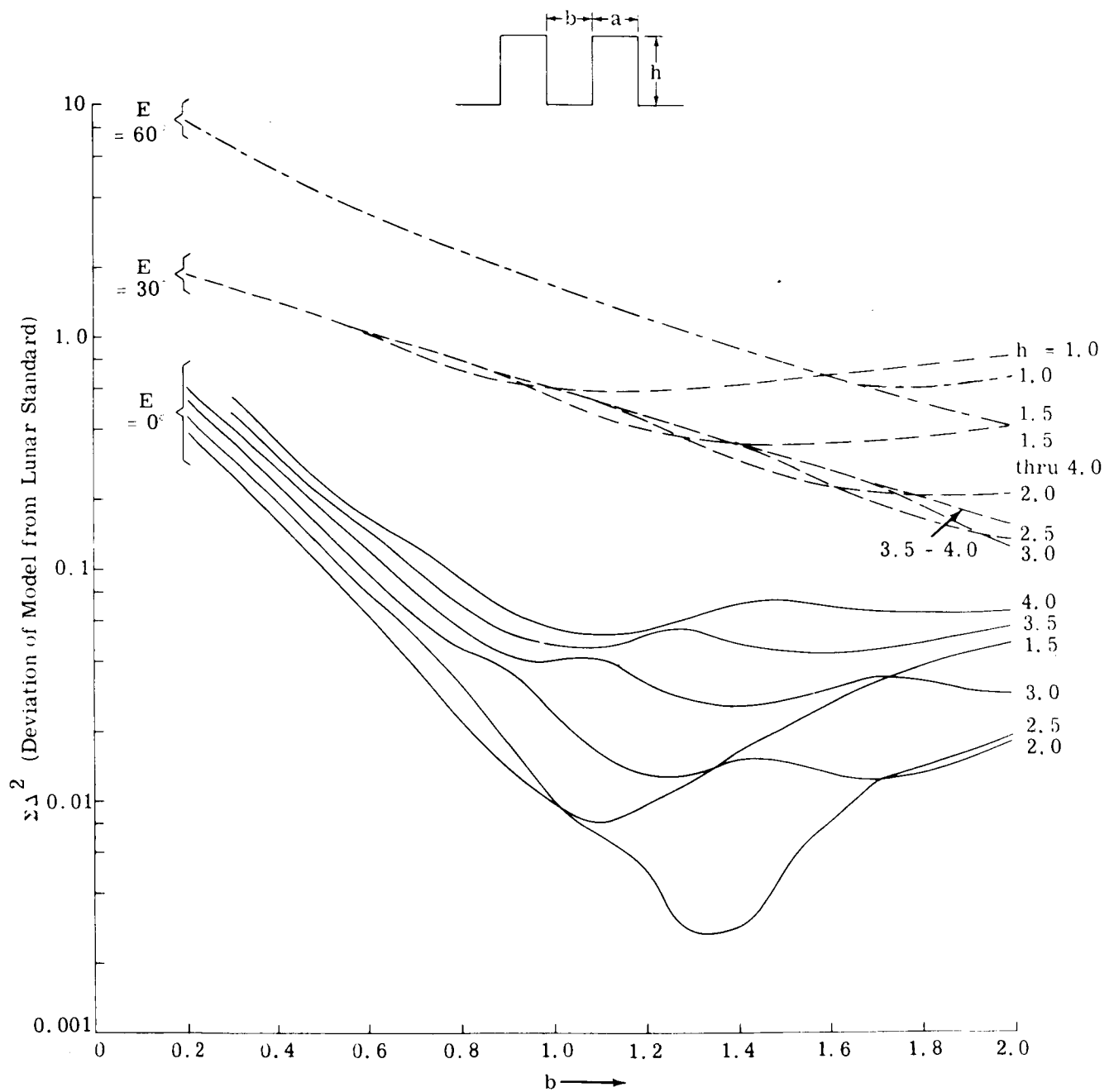


Fig. 30c Extent of Moon - Model Photometric Deviations -  
Furrow Model (Lambert Scattering)

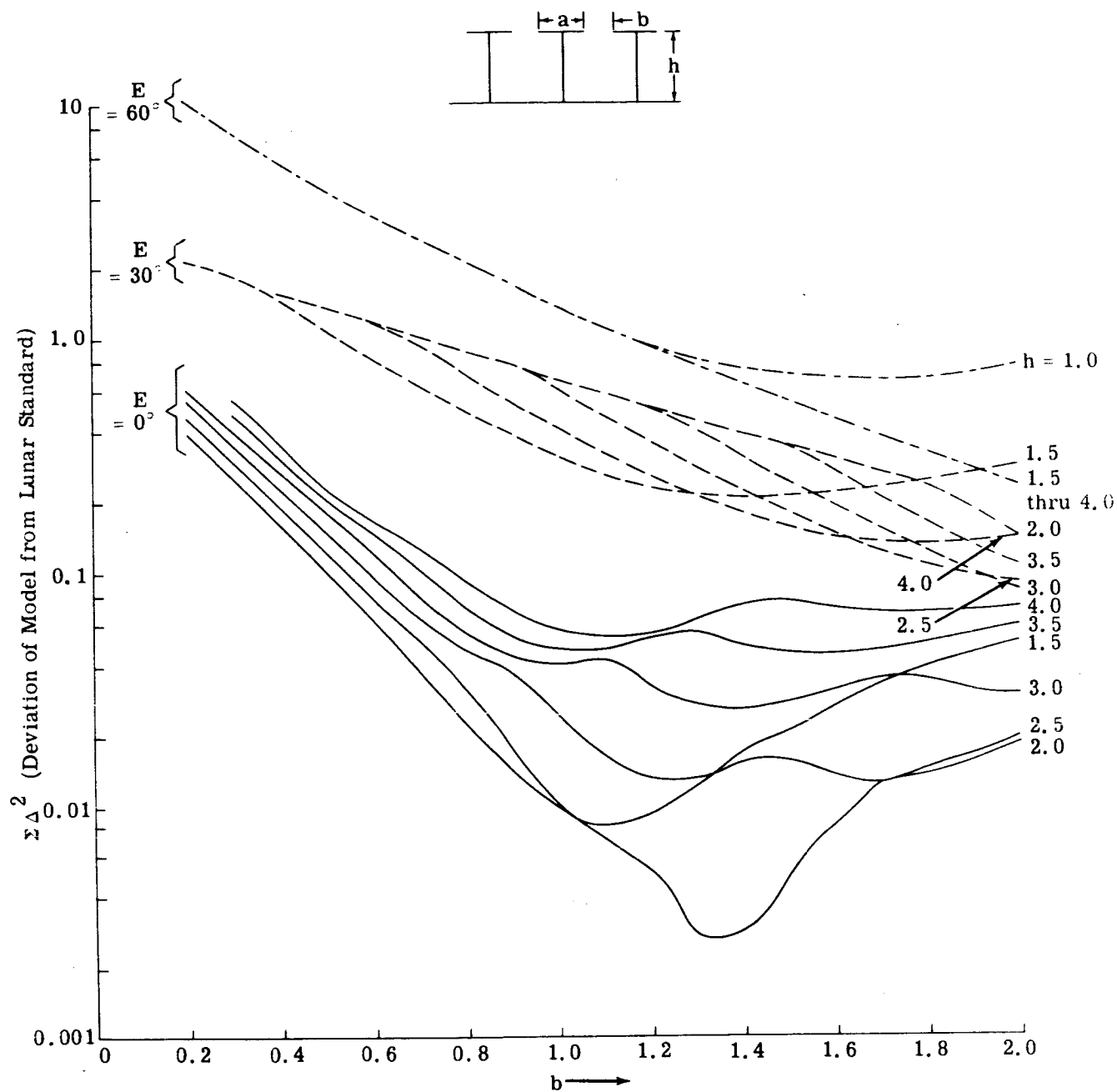


Fig. 30d Extent of Moon - Model Photometric Deviations -  
T-Model (Lambert Scattering)



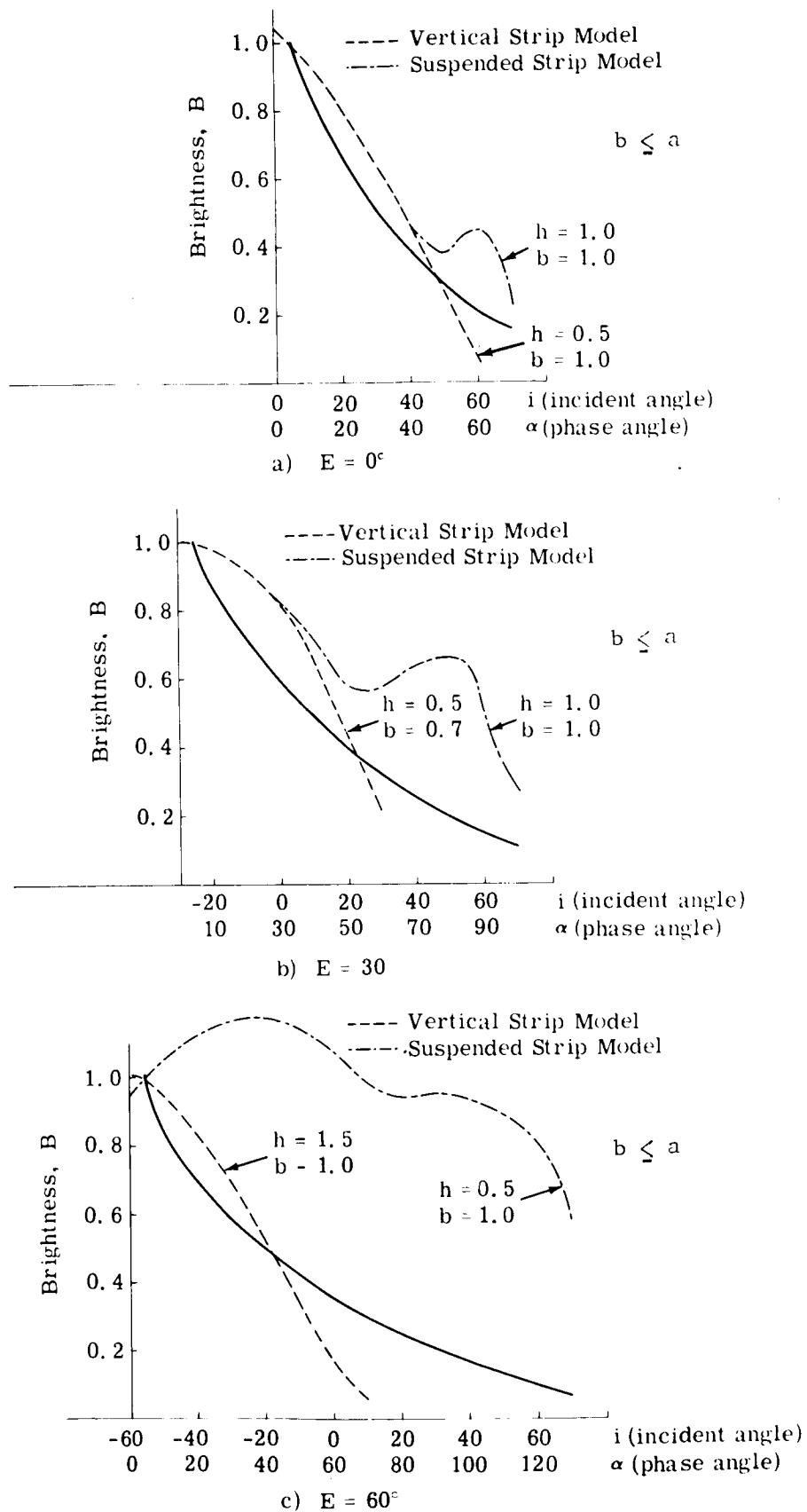


Fig. 31 Photometry of Basic Vertical and Suspended Strip Models (Lambert Scattering)

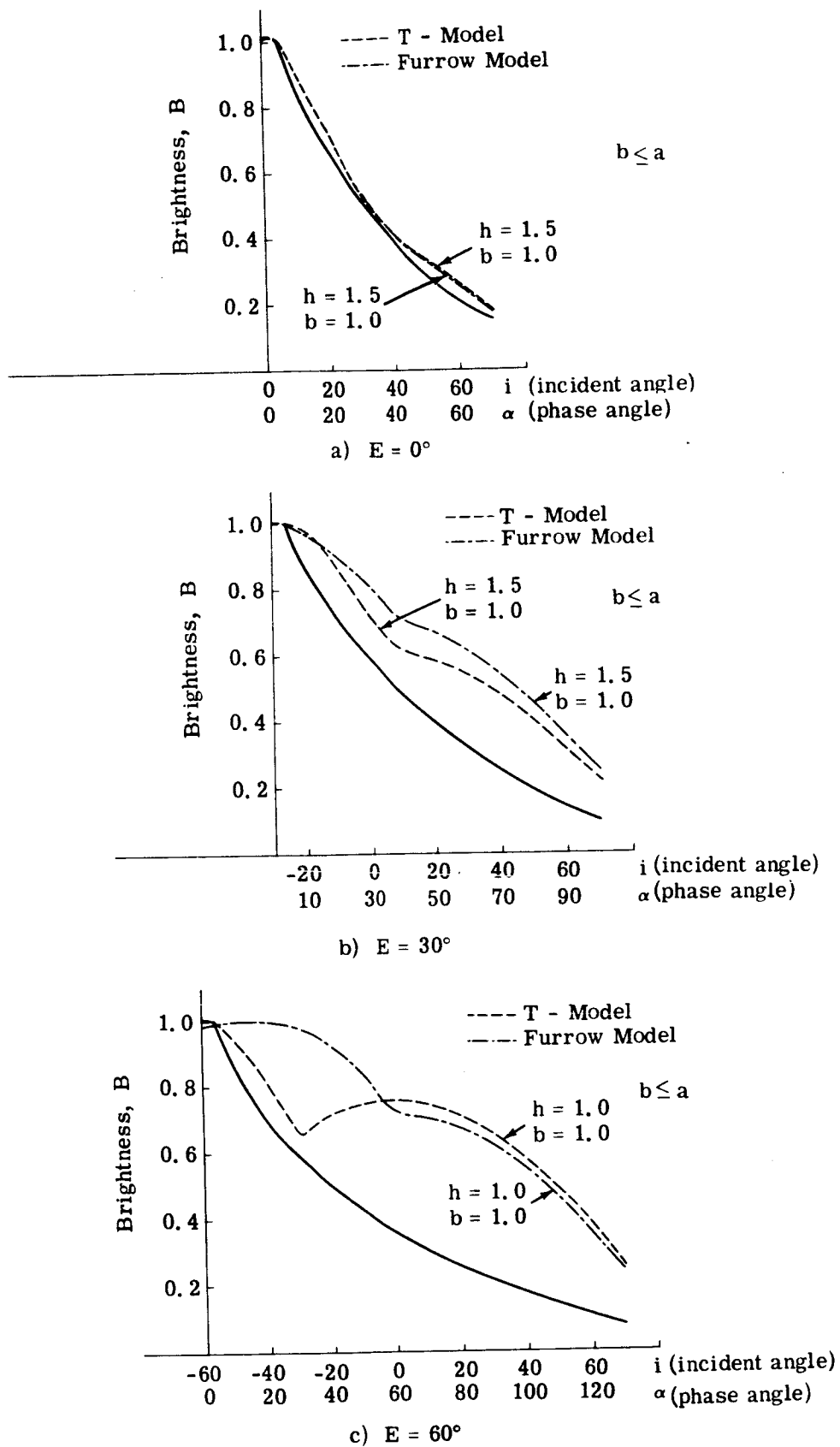
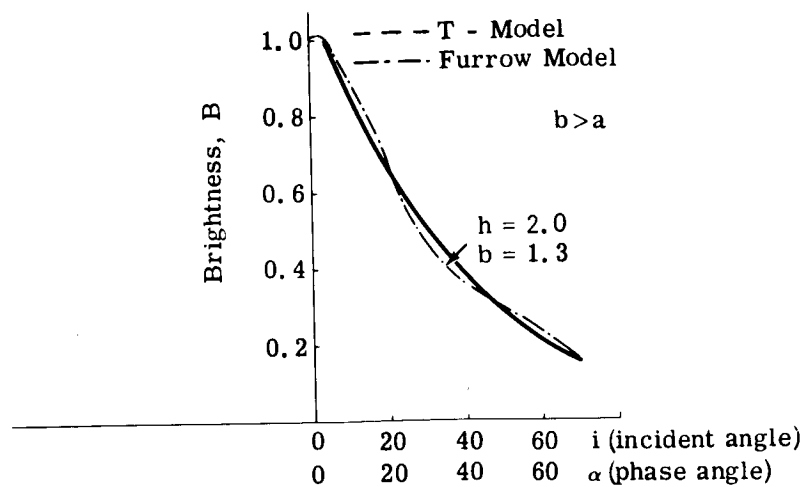
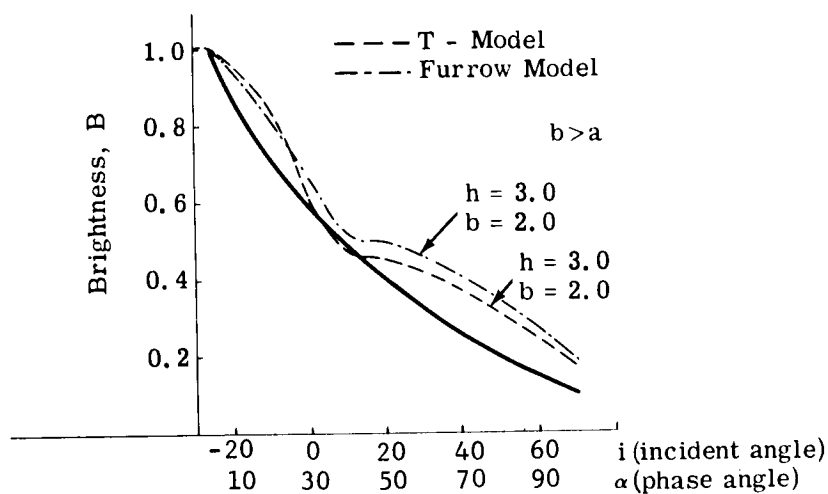


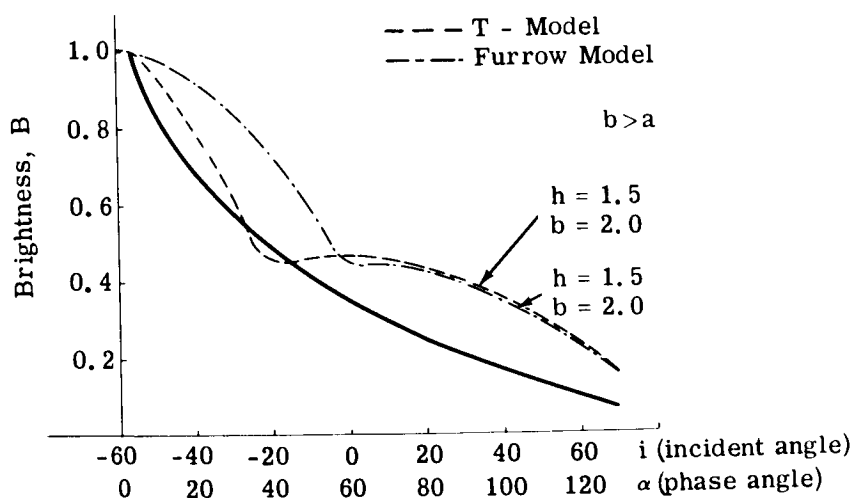
Fig. 32 Photometry of T and Furrow Models (Lambert Scattering)



a)  $E = 0^\circ$



b)  $E = 30^\circ$



c)  $E = 60^\circ$

Fig. 33 Photometry of T and Furrow Models (Lambert Scattering)

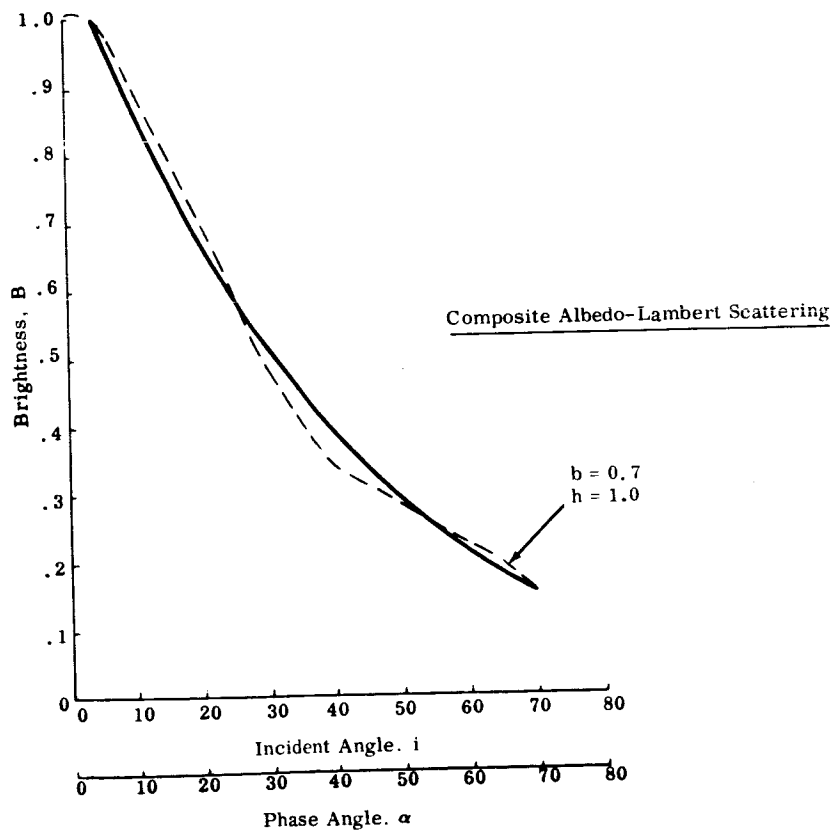
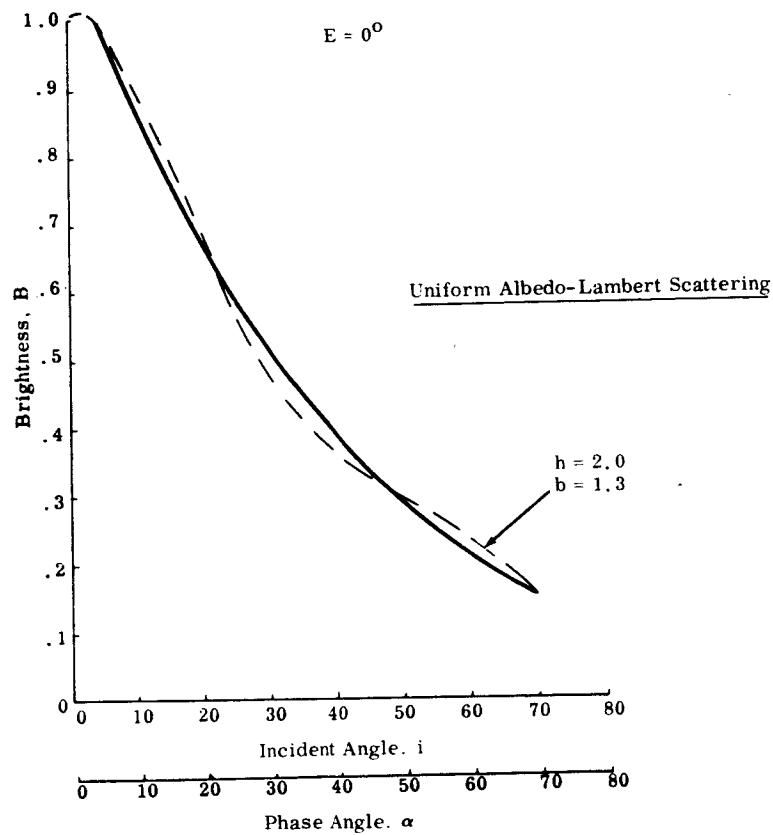


Fig. 34a Photometry of Furrow Model for Different Scattering Law and Albedo Conditions ( $E = 0^\circ$ )

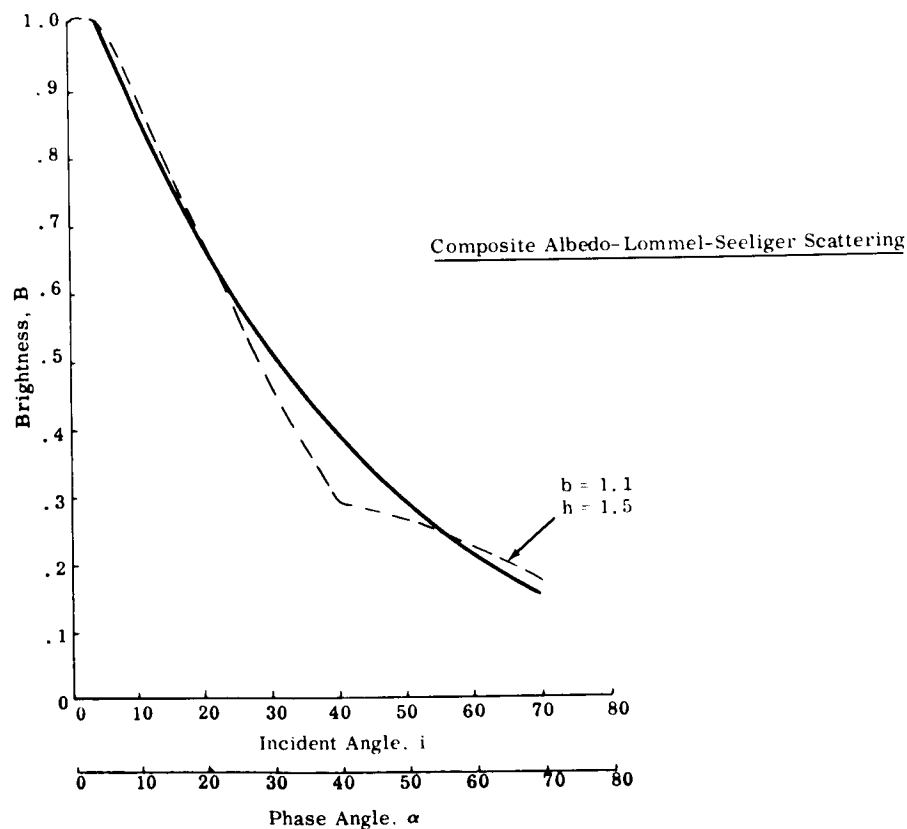
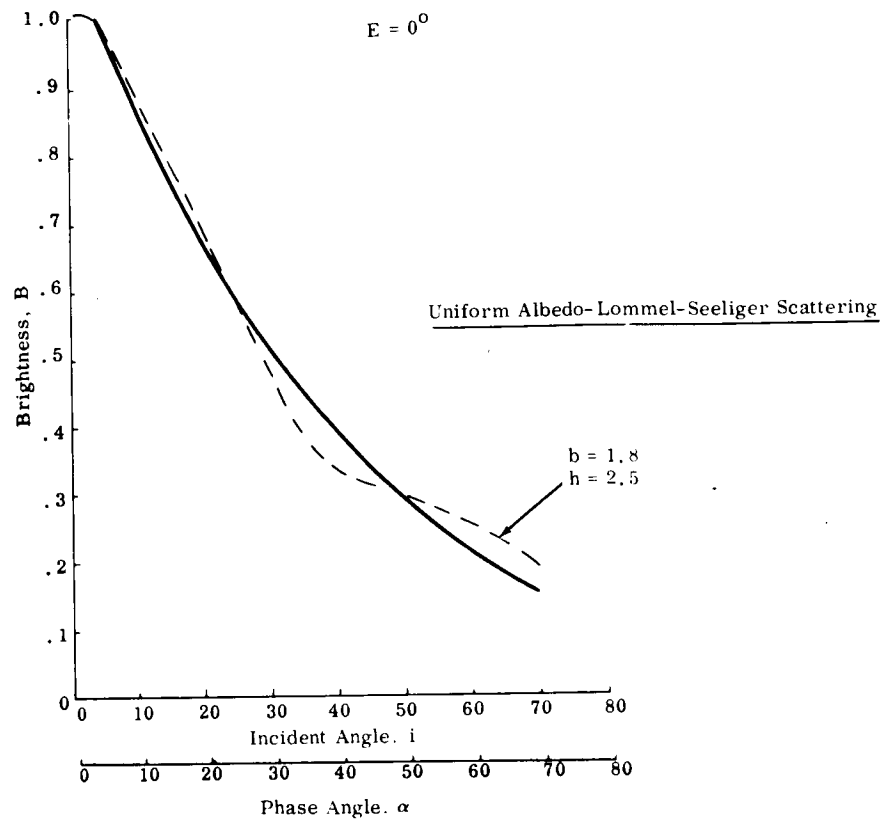


Fig. 34a (Cont) Photometry of Furrow Model for Different Scattering Law and Albedo Conditions ( $E = 0^\circ$ )

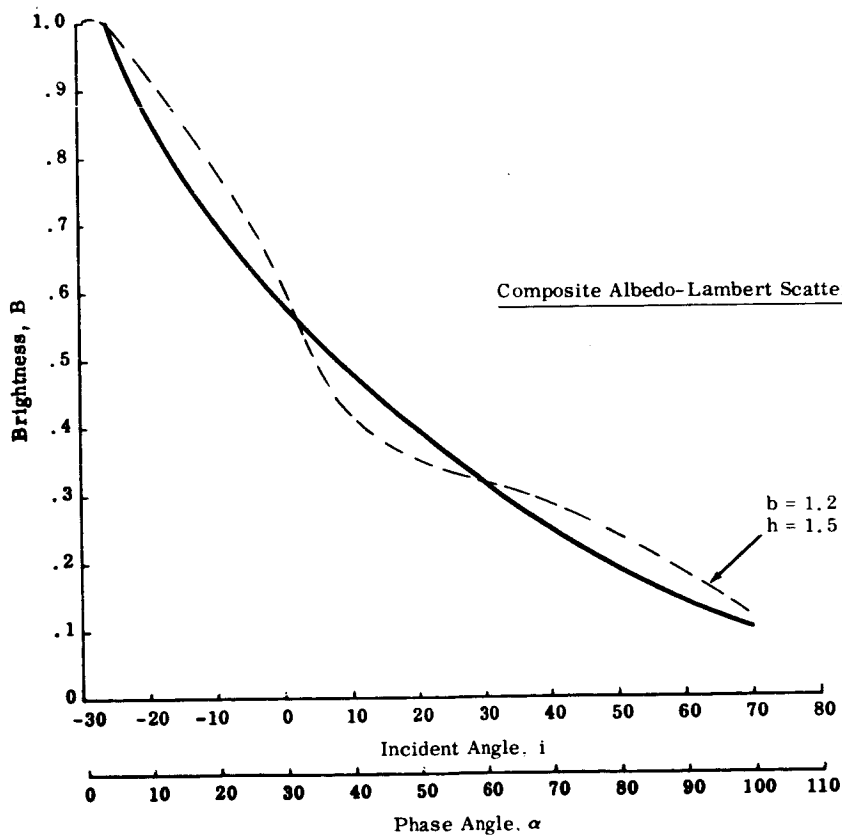
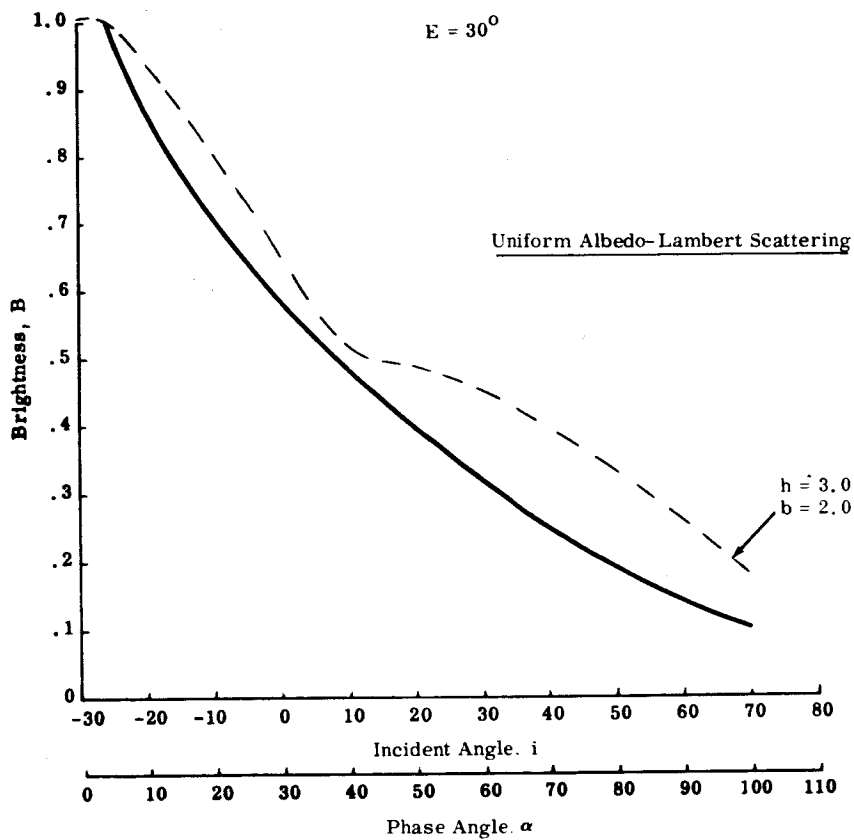


Fig. 34b Photometry of Furrow Model for Different Scattering Law and Albedo Conditions ( $E = 30^\circ$ )

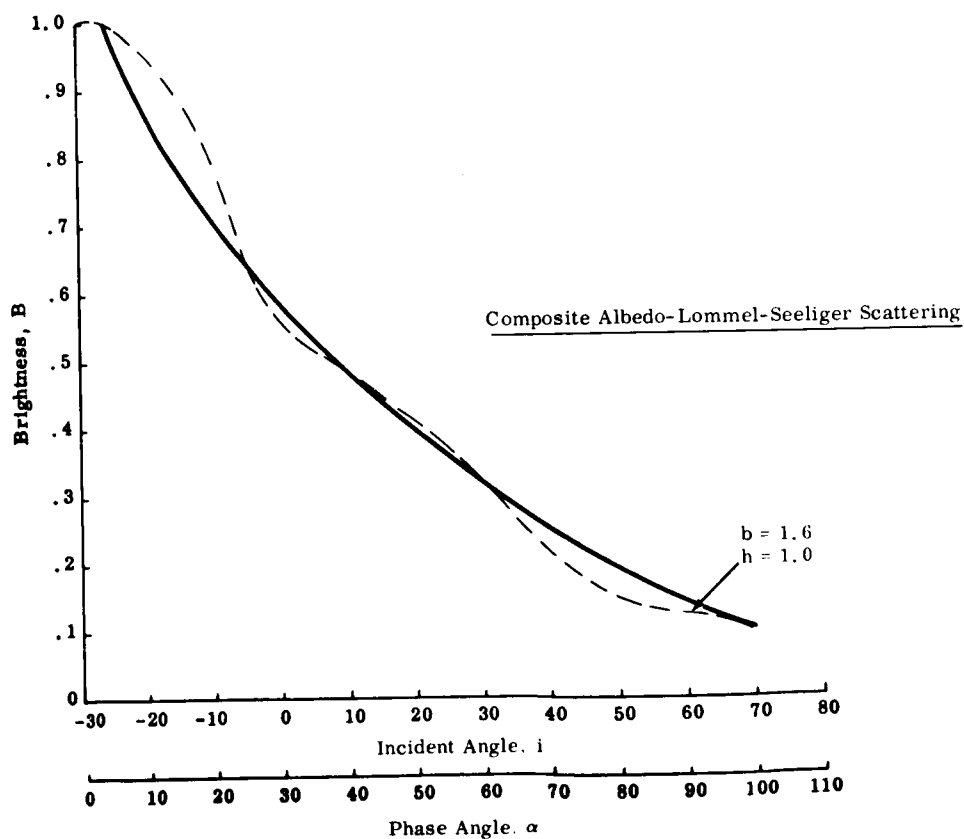
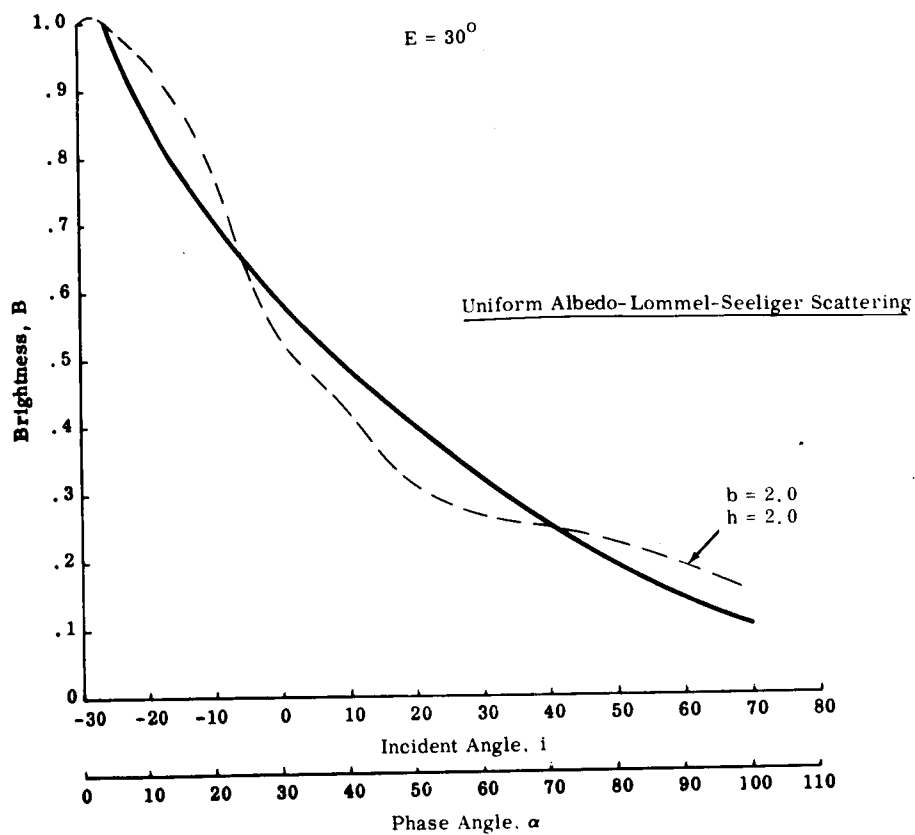


Fig. 34b (Cont) Photometry of Furrow Model for Different Scattering Law and Albedo Conditions ( $E = 30^\circ$ )

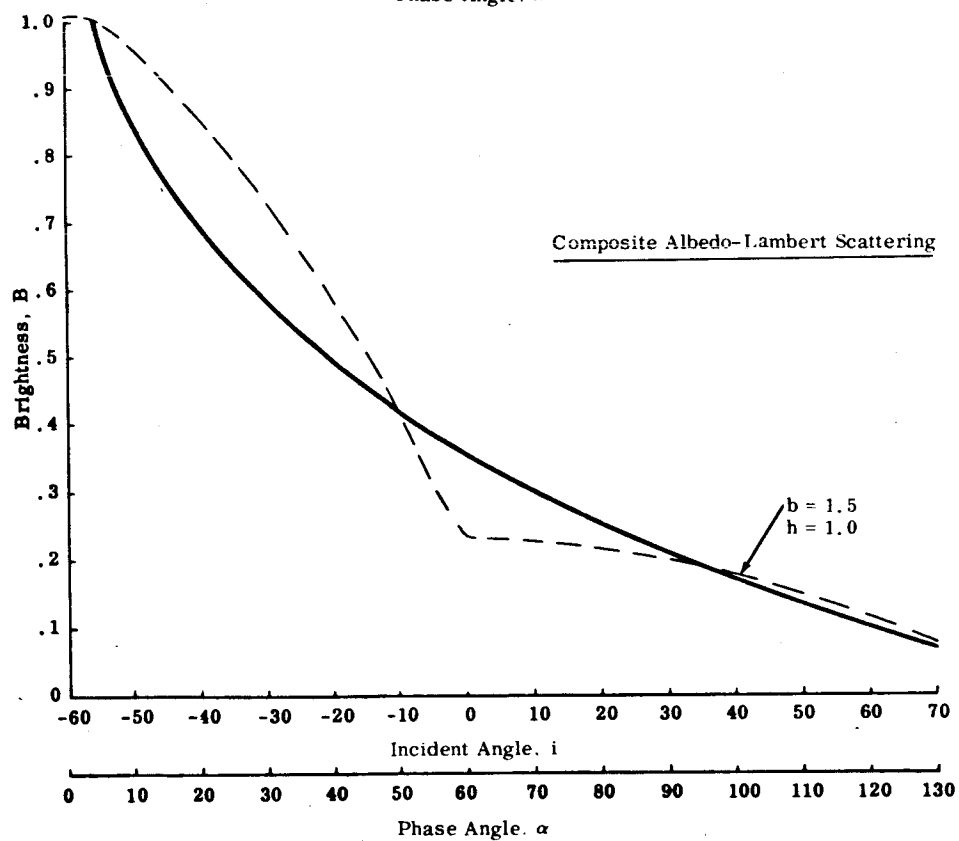
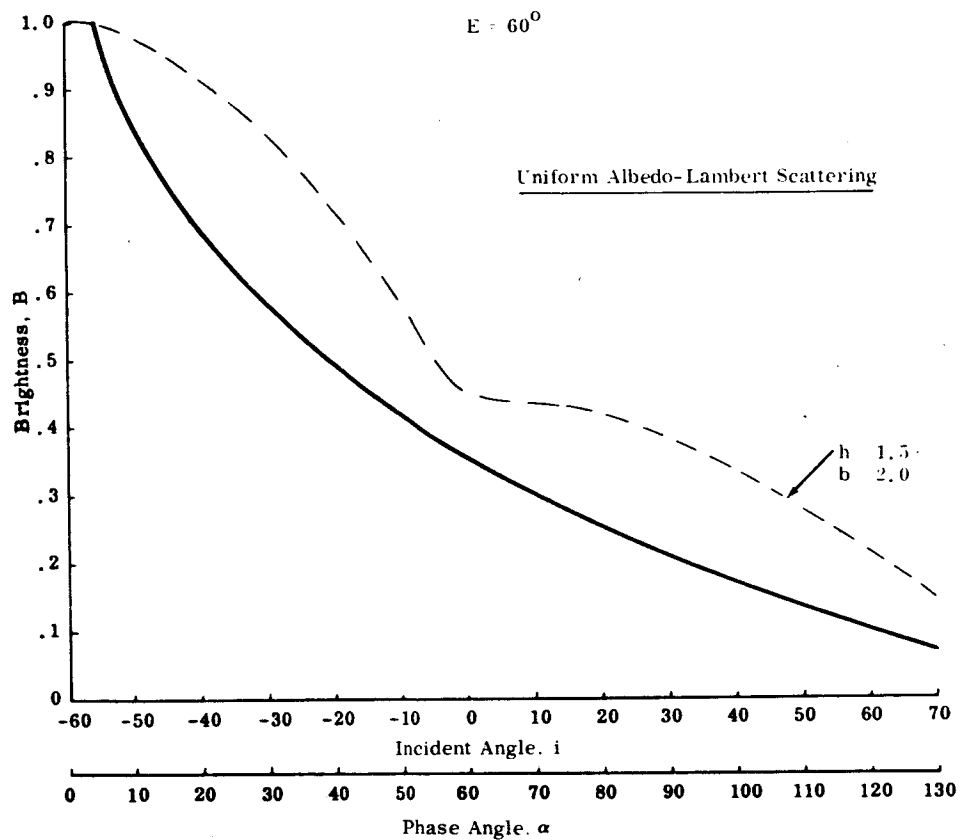


Fig. 34c Photometry of Furrow Model for Different Scattering Law and Albedo Conditions ( $E = 60^\circ$ )



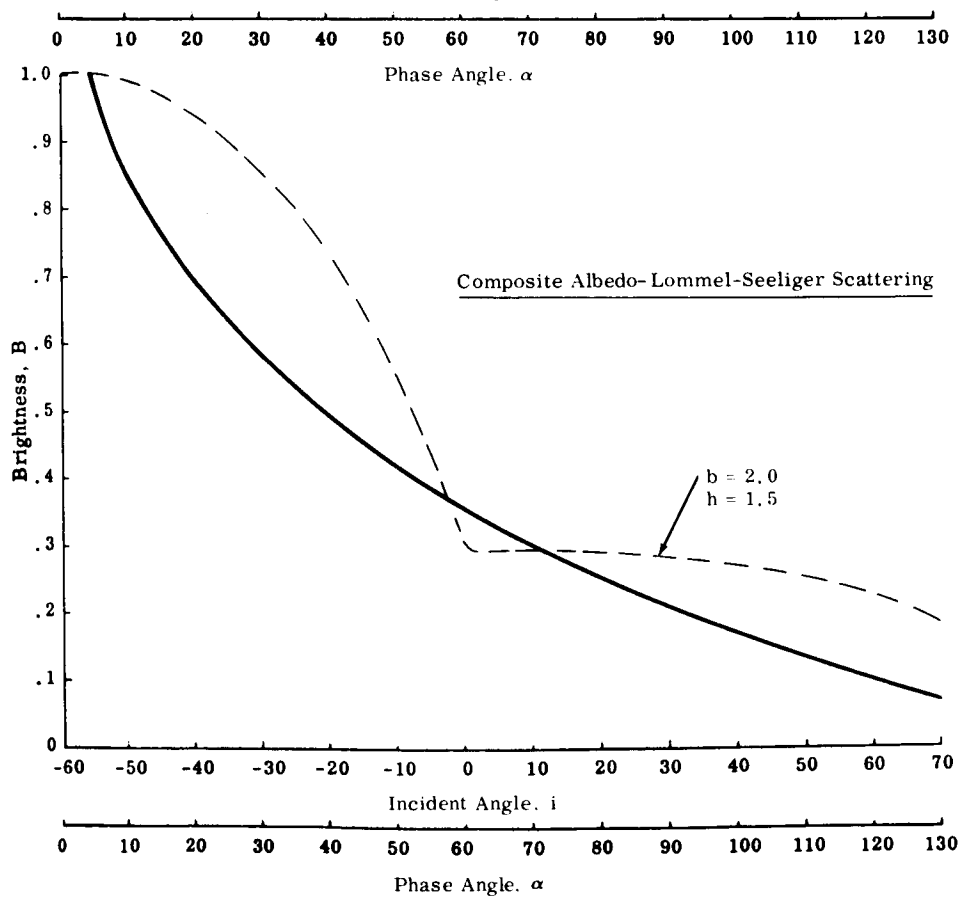
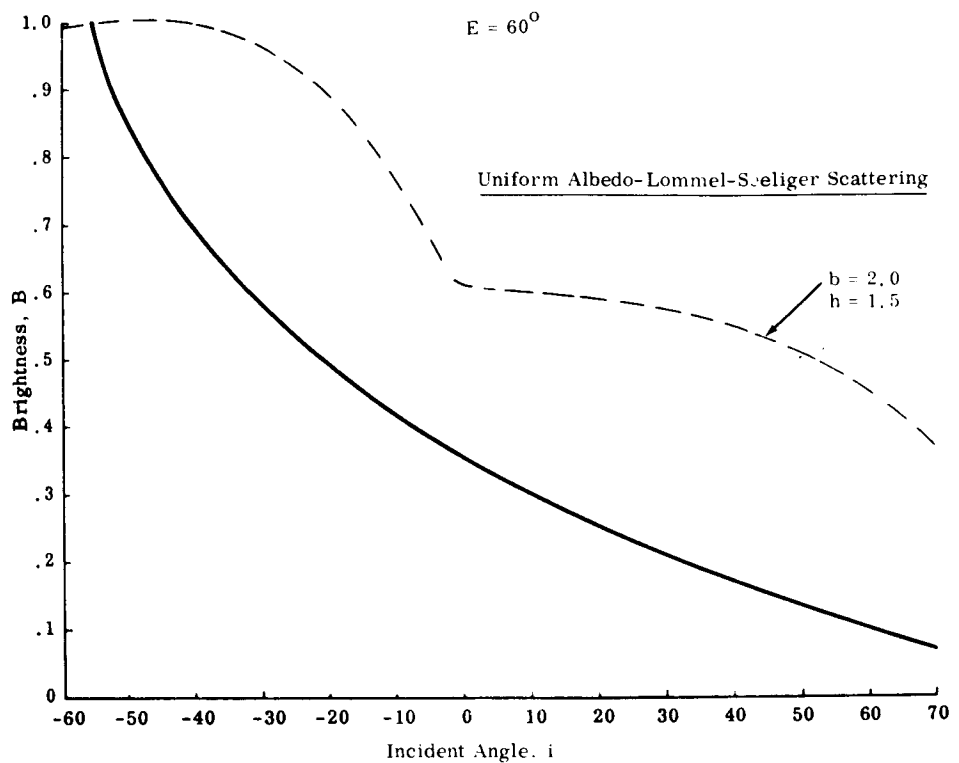


Fig. 34c (Cont) Photometry of Furrow Model for Different Scattering Law and Albedo Conditions ( $E = 60^\circ$ )

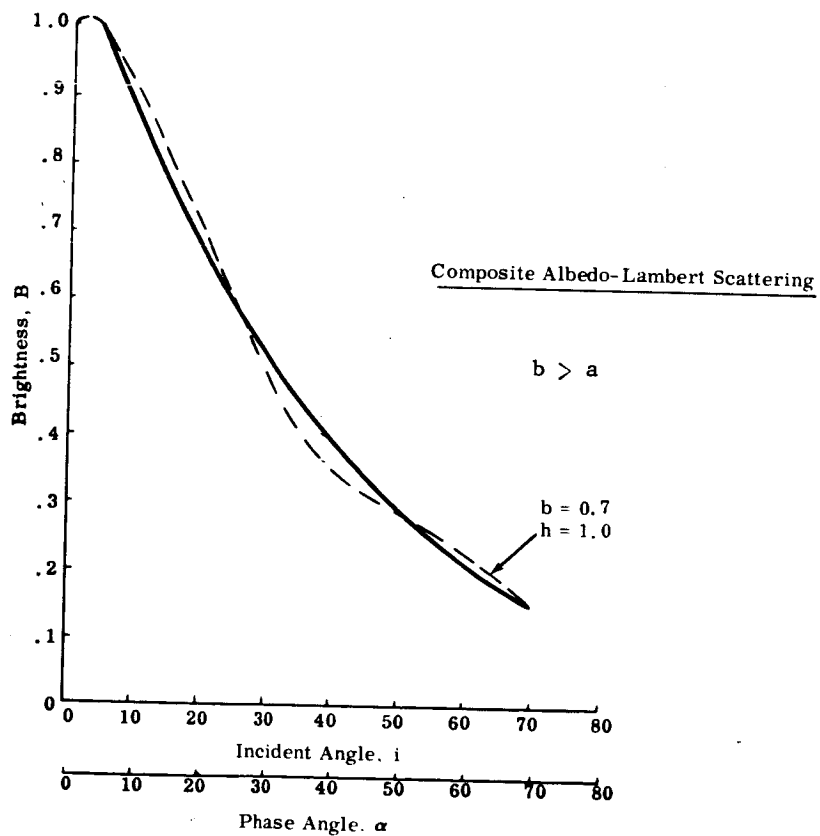
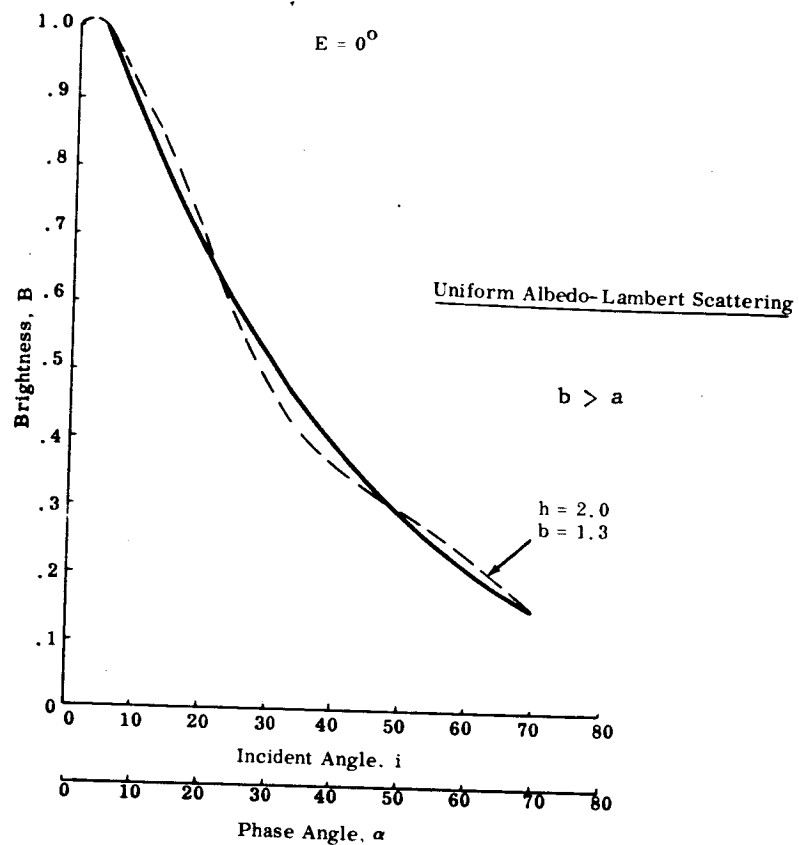


Fig. 35a Photometry of Basic T-Model for Different Scattering Law and Albedo Conditions ( $E = 0^\circ$ )

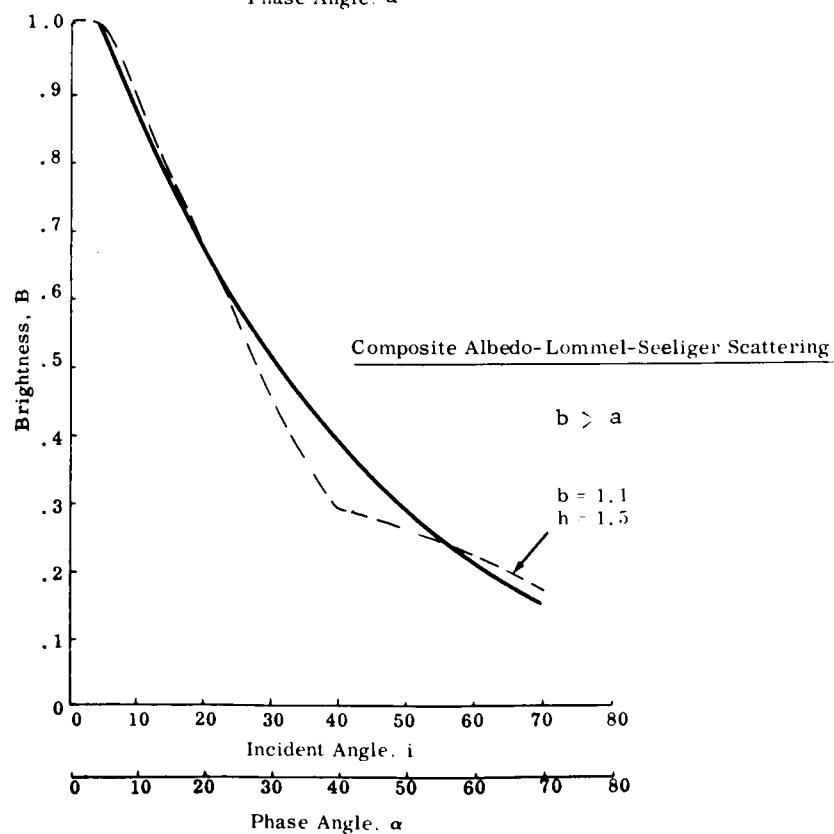
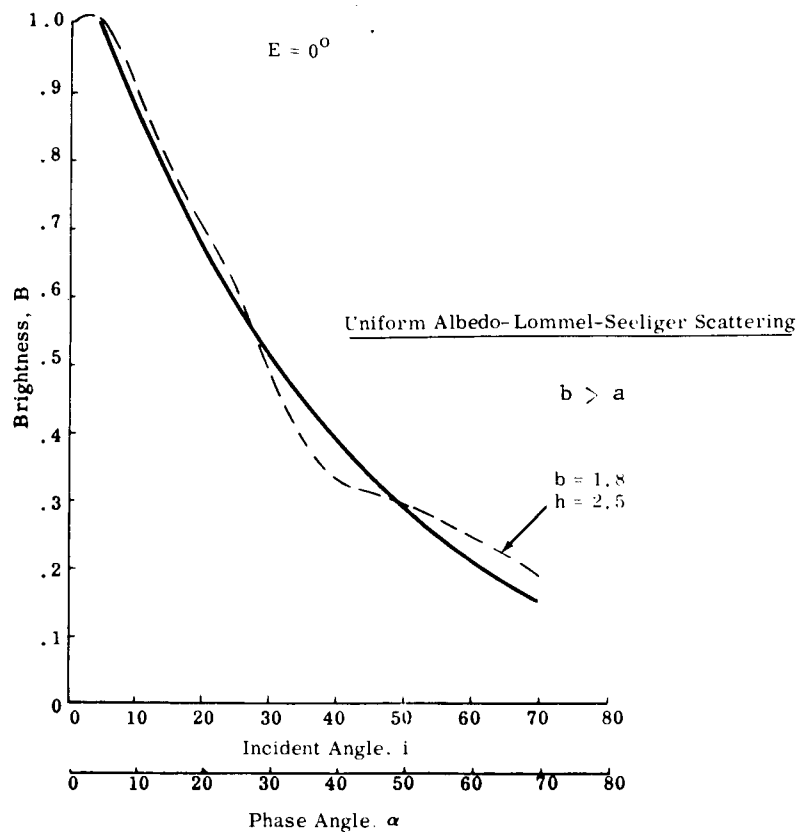


Fig. 35a (Cont) Photometry of Basic T-Model for Different Scattering Law and Albedo Conditions ( $E = 0^\circ$ )

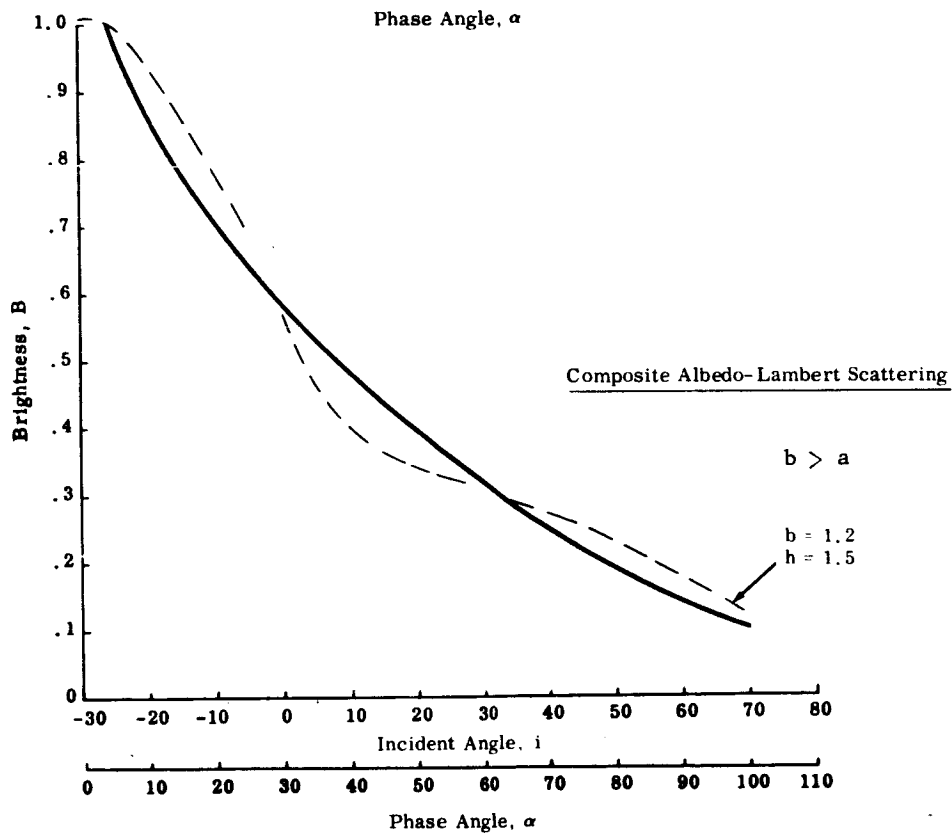
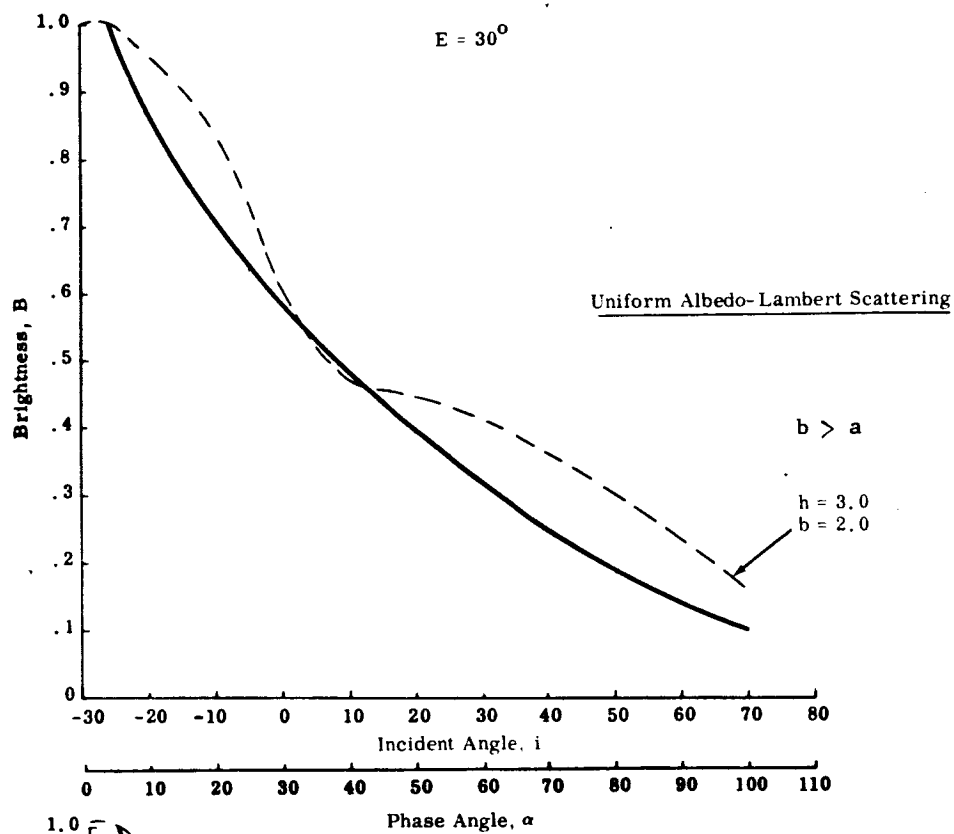


Fig. 35b Photometry of Basic T-Model for Different Scattering Law and Albedo Conditions ( $E = 30^\circ$ )

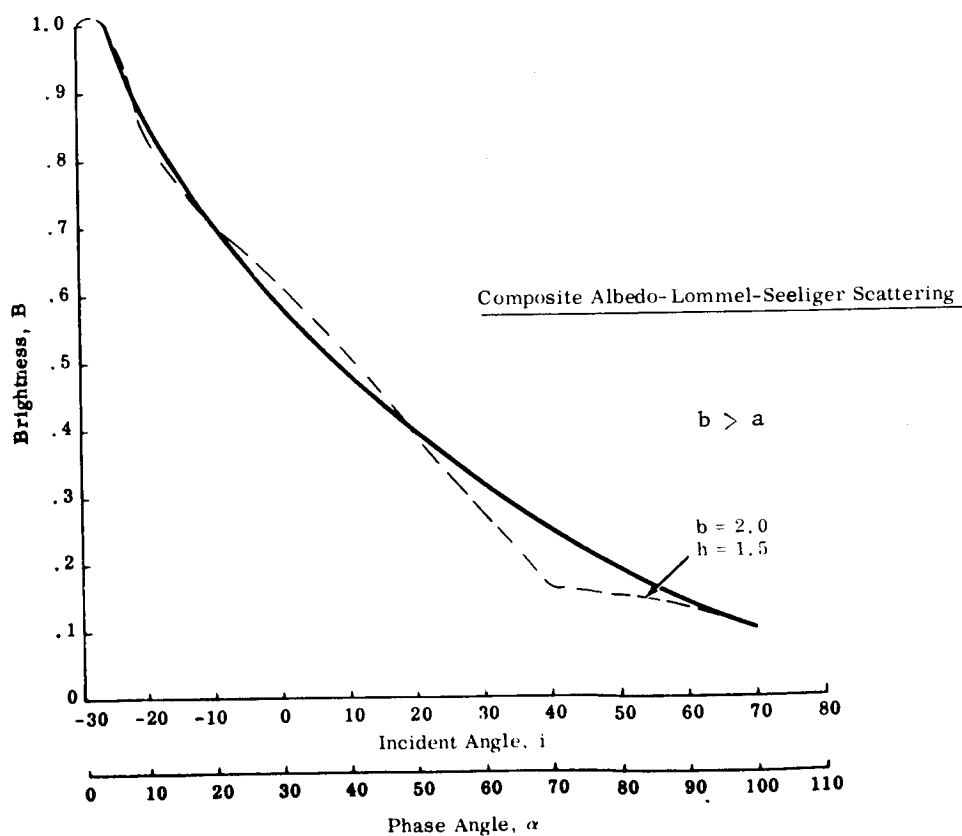
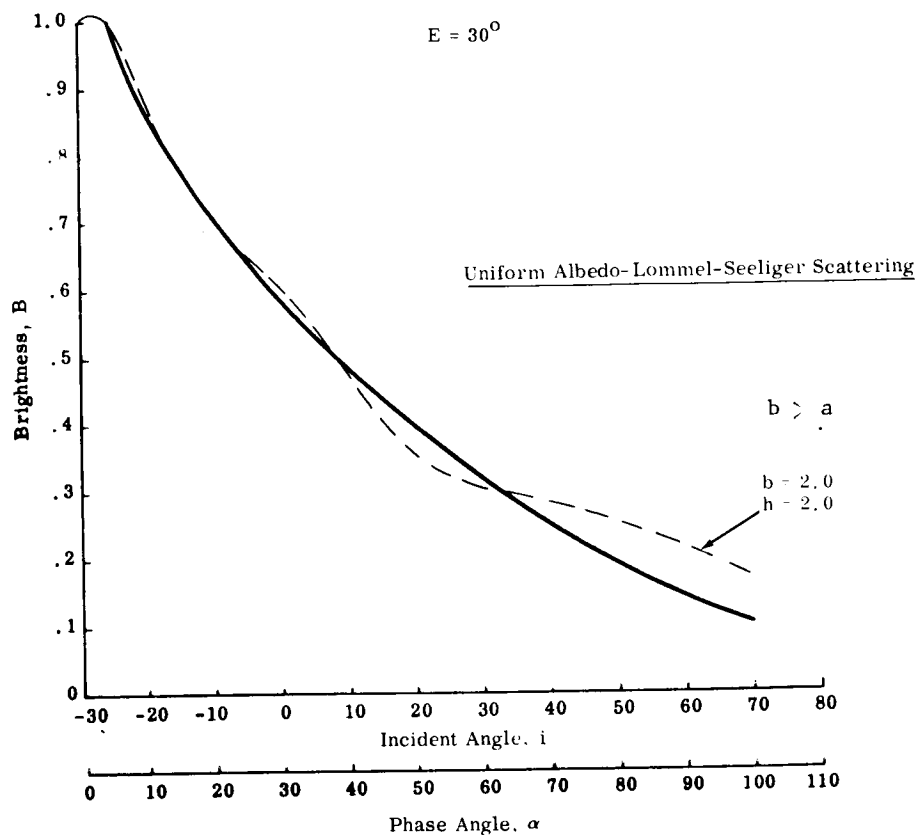


Fig. 35b (Cont) Photometry of Basic T-Model for Different Scattering Law and Albedo Conditions ( $E = 30^\circ$ )

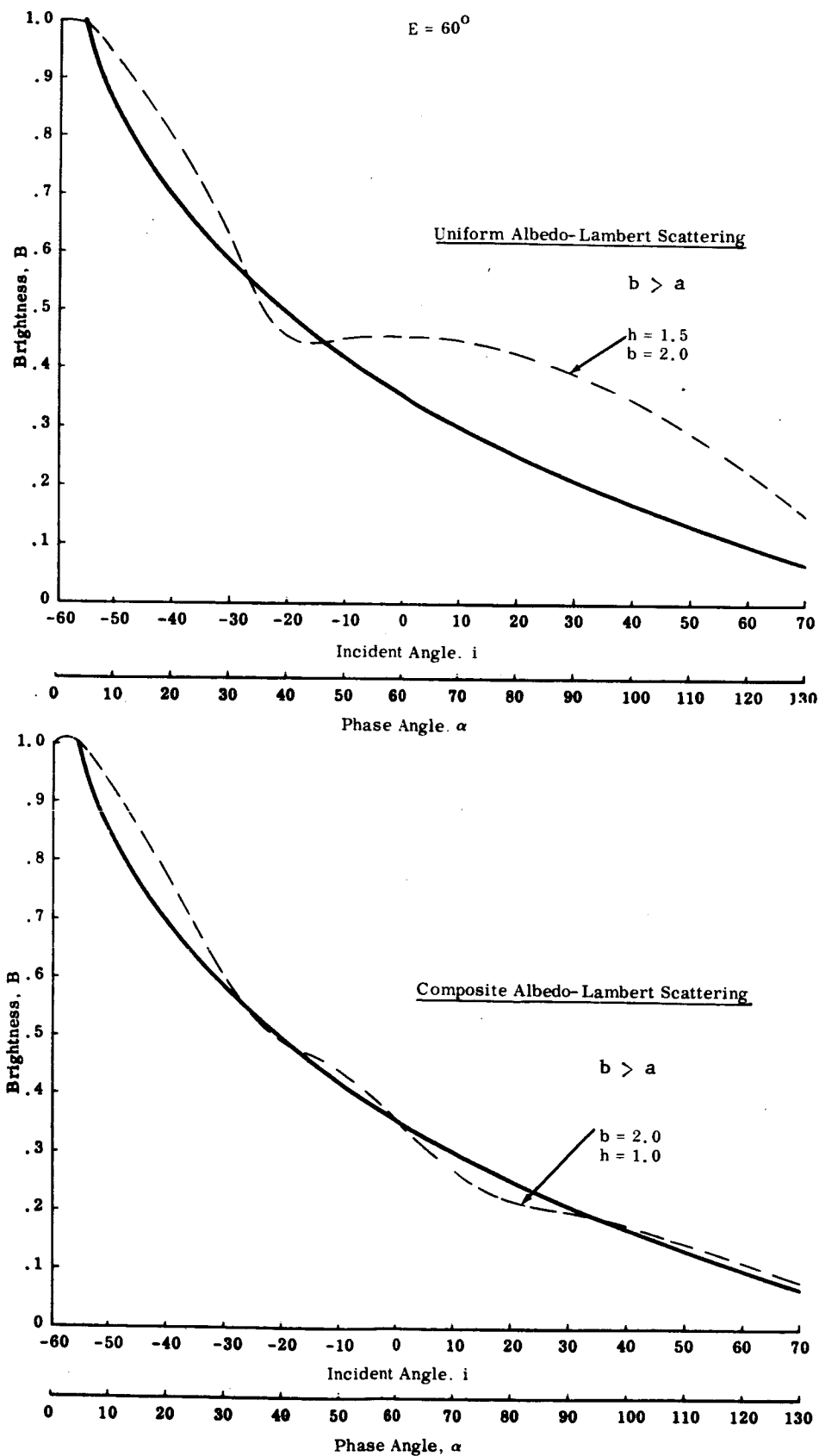


Fig. 35c Photometry of Basic T-Model for Different Scattering Law and Albedo Conditions ( $E = 60^\circ$ )

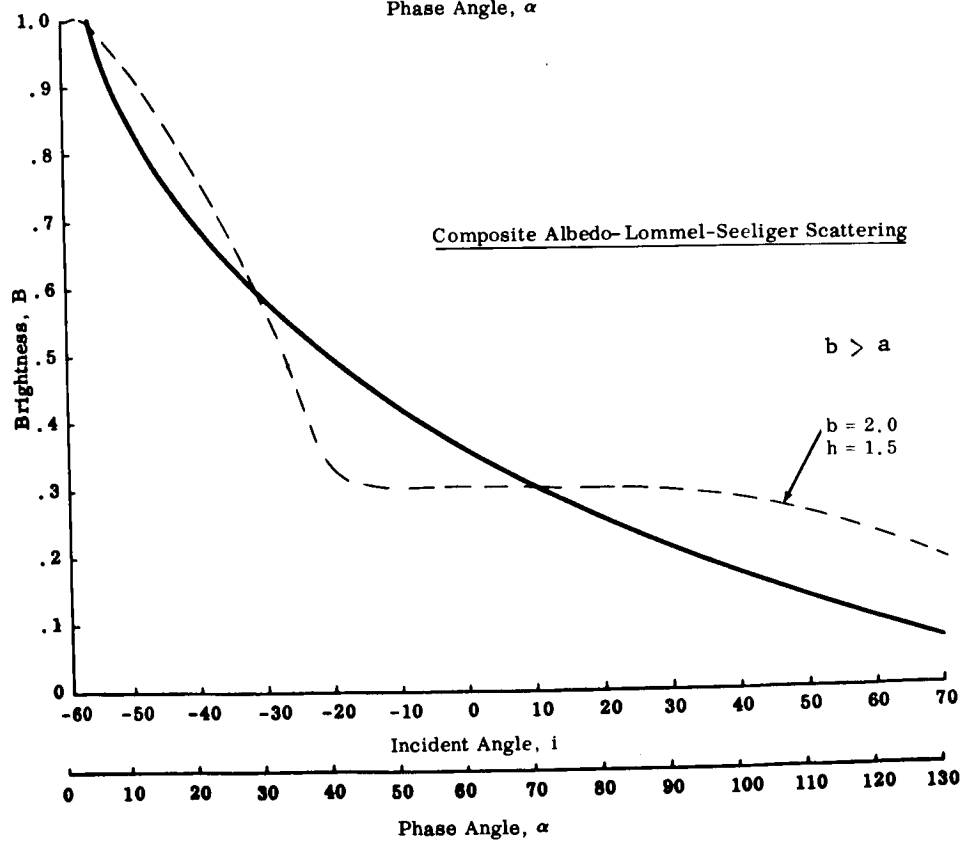
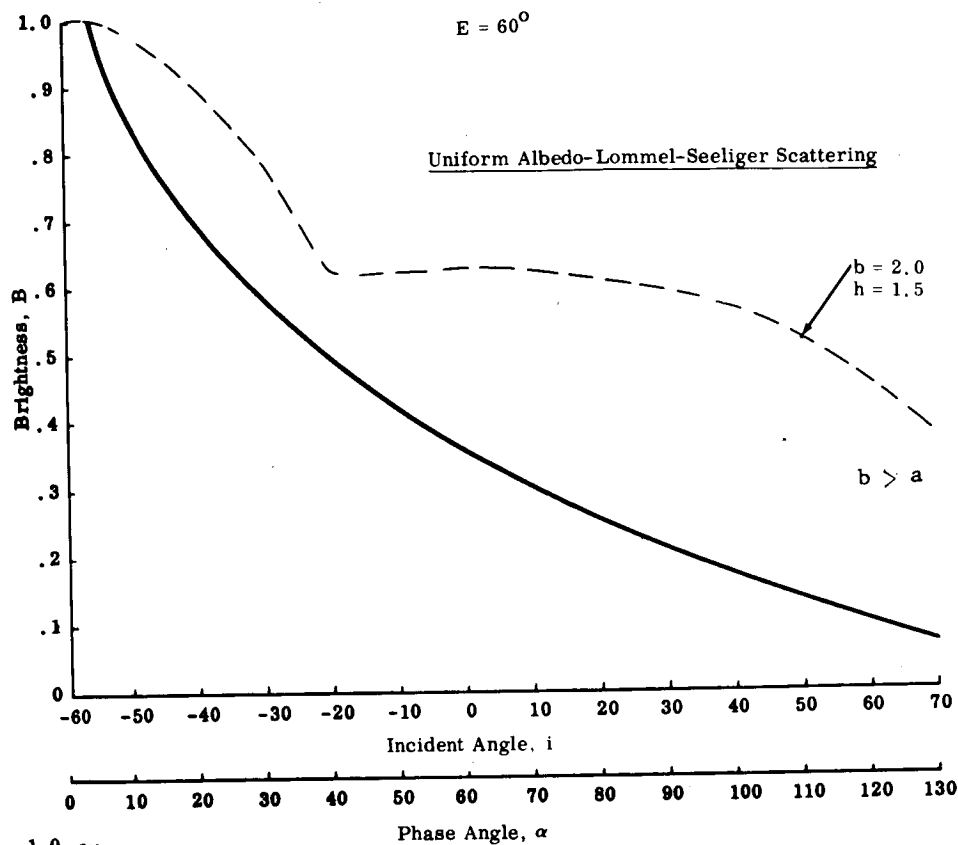


Fig. 35c (Cont) Photometry of Basic T-Model for Different Scattering Law and Albedo Conditions ( $E = 60^\circ$ )

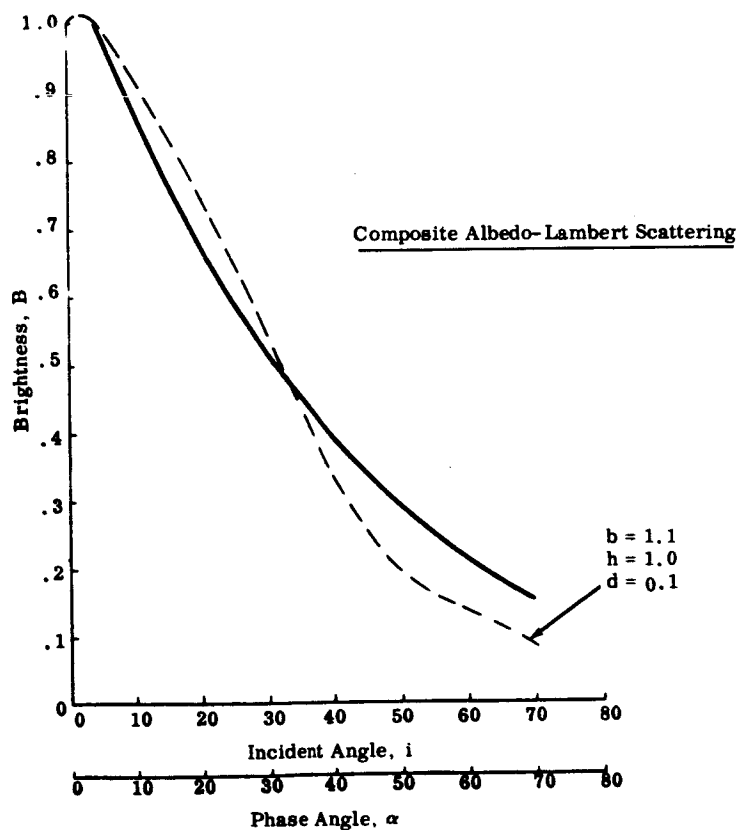
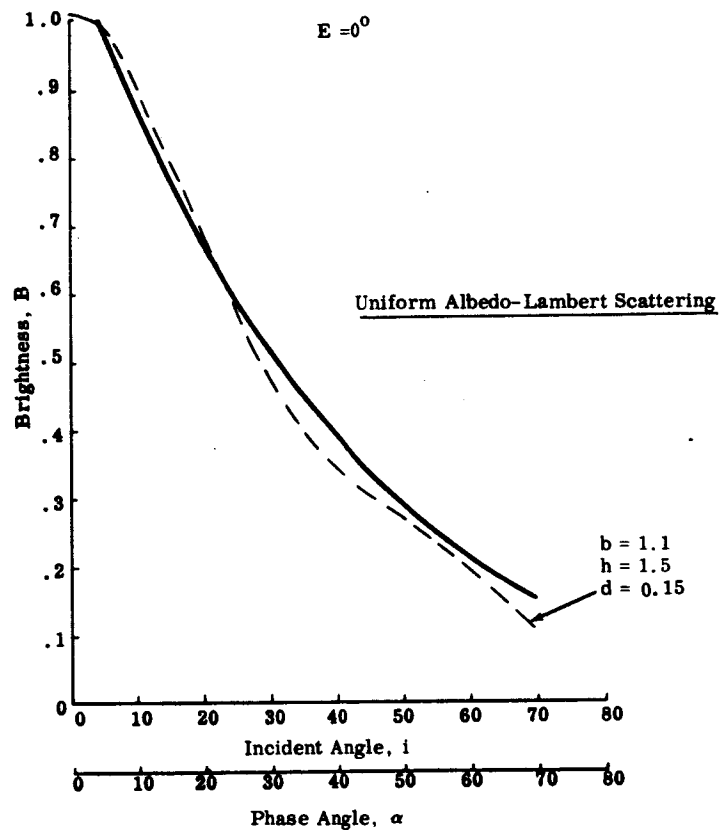


Fig. 36a Photometry of Modified T-Model for Different Scattering Law and Albedo Conditions ( $E = 0^\circ$ )



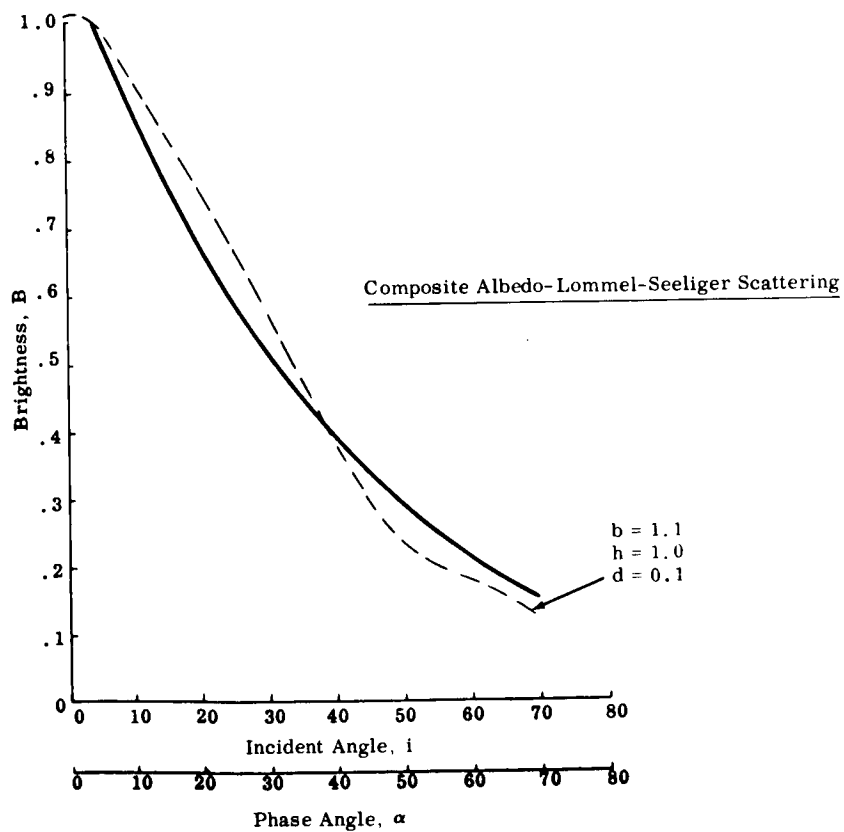
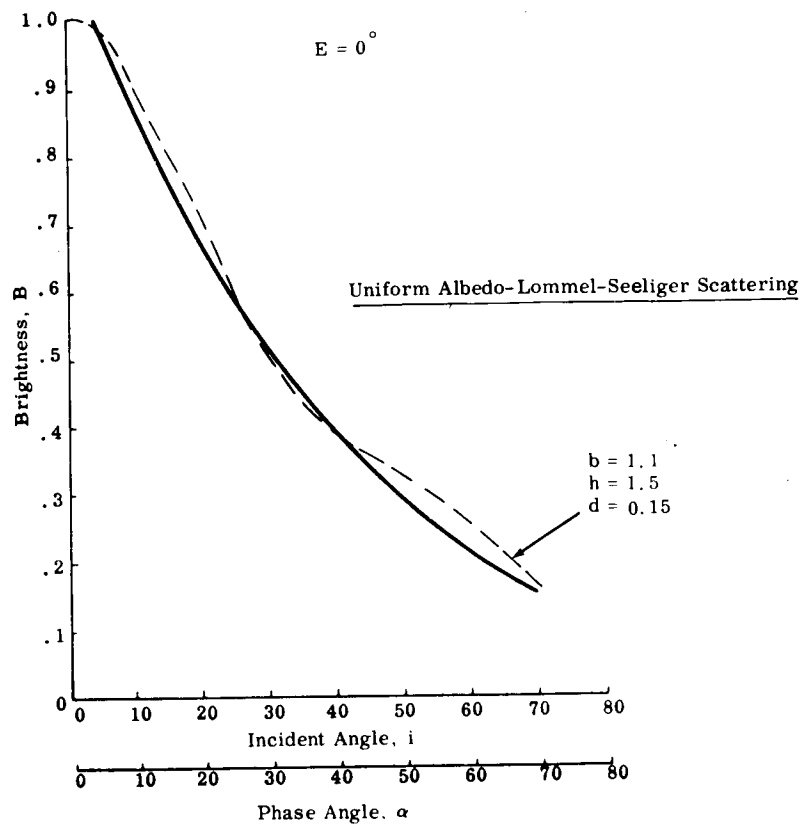


Fig. 36a (Cont) Photometry of Modified T-Model for Different Scattering Law and Albedo Conditions ( $E = 0^\circ$ )

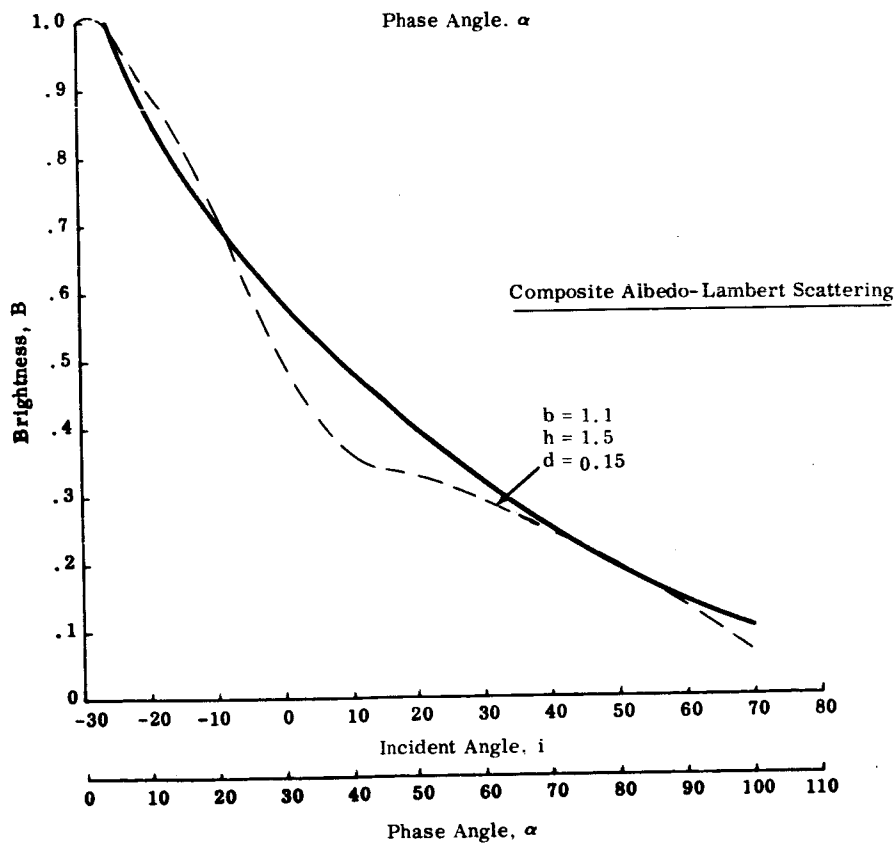
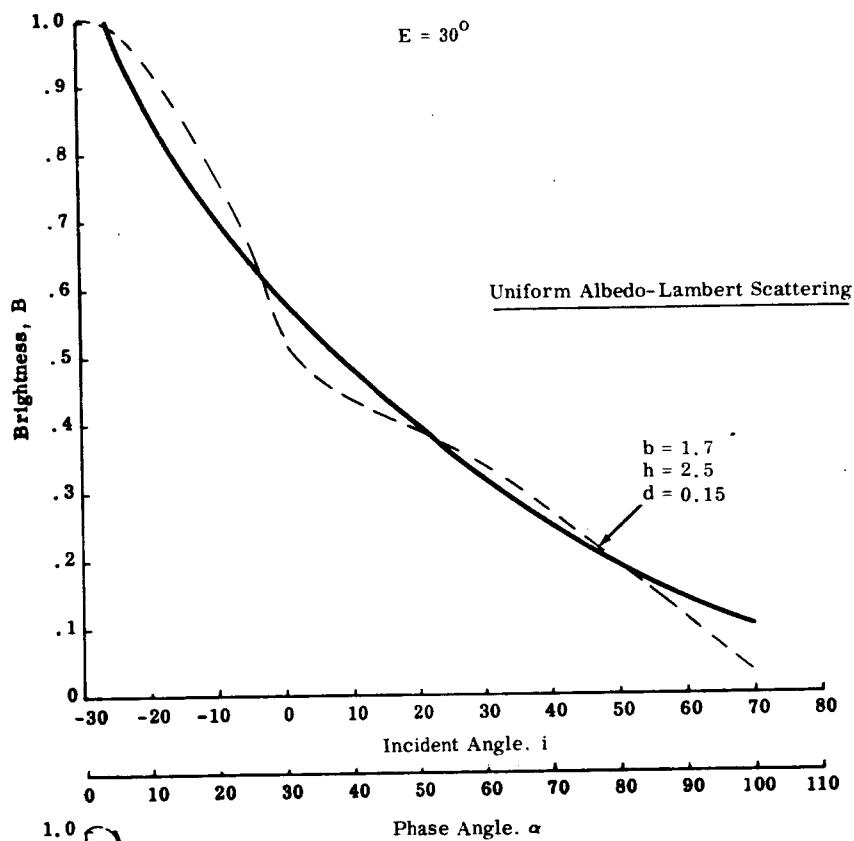


Fig. 36b Photometry of Modified T-Model for Different Scattering Law and Albedo Conditions ( $E = 30^\circ$ )

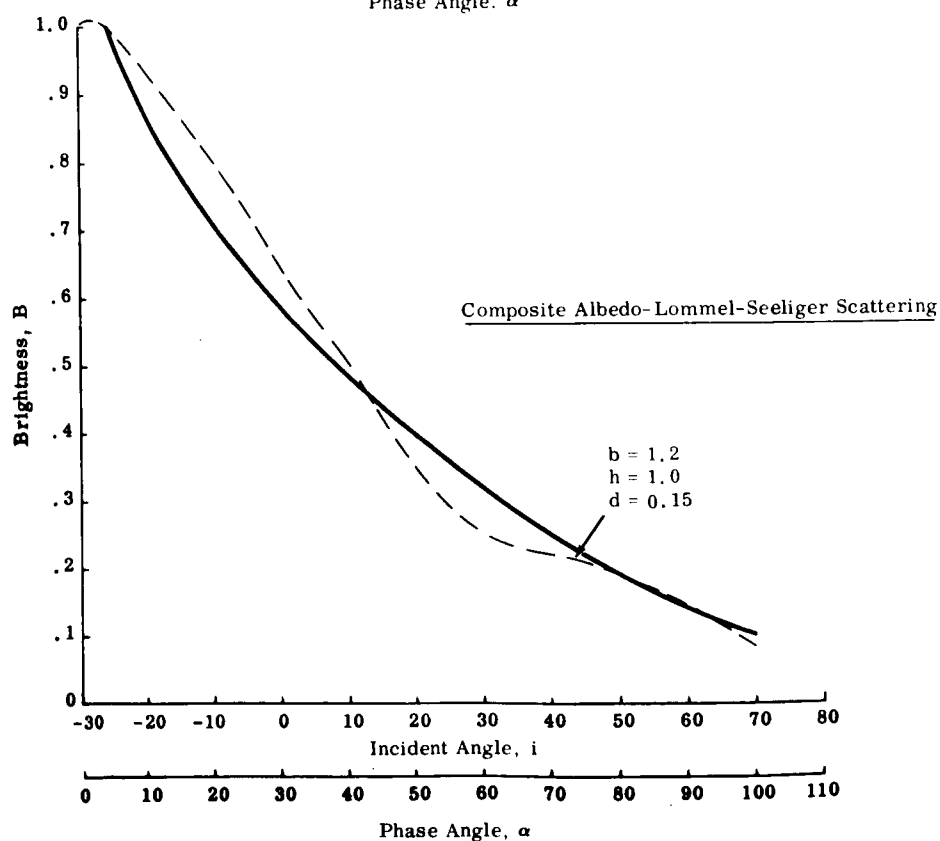
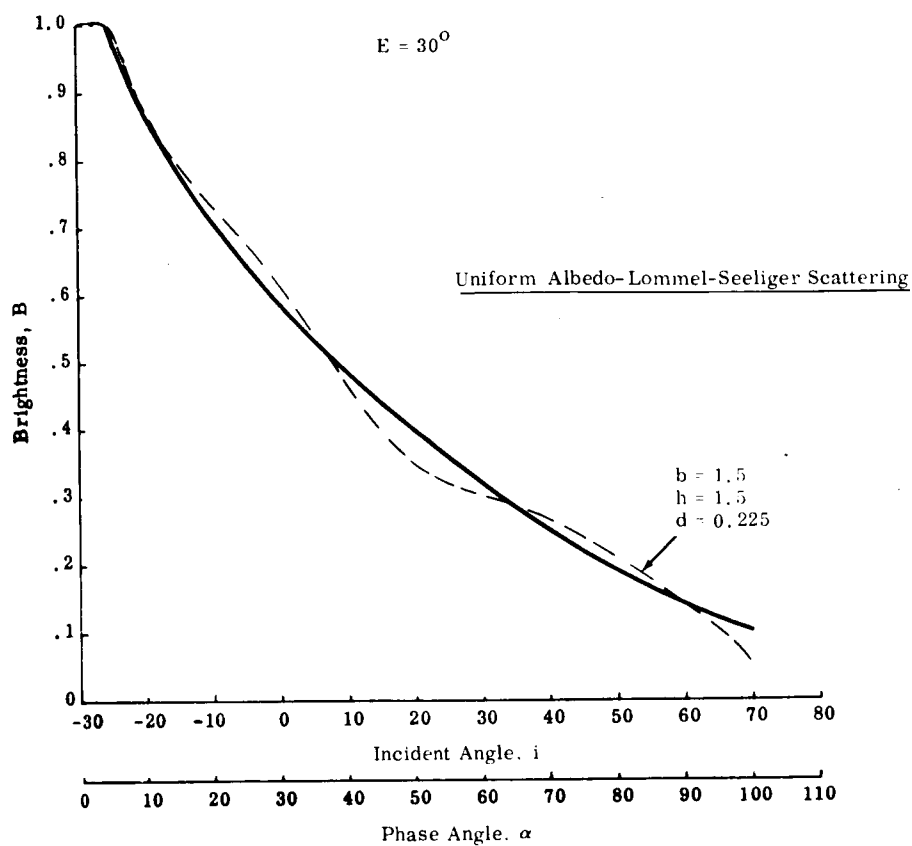


Fig. 36b (Cont) Photometry of Modified T-Model for Different Scattering Law and Albedo Conditions ( $E = 30^\circ$ )

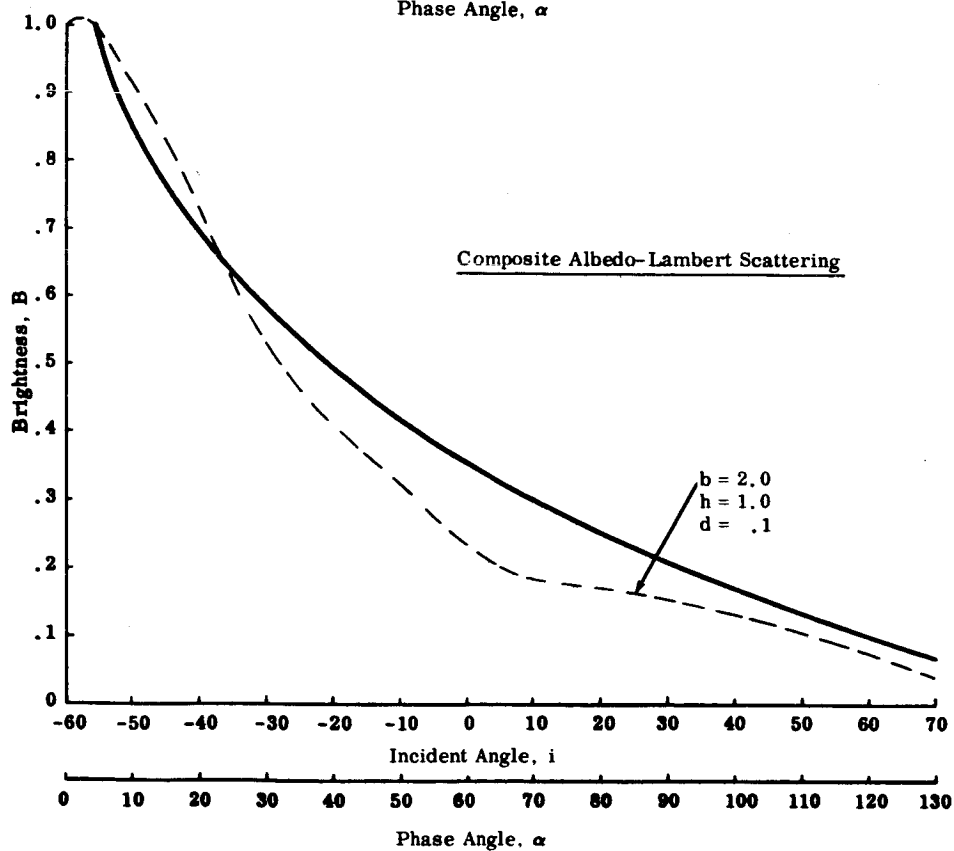
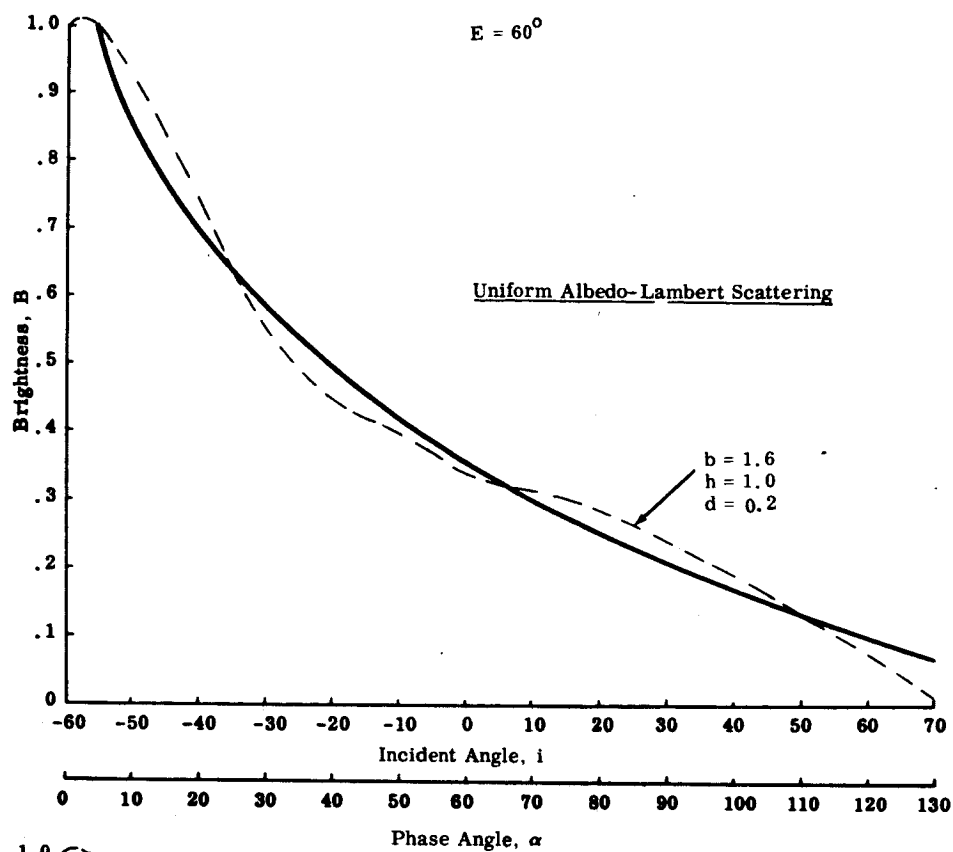


Fig. 36c Photometry of Modified T-Model for Different Scattering Law and Albedo Conditions ( $E = 60^\circ$ )

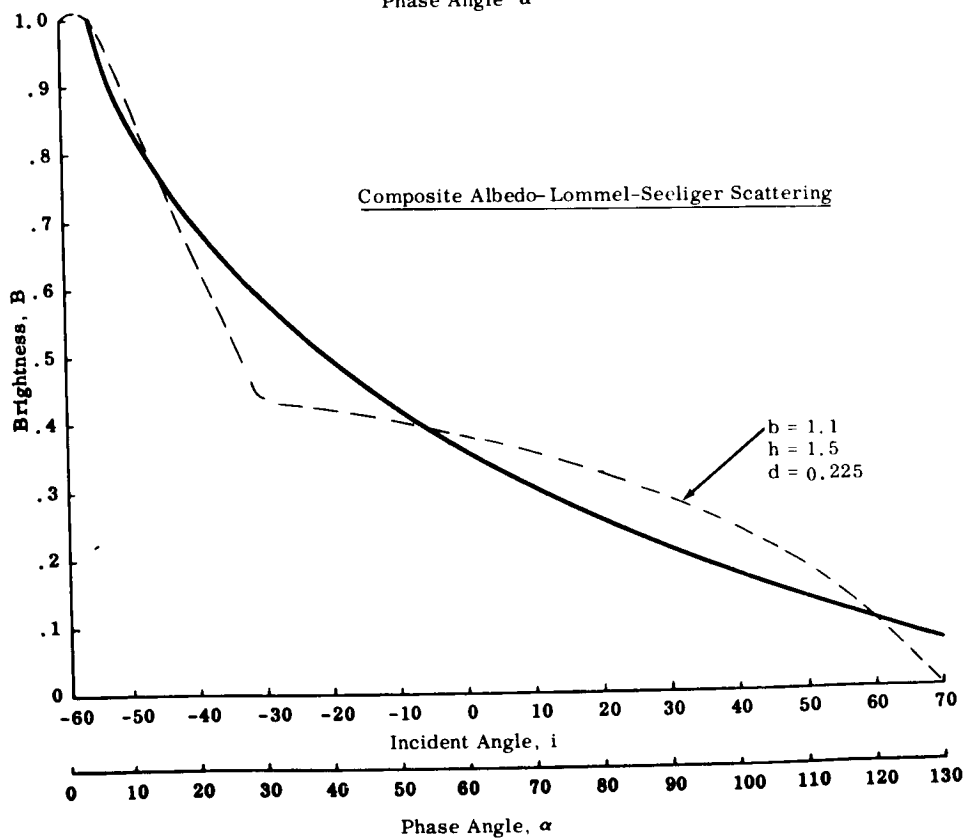
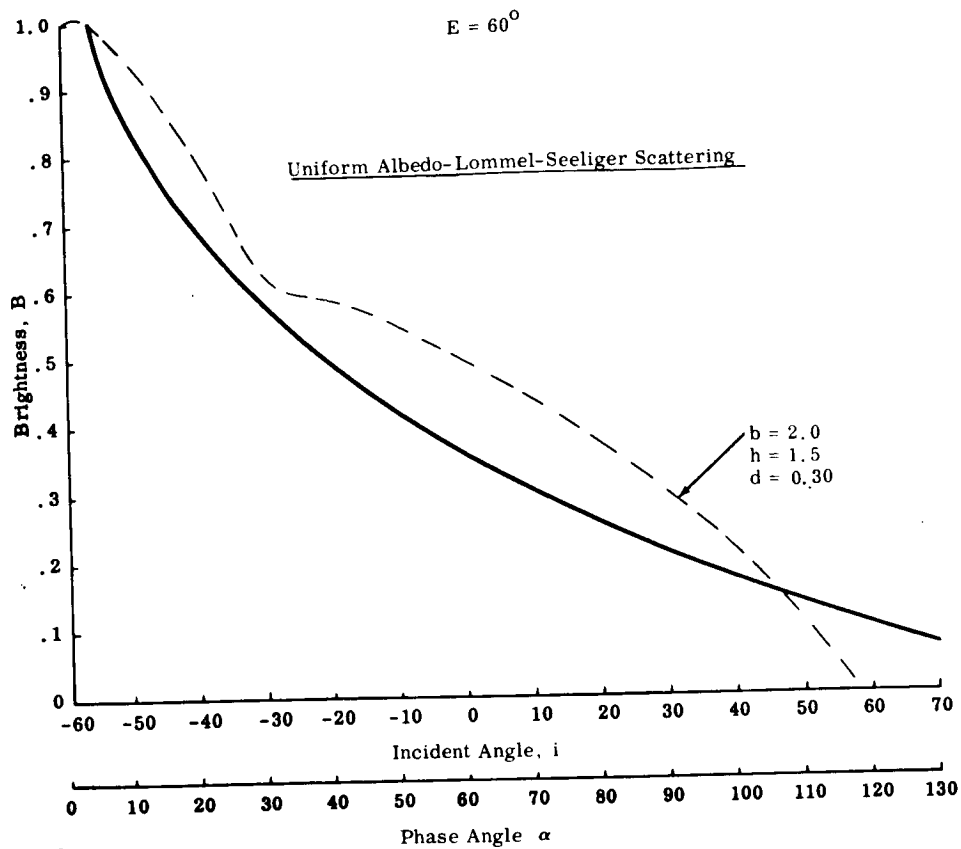
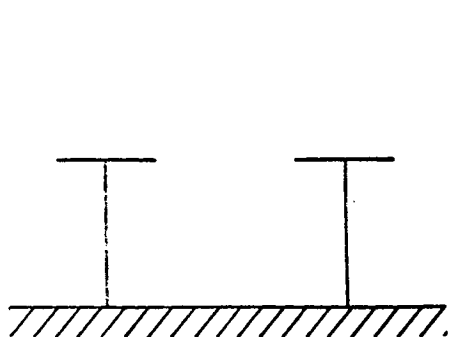
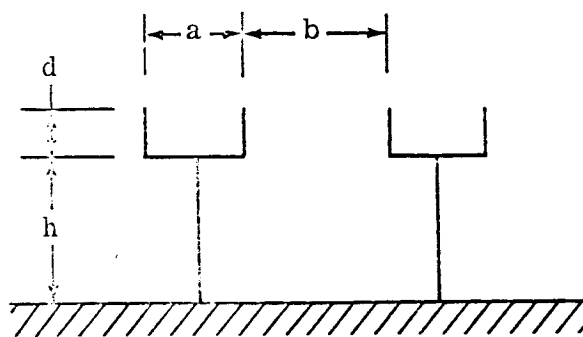


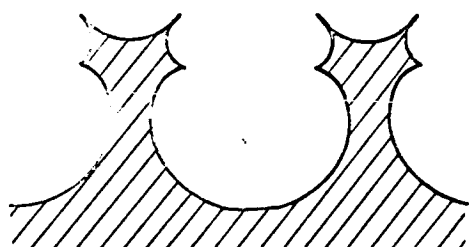
Fig. 36c (Cont) Photometry of Modified T-Model for Different Scattering Law and Albedo Conditions ( $E = 60^\circ$ )



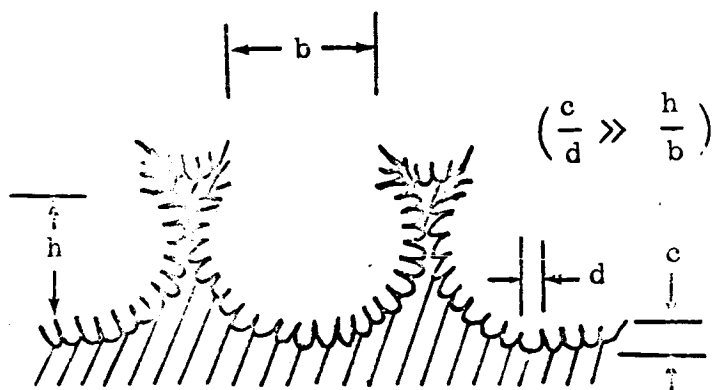
(a) Basic T-Model



(b) Modified T-Model  
(To improve backscatter)



(c) Cellular Module  
(evolved from Modified T-Model)



(d) Modified Cellular Module  
(To account for "opposition effect")

Fig. 37 Evolution of Building Block for a Lunar Photometric Model

## CONCLUSIONS

In Phase I, where our major objective was to study experimentally the wavelength dependence of albedo and photometry, we found that the over-all photometric function of the six investigated specimens, unlike their albedo, is relatively insensitive to changes in wavelength within the investigated spectrum interval of about  $0.48\mu$  to  $1.0\mu$ , except at very small and very large phase angles where color effects appear to predominate.

At the very small phase angles (referred to in the literature as the "opposition" region) we were successful in reproducing, by means of instrumental refinements, the nonlinear surge of brightness recently observed on the moon shortly before and after an eclipse. The observed opposition effect is most pronounced on coarse volcanic cinders and least pronounced on fine copper oxide powder. It was also observed that the backscatter in the opposition region, unlike the regions beyond it, is wavelength dependent. The brightness in this region is more pronounced in the red end of the spectrum than in the blue for all of the investigated specimens except for the sea coral which also differs from the other specimens in exhibiting a noticeable reddening at very large phase angles as recently observed on the moon.

No major significance can be attached to the above observations at this time other than the fact that the opposition phenomenon recently observed on the moon has been duplicated in the laboratory and that it appears to be largely due to a combination of roughness and color effects. It also appears that the backscatter exhibited by our test specimens and probably by the moon is nearly independent of wavelengths within the optical range and that more information can be gained by extending photometric measurements of the moon and of terrestrial analogs (in the laboratory or in the field) to longer wavelengths (such as in the near infrared) than by confining the studies to the shorter wavelengths used to date. It is known, for instance, that the moon is limb bright at optical wavelengths but limb dark at radar wavelengths. Closing the gap in our knowledge of the reflection properties of the moon between these two wavelength regions could conceivably lead to a better estimate of the microstructure of the lunar surface, and aid in the search of those lunar areas that are relatively free of "subtelescopic" topographic roughnesses. Such an earth-based effort could precede or follow the mission of unmanned lunar probes and complement the findings of these high-resolution probes in identifying suitable lunar landing sites. We recommend

that high-spatial resolution lunar photometric measurements at near infrared wavelengths ( $1\mu$ -  $3\mu$ ) be initiated as soon as possible and that the feasibility of scanning the moon with laser beams at longer wavelengths be looked into. The latter measurements would of necessity be confined to a study of limb darkening rather than of brightness variation with phase angle. The investigations of laboratory analogs at these wavelengths could precede the actual lunar measurements.

In Phase II, numerical studies based on an analysis developed by Walker (Ref. 15) were carried out on a highly idealized dust cloud model consisting of a relatively compact underlying base material above which is suspended a tenuous distribution of randomly oriented diffuse scatterers. The results obtained for various assumed values of particle size, interparticle distance, etc., illustrate quite clearly that such models fail to reproduce the characteristic features of the lunation curves of the moon, especially in the critical "opposition" region. The experimental results obtained with laboratory models consisting of suspended particles agree with the analytical findings insofar as they fail to produce the lunar backscatter. However, this observation should not be considered conclusive in view of the shortcomings of the physical models.

An idealized model whose photometric properties match reasonably well those of the moon has emerged in Phase III, from a computer program designed to analyze the photogeometric relationship of various basic shadow casting patterns under a wide range of boundary conditions. Successive changes introduced into this model indicate that "secondary" sharp edges play as important a role in reproducing the type of backscatter exhibited by the moon as "primary" vertical and/or horizontal elements patterned in such a manner as to form hollow cavities. The analytical model evolved approaches a vesicular structure and confirms earlier experimental results in suggesting a lunar microstructure made of innumerable cavities. A wide distribution in cavity size appears necessary to account for the opposition effect. The observed behavior of contrived models under various input conditions indicates that the photometric function is more sensitive to changes in geometry and albedo, than in the form of basic scattering law. Generally, the results of the computer program confirm and refine previously reported qualitative analyses and promise to pave the way to a quantitative estimate of the porosity of the optical layer of the lunar surface.



## RECOMMENDATIONS

Photometric investigations could potentially contribute to lunar landing site selection insofar as the photometry of a surface is a sensitive index of its microstructure, porosity, and roughness. Unfortunately, we are rapidly approaching the point of diminishing return of useful information from the lunar photometric standards which have been used in our work to date. These standards are based on relatively meager and poor resolution lunar observations, and represent the average photometric functions of vast areas of the moon that could possibly encompass numerous anomalies. If, in fact, such local anomalies do exist they should be spotted and interpreted. The analytical and experimental techniques developed in the search for lunar "models" on the basis of these standards, can now be used to assess the photometrically relevant engineering properties of discrete areas of the moon, provided, of course, detailed photometric data on these areas become available and certain additional improvements are made in data interpretation. Consequently, we recommend that the following programs of lunar photometric observations and analysis be implemented as soon as possible.

### Lunar Observations

More and better lunar photometric data are urgently needed. However, before a relatively expensive program of lunar observations is initiated, it is highly desirable to study and evaluate all data measured subsequent to the establishment of the photometric standards used to date. Notable among recent lunar measurements are those made by Gehrels at the Lunar and Planetary Laboratories of the University of Arizona and Shorthill and Saari of the Boeing Scientific Research Laboratories. Unfortunately, Gehrels' published data, although quite good, is limited and inadequate for the needs of the lunar program, and the unpublished Boeing data, although extensive, need considerable processing before they can be readily interpreted. The latter measurements cover the entire lunar disk at about 8" to 10" of arc resolution and include some 25 observations made during a full lunation. We recommend that these data be reduced immediately and brightness vs. phase angle curves of selected sites be derived and evaluated in terms of microstructure and terrain smoothness. The results could reveal, at best, the "localized" information about the moon we are looking for or, at least, pave the way to more limited but higher resolution photometric measurements of promising areas.

When new observations of the moon are made, it is desirable to extend albedo, photometric, and polarimetric measurements beyond the optical region as far as  $3\mu$ . Wavelength — correlated scattering functions could provide additional clues to the microstructure of the surface.

### Terrestrial Observation

Similar measurements of the photometric properties of suitable terrestrial formations could be made from an airborne platform. The geologically young lava flows in Oregon we recently surveyed are excellent candidate sites. Photometric data on a topographic scale and under resolutions ranging from coarse to fine could be very useful in interpreting lunar data for the purpose of selecting landing sites on the moon and confirming the suitability of the Oregon lava fields as simulation sites for LEM landing and obstacle recognition exercises.

### Laboratory Experiments

Measurements of albedo, photometry and polarimetry on "natural" and "artificial" models should be extended to the  $1\mu$  -  $3\mu$  region in an attempt to interpret corresponding lunar measurements recommended above. Investigations of the ratio of "order of roughness to viewed area" are important in interpretation of high resolution lunar photometric data in terms of microstructure and "subtelescopic" topographic roughness.

### Theoretical Analyses

Most lunar photometric functions or models are based on the scattering of particulate (i.e., convex) surfaces. Since cellular structures appear equally promising, the scattering function of concave surfaces should be studied. Such a function is needed to bring the contrived photometric models (analyzed in Phase III) a step closer to realism in terms of lunar microstructure and albedo. An estimate of the porosity of the optical layer of the lunar surface might then become possible. This estimate might be independently verified utilizing the results of recent polarimetric studies (Ref. 5). The techniques we used in developing our contrived, photometric models should be extended to learn whether these models could, with some modifications be made to yield information

which is compatible with the polarimetric properties of the moon. These properties still remain largely a puzzle despite some progress made at reproducing them by means of natural specimens (Ref. 5). Model-matching for its own sake is not meaningful if it does not reveal the pertinent variables and their relative contribution to the observed phenomena. The "synthetic" approach as a supplement to the experimental investigations of polarization appears to promise greater insight into the polarimetric properties of the moon (Ref. 16).

## REFERENCES

1. Halajian, J. D., and Spagnolo, F. A., Photometric Measurements of Simulated Lunar Surfaces, First Quarterly Progress Report, Contract No. NAS 9-3182, Grumman Research Department Memorandum RM-297, October 1965.
2. Halajian, J. D., and Spagnolo, F. A., Photometric Measurements of Simulated Lunar Surface, Second Quarterly Progress Report Contract No. NAS 9-3182, Grumman Research Department Memorandum RM-308, January 1966.
3. Halajian, J. D., Photometric Measurements of Simulated Lunar Surfaces, Interim Report, Contract No. NAS 9-3182, Grumman Research Department Report RE-219, July 1965.
4. Photometric Measurements of Simulated Lunar Surfaces, Grumman Research Department Proposal RP-255, File No. 65-83NAS, June 1965.
5. Egan, W. G., and Smith, L. L., Polarimetric Measurements of Simulated Lunar Surfaces, Progress Report, Contract No. NAS 9-4942, Grumman Research Department Memorandum RM-312, February 1966, and RM-315, March 1966.
6. Halajian, J. D., and Reichman, J., Correlation of Mechanical and Thermal Properties of Extraterrestrial Materials, Progress Report, Contract NAS 8-20084, Grumman Research Department Memorandum RM-309, February 1966.
7. Gehrels, T., Coffeen, T., and Owings, D., "Wavelength Dependence of Polarization of the Lunar Surface," Astronomical Journal, Vol. 69, No. 10, December 1964.
8. Markov, M. N., and Khokhlova, V. L., "Coefficients of Emission in the Infrared of the Lunar Seas and Continents," Soviet Physics-Doklady, Vol. 9, No. 8, February 1965.
9. Harris, D. L., "Photometry and Colorimetry of Planets and Satellites," Planets and Satellites, G. P. Kuiper and B. M. Middlehurst, Editors, University Chicago Press, 1962.
10. Sharanov, V. V., "Some Results of Photometric and Colorimetric Comparison of Terrestrial Volcanic Crusts with the Lunar Surface," Annals of the N. Y. Academy of Sciences, F. 123, Art. 2, p. 741-750.

11. Wattson, R. B., and Danielson, R. E., "The Infrared Spectrum of the Moon," Astrophysical Journal, Vol. 142, No. 1, July 1965.
12. Kuprevitch, N. F., "New Data on the Structure of the Lunar Surface," Soviet Astronomy, Vol. 7, No. 5, March-April 1964.
13. Singer, S. F., and Walker, E. H., "Electrostatic Dust Transport on the Lunar Surface," Icarus 7, pp. 112-120, 1962.
14. Van de Hulst, H. C., Light Scattering by Small Particles, John Wiley and Sons, New York, 1957.
15. Walker, E. H., Dust Clouds Produced by Space Vehicles Impacting on the Lunar Surface, University of Miami, School of Interplanetary Sciences, June 1965.
16. Egan, W.G., Smith, L.L., and McCoyd, G.C., Polarimetric Measurements of Simulated Lunar Surfaces, Final Report, Contract No. NAS 9-4942, Grumman Research Department Report (in preparation).

## APPENDIX

### List of Symbols

- a = length of horizontal elements
- b = length of opening between horizontal and/or vertical elements
- B = computed brightness
- c = length of elements in direction perpendicular to intensity equator
- d = length of vertical secondary roughness elements ("lips")
- E = viewing angle of photometer
- h = length of vertical elements
- i = angle of incidence of illumination
- K = normalization constant
- $\rho_A$  = average reflectivity of horizontal elements
- $\rho_B$  = average reflectivity of base material
- $\rho_D$  = average reflectivity of secondary roughness elements ("lips")
- $\rho_V$  = average reflectivity of vertical elements

## Discussion of Computer Program

Utilizing the five "simple" geometric configurations described in the section on analytical models, a computer program was written based upon the geometrical analyses given in this Appendix.

The mathematical logic of the program is straightforward and can be described briefly as follows:

For all models, more than one case (A, B, C, etc.) is presented, each being defined by the viewing angle  $E$ , and particular combinations of the linear elements  $a$ ,  $b$ ,  $h$ , and  $d$ . For all cases, the brightness,  $B$ , expressed as a product of the optical scattering law and a surface area that is both illuminated and viewed by the photometer, is given alongside the corresponding region of validity defined by the boundary conditions on the angle of incidence,  $i$ . As can be readily observed, the complete interval on  $i$  extends from the photometer position,  $E$ , to a value of  $i$  approaching  $+90^\circ$  in most cases, corresponding to a motion of the source from left to right along the intensity equator.

In addition to the different cases mentioned, the validity of the equations is further restricted according to values of  $b$  which are greater than, equal to, or less than  $a$ . Though not shown in this Appendix, the brightness for some models was for comparison purposes, computed for two different forms of the scattering law, namely, Lambert's law of diffuse reflection and the law of Lommel-Seeliger. The results for the latter case, shown in Figs. 34 through 36, were obtained by simply replacing the terms:

$$[\cos |i| \cos E] \text{ and } \left[ \cos \left( \frac{\pi}{2} - |i| \right) \cdot \cos \left( \frac{\pi}{2} - E \right) \right], \text{ by:}$$
$$\left[ \frac{\cos |i|}{\cos |i| + \cos E} \right] \text{ and } \left[ \frac{\cos \left( \frac{\pi}{2} - |i| \right)}{\cos \left( \frac{\pi}{2} - |i| \right) + \cos \left( \frac{\pi}{2} - E \right)} \right] \text{ respectively,}$$

wherever they appear in the present analysis.

For a given set of input parameters for each model, namely  $a$ ,  $b$ ,  $h$ , and  $d$ , the computer determines for a particular viewing angle ( $0^\circ$ ,  $30^\circ$ , or  $60^\circ$ ), the case and consequently, which set of equations it shall use to compute the called-for information. The results desired in the present instance are: 1) the normalized

brightness versus phase curves for all models, viewing angles, and possible combinations of linear elements prescribed in the input data; and 2) the computation of the sum of the squares of the deviations (computed at regular predetermined values of the phase angle) between the normalized photometric curves determined in 1), and those of the actual lunation curves of the moon. Expressed mathematically, the latter sum can be written as:

$$(\Sigma \Delta^2) = \sum_{i=i_0}^{i=70^\circ} |B_{L_i} - B_{C_i}|^2,$$

where  $B_L$  and  $B_C$  represent the lunar and contrived model brightnesses respectively, and the summation indices run from a value of  $i = i_0$  (corresponding to a phase angle,  $\alpha = |E| + i$ , equal to  $4^\circ$ ), to a value of  $i = 70^\circ$ , which is the largest angle of incidence for which the standard lunation curves are given. Information on the  $B_L$ 's (lunar brightnesses) for all three viewing angles were taken from Ref. 3 and introduced numerically into the program as input. Because the brightness curves for the moon are already normalized to correspond to a value of one at  $4^\circ$  phase angle, the curves computed in 1, and later used for comparison with the lunar data in 2, had also to be normalized at the same phase angle before any meaningful interpretation could be given to them. The latter was accomplished by the use of a subroutine, utilizing the normalization factor,  $K$ , which had to be evaluated for all combinations of input data. In addition to the parameters already mentioned as input data, values of  $c$  (length of elements in direction perpendicular to intensity equator),  $\rho_A$ ,  $\rho_B$ ,  $\rho_V$ , and  $\rho_D$  (average reflectivity values) were selected. Under conditions of uniform albedo, the average reflectivity values were all taken to be equal to 0.1. To dramatize the effects of "composite albedo" in some models, however, these values were varied. A brief summary of all the input information (excluding input data on the lunation curves) is given in Table 2, which also shows the minimum, maximum and incremental values of all the linear elements.



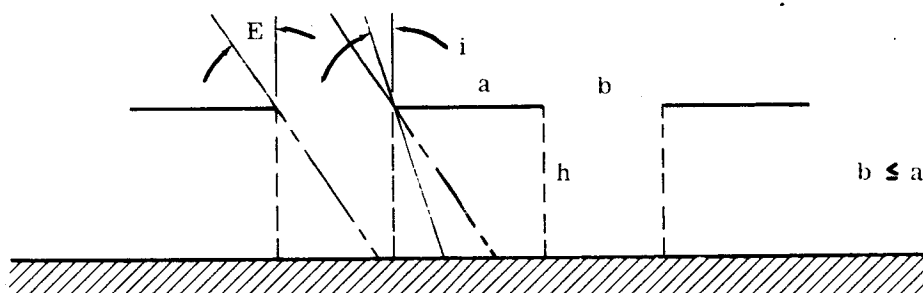
Table 2

SUMMARY OF INPUT DATA

Linear Element	Average Reflectivity		Minimum	Maximum	Increment
	Uniform Albedo	Composite Albedo			
a	$\rho_A = .1$	$\rho_A = .05$	1	1	0
b	—	—	.1a	2.0a	.1a
h	$\rho_V = .1$	$\rho_V = .15$	.5a	4.0a	.5a
d	$\rho_D = .1$	$\rho_D = .05$	.1h	.25h	.05h
c	—	—	1	1	0
Base Material	$\rho_B = .1$	$\rho_B = .1$	—	—	—

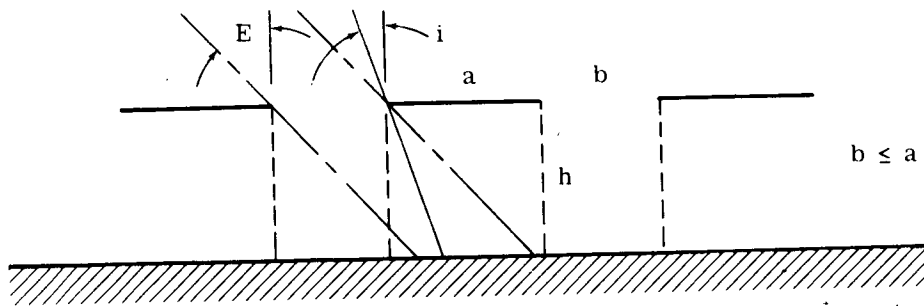
# Photogeometric Analysis of Contrived Models

SUSPENDED STRIP MODEL



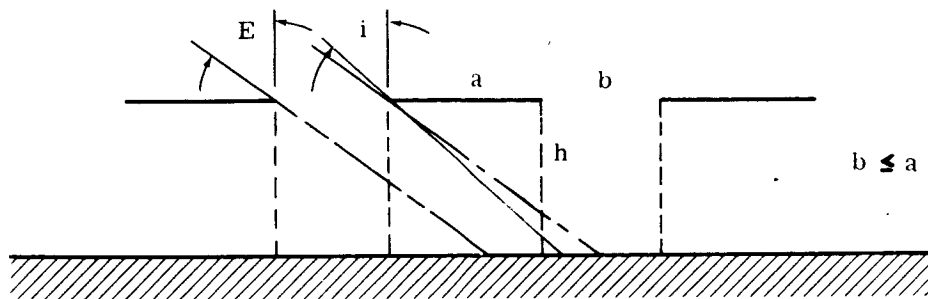
Case A:  $\tan^{-1}(0) \leq E \leq \tan^{-1}\left(\frac{b}{h}\right)$

Boundary Condition on $i$ :	Brightness, $B$
$-E \leq i \leq \tan^{-1}\left(\frac{b-h \tan E}{h}\right)$	$K \cos  i  \cos E \left[ (\rho_A a + \rho_B (b - h \tan E - h \tan i)) \right] c$
$\tan^{-1}\left(\frac{b-h \tan E}{h}\right) \leq i \leq \tan^{-1}\left(\frac{a-h \tan E}{h}\right)$	$K \cos  i  \cos E (\rho_A a) c$
$\tan^{-1}\left(\frac{a-h \tan E}{h}\right) \leq i \leq \tan^{-1}\left(\frac{a+b-h \tan E}{h}\right)$	$K \cos  i  \cos E \left[ \rho_A a + \rho_B (h \tan i - a + h \tan E) \right] c$
$\tan^{-1}\left(\frac{a+b-h \tan E}{h}\right) \leq i \leq \tan^{-1}\left(\frac{a+2b-h \tan E}{h}\right)$	$K \cos  i  \cos E \left[ \rho_A a + \rho_B (a + 2b - h \tan E - h \tan i) \right] c$
$\tan^{-1}\left(\frac{a+2b-h \tan E}{h}\right) \leq i \leq \tan^{-1}\left(\frac{2a+b-h \tan E}{h}\right)$	$K \cos  i  \cos E (\rho_A a) c$
$\tan^{-1}\left(\frac{2a+b-h \tan E}{h}\right) \leq i \leq \tan^{-1}\left(\frac{2a+2b-h \tan E}{h}\right)$	$K \cos  i  \cos E \left[ \rho_A a + \rho_B (h \tan i - (2a + b - h \tan E)) \right] c$
$\tan^{-1}\left(\frac{2a+2b-h \tan E}{h}\right) \leq i \leq \tan^{-1}\left(\frac{2a+3b-h \tan E}{h}\right)$	$K \cos  i  \cos E \left[ \rho_A a + \rho_B ((2a + 3b - h \tan E) - h \tan i) \right] c$
$i = \frac{\pi}{2}$	0



Case B:  $\tan^{-1}\left(\frac{b}{h}\right) \leq E \leq \tan^{-1}\left(\frac{a}{h}\right)$

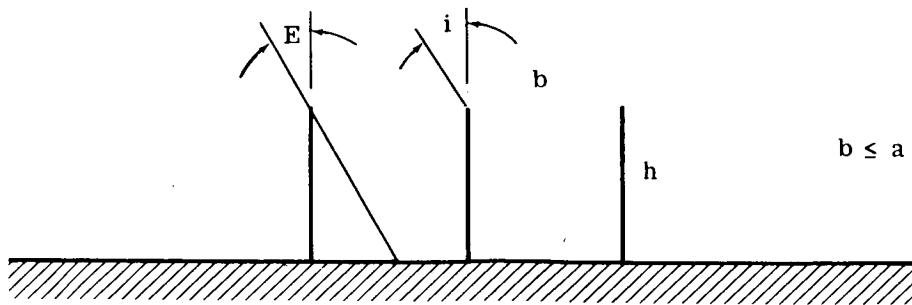
Boundary Condition on $i$ :	Brightness, $B$
$-E \leq i \leq -\tan^{-1}\left(\frac{h \tan E - b}{h}\right)$	$K \cos  i  \cos E \left[ \rho_A a + \rho_B (h \tan  i  - h \tan E + b) \right] c$
$-\tan^{-1}\left(\frac{h \tan E - b}{h}\right) \leq i \leq \tan^{-1}\left(\frac{a - h \tan E}{h}\right)$	$K \cos  i  \cos E (\rho_A a) c$
$\tan^{-1}\left(\frac{a - h \tan E}{h}\right) \leq i \leq \tan^{-1}\left(\frac{a - h \tan E + b}{h}\right)$	$K \cos  i  \cos E \left[ \rho_A a + \rho_B (h \tan i - (a - h \tan E)) \right] c$
$\tan^{-1}\left(\frac{a - h \tan E + b}{h}\right) \leq i \leq \tan^{-1}\left(\frac{a + 2b - h \tan E}{h}\right)$	$K \cos  i  \cos E \left[ \rho_A a + \rho_B (a + 2b - h \tan E - h \tan i) \right] c$
$\tan^{-1}\left(\frac{a + 2b - h \tan E}{h}\right) \leq i \leq \tan^{-1}\left(\frac{2a + b - h \tan E}{h}\right)$	$K \cos  i  \cos E (\rho_A a) c$
$\tan^{-1}\left(\frac{2a + b - h \tan E}{h}\right) \leq i \leq \tan^{-1}\left(\frac{2a + 2b - h \tan E}{h}\right)$	$K \cos  i  \cos E \left[ \rho_A a + \rho_B (h \tan i - (2a + b - h \tan E)) \right] c$
$\tan^{-1}\left(\frac{2a + 2b - h \tan E}{h}\right) \leq i \leq \tan^{-1}\left(\frac{2a + 3b - h \tan E}{h}\right)$	$K \cos  i  \cos E \left[ \rho_A a + \rho_B ((2a + 3b - h \tan E) - h \tan i) \right] c$
$i = \frac{\pi}{2}$	0



Case C:  $\tan^{-1}\left(\frac{a}{h}\right) \leq E \leq \tan^{-1}\left(\frac{a+b}{h}\right)$

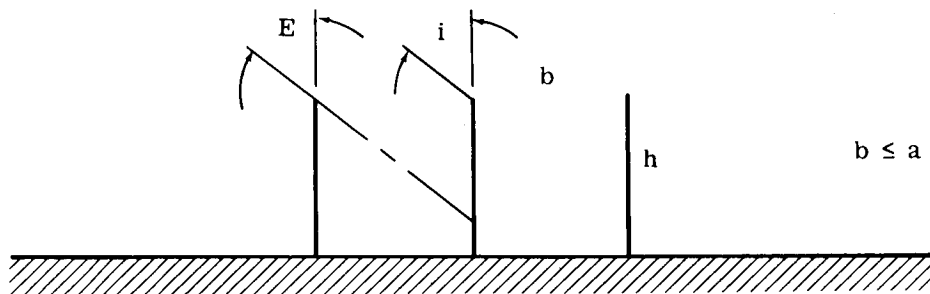
Boundary Condition on $i$ :	Brightness, $B$
$-E \leq i \leq -\tan^{-1}\left(\frac{h \tan E - b}{h}\right)$	$K \cos  i  \cos E \left[ \rho_A a + \rho_B [h \tan  i  - (h \tan E - b)] \right] c$
$-\tan^{-1}\left(\frac{h \tan E - b}{h}\right) \leq i \leq -\tan^{-1}\left(\frac{h \tan E - a}{h}\right)$	$K \cos  i  \cos E (\rho_A a) c$
$-\tan^{-1}\left(\frac{h \tan E - a}{h}\right) \leq i \leq \tan^{-1}(0)$	$K \cos  i  \cos E \left[ \rho_A a + \rho_B (h \tan E - a) - h \tan  i  \right] c$
$\tan^{-1}(0) \leq i \leq \tan^{-1}\left(\frac{a+b-h \tan E}{h}\right)$	$K \cos  i  \cos E \left[ \rho_A a + \rho_B (a + (h \tan E - a) + h \tan i) \right] c$
$\tan^{-1}\left(\frac{a+b-h \tan E}{h}\right) \leq i \leq \tan^{-1}\left(\frac{a+2b-h \tan E}{h}\right)$	$K \cos  i  \cos E \left[ \rho_A a + \rho_B (a + 2b - h \tan E - h \tan i) \right] c$
$\tan^{-1}\left(\frac{a+2b-h \tan E}{h}\right) \leq i \leq \tan^{-1}\left(\frac{2a+b-h \tan E}{h}\right)$	$K \cos  i  \cos E (\rho_A a) c$
$\tan^{-1}\left(\frac{2a+b-h \tan E}{h}\right) \leq i \leq \tan^{-1}\left(\frac{2a+2b-h \tan E}{h}\right)$	$K \cos  i  \cos E \left[ \rho_A a + \rho_B [h \tan i - (2a + b - h \tan E)] \right] c$
$\tan^{-1}\left(\frac{2a+2b-h \tan E}{h}\right) \leq i \leq \tan^{-1}\left(\frac{2a+3b-h \tan E}{h}\right)$	$K \cos  i  \cos E \left[ \rho_A a + \rho_B [(2a + 3b - h \tan E) - h \tan i] \right] c$
$i = \frac{\pi}{2}$	0

# VERTICAL STRIP MODEL



Case A:  $\tan^{-1}(0) \leq E \leq \tan^{-1}\left(\frac{b}{h}\right)$

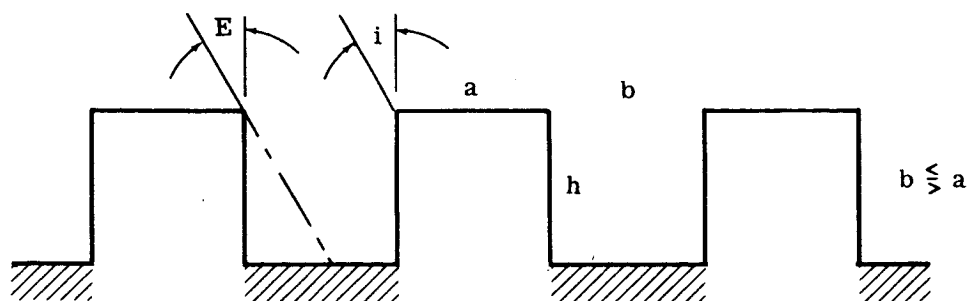
Boundary Condition on $i$ :	Brightness, $B$
$-E \leq i \leq \tan^{-1}(0)$	$K \left\{ \cos  i  \cos E \cdot \rho_B (b - h \tan E) + \rho_V \cos\left(\frac{\pi}{2} -  i \right) \cos\left(\frac{\pi}{2} - E\right) h \right\} c$
$\tan^{-1}(0) \leq i \leq \tan^{-1}\left(\frac{b - h \tan E}{h}\right)$	$K \cos  i  \cos E \cdot \rho_B [(b - h \tan E) - h \tan i] c$
$\tan^{-1}\left(\frac{b - h \tan E}{h}\right) \leq i$	0



Case B:  $\tan^{-1}\left(\frac{b}{h}\right) \leq E$

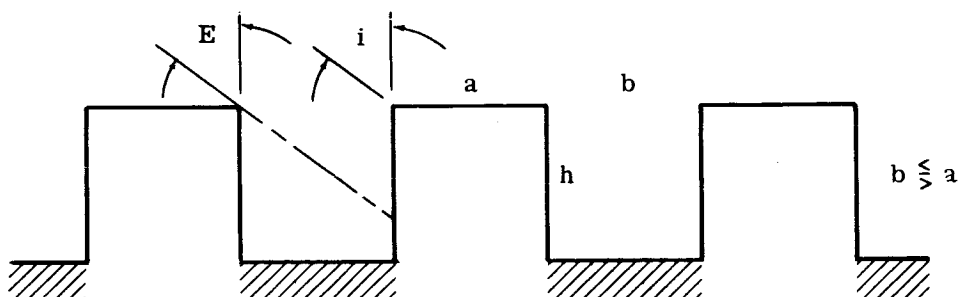
Boundary Condition on $i$ :	Brightness, $B$
$-E \leq i \leq \tan^{-1}(0)$	$K \left[ \cos\left(\frac{\pi}{2} -  i \right) \cos\left(\frac{\pi}{2} - E\right) \cdot \rho_V \left(\frac{b}{\tan E}\right) \right] c$
$\tan^{-1}(0) \leq i$	0

# FURROW MODEL



Case A:  $\tan^{-1}(0) \leq E \leq \tan^{-1}\left(\frac{b}{h}\right)$

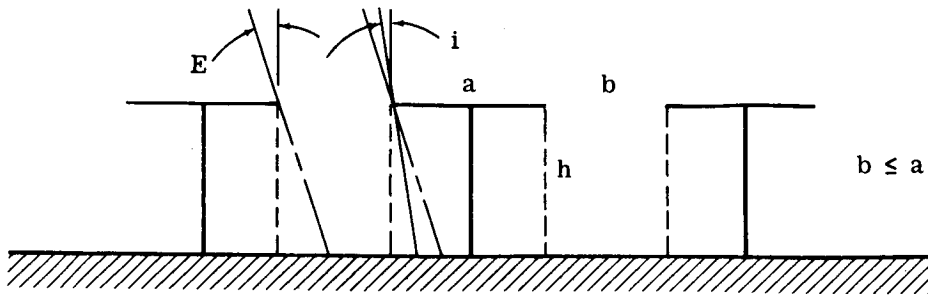
Boundary Condition on $i$ :	Brightness, $B$
$-E \leq i \leq \tan^{-1}(0)$	$K \left\{ \cos  i  \cos E \left[ \rho_A a + \rho_B (b - h \tan E) \right] + \rho_V \cos\left(\frac{\pi}{2} -  i \right) \cos\left(\frac{\pi}{2} - E\right) h \right\} c$
$\tan^{-1}(0) \leq i \leq \tan^{-1}\left(\frac{b - h \tan E}{h}\right)$	$K \cos  i  \cos E \left[ \rho_A a + \rho_B (b - h \tan E - h \tan i) \right] c$
$\tan^{-1}\left(\frac{b - h \tan E}{h}\right) \leq i \leq \tan^{-1}(\infty)$	$K \cos  i  \cos E (\rho_A a) c$



Case B:  $\tan^{-1}\left(\frac{b}{h}\right) \leq E$

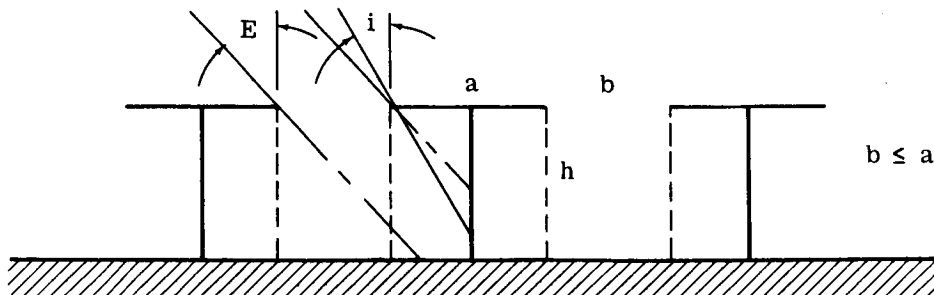
Boundary Condition on $i$ :	Brightness, $B$
$-E \leq i \leq \tan^{-1}(0)$	$K \left\{ \cos  i  \cos E (\rho_A a) + \rho_V \cos\left(\frac{\pi}{2} -  i \right) \cos\left(\frac{\pi}{2} - E\right) \left(\frac{b}{\tan E}\right) \right\} c$
$\tan^{-1}(0) \leq i \leq \tan^{-1}(\infty)$	$K \cos  i  \cos E (\rho_A a) c$

# T-MODEL



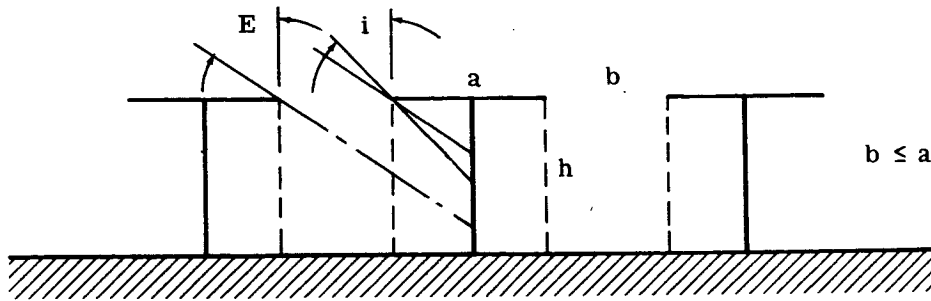
Case A:  $\tan^{-1}(0) \leq E \leq \tan^{-1}\left(\frac{a}{2h}\right)$

Boundary Condition on $i$ :	Brightness, $B$
$-E \leq i \leq \tan^{-1}\left(\frac{b-h \tan E}{h}\right)$	$K \cos  i  \cos E [\rho_A a + \rho_B (b - h \tan E - h \tan i)] c$
$\tan^{-1}\left(\frac{b-h \tan E}{h}\right) \leq i \leq \tan^{-1}(\infty)$	$K \cos  i  \cos E (\rho_A a) c$



Case B:  $\tan^{-1}\left(\frac{a}{2h}\right) \leq E \leq \tan^{-1}\left(\frac{b + \frac{a}{2}}{h}\right)$

Boundary Condition on $i$ :	Brightness, $B$
$-E \leq i \leq -\tan^{-1}\left(\frac{a}{2h}\right)$	$K \left\{ \cos  i  \cos E \left[ \rho_A a + \rho_B \left( \frac{a}{2} + b - h \tan E \right) \right] + \rho_V \cos\left(\frac{\pi}{2} -  i \right) \cos\left(\frac{\pi}{2} - E\right) \left[ h - \frac{a}{2 \tan  i } \right] \right\} c$
$-\tan^{-1}\left(\frac{a}{2h}\right) \leq i \leq -\tan^{-1}\left(\frac{h \tan E - b}{h}\right)$	$K \cos  i  \cos E [\rho_A a + \rho_B (h \tan  i  - h \tan E + b)] c$
$-\tan^{-1}\left(\frac{h \tan E - b}{h}\right) \leq i \leq \tan^{-1}(\infty)$	$K \cos  i  \cos E (\rho_A a) c$

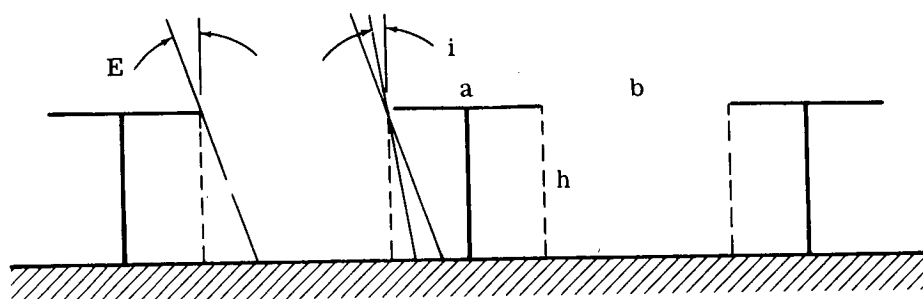


Case C:  $\tan^{-1}\left(\frac{b + \frac{a}{2}}{h}\right) \leq E \leq \tan^{-1}(\infty)$

Boundary Condition on $i$ :	Brightness, $B$
$-E \leq i \leq -\tan^{-1}\left(\frac{\tan E}{2b/a + 1}\right)$	$K \left\{ \cos  i  \cos E(\rho_A a) + \rho_V \left[ \frac{1}{\tan E} \left( b + \frac{a}{2} \right) - \frac{a}{2} \tan \left( \frac{\pi}{2} -  i  \right) \right] \cos \left( \frac{\pi}{2} - E \right) \cos \left( \frac{\pi}{2} -  i  \right) \right\} c$
$\tan^{-1}\left(\frac{\tan E}{2b/a + 1}\right) \leq i \leq \tan^{-1}(\infty)$	$K \cos  i  \cos E(\rho_A a) c$

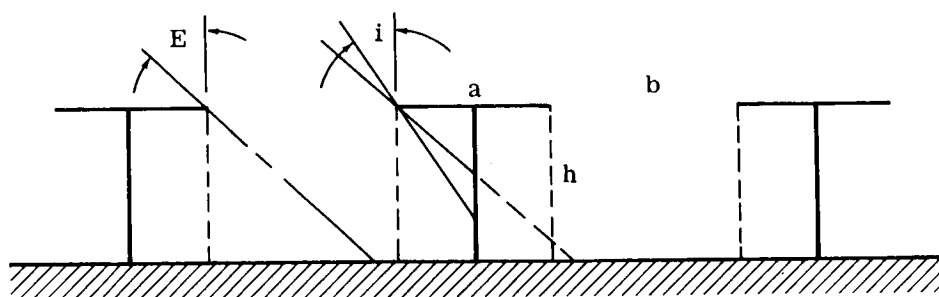


# T-MODEL



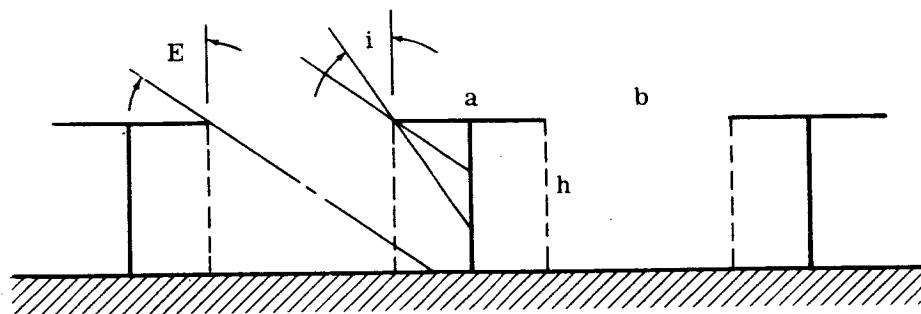
Case A:  $\tan^{-1}(0) \leq E \leq \tan^{-1}\left(\frac{a}{2h}\right)$

Boundary Condition on $i$ :	Brightness, $B$
$-E \leq i \leq \tan^{-1}\left(\frac{b-h \tan E}{h}\right)$	$K \cos  i  \cos E \left[ \rho_A a + \rho_B (b - h \tan E - h \tan i) \right] c$
$\tan^{-1}\left(\frac{b-h \tan E}{h}\right) \leq i \leq \tan^{-1}(\infty)$	$K \cos  i  \cos E (\rho_A a) c$



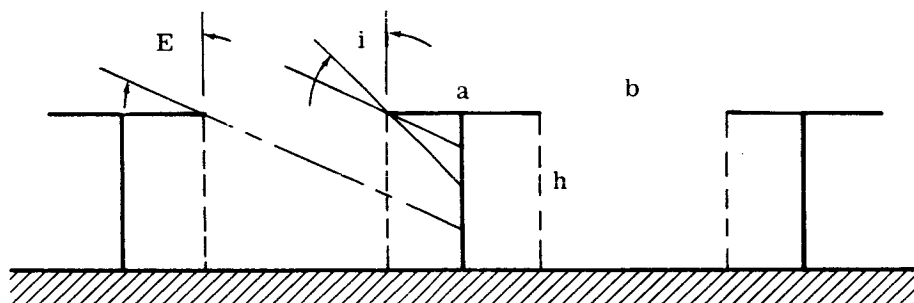
Case B:  $\tan^{-1}\left(\frac{a}{h}\right) \leq E \leq \tan^{-1}\left(\frac{b}{h}\right)$

Boundary Condition on $i$ :	Brightness, $B$
$-E \leq i \leq -\tan^{-1}\left(\frac{a}{2h}\right)$	$K \left\{ \cos  i  \cos E \left[ \rho_A a + \rho_B \left( \frac{a}{2} + b - h \tan E \right) \right] + \rho_V \cos\left(\frac{\pi}{2} -  i \right) \cos\left(\frac{\pi}{2} - E\right) \left[ h - \frac{a}{2 \tan  i } \right] \right\} c$
$-\tan^{-1}\left(\frac{a}{2h}\right) \leq i \leq \tan^{-1}(0)$	$K \cos  i  \cos E \left[ \rho_A a + \rho_B (b - h \tan E + h \tan  i ) \right] c$
$\tan^{-1}(0) \leq i \leq \tan^{-1}\left(\frac{b-h \tan E}{h}\right)$	$K \cos  i  \cos E \left[ \rho_A a + \rho_B (b - h \tan E - h \tan i) \right] c$
$\tan^{-1}\left(\frac{b-h \tan E}{h}\right) \leq i \leq \tan^{-1}(\infty)$	$K \cos  i  \cos E (\rho_A a) c$



Case C:  $\tan^{-1}\left(\frac{b}{h}\right) \leq E \leq \tan^{-1}\left(\frac{b + \frac{a}{2}}{h}\right)$

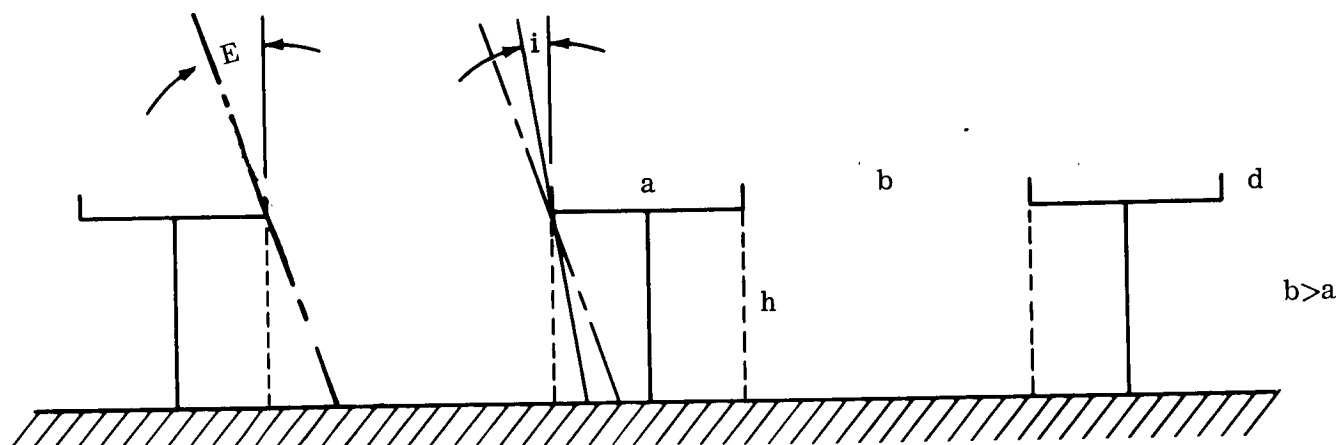
Boundary Condition on $i$ :	Brightness, $B$
$-E \leq i \leq -\tan^{-1}\left(\frac{a}{2h}\right)$	$K \left\{ \cos  i  \cos E \left[ \rho_A a + \rho_B \left( \frac{a}{2} + b - h \tan E \right) \right] + \rho_V \cos\left(\frac{\pi}{2} -  i \right) \cos\left(\frac{\pi}{2} - E\right) \left[ h - \frac{a}{2} \frac{1}{\tan  i } \right] \right\} c$
$-\tan^{-1}\left(\frac{a}{2h}\right) \leq i \leq -\tan^{-1}\left(\frac{h \tan E - b}{h}\right)$	$K \left\{ \cos  i  \cos E \left[ \rho_A a + \rho_B (h \tan  i  - h \tan E + b) \right] \right\} c$
$-\tan^{-1}\left(\frac{h \tan E - b}{h}\right) \leq i \leq \tan^{-1}(\infty)$	$K \cos  i  \cos E (\rho_A a) c$



Case D:  $\tan^{-1}\left(\frac{b + a/2}{h}\right) \leq E \leq \tan^{-1}(\infty)$

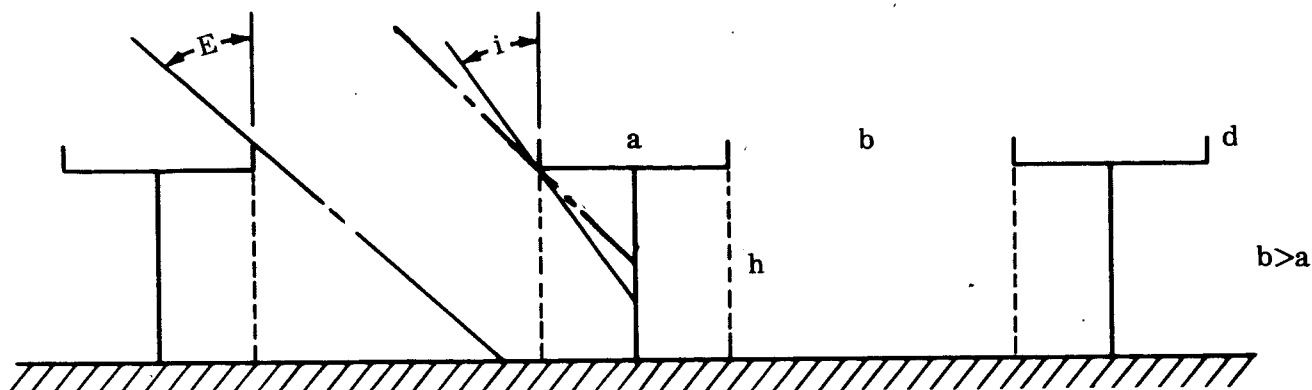
Boundary Condition on $i$ :	Brightness, $B$
$-E \leq i \leq -\tan^{-1}\left(\frac{\tan E}{\frac{2b}{a} + 1}\right)$	$K \left\{ \cos  i  \cos E \cdot (\rho_A a) + \rho_V \left[ \frac{1}{\tan E} \left( b + \frac{a}{2} \right) - \frac{a}{2} \tan\left(\frac{\pi}{2} -  i \right) \right] \cos\left(\frac{\pi}{2} - E\right) \cos\left(\frac{\pi}{2} -  i \right) \right\} c$
$-\tan^{-1}\left(\frac{\tan E}{\frac{2b}{a} + 1}\right) \leq i \leq \tan^{-1}(\infty)$	$K \cos  i  \cos E (\rho_A a) c$

# Modified T-Model



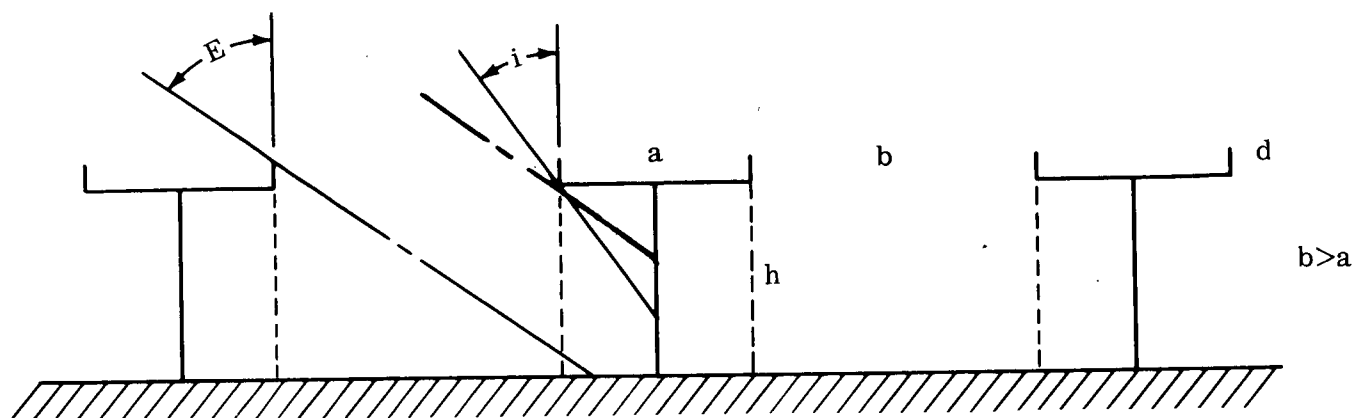
Case A:  $\tan^{-1}(0) \leq E \leq \tan^{-1}\left(\frac{a}{2h}\right)$

Boundary Condition on $i$ :	Brightness, $B$
$-E \leq i \leq \tan^{-1}(0)$	$K \left\{ \cos  i  \cos E \left[ \rho_A (a - d \tan E) + \rho_B [b - (h + d) \tan E + h \tan  i ] \right] + 2\rho_D \cos \left( \frac{\pi}{2} -  i  \right) \cos \left( \frac{\pi}{2} - E \right) \cdot d \right\} c$
$\tan^{-1}(0) \leq i \leq \tan^{-1}\left(\frac{b - (h + d) \tan E}{(h + d)}\right)$	$K \left\{ \cos  i  \cos E \left[ \rho_A (a - d \tan E - d \tan i) + \rho_B [b - (h + d) \tan E - (h + d) \tan i] \right] \right\} c$
$\tan^{-1}\left(\frac{b - (h + d) \tan E}{(h + d)}\right) \leq i \leq \tan^{-1}(\cdot)$	$K \cos  i  \cos E \cdot \rho_A [a - d(\tan E + \tan i)] c$



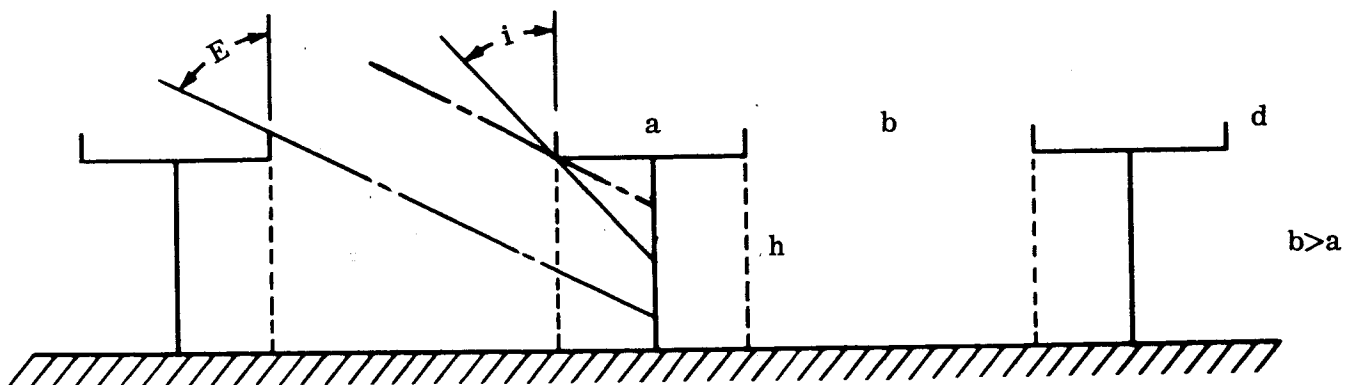
Case B:  $\tan^{-1} \left( \frac{a}{2h} \right) \leq E \leq \tan^{-1} \left( \frac{b}{h+d} \right)$

Boundary Condition on $i$ :	Brightness, $B$
$-E \leq i \leq -\tan^{-1} \left( \frac{a}{2h} \right)$	$K \left\{ \cos  i  \cos E \left[ \rho_A (a - d \tan E) + \rho_B \left( \frac{a}{2} + b - (h+d) \tan E \right) \right] \right.$
$-\tan^{-1} \left( \frac{a}{2h} \right) \leq i \leq \tan^{-1}(0)$	$\left. + \left[ \rho_V \left( h - \frac{a}{2 \tan  i } \right) + 2\rho_D d \right] \cos \left( \frac{\pi}{2} -  i  \right) \cdot \cos \left( \frac{\pi}{2} - E \right) \right\} c$
$\tan^{-1}(0) \leq i \leq \tan^{-1} \left( \frac{b - (h+d) \tan E}{(h+d)} \right)$	$K \left\{ \cos  i  \cos E \left[ \rho_A (a - d \tan E) + \rho_B [b - (h+d) \tan E + h \tan  i ] \right] \right.$
$\tan^{-1} \left( \frac{b - (h+d) \tan E}{(h+d)} \right) \leq i \leq \tan^{-1}(\infty)$	$\left. + 2\rho_D \cos \left( \frac{\pi}{2} -  i  \right) \cos \left( \frac{\pi}{2} - E \right) \cdot d \right\} c$
	$K \left\{ \cos  i  \cos E \left[ \rho_A (a - d \tan E - d \tan i) + \rho_B [b - (h+d) \tan E - (h+d) \tan i] \right] \right\} c$
	$K \cos  i  \cos E \cdot \rho_A [a - d(\tan E + \tan i)] c$



Case C:  $\tan^{-1} \left( \frac{b}{(h+d)} \right) \leq E \leq \tan^{-1} \left( \frac{b+a/2}{(h+d)} \right)$

Boundary Condition on $i$ :	Brightness, $B$
$-E \leq i \leq -\tan^{-1} \left( \frac{a}{2h} \right)$	$K \left\{ \cos  i  \cos E \left[ \rho_A (a - d \tan E) + \rho_B \left[ \frac{a}{2} + b - (h+d) \tan E \right] \right] \right.$ $\left. + \left[ \rho_V \left( h - \frac{a}{2} \frac{1}{\tan  i } \right) + 2\rho_D d \right] \cos \left( \frac{\pi}{2} -  i  \right) \cos \left( \frac{\pi}{2} - E \right) \right\} c$
$-\tan^{-1} \left( \frac{a}{2h} \right) \leq i \leq -\tan^{-1} \left( \frac{(h+d) \tan E - b}{h} \right)$	$K \left\{ \cos  i  \cos E \left[ \rho_A (a - d \tan E) + \rho_B [h \tan  i  - (h+d) \tan E + b] \right] \right.$ $\left. + 2\rho_D \cos \left( \frac{\pi}{2} -  i  \right) \cos \left( \frac{\pi}{2} - E \right) \cdot d \right\} c$
$-\tan^{-1} \left( \frac{(h+d) \tan E - b}{h} \right) \leq i \leq \tan^{-1}(0)$	$K \left\{ \cos  i  \cos E \left[ \rho_A (a - d \tan E) \right] + 2\rho_D \cos \left( \frac{\pi}{2} -  i  \right) \cos \left( \frac{\pi}{2} - E \right) \cdot d \right\} c$
$\tan^{-1}(0) \leq i \leq \tan^{-1}(\infty)$	$K \cos  i  \cos E \cdot \rho_A [a - d(\tan E + \tan  i )] c$



Case D:  $\tan^{-1} \left( \frac{b + a/2}{(h + d)} \right) \leq E \lesssim \tan^{-1}(\infty)$

Boundary Condition on $i$ :	Brightness, $B$
$-E \leq i \leq \tan^{-1} \left( \frac{\tan E}{\frac{1}{2}(b - d \tan E) + 1} \right)$	$K \left\{ \cos  i  \cos E \left[ r_A (a - d \tan E) \right] + \left[ r_V \frac{1}{\tan E} \left( b + \frac{a}{2} \right) - d - \frac{a}{2} \tan \left( \frac{\pi}{2} -  i  \right) \right] \right. \\ \left. + 2r_D d \cos \left( \frac{\pi}{2} -  i  \right) \cos \left( \frac{\pi}{2} - E \right) \right\} c$
$\tan^{-1} \left( \frac{\tan E}{\frac{1}{2}(b - d \tan E) + 1} \right) \leq i \leq \tan^{-1}(\infty)$	$K \cos  i  \cos E \cdot r_A [a - d(\tan E + \tan i)] c$